ISSN: 1301-9724 e-ISSN: 2146-1511

https://dergipark.org.tr/tr/pub/ijot

International Journal of Thermodynamics

Editor-in-Chief

L. Kuddusi

Honorary Editors

A. Bejan

M. J. Moran

J. Szargut

G. Tsatsaronis

A. Valero

M. R. von Spakovsky

Abstracting and Indexing:

Chemical Abstracts Services, Copernicus, DOAJ, EBSCO, Emerging Sources Citation Index, Engineering Index, Google Scholar, Scopus, and ULAKBIM



International Centre for Applied Thermodynamics

International Journal of Thermodynamics

https://dergipark.org.tr/tr/pub/ijot

Editor-in-Chief

Prof. Dr. Lütfullah KUDDUSİ

Associate Editor-in-Chief

Assoc. Prof. Dr. Patrice ESTELLÉ Prof. Dr. Enrico SCIUBBA

Associate Editor

Prof. Dr. Ali KOSAR Prof. Dr. Derya Burcu ÖZKAN

Prof. Dr. Mustafa ÖZDEMİR Prof. Dr. Ahmet DURMAYAZ

Assoc. Prof. Dr. Onur TAYLAN Prof. Dr. Mehmet ARİK

Prof. Dr. Ayşegül ABUŞOĞLU Prof. Dr. G. Reza VAKİLİ-NEZHAAD

Prof. Dr. Bayram ŞAHİN Assoc. Prof. Dr. Murat ÇAKAN

Editorial Board

Prof. Dr. Yasar DEMİREL Prof. Dr. Lütfullah KUDDUSİ

Prof. Dr. Ahmet DURMAYAZ Prof. Dr. Derya Burcu ÖZKAN

Prof. Dr. Mustafa ÖZDEMİR Prof. Dr. Ali KOSAR

Prof. Dr. Mehmet ARİK Assoc. Prof. Dr. Abdussamet SUBASI

Prof. Dr. Daniel FAVRAT Prof. Silvia Azucena NEBRA

Prof. Dr. Luis SERRA Assoc. Prof. Dr. Onur TAYLAN

Prof. Dr. Francois MARECHAL Prof. Dr. Gian Paolo BERETTA

Prof. Dr. Ayşegül ABUŞOĞLU Prof. Dr. Abel HERNANDEZ-GUERRERO

Prof. Dr. Silvio DE OLÍVEÍRA JUNIOR Prof. Dr. Sean WRIGHT

Prof. Dr. Nilufer EGRİCAN Prof. Dr. G. Reza VAKİLİ-NEZHAAD

Prof. Dr. Bayram ŞAHİN Prof. Dr. Vittorio VERDA

Assoc. Prof. Dr. Murat ÇAKAN

International Journal of Thermodynamics https://dergipark.org.tr/tr/pub/ijot

Publishing Editor

Assoc. Prof. Dr. Abdussamet SUBASI Assist. Prof. Dr. Mustafa Yasin GÖKASLAN

Res. Assist. Ali Murat BİNARK Res. Assist. Kasım ERDEM

Language Editor

Assoc. Prof. Dr. Abdussamet SUBASI

Journal Contacts

Editor-in-Chief

Prof. Dr. Lütfullah Kuddusi

ISTANBUL TECHNICAL UNIVERSITY kuddusi@itu.edu.tr

Department of Mechanical Engineering Istanbul Technical University Gumussuyu, 34437 Istanbul Turkey

Volume: 28

Issue: 4

Web: https://dergipark.org.tr/tr/pub/ijot

International Journal of Thermodynamics (IJoT)

ISSN:1301-9724 / e-ISSN:2146-1511

International Journal of Thermodynamics

https://dergipark.org.tr/tr/pub/ijot

ISSN 1301-9724 / e-ISSN 2146-1511

Volume: 28 / No: 4 – December / 2025

CONTENTS	
Research Article	
1. Investigations on Ideal Inverted Brayton Cycle Engines	222-229
M. Karabacak, O. Turan	
Research Article	
2. 4E Analysis of Enhanced Ejector Compression Absorption Cascade Cycle Working with Low GWP and ODP Refrigerants	230-242
B. Mebarki	
Research Article	
3. The Effect of Inlet Baffle on the Skin Friction Coefficient and Turbulence Intensity in an Air-Cooled Channel	243-249
L. N. Thanh, M. P. Nguyen, M. H. Nguyen, H. S. N. Le, N. H. Lai	
Research Article	
4. Cosmic Expansion Driven by Barrow Entropy	250-255
M. F. Karabat	
Research Article	
5. Exergy Analysis of Cyprus International University Solar Power Plants	256-264
M. Yılmaz, M. Atmaca Research Article	
6. Enhanced Prosumer Energy Management Using Modified Social Group Optimization for Cost-Effective and Sustainable Energy Utilization	265-278
S. Singh, R. Bhasker	
Research Article	
7. Numerical Study on Channel-Driven U-Shaped Cavity Flow with Adiabatic Baffles: PEC for W/EG Mixture-Based TiO ₂ -SiO ₂ Hybrid Nanofluid	279-291
M. Jourabian	
Research Article	
8. How Much Labor Was Lost in the US During the Covid-19 Pandemic	292-295
M. Özilgen Research Article	
9. Comparative Study on The Effect of Oxygen-Enriched Air on Combustion of a Spark Ignition Engine Fuelled with Methanol and Ethanol	296-307
Nidhi	
Review Article	
10. Performance, Emissions, Optimization of Ammonia and Biodiesel Utilization in Compression Ignition Diesel Engines: A Review	308-319
D. H. T. Prasetiyo, A. Sanata, G. A. Rahardi, A. Muhammad	

Research Article

Vol. 28 (No. 4), pp. 222-229, 2025 doi: 10.5541/ijot.1649340 Published online: December 1, 2025

Investigations on Ideal Inverted Brayton Cycle Engines

¹*M. Karabacak , ²O. Turan

¹ Necmettin Erbakan University, Department of Aerospace Engineering, Konya, Turkey
² Eskisehir Technical University, Department of Airframe and Powerplant Maintenance, Eskisehir, Turkey
E-mail: 1*karabacak7@itu.edu.tr

Received 1 March 2025, Revised 26 April 2025, Accepted 21 May 2025

Abstract

In this study, T-S and P-V diagrams of the ideal inverted Brayton cycle engine are obtained by using numerical methods in Matlab® environment. The thermodynamic analysis of the inverted Brayton cycle engine is carried out to determine the limitations and development possibilities of this engine type and thus to guide the designer in this field. In the T-S and P-V diagram analysis, many findings about the limits and potential of the engine are obtained. It is observed that in the inverted Brayton cycle engine, unlike the Brayton cycle engine, there is no optimum compressor pressure ratio and the specific work increases as the compressor pressure ratio increases. Regardless of the flight Mach number, entropy generation in the afterburner is approximately $800 \text{ J/(kg\cdot K)}$, and entropy destruction in the cooling section is approximately $1000 \text{ J/(kg\cdot K)}$. Entropy generation in the preburner decreases from around $1800 \text{ J/(kg\cdot K)}$ under takeoff conditions to nearly zero during hypersonic flight, in parallel with the ram compression taking over the function of the preburner.

Keywords: T-S and P-V diagrams; ideal brayton cycle; inverted brayton cycle engines; supersonic speeds.

1. Introduction

Considering that modern aviation started with the first flight of the Wright Brothers in 1903 and has continued its development very rapidly until today, there is one design goal that has remained unchanged in this process, which is to reach higher speeds [1]. In order to achieve this, developments in aircraft design are important, but much more important are the developments in the systems that generate thrust.

Providing thrust to the aircraft with the propeller system powered by internal combustion piston engines seen on the first flight of the Wright Brothers was an indispensable tool in the infancy of aviation [2, 3]. However, propeller engines were insufficient to propel the aircraft to high speeds due to the shock formation on the propeller blades [4]. As a solution to this inadequacy, jet engines developed by two independent inventors in Germany and Britain on the eve of World War II are presented. The first jet engine developed was the turbojet engine, which satisfied the need for higher speeds during the war [5, 6]. However, it was later seen that the turbojet engine concept was insufficient to reach very high Mach numbers.

Introduced in World War II, the ramjet engine was thought to be a key to reach high Mach numbers, but its use was limited, due to its inability to operate efficiently, at low Mach numbers and to reach hypersonic speeds [7,8]. The scramjet concept, which was inspired by the ramjet concept where combustion takes place under supersonic flow conditions [9,10], was thought to be sufficient to take an aircraft to hypersonic speeds [11]. However, combustion at

performance. It is compared to an inverted Brayton cycle engine with an afterburner turbojet engine at supersonic

supersonic flow speeds has been a great challenge and the application of this concept still remains so [12-14].

Over the years, innumerable modifications have been introduced to improve the Brayton cycle. Among them, intercooling, reheating, and combined cycle integration are particularly important. Intercooling reduces the work required by the compressor by cooling the air between compression stages, thereby improving the overall cycle efficiency. Similarly, reheating involves the addition of heat between turbine expansion stages, which increases the energy of the working fluid and allows for greater work output. In combined cycle applications, the waste heat from the Brayton cycle is utilized by a Rankine cycle, significantly boosting the total thermal efficiency of the system. These modifications play a crucial role in reducing fuel consumption and minimizing environmental impact in modern energy generation systems. However, these implementations have not been sufficient to enable jet engines to reach much higher Mach numbers.

In the past decades, the increase in temperature at the inlet of existing gas turbine, like in the turbojet and turbofan engines, have been seen as a way to increase flight Mach number of aeronautical vehicles [15,16]. And the subject has increasingly continued to attract the attention of the aeronautical engineering community. Although jet engine research has focused on increasing turbine inlet temperature to improve performance [17-19], Karabacak et al. [20] proposed a concept of a new jet engine, which can be referred to as inverted Brayton cycle engine, instead of developing turbine inlet temperature technologies to improve

speed (Mach 2.5) and concluded that the concept of the inverted Brayton cycle engine has a performance advantage

*Corresponding Author Vol. 28 (No. 4) / 222

with lower specific fuel consumption and higher thrust and exergy efficiency. It is also examined the inverted Brayton cycle engine in hypersonic flight conditions and observed that this new concept generates thrust at a much higher Mach number than the ramjet and concluded that this concept exhibits higher performance in hypersonic flight conditions than the ramjet. It is made a significant contribution to the studies in this field by observing that the inverted Brayton cycle engine can generate thrust at takeoff and at low Mach numbers and concluded that it generates thrust at a much higher Mach number than the ramjet. It is analyzed the design point and Karabacak and Turan [21] performed the off-design point analysis of the inverted Brayton cycle engine. It is concluded that the thrust reaches the maximum efficiency between Mach 5 and 6 in the off-design point analysis they performed for the first time in the literature and proved once again the superiority of the concept of the inverted Brayton cycle engine in hypersonic flight from a different perspective and made an important contribution to the engine concept studies that will work under hypersonic flight conditions from this point.

Karabacak and Turan [22] continued to contribute to the studies in this field by presenting an optimized version of the inverted Brayton cycle engine for hypersonic conditions at the design point. As a result of the optimization of the inverted Brayton cycle engine in hypersonic flight, a very high specific thrust value with a specific thrust value of over 450 m/s is obtained. But it was not considered in this study the off-design point while optimizing the inverted Bravton cycle engine [20]. The inverted Brayton cycle engine has been investigated before [20-25]. Although recent studies have also appeared in the literature (Karabacak et al. [20] and Karabacak and Turan [21,22]) they are now considered as an auxiliary accessory rather than a new concept for jet engine design [23-25]. But their pioneering work has gained many followers. Battista et al. [24] conducted a thermodynamic assessment of the opportunity to use the inverted Brayton cycle as a power unit to a turbocharged diesel engine. In this work, the most important parameters affecting the possible recovery range (turbine and compressor efficiencies, pressure drops) were evaluated. The aim was to increase the recovery rate by optimizing the pressure ratio. After analyses of a number of technologies available to recover waste heat to reduce fuel consumption and cut down carbon dioxide emissions, including Otto and Diesel cycles, Kennedy and co-workers [25] concluded that the inverted Brayton cycle is certainly one of them.

Murray et al. [23] claimed that heat exchangers with power transfer rates of up to 1 megawatt per kilogram can be manufactured and used in practice. Pre-cooled cycles such as Scmitar [26], ATREX [27] and SABRE [28] are planned to

be developed for the next generation of low-cost transportation [29], but Murray et al. [23] believe that current heat exchanger technologies are still not sufficient to apply this concept. Therefore, the inverted Brayton cycle is expected to be an emerging technology for the aerospace industry [24] to replace the existing heat exchanger technologies [25].

Although the inverted Brayton cycle engine has been studied many times before, the topic examined in this work has never been investigated. The novelty of this study lies in proposing to plot P-V diagrams of the inverted Brayton cycle engine and investigate performance parameters of this new thermodynamic cycle, based on P-V and T-S diagrams.

The aim of this study is to provide theoretical design tools for future designers of the inverted Brayton cycle engines for both military and civil applications.

2. The Thermodynamic Approach

As in the conventional Brayton cycle engine, in the inverted Brayton cycle engine fresh air at ambient conditions is drawn into the engine through an appropriate inlet. The primary function of the inlet (diffuser) is to slow down the incoming high-speed airflow in order to provide the preburner with air at appropriate pressure and velocity. In this component, it is assumed under ideal conditions that the flow is adiabatic and there is no pressure loss. In the subsequent preburner, energy is added to the airflow through combustion, increasing the air temperature. This raises the energy level of the airflow, making it suitable for expansion in the turbine. It is assumed that combustion occurs with 100% efficiency and without any pressure losses in the preburner. The turbine absorbs the energy of the hightemperature airflow through an isentropic process, converting it into mechanical work that is transferred via a shaft to the compressor. Past the turbine, the temperature of the airflow in the cooling section is reduced to enable higher pressures at the compressor outlet. This process is carried out without any pressure loss. Next, the airflow is compressed isentropically using the mechanical energy transferred from the turbine through a shaft with 100% efficiency. The highpressure air in the compressor then enters the afterburner. As in the preburner, the temperature of the airflow is increased at constant pressure, assuming complete combustion efficiency. Finally, as in a conventional Brayton cycle, the expansion process takes place in a nozzle, where the hightemperature and high-pressure air rapidly expands and is thrown out to the atmosphere. The resulting change in momentum produces thrust.

A schematic diagram of the inverted Brayton cycle engine is shown on Figure 1.

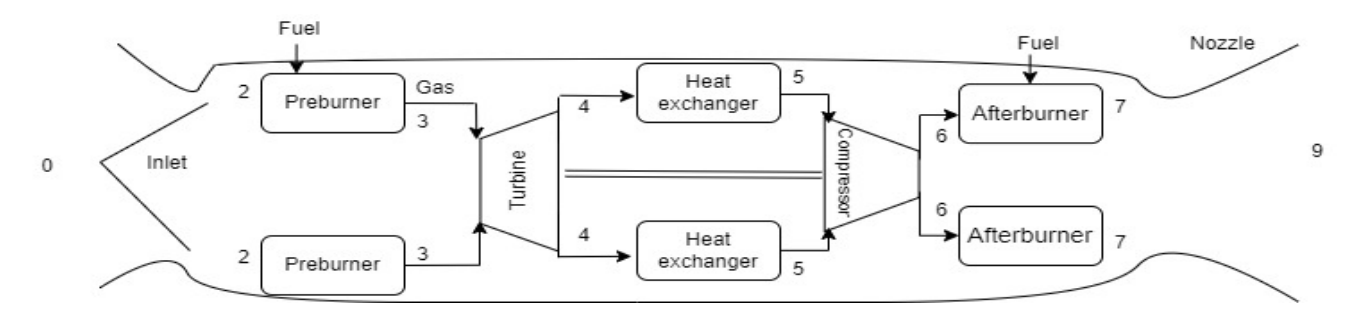


Figure 1. Schematic diagram of the inverted Brayton cycle engine [20].

Design parameters of the inverted Brayton cycle engine are displayed in Table 1 below.

Table 1. Design parameters of the inverted Brayton cycle engine [20].

0 1	
Parameter	Value
Preburner Exit Total Temperature	1500 K
Turbine Total Pressure Ratio	0.1
Total Temperature Decrease at Cooling Section	500 K
Afterburner Exit Total Temperature	2300 K

2.1 The Governing Equations of the Inverted Brayton Cycle Engine

Equations used to determine the performance parameters of the ideal inverted Brayton cycle engine (in accordance with the nomenclature presented in Figure 1) are as follows (Eqs.1-20) [20]:

It is assumed that the inlet flow Mach number is equal to the flight Mach number and by applying isentropic relations of total temperature and total pressure at the inlet expressed as the following:

$$P_{t_0} = P_a \times (1 + \frac{y-1}{2} \times M^2)^{\frac{y}{y-1}}$$
 (1)

$$T_{t_0} = T_a \times \left(1 + \frac{y-1}{2} \times M^2\right)$$
 (2)

Inlet flow pressure losses occur due to the viscosity of air and friction at the inlet solid layer between airflow and due to the shock generation because of the supersonic and hypersonic flow in the inlet, but in this study, it is assumed that the ideal engine that is no losses of the pressure as described equation:

$$P_{t_2} = P_{t_0} \tag{3}$$

In the inlet heat flow between the inlet wall and the atmosphere, so it is expected that total temperature losses occur, but according to the ideal engine assumption, there are no losses of total temperature at the inlet, as shown in equation:

$$T_{t_2} = T_{t_0} \tag{4}$$

Turbulence is the desired state for combustion due to air and fuel mixing requirement and on the other hand, turbulence flow at combustion leads to total pressure losses, but in this study, losses are neglected as expressed in equation:

$$P_{t_3} = P_{t_2} \tag{5}$$

Preburner exit total temperature is limited by the turbine section total temperature limit as defined as;

$$T_{t_3} = T_{t_{\text{limit}}} \tag{6}$$

The turbine total temperature ratio is defined by isentropic relations by applying the isentropic turbine assumption as expressed:

$$\mathfrak{r}_{t} = \mathfrak{n}_{t}^{\frac{y-1}{y}} \tag{7}$$

Turbine exit total temperature depends on the total temperature ratio, is expressed below:

$$T_{t_{4}} = T_{t_{3}} \times r_{t} \tag{8}$$

Turbine exit total pressure is determined depending on the turbine total pressure ratio and turbine inlet total pressure as expressed below:

$$P_{t_4} = P_{t_3} \times \pi_t \tag{9}$$

It is assumed that the total pressure losses at the cooling section are neglected as determined by the equation:

$$P_{t_5} = P_{t_4} \tag{10}$$

To reach a higher total pressure at compressor exit cooling is applied at the cooling section. Compressor inlet total temperature dependent on the total temperature decreases at the cooling section as expressed:

$$T_{t_5} = T_{t_4} - T_{t_{\text{cooling}}} \tag{11}$$

The compressor exit total temperature based on the energy balance between the turbine and compressor is expressed:

$$T_{t_6} = (T_{t_3} - T_{t_4}) + T_{t_5}$$
 (12)

Compressor total temperature ratio, τ_c , depending on compressor exit total temperature, T_{t_6} , and compressor inlet total temperature, T_{t_κ} , determined as the following:

$$\tau_c = \frac{\tau_{t_6}}{\tau_{t_5}} \tag{13}$$

Compressor total pressure ratio, π_c , is expressed by applying the isentropic compressor assumption, by isentropic relations as,

$$\pi_{c} = r_{c}^{\frac{y}{y-1}} \tag{14}$$

Compressor exit total pressure, P_{t6}, dependent on compressor total pressure ratio and compressor inlet total pressure, expressed as the following:

$$P_{t_6} = P_{t_5} \times \pi_c \tag{15}$$

$$T_{t_6} < T_{c_{limit}} \tag{16}$$

Similar to the preburner, afterburner exit total temperature equals afterburner inlet total temperature as shown,

$$P_{t_7} = P_{t_6}$$
 (17)

Similar to the preburner, afterburner exit total temperature is limited by the nozzle section total temperature limit as defined as,

$$T_{t_7} = T_{n_{\text{limit}}} \tag{18}$$

Similar to the inlet, there is heat flow between the nozzle wall and the atmosphere and heat losses due to the shock generation; therefore, it is expected that total temperature losses occur, but according to the ideal engine assumption there are no losses of total temperature at the inlet, as shown in equation:

$$T_{t_9} = T_{t_7}$$
 (19)

Similar to the inlet, nozzle flow pressure losses occur, due to the viscosity of air and friction between the nozzle solid layer and air flow and due to the shock generation owing to the supersonic and hypersonic flow in the nozzle; however, in this study, it is assumed that the ideal engine that is no flow losses of the pressure, as expressed equation:

$$P_{t_0} = P_{t_7} \tag{20}$$

2.2 T-S and P-V Diagrams Governing Equations

The differential entropy change is given:

$$dS = \frac{dH}{T} - \frac{VdP}{T} \tag{21}$$

While the differential enthalpy and the ideal gas equations by:

$$dH = c_P dT (22)$$

$$PV = RT (23)$$

Under the assumption that the specific heat remains constant—in reality, as we know, specific heats vary with T— and by making of use of Eqs. (22) and (23), Eq. (21) can be re-written as

$$dS = \frac{c_P dT}{T} - \frac{RdP}{P} \tag{24}$$

Integration of Eq. (24) yields

$$S = c_p \ln T - R \ln P \text{ or } S = c_p \ln T - R \ln \frac{RT}{V}$$
 (25)

2. Results and Discussions

As can be seen in Figures 2, 4, 6, 8, and 10, increasing the afterburner exit total temperature and decreasing the preburner exit total temperature increases the specific work. However, considering that the afterburner exit total temperature is limited by the material strength temperature, it is clear that the limits of the technology must be pushed to increase the specific work. On the other hand, in order to reduce the preburner exit total temperature, the limitation of not falling below the freezing temperature of the air at the cooling section exit should be taken into consideration. If the water molecules in the gas flow freeze at the outlet of the cooling section, the blades in the compressor stage are physically damaged by the impact of ice particles and can no longer function. As can be seen in Figure 2, increasing the compressor total pressure ratio increases the specific work value without any limit. However, when the Brayton cycle is examined, it is known that the compressor pressure ratio has an optimum value that will maximize the specific work value. At this point, when the compressor total pressure ratio limitation is examined, it is seen that there is a limitation that the gas components fall below the freezing point at the outlet

of the cooling section. It is known that in order to increase the compressor total pressure ratio, the temperature decrease in the cooling section should be increased, but when the temperature decrease in the cooling section is increased, the temperature at the exit of the cooling section decreases and we are faced with the limitation that the temperature drops below the freezing point of the gas components. At this point, the obstacle to increasing the compressor pressure ratio and consequently the specific work is understood.

From the P-V diagrams, one can be observed that as the compressor pressure ratio increases, the pressure at the afterburner inlet also increases, and so does the specific work. At given pressure and specific volume conditions, unlike in the conventional Brayton cycle engine, the turbine is installed prior to the compressor. For this reason, the greater the compressor pressure ratio - along with the increase in the temperature drop in the cooling section- the greater the specific work at given turbine inlet conditions. When examining the P-V diagram of conventional Brayton cycle engines, it is seen that turbine inlet conditions change as the compressor pressure ratio increases. On the one hand, the increase in the pressure ratio raises the pressure at the compressor outlet and turbine inlet, thus positively affecting the specific work, on the other hand, it reduces the specific volume at the turbine inlet, negatively affecting the specific work. These two opposing effects suggest an optimal pressure ratio that maximizes specific work. However, in a inverted Brayton cycle engine, since the compressor pressure ratio does not affect turbine inlet conditions, there is no optimal pressure ratio to be achieved. Instead, specific work continues to increase as the compressor pressure ratio increases.

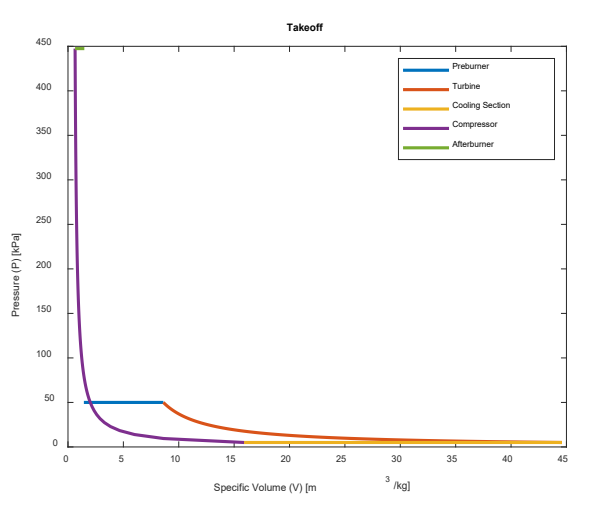


Figure 2. P-V diagram of the inverted Brayton cycle engine at takeoff condition.

When Figures 3, 5, 7, 9 and 11 are analyzed and compared, we obtain a unique perspective in terms of revealing the relationship between the preburner exit total temperature and the specific work. As can be seen in Figure 11, for the atmospheric conditions expressed and at Mach 5 and the inverted Brayton cycle engine design parameters expressed (1500 K preburner exit temperature), since the total preburner exit temperature is reached with ram compression, there is no need for a preburner and the specific work reaches the highest point with design without preburner component, that is, when the desired temperature is reached with ram compression. Figures 3, 5, 7 and 9 show that the need for the preburner to operate to reach the required turbine

inlet temperature reduces the specific work. On the other hand, since it is known that the compressor pressure ratio increases with the increase in the preburner exit total temperature, it is also seen that the preburner exit total temperature indirectly increases the specific work, i.e. by increasing the compressor pressure ratio. At this point, it is understood that when searching for ways to increase the specific work of the inverted Brayton cycle engine, the interaction of the components should be taken into consideration instead of examining the components individually. Considering that the compressor total pressure ratio increase will increase the specific work and hence the thrust, it is understandable that ways should be sought to increase the compressor total pressure ratio without increasing the total temperature at the preburner exit. Increasing the temperature decrease in the cooling section is the only option at this point. However, increasing the temperature decrease in the cooling section faces technical limitations such as the limitation of falling below the freezing temperature of the gas components. This is because the current heat exchanger technologies to achieve cooling at a specific required level is insufficient.

Entropy generation occurs in both the preburner and afterburner, while entropy destruction takes place in the cooling section. At low Mach number flight, entropy generation in the preburner is higher than that in the afterburner. However, as the flight Mach number increases, the effect of ram compression leads to a decrease in entropy generation within the preburner. Entropy generation in the afterburner remains constant at approximately 800 J/(kg·K) across all Mach numbers due to the inlet and outlet conditions of the afterburner being independent of flight Mach number. On the other hand, entropy generation in the preburner decreases from around 1800 J/(kg·K) under takeoff conditions to nearly zero during hypersonic flight, in parallel with the ram compression taking over the function of the preburner. In the cooling section, entropy destruction of approximately 1000 J/(kg·K) is observed, which is higher than the entropy generation occurring in the afterburner.

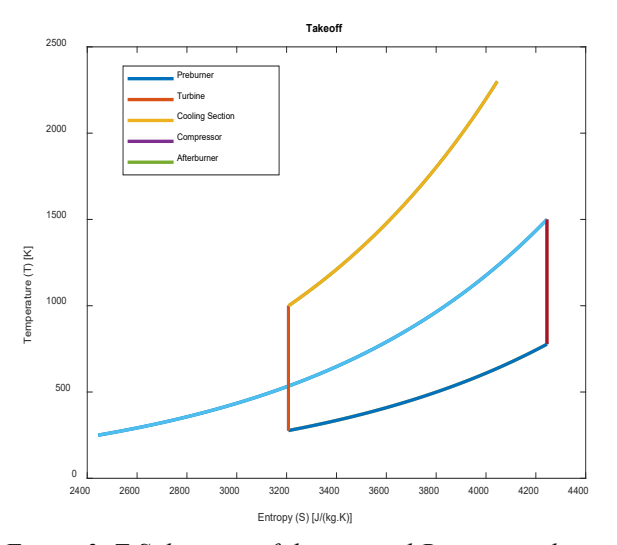


Figure 3. T-S diagram of the inverted Brayton cycle engine at takeoff condition.

In order to increase the specific work, energy must be added to the airflow in the two combustion chambers (afterburner and preburner). However, the energy added to the airflow is restricted by the metallurgical limit. Under current material temperature limitations, the only design option is to force the energy added to the airflow be shared between combustion chambers. Otherwise, the structural integrity of the turbojet engine components will be compromised.

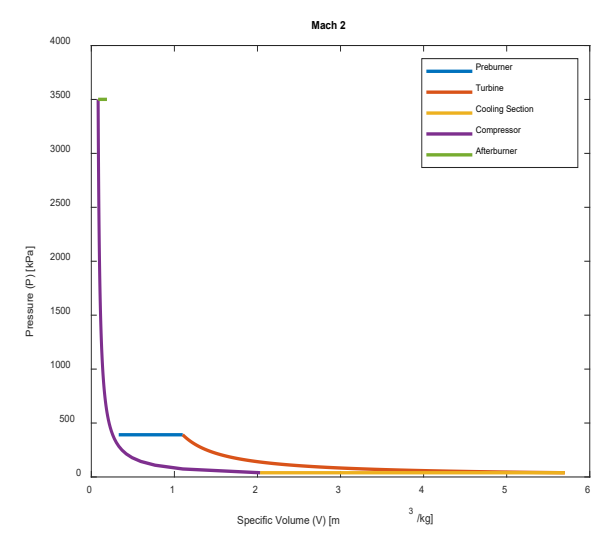


Figure 4. P-V diagram of the inverted Brayton cycle engine on Mach 2 flight condition.

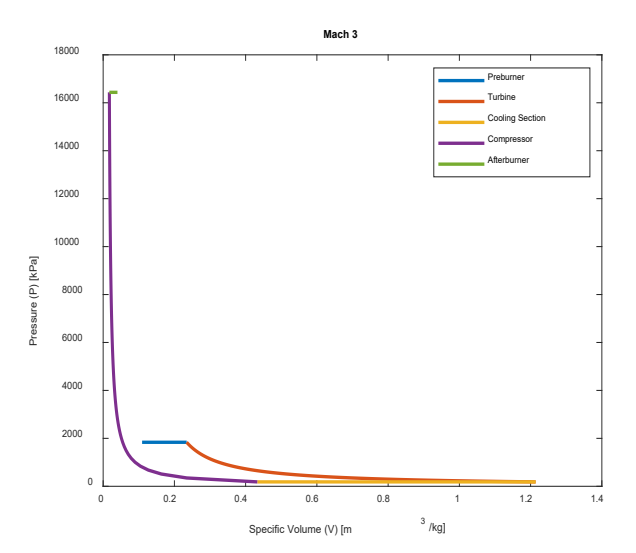


Figure 5. T-S diagram of the inverted Brayton cycle engine on Mach 2 flight condition.

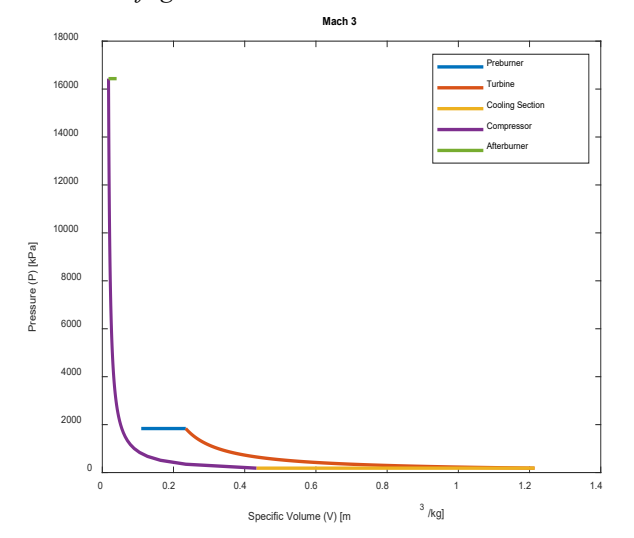


Figure 6. P-V diagram of the inverted Brayton cycle engine on Mach 3 flight condition.

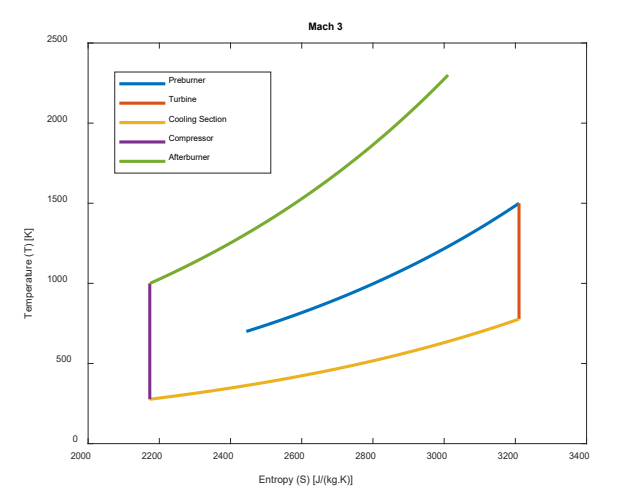


Figure 7. T-S diagram of the inverted Brayton cycle engine on Mach 3 flight condition.

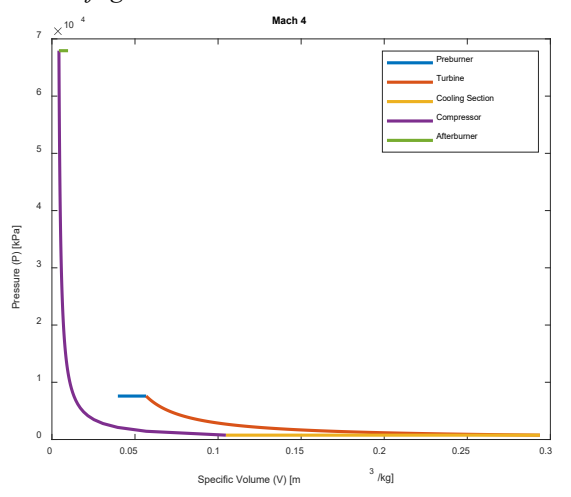


Figure 8. P-V diagram of the inverted Brayton cycle engine on Mach 4 flight condition [30, 31].

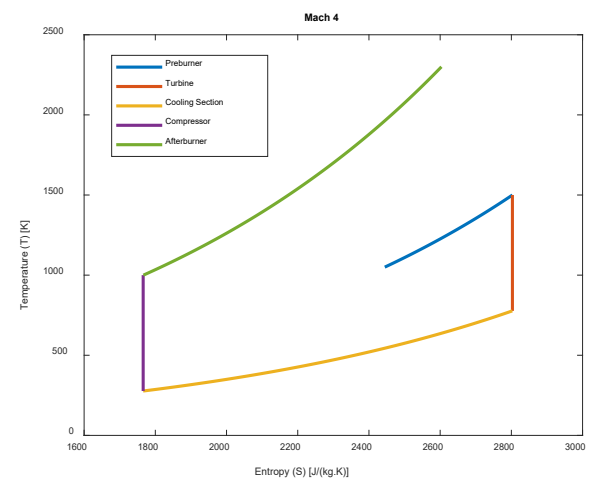


Figure 9. T-S diagram of the inverted Brayton cycle engine at on Mach 4 flight condition.

The most effective way to increase specific work is to raise the temperature at the exit of the afterburner. Unfortunately, a restrictive factor (the metallurgical limit) comes into play at this stage of the design. A too high temperature would compromise the material's structural integrity at the exit of the afterburner. A viable alternative would be to use thermal barrier coatings or implement regenerative cooling. Either of these would permit a substantial increase in temperature, producing a significant rise in the specific work.

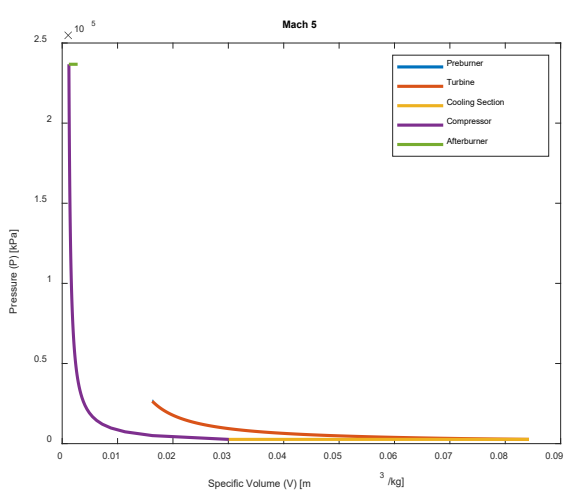


Figure 10. P-V diagram of inverted Brayton cycle engine on Mach 5 flight condition [30, 31].

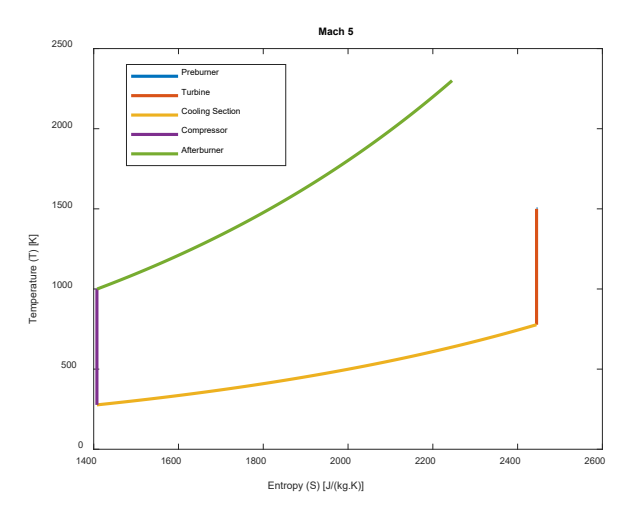


Figure 11. T-S diagram of inverted Brayton cycle engine on Mach 5 flight condition [30, 31].

An ideal (thermodynamic) cycle operates in a closed loop. In an actual cycle the working fluid is renewed at the end of each cycle instead of being recirculated. As such, this study is incomplete and called for a real cycle analysis in future work.

4. Conclusions and Further Work

Given the state-of-the-art technology of the design of modern jet engines, the authors suggest the following:

- Increasing the afterburner exit total temperature and decreasing the preburner exit total temperature increases the specific work. However, the afterburner exit total temperature is restricted by the metallurgical limit. As such the limits imposed by todays' technology must be pushed forward in order to make possible an increase in the specific work of the cycle engine. By the same token, in order to reduce the temperature at the exit of the preburner, air must be kept above the freezing temperature at the cooling exit section. And this is a technological challenge.
- At least at the atmospheric conditions of Mach 5, there is no need for installing a preburner, a component not even required by engine design parameters.
- The need for a preburner to operate to reach the required turbine inlet temperature reduces the specific work. Having said that, there is a need for searching alternative ways to increase the specific work of the engine cycle. The

interaction between components should be taken into consideration rather than examining them individually.

The inverted Brayton cycle engine is a candidate with great potential to propel jet engines in future hypersonic flight. However, it faces a major challenge: the design of better performing heat exchangers. In order to ensure the feasibility of the inverted Brayton cycle engine, the design of future heat exchangers must meet one crucial requirement: the cooling load at low weight and volume.

The plot of thermodynamic diagrams for the real inverted Brayton cycle will be the aim of future work.

Conflict of Interest

Authors approve that to the best of their knowledge; there is not any conflict of interest or common interest with an institution/organization or a person that may affect the review process of the paper.

Credit Author Statement

Mustafa Karabacak: Conceptualization, Methodology, Software, Data curation, Writing- Original draft preparation, Visualization, Investigation. **Onder Turan:** Supervision, Validation, Writing- Reviewing and Editing.

Nomenclature

Nomence	iatui C
c_p	Constant pressure specific heat [J/(kg.K)]
H	Enthalpy [J/kg]
M	Fight mach number [-]
m	Mass flow rate [kg/s]
P_a	Atmosphere pressure [Pa]
P_{t_0}	Engine inlet total pressure [Pa]
P_{t_2}	Preburner inlet total pressure [Pa]
P_{t_3}	Turbine inlet total pressure [Pa]
P_{t_4}	Cooling section inlet total pressure [Pa]
P_{t_5}	Compressor inlet total pressure [Pa]
P_{t_6}	Afterburner inlet total pressure [Pa]
P_{t_7}	Nozzle inlet total pressure [Pa]
P_{t_9}	Engine outlet total pressure [Pa]
R	Molar gas constant [J/(kg.K)]
S	Entropy [J/(kg.K)]
T_a	Atmosphere temperature [K]
T_{t_0}	Engine inlet total temperature [K]
T_{t_2}	Preburner inlet total temperature [K]
T_{t_3}	Turbine inlet total temperature [K]
T_{t_4}	Cooling section inlet total temperature [K]
T_{t_5}	Compressor inlet total temperature [K]
T_{t_6}	Afterburner inlet total temperature [K]
T_{t_7}	Nozzle inlet total temperature [K]
T_{t_9}	Engine outlet total temperature [K]
$T_{t_{\text{cooling}}}$	Total temperature decrease at cooling section [K]
$T_{t_{limit}}$	Turbine temperature limit [K]
$T_{n_{limit}}$	Nozzle temperature limit [K]
V	Specific volume [m³/kg]
у	Specific heat ratio [-]
ŋ	Efficiency [-]
π_c	Compressor total pressure ratio [-]
π_t	Turbine total pressure ratio [-]
	~

Compressor total temperature ratio [-]

Turbine total temperature ratio [-]

References

- [1] J. Tobin, *To Conquer the Air: The Wright Brothers and the Great Race for Flight*, New York, NY, USA: Simon & Schuster, 2003.
- [2] R. Decher, Powering the World's Airliners: Engine Developments from the Propeller to the Jet Age, Barnsley: Air World, 2020.
- [3] J. D. Anderson, *Introduction to flight*, 5th ed. New York, NY, USA: McGraw-Hill, 2005.
- [4] M. R. Anvekar, *Aircraft Propulsion*, New Delhi, India: PHI Learning Private Limited, 2016.
- [5] S. M. Pavelec, *The Jet Race and the Second World War*, New York, NY, USA: Bloomsbury Publishing USA, 2007.
- [6] O. E. Lancaster, *Jet Propulsion Engines*, vol. 3931, Princeton, NJ, USA: Princeton University Press, 2015.
- [7] S. Sarkar, *Jet Engines: A Comprehensive Analysis of History, Design Principles, and Future Trends*, Dhaka: CATECH Publications, 2011.
- [8] S. Luo, Y. Feng, J. Song, D. Xu, and K. Xia, "Progress and challenges in exploration of powder fueled ramjets," *Applied Thermal Engineering*, vol. 213, Aug. 2022, Art. no. 118776, doi: 10.1016/j.applthermaleng.2022.118776.
- [9] G. Choubey and M. Tiwari, *Scramjet Combustion:* Fundamentals and Advances, Oxford, UK: Butterworth-Heinemann, 2022.
- [10] C. Segal, *The Scramjet Engine: Processes and Characteristics*, vol. 25, 1st ed. Cambridge, UK: Cambridge University Press, 2009.
- [11] E. Prisell, "The scramjet: A solution for hypersonic aerodynamic propulsion," in *Proc. 41st AIAA/ASME/SAE/ASEE Joint Propulsion Conf. & Exhibit*, Tucson, AZ, USA, Jul. 2005, p. 3550. doi: 10.2514/6.2005-3550.
- [12] Z. Ren, B. Wang, G. Xiang, D. Zhao, and L. Zheng, "Supersonic spray combustion subject to scramjets: Progress and challenges," *Progress in Aerospace Sciences*, vol. 105, pp. 40–59, Feb. 2019, doi: 10.1016/j.paerosci.2018.12.002.
- [13] J. J. Chang, J. Zhang, W. Bao, and D. Yu, "Research progress on strut-equipped supersonic combustors for scramjet application," *Progress in Aerospace Sciences*, vol. 103, pp. 1-30, Nov. 2018, doi: 10.1016/j.paerosci.2018.10.002.
- [14] Z. Lv, J. Xu, G. Song, R. Li, and J. Ge, "Review on the aerodynamic issues of the exhaust system for scramjet and turbine based combined cycle engine," *Progress in Aerospace Sciences*, vol. 143, Nov. 2023, Art. no. 100956, doi: 10.1016/j.paerosci.2023.100956.
- [15] A. F. El-Sayed, Fundamentals of Aircraft and Rocket Propulsion. Cham, Switzerland: Springer, 2016.
- [16] C. Fan, R. Jiang, and S. Zhang, "Current Status and Future Prospects of Jet Engines," Highlights in Science, Engineering and Technology, vol. 29, pp. 240–246, Jan. 2023, doi: 10.54097/hset.v29i.4836.

 \mathfrak{r}_c

 \mathfrak{r}_c

- [17] E. Benini and S. Giacometti, "Design, manufacturing and operation of a small turbojet-engine for research purposes," *Applied Energy*, vol. 84, no. 11, pp. 1102–1116, Nov. 2007, doi: 10.1016/j.apenergy.2007.05.006.
- [18] M. Siyahi, H. Siyahi, M. Fallah, and Z. Mohammadi, "Thermodynamic Optimization and Energy-Exergy Analyses of the Turboshaft Helicopter Engine," *International Journal of Thermodynamics*, vol. 27, no. 3, pp. 15–25, Sep. 2024, doi: 10.5541/ijot.1458027.
- [19] M. Elwardany, A. E. M. NassiB, and H. A. Mohamed, "Comparative Evaluation for Selected Gas Turbine Cycles," *International Journal of Thermodynamics*, vol. 26, no. 4, pp. 57–67, Dec. 2023, doi: 10.5541/ijot.1268823.
- [20] M. Karabacak, M. Kirmizi, H. Aygun, and O. Turan, "Application of exergetic analysis to inverted Brayton cycle engine at different flight conditions," *Energy*, vol. 283, Nov. 2023, Art. no. 129054, doi: 10.1016/j.energy.2023.129054.
- [21] M. Karabacak and O. Turan, "Off-design analysis of the inverted Brayton cycle engine," *Aircraft Engineering and Aerospace Technology*, vol. 96, no. 7, pp. 954–963, Aug. 2024, doi: 10.1108/AEAT-02-2024-0032.
- [22] M. Karabacak and O. Turan, "Inverted Brayton Cycle Engine Optimization for Hypersonic Flight," *Eskişehir Technical University Journal of Science and Technology A Applied Sciences and Engineering*, vol. 24, no. 4, pp. 257–274, Dec. 2023, doi: 10.18038/estubtda.1270986.
- [23] J. J. Murray, A. Guha, and A. Bond, "Overview of the development of heat exchangers for use in air-breathing propulsion pre-coolers," *Acta Astronautica*, vol. 41, no. 11, pp. 723–729, Dec. 1997, doi: 10.1016/S0094-5765(97)00199-9.
- [24] D. Di Battista, F. Fatigati, R. Carapellucci ve R. Cipollone, "Inverted Brayton Cycle for waste heat recovery in reciprocating internal combustion

- engines," *Applied Energy*, vol. *253*, Nov. 2019, Art. no. 113565, doi: 10.1016/j.apenergy.2019.113565.
- [25] I. Kennedy, Z. Chen, B. Ceen, S. Jones ve C. D. Copeland,"Experimental investigation of an inverted Brayton cycle for exhaust gas energy recovery, "Journal of Engineering for Gas Turbines and Power, vol. 141, no. 3, p. 032301, Oct. 2019, doi: 10.1115/1.4041109.
- [26] P. C. Dong, H. L. Tang, and M. Chen, "Study on multicycle coupling mechanism of hypersonic precooled combined cycle engine," *Applied Thermal Engineering*, vol. 131, pp. 497–506, Feb. 2018, doi: 10.1016/j.applthermaleng.2017.12.002.
- [27] T. Sato, N. Tanatsugu, Y. Naruo, J. Omi, J. Tomike, and T. Nishino, "Development Study on Atrex Engine," *Acta Astronautica*, vol. 47, no. 11, pp. 799– 808, Dec. 2000, doi: 10.1016/S0094-5765(00)00129-6.
- [28] H. Webber, A. Bond, and M. Hempsell, "Sensitivity of pre-cooled air breathing engine performance to heat exchanger design parameters," in Proc. 57th Int. Astronautical Congress, Valencia, Spain, Oct. 2006, pp. D2–P.
- [29] X. Yu, C. Wang, and D. Yu, "Thermodynamic design and optimization of the multi-branch closed Brayton cycle based precooling-compression system for a novel hypersonic aeroengine," *Energy Conversion and Management*, vol. 205, Feb. 2020, Art. no. 112412, doi: 10.1016/j.enconman.2019.112412.
- [30] M. Karabacak, Design and Performance Optimization of Engines for Low-Observable Aircraft with Supercruise Capability, Ph.D. dissertation, Dept. of Aircraft and Powerplant Maintenance, Eskisehir Technical Univ., Eskisehir, Turkey, (in Turkish), 2024.
- [31] M. Karabacak, *Propulsion Systems Design Projects*, Ankara, Turkey, Akademisyen Kitabevi, (in Turkish), 2024.

Research Article

Vol. 28 (No. 4), pp. 230-242, 2025 doi: 10.5541/ijot.1566242 Published online: December 1, 2025

4E Analysis of Enhanced Ejector Compression Absorption Cascade Cycle Working with Low GWP and ODP Refrigerants

*B. Mebarki

Laboratory of Built Environment, Department of Structures and Materials, Faculty of Civil Engineering, University of Science and Technology Houari Boumediene (USTHB), Bab Ezzouar, Algiers, Algeria E-mail:*billal.mebarki@usthb.edu.dz

Received 13 October 2024, Revised 29 December 2024, Accepted 14 April 2025

Abstract

In this paper, a new ejector compression absorption cascade cycle is presented. The energy, exergy, economic, and environmental analyses of the enhanced ejector compression cascade cycle are carried out. The model of the ejector and the compression absorption cascade cycle are validated using numerical and experimental results from literature in the same operating conditions. The thermodynamic performance of 9 refrigerant fluids with low GWP and ODP are compared. Then comparison of the performance of the proposed cycle and the conventional compression absorption cascade cycle is presented and the effect of the same conception parameter on the performance of the proposed cycle is defined. The results show that the RE170 has a higher coefficient of performance and exergy efficiency and a lower annual cost of the proposed cycle than the other 8 refrigerants, further the RE170 has GWP equal to 0.1 and ODP equal to 0. The enhancement in the coefficient of performance and in the exergy efficiency of proposed cycle is 3.27 and 2.7 % respectively compared with conventional compression absorption cascade cycle. Also, the diminution of the annual cost and the equivalent mass emission of CO₂ of proposed cycle is 7.93, 2.3 % compared with conventional compression absorption cascade cycle. The analysis of obtained results allows the conclusion that there is a generation temperature in which the coefficient of performance and the exergy efficiency of the proposed cycle are at maximum value and its annual cost is at minimum value. The coefficient of performance and the exergy efficiency of the proposed cycle are positively affected by increasing the sub-cooling heat exchanger efficiency and both its annual cost and its equivalent mass of CO2 emission are negatively affected, contrary to the inlet temperature of the absorption cycle section in the cascade heat exchanger. The heat exchanger components of the proposed cycle are responsible for the most the destruction of exergy. The performances of the proposed cycle are promoted.

Keywords: Absorption cascade; ejector compression; enhanced ejector; COP; exergy efficiency.

1. Introduction

The compression absorption cascade refrigeration cycle has become an attractive cycle because of its low consumption of electrical energy and its low environmental impact [1]. Moreover, in 2022, the European Commission restricted using of refrigerants with high global warming potential (GWP) to more than 150 except for the primary fluid of the cascade refrigeration cycle can be equal to 1500 [2].

Many studies were carried out about the compression absorption cascade cycle (CACC). Khelifa et al. [1] studied the conventional compression absorption cascaded cycle using different combinations like refrigerants R1234yf, R1234ze (E), and R1233zd (E) for compression cycle and (LiCl-H₂O) and (LiBr-H₂O) for absorption cycle. The geothermal energy of Guelma which is province in Algeria is used as the heat of generation. They found that the diminution of the electrical energy consumed by the cascade compression absorption cycle can reach 54.16% compared with the vapor compression refrigeration cycle in the same operating conditions. Du et al. [3] simulated the conventional

compression absorption cascaded cycle working with different refrigerants for the compression cycle and (LiBr- $\rm H_2O$) for the absorption cycle. They found that the coefficient of performance and the exergy efficiency of refrigerant RE170 are better than the other 15 refrigerants studied.

Many attempts are made for enhancing the performance of absorption cooling machine, Salek et al. [4] studied the effect of add rectifier to ammonia water absorption cycle to have maximum purity of ammonia refrigerant. Its analysis based on two approaches the first is energetic and the second is exergetic. They found that the use of rectifier for ammonia water absorption cycle enhances the coefficient performance and the exergy efficiency of cycle and reduced the exergy destruction total of cycle. B. Gurevich and A. Zohar [5] coupled an ammonia water absorption cycle with solar collector to study the variation of its performance with the daily and the monthly variation of the exterior temperature and same design parameter like solar collector area. They found that the coefficient of performance of cycle and the cooling production by the cycle are slightly affected by the

*Corresponding Author Vol. 28 (No. 4) / 230

growth of area of solar collector contrary for the generation heat.

The use of ejectors for enhancement of the performance of vapor compression is the subject of many articles, Maalem et al. [6] investigated the use of new refrigerant R1311 with zero GWP as substitute refrigerant R134a in vapor compression coupled with an ejector. They found that in the most case the cycle working with R1311 has better performance than the cycle use R134a. Fingas et al. [7] studied experimentally a vapor compression cycle used as a heat pump working with two different technology expansion valves and ejectors. They found that the heating coefficient of performance of the cycle using the ejector is higher by 38% than the cycle using the expansion valve.

Zou et al. [8] proposed a new vapor compression cycle working with both vapor injection and enhanced injector. The results show that the coefficient of performance of the proposed cycle is higher by 38.4 % than the conventional vapor compression cycle.

Also, the use of sub cooling heat exchanger is proposed by many researchers to improve the performance of the vapor compression cycle. Qi et al [9] introduced a subcooling heat exchanger to enhance the ejector vapor compression heat pump. They found a positive effect of the use of sub-cooling on the performance of enhanced ejector heat pumps. Moreover, Pitrach et al. [10-12] studied the experimental effect of the use of sub cooling heat exchanger on the performance of the vapor compression cycle using as heat pump. They found the use of sub-cooling can increase the coefficient of performance by 31 % compared with the vapor compression cycle without sub-cooling.

The previous studies on the absorption cooling cycle used principally two working pairs which are the NH₃-H₂O and H₂O-BrLi. Cimsit and Ozturk [13] compared the performance of CACC using two pairs. They found that the CACC used H₂O-LiBr has a higher coefficient of performance by 33% compared with CACC used NH₃-H₂O. Moreover, Seyfouri and Ameri [14] found that for CACC using NH₃-H₂O, the electrical energy consumed by the solution pump was high due to the high difference in pressure between the absorber and the generator. Therefore, the working pair choices for the absorption cycle section in this work are H₂O-LiBr.

In this paper, a new cycle of ejector compression absorption cascade cycle is presented. The energy, exergy, economic, and environment studies of enhanced ejector compression absorption cascade cycle are carried out. The model developed is validated using two steps, the first step is to compare the results obtained in this work with literature results of the compression absorption cascade cycle and the second step is the comparison of ejector model obtained in this work with experimental and numerical results found in literature in same operating conditions. The performance of the proposed cycle working with 9 low GWP and ODP refrigerants of the vapor compression section is compared the thermodynamic performance and the annual of proposed cycle cost are compared with the conventional compression absorption cascade cycle. Also, the effect of the generation temperature, the outlet temperature of the absorption section of the proposed cycle, and the sub-cooling heat exchanger efficiency are analyzed. The exergy destruction and the investment cost of the main component of the proposed cycle are studied.

2. The Proposed Solution to Develop Performance of Conventional Compression Absorption Cascaded Cycle

In this paper, a new solution is proposed to enhance the conventional compression-absorption cascaded performance cycle by incorporating an ejector, a sub-cooling heat exchanger, and an expansion valve, and separator to reduce the inlet mass flow of the compressor and its work by division into two parts the first enters the evaporator and continues to the compressor and the second compresses in the ejector and joined the first part in the compressor by using separator at a pressure equal to outlet ejector pressure and for enhancement the cooling production, the second part of refrigerant vaporizes in the sub-cooling heat exchanger after it expanded in expansion valve and the first part is sub cooling in the sub-cooling heat exchanger to maximize the cooling production in the evaporator.

3. Enhanced Ejector Compression Absorption Cascaded Cycle Description

Figure 1 illustrates the enhanced ejector compression absorption cascaded cycle (EECACC) which its components are a generator, an absorber, a condenser, a solution pump, a solution heat exchanger, a cascade heat exchanger, a liquid-vapor exchanger, a sub-cooling heat exchanger, an evaporator, an ejector, a separator tank, a compressor, three expansion valves, and a reducer pressure valve.

At point (7), the liquid-vapor mixture of H₂O enters the cascade heat exchanger absorbs the heat from the refrigerant of the enhanced ejector compression cycle, thus the absorption cycle refrigerant vaporizes and leaves the cascade heat exchanger in a vapor-saturated state at point (8). Then it heats in the liquid-vapor heat exchanger to reach point (9) which is the state of entering the absorber and absorbs by a weak solution coming from the reduced valve at point (15), the result is a strong solution cools at the absorber which it leaves at the point (10). The strong solution at point (10) undergoes an enhancement of pressure to condensation pressure at point (11) by passing the pump solution. The strong solution at point (11) heats by the weak solution leaving the generator at the solution heat exchanger to achieve point (12) which is the state of entering of the generator. The weak solution leaves the generator at point (13) is cooling in the solution heat exchanger by the strong solution and it leaves the heat exchanger at point (14) which undergoes an expansion in the reducer valve to reach point (15) and completes the cycle of solution. On the other hand, the saturated water vapor left the generator at point (16) condensed in the condenser, and left at point (5). The saturated water liquid is sub cooled in the liquid-vapor heat exchanger by water vapor left of the evaporator to achieve the point (6). The sub-cooling water liquid at point (6) expands in the expansion valve to close the absorption cycle at point (7).

For the enhanced ejector compression cycle, the cooling refrigerant vapor in the cascade heat exchanger at point (3) enters the ejector as primary fluid to entrain the secondary fluid of the ejector entering at point (4). The ejector compression fluid leaves the ejector at point (25) divided into two parts in the separator tank, the first is in a liquid state at point (26) cooled in the sub-cooling heat exchanger to reach a point (27) by the secondary ejector fluid which is a part of refrigerant of point (27) expands to the point (28) in the expansion valve EV03 and heats in the sub-cooling

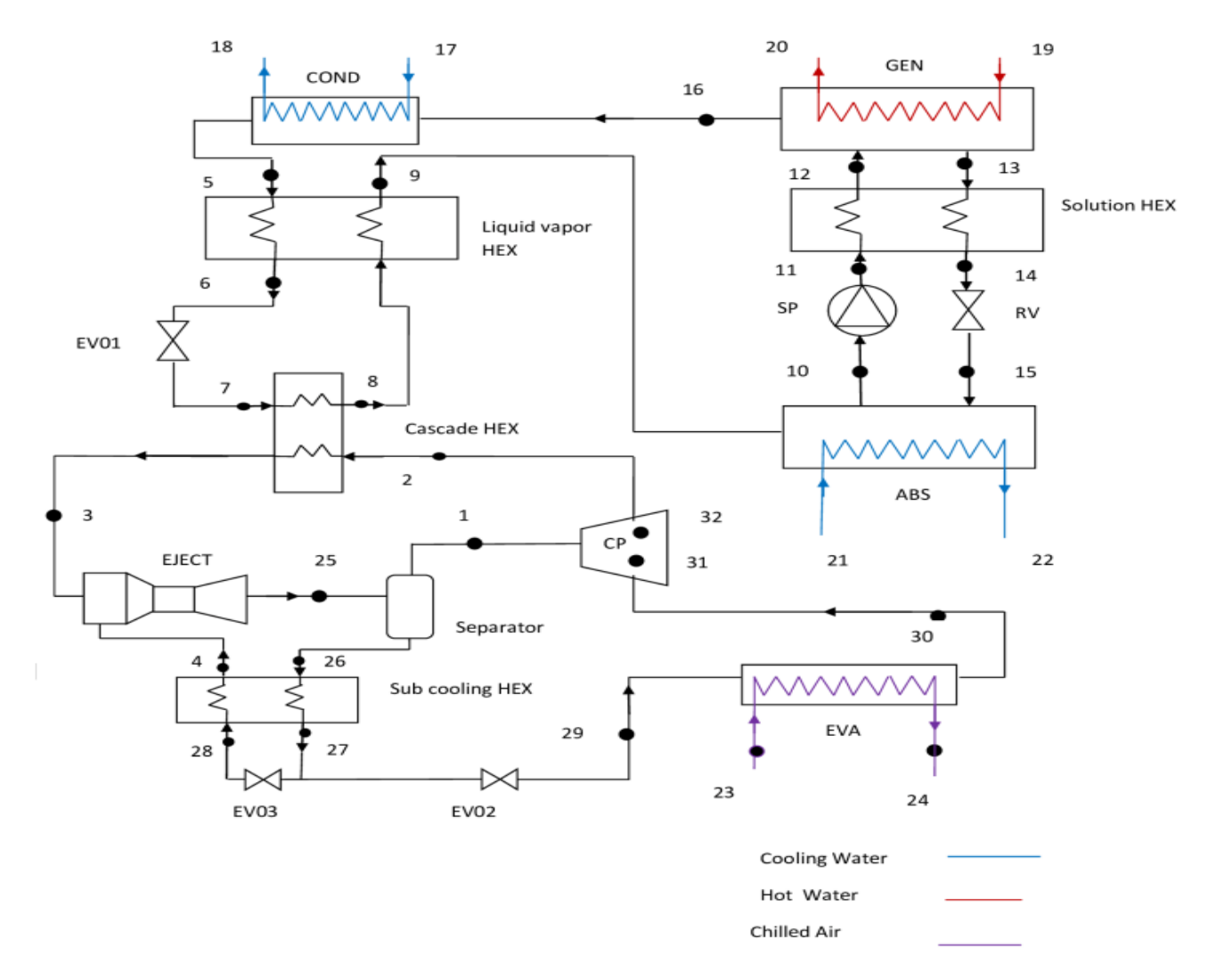


Figure 1. Schematic of Enhanced Ejector Compression Absorption Cascade Cycle (EECACC).

heat exchanger to the point (4). The other part of the refrigerant expands in the expansion valve EV02 to become a mixture of liquid vapor state at point (29) and evaporates in the evaporator and leaves in the saturated vapor state at point (30) and compresses in the compressor from the evaporation pressure to the outlet ejector pressure at point (31), than meets the second part of refrigerant left the separator tank at vapor saturated state at the point (1). The mixed superheated refrigerant vapor at point (32) is compressed at the compressor to point (2) and cooled in the cascade heat exchanger to point (3).

Figure 2 illustrates the conventional compression absorption cascade cycle (CCACC) which is explained by Du et al. [3]. The CCACC energy, exergy, and economic models are used in this paper for validation and comparison purposes.

4. Thermodynamic Cycle Modeling

4.1 Ejector Model

The ejector model used in this study is based on the model presented by Cheng et al. [15]. The type of model is the one-dimensional constant pressure of the mixing section. The following assumptions are taken in this study [15]:

- There is no exchange of heat between the ejector and exterior.
- The velocities of primary and secondary fluid of the ejector in the inlet of the ejector are neglected.

- The velocity of the fluid at the outlet of the ejector is neglected.
- The efficiency of the ejector nozzle, mixing, and diffuser section is considered constant.
- The refrigerant flow energy losses in the ejector are taken into account by using different ejector section efficiency.

The use of the energy, mass, and momentum conservation laws for every ejector section like as nozzle, mixing, and diffuser allows for defining the thermo physics parameters of the ejector as follows:

The outlet nozzle chamber velocity of primary fluid can be defined by the following equation [15]:

$$U_{n,out} = \sqrt{\eta_n \cdot (h_{p,in} - h_{n,out,is}) \cdot 1000}$$
 (1)

where, U is the primary fluid velocity, $h_{p,in}$ is the primary fluid enthalpy at the inlet of the nozzle chamber, η_n is the isentropic efficiency of the nozzle chamber, the subscript in is the inlet, out is the outlet and the is the isentropic expansion.

The outlet mixing chamber fluid velocity and enthalpy can be calculated as follows [15]:

$$U_{m,out} = \frac{U_{n,out}}{I + \mu} \sqrt{\eta_m}$$
 (2)

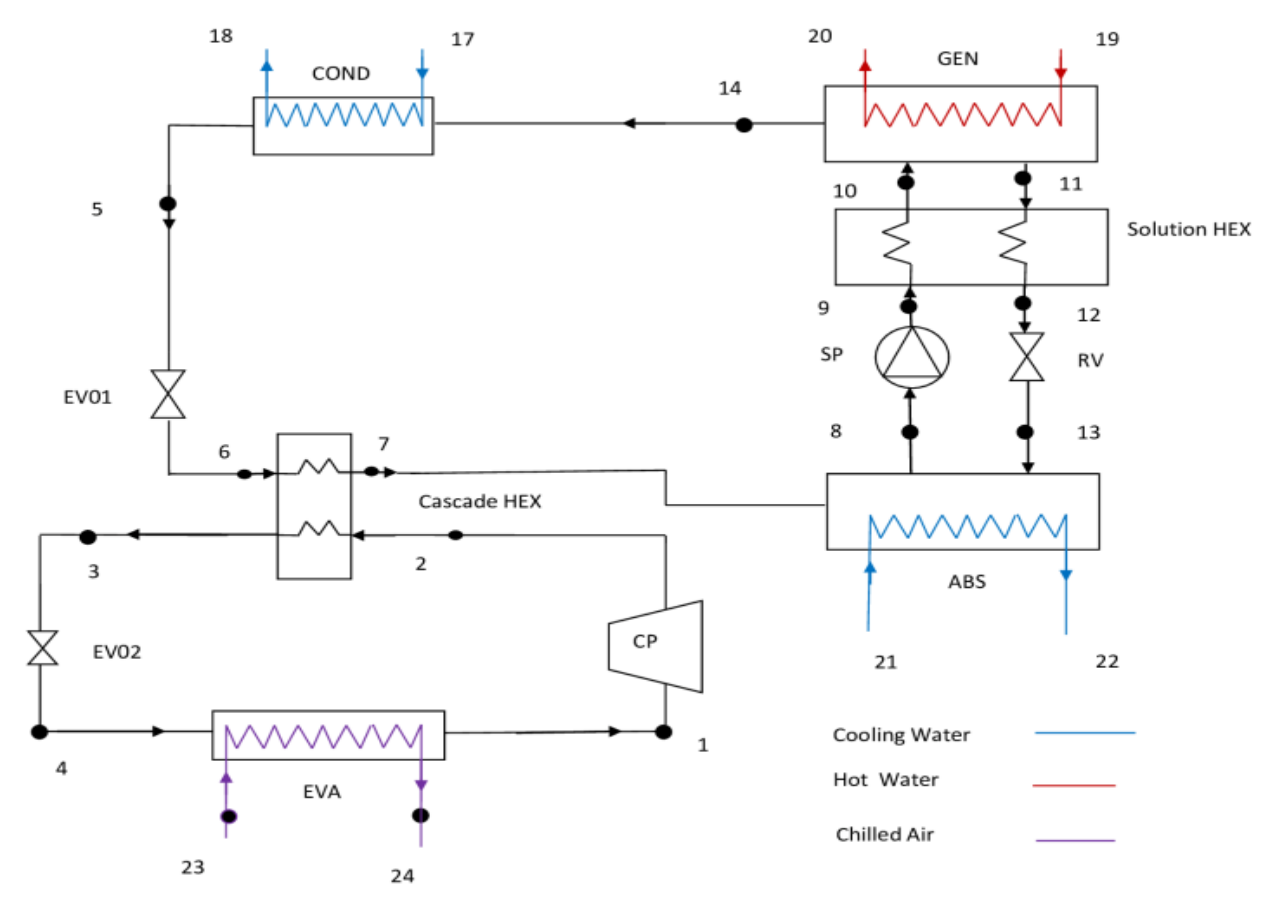


Figure 2. Schematic of Compression Absorption Cascade Cycle (CCACC).

$$h_{m,out} = \frac{h_{n,in} + \mu \cdot h_{s,in}}{1 + \mu} - \left(\frac{U_{n,out}^2}{2}\right) / 1000$$
 (3)

where, $h_{s,in}$ is the secondly fluid enthalpy at the nozzle chamber inlet, η_m is the efficiency of the mixing chamber and μ represents the entrainment ratio which can be calculated by the following equation [15]:

$$\mu = \frac{m_p}{m_s} \tag{4}$$

The outlet diffuser chamber fluid enthalpy which is the fluid enthalpy at the ejector outlet calculated by the following equation [15]:

$$h_{d,out} = h_{m,out} + \frac{h_{d,out,is} - h_{m,out}}{\eta_d}$$
 (5)

where, η_d is the efficiency of the diffuser chamber.

The entrainment ratio of the ejector can be evaluated using previous equations [15]:

$$\mu = \sqrt{\eta_n \cdot \eta_m \cdot \eta_d \frac{h_{p,in} - h_{n,out,is}}{h_{d,out,is} - h_{m,out}}} - 1$$
 (6)

4.2 Thermodynamic Model

Applying mass conservation, the first and second laws of thermodynamics for each component of the cycle allows defining the energy and the exergy balance of each component of cycle and the analysis of the thermodynamic performance of the cycle. Many assumptions must be made to simplify the study:

- The proposed cycle is under steady conditions [17], [16].
- Except in the ejector, the loss of pressure in all cycle components is negligible [16].
- There is no heat exchange between the cycle and environment except what is considered in the study [17].
- The outlet refrigerant state of the condenser, evaporator, and cascade heat exchanger are in saturated liquid, saturated vapor, and saturated vapor, respectively [17].

4.2.1 Mass Conservation

The mass conservation law can be defined as follows [15]:

$$\sum m_i - \sum m_o = 0 \tag{7}$$

$$\sum m_i \cdot x_i - \sum m_o \cdot x_o = 0 \tag{8}$$

where, m is the mass flow of refrigerant rate and x is the lithium bromide mass fraction in the solution, the subscript i is the inlet and o is the outlet.

4.2.2 The First Law of Thermodynamics

The first thermodynamic law which is the energy conservation law of component can be found by applying flowing equation [18]:

$$\left(\sum m_i.h_i - \sum m_0.h_0\right) + \left(\sum Q_i - \sum Q_0\right) + W = 0$$
 (9)

where, h is the specific enthalpy, Q is heat exchanged and W is the mechanical work to or from to component, the subscript i is the inlet and o is the outlet.

The energy balance equations of CCACC and EECACC are presented in Table 1.

4.2.3 The Second Law of Thermodynamics

The exergy study of the cycle allows us to optimize the performance and to understand the weak point from the point of view of finding the component that produces more exergy destruction to find a solution to decrease it in the future. In this study, only the physics exergy is taken into consideration [3]. Thus, the component exergy flow rate can be found by the following equation [15]:

$$Ex = \sum_{i} Q_{j} \cdot (1 - \frac{T_{0}}{T_{i}}) + (\sum_{i} (m_{i} \cdot ex_{i})_{in} - (\sum_{i} m_{i} \cdot ex_{i})_{out} - W$$
 (10)

Table 1. The energy balance of different components of cycle.

Cycle	Cycle component	The energy balance
CCACC	Generator	$Q_g = m_{14}.h_{14} + m_{10}.h_{10} - m_{11}.h_{11}$
	Absorber	$Q_a=m_7.h_7+m_{13}.h_{13}-m_8.h_8$
	Condenser	$Q_c = m_{14}.h_{14}-m_5.h_5$
	Cascade heat exchanger	$Q_{chx} = m_7.h_7 - m_6.h_6$
	Evaporator	$Q_e = m_1.h_1 - m_4.h_4$
	Expansion valve EV01	$h_5=h_6$
	Expansion valve EV02	$h_3=h_4$
	Reducing valve	$h_{12} = h_{13}$
	Solution heat exchanger	$T_{12} = T_{11} - \varepsilon_{\text{she}} \cdot (T_{11} - T_9)$ $h_{10} = \frac{m_{11}}{m_{10}} \cdot (h_{11} - h_{12}) + h_9$ $h_{21} - h_4$
	Compressor	$W_{\text{com}} = m_1 \cdot \frac{h_{2, \text{ is}} - h_1}{\eta_{\text{is, com}} \cdot \eta_{\text{el}}}$
EECACC	Generator	$Q_g = m_{13}.h_{13} + m_{16}.h_{16} - m_{12}.h_{12}$
	Absorber	$Q_a = m_9.h_9 + m_{15}.h_{15} - m_{10}.h_{10}$
	Condenser	$Q_c = m_{16}.h_{16}-m_5.h_5$
	Cascade heat exchanger	$Q_{chx} = m_8.h_8 - m_7.h_7$
	Evaporator	$Q_e = m_{30}.h_{30}-m_{29}.h_{29}$
	Expansion valve EV01	$h_6=h_7$
	Expansion valve EV02	h ₂₇ =h ₂₉
	Expansion valve EV03	h ₂₈ =h ₂₉
	Reducing valve	$h_{14} = h_{15}$
	Solution heat exchanger	$T_{14} = T_{13} - \varepsilon_{\text{she}} \cdot (T_{13} - T_{11})$ $h_{12} = \frac{m_{13}}{m_{11}} \cdot (h_{13} - h_{14}) + h_{11}$
	Liquid vapor heat exchanger	$T_{6} = T_{5} - \varepsilon_{\text{che}} \cdot (T_{5} - T_{8})$ $h_{9} = \frac{m_{5}}{m_{7}} \cdot (h_{5} - h_{6}) + h_{8}$ $T_{7} = T_{7} - \varepsilon_{8} \cdot (T_{7} - T_{7})$
	Sub cooling heat exchanger	$T_{27} = T_{26} \cdot \varepsilon_{\text{sbhe}} \cdot (T_{26} \cdot T_{28})$ $h_4 = \frac{m_{26}}{m_4} \cdot (h_{26} - h_{27}) + h_{28}$
	Compressor	$W_{\text{com}} = m_{30} \cdot \frac{h_{31, \text{ is}} - h_{30}}{\eta_{\text{is}, \text{ com}}, \eta_{\text{el}}} + m_2 \cdot \frac{h_{2, \text{ is}} - h_{31}}{\eta_{\text{is}, \text{ com}}, \eta_{\text{el}}}$

where, ex_i is the specific exergy at each state point of cycle which is defined as follows [18]:

$$ex_i = (h_i - h_0) - T_0 \cdot (s_i - s_0)$$
 (11)

where, h_0 , T_0 and S_0 are representing the specific enthalpy, temperature, and specific entropy of reference environmental state which are $T_0 = 25$ °C and $P_0 = 101$ kPa.

The different component exergy destruction of EECACC is presented in Table 2.

Table 2. The exergy destruction of different components of EECACC.

Cycle component	The destruction exergy
Generator	$Ex_g = m_{12}.ex_{12} + m_{19}.ex_{19} - m_{13}.ex_{13} - m_{16}.ex_{16}$
	$-m_{20}.ex_{20}$
Absorber	$Ex_a = m_9.ex_9 + m_{15}.ex_{15} + m_{21}.ex_{21} - m_{10}.ex_{10}$
	$m_{22}.ex_{22}$
Condenser	$Ex_c = m_{16}.ex_{16} + m_{17}.ex_{17} - m_5.ex_5 - m_{18}.ex_{18}$
Cascade heat exchanger	$Ex_{chex} = m_2.ex_2 + m_7.ex_7 - m_3.ex_3 - m_8.ex_8$
Evaporator	$Ex_e = m_{23}.ex_{23} + m_{29}.ex_{29} - m_{24}.ex_{24} - m_{30}.ex_{30}$
EV 01	$Ex_{ev1}=m_6.T_0.(S_6-S_7)$
EV 02	$Ex_{ev2}=m_{29}.T_0.(S_{27}-S_{29})$
EV 03	$Ex_{ev3}=m_{28}.T_0.(S_{27}-S_{28})$
Solution heat exchanger	$Ex_{hx} = m_{11}.ex_{11} + m_{13}.ex_{13} - m_{12}.ex_{12} - m_{14}.ex_{14}$
Separator tank	$Ex_{st} = m_{25}.ex_{25} - m_1.ex_1 - m_{26}.ex_{26}$
Liquid vapor heat	$Ex_{1vhex} = m_5.ex_5 + m_8.ex_8 - m_6.ex_6 - m_9.ex_9$
exchanger	
Sub cooling heat	$Ex_{Sbhx} = m_{26}.ex_{26} + m_{28}.ex_{28} - m_{4}.ex_{4} - m_{27}.ex_{27}$
exchnager	
Compressor	$Ex_{com} = m_{30}.ex_{30}$
	$+ m_{32}.ex_{32}- m_2.ex_2- m_{31}.ex_{31}+W_{com}$
Ejector	$Ex_{ej} = m_3.ex_3 + m_4.ex_4 - m_{25}.ex_{25}$

The total destruction exergy of the EECACC which is the sum of the exergy production of each component can be found by following the equation [15]

$$Ex_{dt} = \sum Ex_i \tag{12}$$

The EECACC and the CCACC coefficient performance are calculated using the following equation [15]:

$$COP = \frac{Q_{ev}}{Q_{\sigma} + W_{com}} \tag{13}$$

The ECACC and the CCACC exergy efficiency are calculated by following equation [15]

$$\eta_{ex} = \frac{Q_{ev} \cdot \left(I - \frac{T_0}{T_{ev}}\right)}{Q_g \cdot \left(I - \frac{T_0}{T_o}\right) + W_{com}}$$
(14)

4.3 The Economic Study

The economic analysis is the cost study of investment, operating, and maintenance of the cycle during the lifetime of operation but it is presented in the form of annual cost. The model used in this study is defined by Jain and al [19] and calculated by following equation:

$$C_T = t_{op} \cdot (C_f Q_g + C_{ele} \cdot W_{comp}) + C_r \cdot M \cdot \sum_{i} Z_i + C_{env}$$
 (15)

where, C_T is the cost total of cycle, t_{op} is annual operation time, C_f is the cost fuel of heat generation, C_{ele} is the electrical energy cost, M is the maintenance factor, Z_i in the investment cost of cycle component, C_{env} is the social cost

of CO_2 emission of cycle and C_r is the capital recovery factor which is defined by the following equation [4]:

$$C_r = \frac{i.(i+1)^L}{(i+1)^L - 1} \tag{16}$$

where, i is the interest annual rate and L is the cycle lifetime.

The investment cost of heat exchangers of cycle is depending to its exchange area which can be concluded using the following equation:

$$Q_i = U_i \cdot A_i \cdot LMTD_i \tag{17}$$

where, *LMTD* is the logarithmic mean temperature difference and it can be calculated with the following equation:

$$LMTD_{i} = \frac{\Delta T_{i}^{H} - \Delta T_{i}^{c}}{ln\left(\frac{\Delta T_{i}^{H}}{\Delta T_{i}^{c}}\right)}$$
(18)

In Table 3, the global heat exchange coefficient and *LMTD* of all heat exchangers of cycle are presented.

The investment cost of heat exchangers is defined by following equation [23]:

$$Z_{invi} = 516.62 x A_i + 268.45 \tag{19}$$

Table 3. The heat exchanger coefficient and LMTD of heat exchangers of cycle [24, 25].

	J J L	
Component	$U(kW/(m^2\cdot K))$	LMTD
GEN	1.5	LMTD _{gen} = $\frac{(T_{19}-T_{13})-(T_{20}-T_{16})}{\ln{(\frac{T_{19}-T_{13}}{T_{19}-T_{16}})}}$
ABS	0.7	LMTD _{abs} = $\frac{(T_{15} - T_{22}) - (T_{10} - T_{21})}{\ln(\frac{T_{15} - T_{22}}{T_{15} - T_{22}})}$
CON	2.5	LMTD _{cond} = $\frac{(T_5 - T_{17}) - (T_5 - T_{18})}{\ln(\frac{T_5 - T_{17}}{T_5 - T_{17}})}$
SHE	1	$LMTD_{SHE} = \frac{(T_{12} - T_{13}) - (T_{11} - T_{14})}{\ln(\frac{T_{12} - T_{13}}{T_{13}})}$
LVHE	1	$LMTD_{LVHE} = \frac{(T_5 - T_9)^{T_{11} - T_{14}} - (T_6 - T_8)}{\ln(\frac{T_5 - T_9}{T_6 - T_8})}$
SBHE	1	LMTD _{SBHE} = $\frac{(T_{26} - T_4) - (T_{27} - T_{28})}{\ln(\frac{T_{26} - T_4}{T_{77} - T_{28}})}$
CHE	0.55	$LMTD_{CHE} = T_3 - T_8$
EVA (EECACC)	1.5	$LMTD_{EVA} = \frac{(T_{23} - T_{29}) - (T_{24} - T_{29})}{\ln{(\frac{T_{23} - T_{29}}{T_{24} - T_{29}})}}$
EVA (CCACC)	1.5	$LMTD_{EVA} = \frac{(T_{23} - T_4) - (T_{24}^{-1} - T_4)}{\ln(\frac{T_{23} - T_4}{T_{24} - T_4})}$

The compressor investment cost is calculated by following equation [2]:

$$\begin{split} Z_{inv\text{-}comp} &= (\frac{573.\,m_2}{0,\,8996 - \eta_{is,com}}) \cdot \left(\frac{P_{32}}{P_2}\right) \cdot ln\left(\frac{P_{32}}{P_2}\right) \\ &+ (\frac{573.\,m_{30}}{0,\,8996 - \eta_{is,com}}) \cdot \left(\frac{P_{30}}{P_{31}}\right) \cdot ln\left(\frac{P_{30}}{P_{31}}\right) \end{split} \tag{20}$$

The ejector investment cost is defined by following equation [21]:

$$Z_{inv-eje} = 750.m_3. \left(\frac{T_3}{P_3}\right)^{0.05}. \left(\frac{P_{25}}{1000}\right)^{-0.75}$$
 (21)

4.4 The Environmental Study

The environment regulatory requirement is more and more restrict; thus, the study of CO₂ emission is taken into consideration in this study. The annual emission of CO₂ is defined by following equation [22, 23]:

$$m_{co2} = ECF.t_{op}.W_{com} \tag{22}$$

where, *ECF* is emission conversation factor of electricity. The environment cost is defined by following equation [22,23]:

$$C_{env} = \mu_{co2} \cdot \frac{m_{co2}}{1000} \tag{23}$$

where, μ_{co2} is the CO2 emission unit damage cost.

The parameters used in the economy and environmental model are cited in Table 4.

Table 4. The economic and environmental parameters used in this work.

Parameter	Value	Ref.
i	10%	[26]
L	15 years	[26]
M	1.06	[27]
t_{op}	6000 h	[28]
ECF	$0.968~kg.~(kWh)^{-1}$	[29]
C_{f}	0.03785 \$. (kWh) ⁻¹	[2]
C_{e}	$0.0375 \ $ \$. $(kWh)^{-1}$	[2]
μ_{co2}	90 \$.(ton) ⁻¹	[30]

4.5 The 9 Refrigerants Studied

The choice of refrigerant studied based on its impact on the environmental. Table 5 presents the different refrigerants studied and their GWP, ODP.

Table 5. GWP and ODP of 11 refrigerants used in this work [29], [31], [32].

Refrigerant	GWP	ODP	
R600	20	0	
R600a	20	0	
R1234yf	4	0	
R1243zf	<150	0	
R744	1	0	
R290	20	0	
RE170	0.1	0	
R1270	20	0	
R152a	124	0	

5. Results and Discussions

The performance estimation of CCACC and EECACC needs a simulation of functioning by developing a program in engineering equation solver EES based on the thermodynamic, economic, and environmental models given above.

The first step is to define the ejector entrainment ratio by applying an iterative method based on assuming its arbitrary value, then defining the different outlet fluid states of different ejector chambers which are the nozzle, mixing, and diffuser by applying Eqs. (1)-(5) and compare the value assumed with the new entrainment ratio value obtained by Eq. (6), if the difference between the values successive is

under 10⁻⁴ then the algorithm will stop and the entrainment ratio taken value is the last one.

The known entrainment ratio allows for determining all flow mass rates of all state points by applying the mass and energy conservation laws. Then, all energy exchange of all cycle components cited in Table 1 and all exergy destruction cited in Table 2 can be calculated and concluded performance parameters of the cycle. In Figure 3, the simulation flow chart is presented.

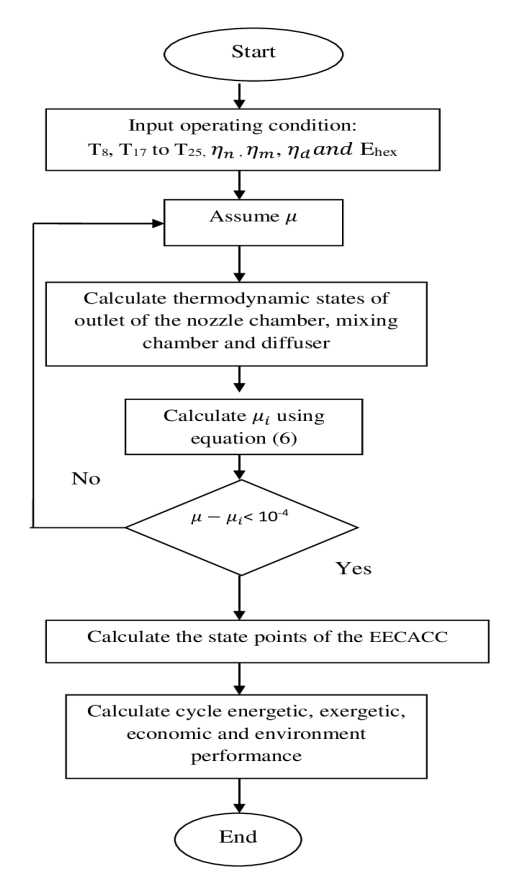


Figure 3. The simulation calculation flowchart.

The working conditions of studied cycle are presented in Table 6.

5.1 Validation of Model

The fact that lack of EECACC simulation results in the literature because it is a novel cycle, the validation of EECACC is based on the validation of its closer model which is the CCACC presented by [3], and the validation of the ejector model separately.

The validation of CCACC is based on the comparison of results obtained from this work and results obtained by [3] of the same cycle using the R134a, R744, R152a and R32 as refrigerants of the vapor compression section. The simulation results are presented in Table 7 in the same operating conditions presented in Table 6. It is clear that the results of the model developed for CCACC in this work are close to the results of [3].

5.2 Performance Comparison of EECAC working with 9 Refrigerant

The coefficient of performance and the exergy efficiency of EECACC working with 9 low GWP and ODP refrigerants are presented in Table 9.

The results show that the thermodynamic performances of all refrigerants studied are very close and two refrigerants R600 and RE170 had the same performance.

The choice of refrigerant of EECACC was studied based on the environmental impact of refrigerant and consequently, the fluid choice is RE170.

Table 6. Operating condition using in this study.

Parameter	Value	Parameter	Value
Qev	250 kW	ΔT_{eva}	8 K
T_{g}	363.15 K	ΔT_{con}	8 K
T_7	283.15 K	ΔT_{gen}	8 K
T_{17}	300.15 K	ΔT_{abs}	8 K
T_{18}	305.15 K	ΔT_{che}	8 K
T_{19}	381.15 K	$\epsilon_{ m she}$	0.7
T_{20}	371.15 K	ϵ_{Lvhe}	0.7
T_{21}	300.15 K	$\epsilon_{\rm sche}$	0.7
T_{22}	305.15 K	$\eta_{is, com}$	0.8
T_{23}	271.15 K	$\eta_{el,\;com}$	0.9
T ₂₄	266.15 K		

5.3 Performance Comparison Between EECACC and CCACC:

In this section, the thermodynamic performances and annual economic cost of EECACC and CCACC are compared according to the model presented above under the same operating conditions shown in Table 5.

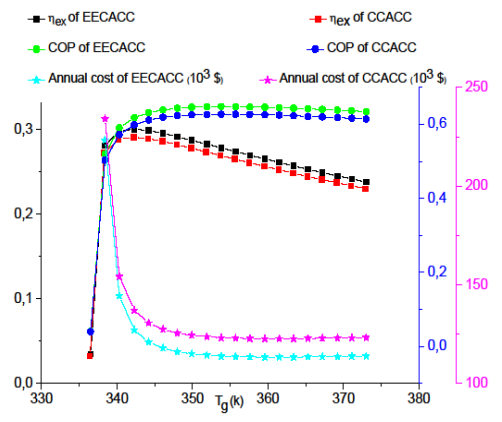


Figure 4. the variation of the exergy efficiency, COP and annual cost of EECACC and CCACC with the variation of generation temperature.

Figure 4 shows the effect of the generation temperature on the exergy efficiency, COP and the annual cost of EECACC and CCACC, the COP of the two systems increases from 0.04 and 0.039 to 0.6435 and 0.6231, respectively with the increasing of generation temperature up to 348 K and then tends to stabilize around 0.64 and, 0.62 respectively and the coefficient of performance of EECACC is higher than the coefficient of performance of CCACC and the maximum value of the coefficient of performance of EECACC is 0.6477 at the generation temperature equal to 353.8 k. In addition, the coefficient of performance of the proposed EECACC cycle is 3.27% higher than the coefficient of performance of the CCACC cycle.

The exergy efficiency of EECAC and CCACC increases to the maximum values of 0.3 and 0.2921 at a generation temperature equal to 342.3 K, then decreases with increasing the generation temperature, and the EECACC exergy efficiency is higher than the CCACC by 2.7 %.

Table 7. Comparison of results obtained from this work and from [3] (COP_{ABS}: COP of absorption cycle, COP_{COM}: COP of

vapor compression section, COP_{CCACC} : cop of CCACC).

	R	134a/H₂O-LiF	3r	R	744/H ₂ O-Li	Br	R1	52a/H₂O-I	LiBr	R	32/H ₂ O-LiB	r
Parameters	Ref [3]	This work	Ref [3]	This work	dev (%)	Ref [3]	Ref [3]	This work	dev (%)	Ref [3]	This work	dev (%)
$Q_{GEN}(kW)$	362.65	361.30	361.73	360.40	0.369	363.62	361.73	360.40	0.369	363.62	362.30	0.364
$Q_{CHE}(kW)$	287.74	287.70	287.02	287.00	0.006	288.52	287.02	287.00	0.006	288.52	288.50	0.007
$Q_{ABS}(kW)$	344.48	343.10	343.61	342.30	0.383	345.40	343.61	342.30	0.383	345.40	344.10	0.377
$Q_{CON}(kW)$	305.91	305.90	305.14	305.10	0.013	306.73	305.14	305.10	0.013	306.73	306.70	0.009
$W_{COM}(kW)$	41.91	41.93	41.13	41.14	0.024	42.800	41.13	41.14	0.024	42.800	42.80	0.000
COP_{ABS}	0.794	0.796	0.794	0.796	0.251	0.794	0.794	0.796	0.251	0.794	0.796	0.251
COP_{COM}	5.961	5.962	6.078	6.077	0.016	5.842	6.078	6.077	0.016	5.842	5.841	0.017
COP_{CCACC}	0.618	0.620	0.621	0.622	0.161	0.615	0.621	0.622	0.161	0.615	0.617	0.162
η_{ex}	0.234	0.247	0.236	0.249	5.508	0.232	0.236	0.249	5.508	0.232	0.245	5.603

Contrary to the COP, the annual cost of EECAC and CCACC decreases to 116 and 125.4 thousand dollars respectively at a generation temperature equal to 348 k then trends to stabilize around 113.5 and 122.5 thousand dollars respectively with increasing the generation temperature and the annual cost of EECAC is lower the CCACC annual cost by 7.93 %.

Table 8. Comparisons of entrainment ratio of the ejector model used in present study with experimental results of reference [16] and numerical results of reference [15].

Tg	T_c	Entrainment Ratio			Error	Error
$({}^{\circ}C)$	(°C)	Exp. [16]	Num. [15]	Our model	Exp. (%) [16]	Num. (%)[15]
95	31.3	0.4377	0.4584	0.4473	-2.15	2.48
	33.0	0.3937	0.4114	0.4003	-1.65	2.77
90	33.8	0.3488	0.3614	0.3507	-0.54	3.05
	37.5	0.2718	0.2806	0.2700	0.67	3.93
84	33.6	0.3117	0.3286	0.3182	-2.04	3.27
	35.5	0.2880	0.2858	0.2754	4.58	3.78

It can explain the obtained results by increasing the generation temperature. The strong solution increases, including an enhancement in the difference between the strong and the weak solution, which includes a diminution in the solution mass flow and generation energy needed for heating. The strong solution trends to stabilize, for that reason all parameters above presented also trend to stabilize.

Table 9. Comparison of EECACC thermodynamic performance of 9 refrigerants studied in this work.

perjarment aj s rejiro		
Refrigerant	COP	η_{ex}
R600	0. 6437	0.2576
R600a	0.6428	0.2568
R1234yf	0.6388	0.2534
R1243zf	0.6377	0.2525
R744	0.6054	0.2271
R290	0.6400	0.2545
RE170	0.6437	0.2576
R1270	0.6396	0.2541
R152a	0.6431	0.2571

The obtained results conclude that the EECACC has better performance compared with the conventional compression absorption cascade cycle and the generation temperature of EECACC must be not exceed the stabilization temperature 348 K.

The different state point of EECACC is presented in Table 10.

Table 10. The different properties of proposed cycle state point in operating condition cited in Table 5.

No. of	T	P	h	S	X	m
state point	(<i>K</i>)	(kPa)	(kJ/kg)	(kJ/kg.K)	(g/kg)	(kg/sec)
1	268	223.1	486.5	1.82		0.08643
2	307.9	482.8	537.2	1.867		0.6529
3	291.2	482.8	99.12	0.3659		0.6529
4	265.2	200.8	45.13	0.1744		0.534
5	308.2	5.629	146.6	0.5051		0.1169
6	290.7	5.629	73.45	0.2606		0.1169
7	283.2	1.228	73.45	0.2621		0.1169
8	283.2	1.228	2519	8.9		0.1169
9	323.8	1.228	2592	9.152		0.1169
10	308.2	1.228	76.13	0.2415	0.5219	0.6021
11	308.2	5.629	76.13	0.2415	0.5219	0.6021
12	339.2	5.629	132.9	0.446	0.5219	0.6021
13	363.2	5.629	239.7	0.483	0.6477	0.4852
14	324.7	5.629	169.2	0.2795	0.6477	0.4852
15	324.7	1.228	169.2	0.2795	0.6477	0.4852
16	363.2	5.629	2669	8.664		0.1169
25	268	223.1	74.79	0.2847		1.188
26	268	223.1	44.66	0.1724		1.102
27	266	223.1	40.02	0.155		1.102
28	265.2	200.8	40.02	0.1552		0.5354
29	263.2	186.1	40.02	0.1553		0.5665
30	263.2	186.1	481.3	1.831		0.5665
31	271.7	223.1	491.6	1.839		0.5665
32	271.2	223.1	490.9	1.836		0.6529

5.4 Effect of the Inlet Temperature of Absorption Refrigerant Cycle to Cascade Heat Exchanger on the Performance of EECACC

The effect of varying the evaporation temperature of the absorption cycle (T₇ in Figure 1) on the coefficient performance, the exergy efficiency and the annual cost of EECACC is presented in Figure 5. With increasing of T₇from 283 to 289 K, the coefficient of performance decreases from 0.6453 to 0.6304, the exergy efficiency decreases from 0.2592 to 0.2375 and the annual cost increases from 119.1 to 127.4 thousand dollars. The reason behind these results is the work of the compressor increases with increasing the compressor outlet pressure which follows the enhancement of T₇, and the annual cost of the system strongly depends on any variation in the work absorbed by the compressor.

It can be resumed the effect of varying the inlet temperature of absorption cycle refrigerant to the cascade heat exchanger from 283 to 289 K, a diminution in the coefficient of performance and the exergy efficiency of the proposed cycle by 2.36 and 9.14 %, respectively and enhancement in its annual cost by 6.97 %.

It can be concluded in the conception of EECAC cycle, the inlet temperature of absorption cycle to the cascade heat exchanger should be the lower possible.

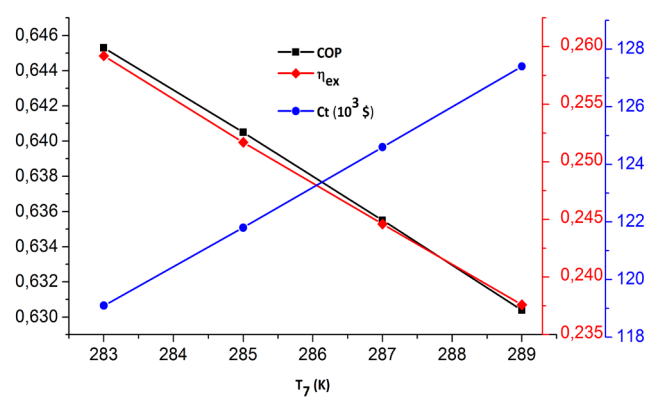


Figure 5. The effect of T_7 on the COP, the exergy efficiency, and the annual cost of EECACC.

Figure 6 shows the effect of sub-cooling heat exchanger efficiency on the coefficient performance, the exergy efficiency and the annual cost of EECACC. The increasing of the sub cooling heat exchanger efficiency from 0.6 to 0.9 includes an enhancement of the coefficient of performance from 0.6423 to 0.6501 and an enhancement of the exergy efficiency from 0.2578 to 0.2601 and a diminution in the annual cost from 119.6 to 118.7 thousand dollar.

These results can be explained by increasing the heat exchanger efficiency, the enthalpy of the ejector secondary fluid inlet increases including an increase in the entrainment ratio, the ejector secondary fluid mass flow as a consequence of a diminution in the evaporator mass flow, and the work of compressor of the first stage and in the whole compressor work

5.5 Effect of Sub Cooling Heat Exchanger Efficiency on the Performance of ECACC $\,$

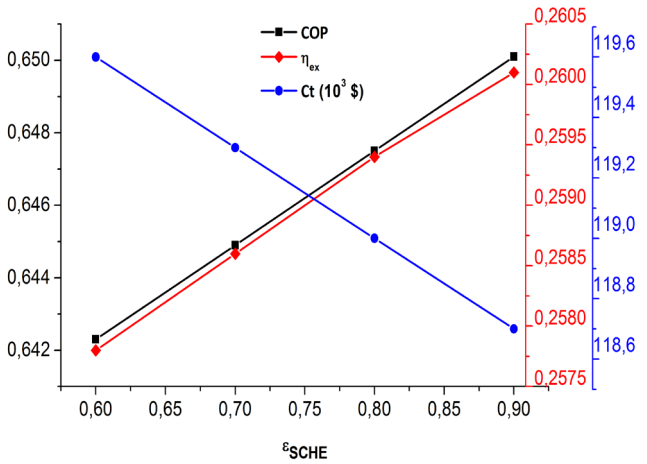


Figure 6. The effect of Sub cooling heat exchanger efficiency of the ejector on the COP, the exergy efficiency, and the annual cost of EECACC.

In can be resumed the effect of varying the sub cooling heat exchanger efficiency from 0.6 to 0.9 by an enhancement in the coefficient of performance and the exergy efficiency of proposed cycle by 0.5 and 0.89%, respectively and diminution in the its annual cost by 0.76 %.

These results shows that the choice of sub cooling heat exchanger must be have an efficiency the higher possible.

5.6 Exergy Analysis of EECACC

The exergy destruction of EECACC components is presented in Figure 7. The cascade heat exchanger (CHE), the sub-cooling heat exchanger (SCHE), the absorber, and the generator are the main components destruction of exergy.

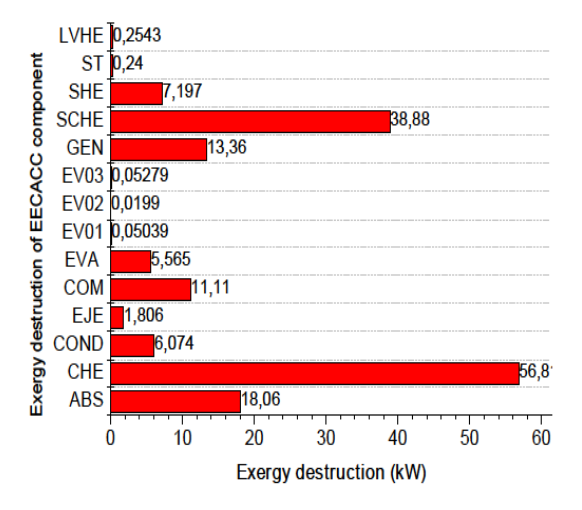


Figure 7. The exergy destruction of different components of EECACC.

It's clear that the heat exchangers are responsible of 91.67 % of the total exergy destruction of cycle. Thus, for reduce the total exergy destruction of cycle and enhance its exergy efficiency, it's indispensable to develop heat exchange in the heat exchangers by using new materials that have thermo physical propriety more adaptive to heat exchange like as high thermal conductivity and low density or new mechanical construction to develop the convection heat exchange coefficient and the global heat exchange coefficient.

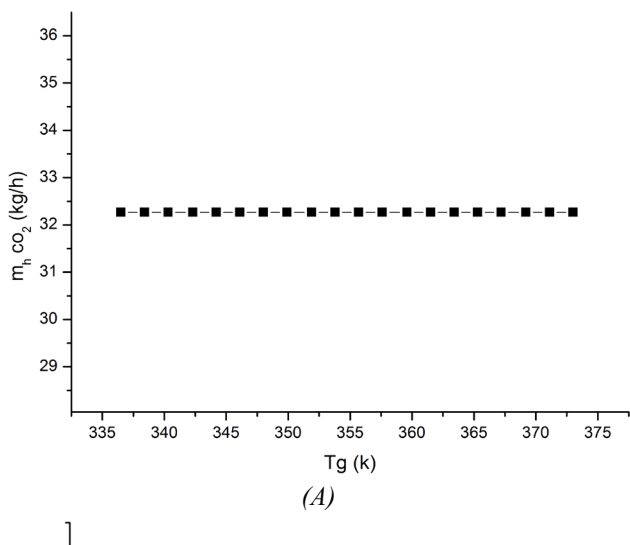
5.7 Environmental Analysis

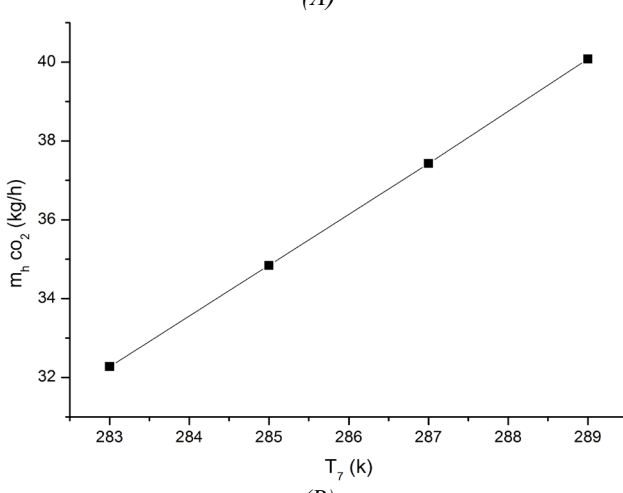
Environmental analysis based on the study of the effect of electrical power consumed by cycle on the environment using the equivalent CO₂ mass emission during one hour of service of the compressor.

Figure 8 presents the effect of the generation temperature, the inlet temperature of absorption cycle refrigerant in the cascade heat exchanger, and the subcooling heat exchanger efficiency on the equivalent mass emission of CO₂. The equivalent mass emission of CO₂ is constant and equal to 32.27 kg/h with variation in generation temperature. It can be explained this result by the mass of CO₂ emission is strongly dependent of the work of the compressor and the operating conditions of the vapor compression cycle were invariable with a variation of generation temperature, thus the work of the compressor is constant. But, the mass of CO2 emission increased from 32.27 to 40.08 kg/h with increasing of the inlet temperature of absorption cycle refrigerant to cascade heat exchange from 283 to 289 K, and the mass of CO₂ emission decreased from 32.28 to 32.5 kg/h with increasing of sub-cooling heat exchanger efficiency from 0.6 to 0.9, it is clear that the variation equivalent emission mass of CO₂ follows the work absorbed by the compressor and the performance efficiency of the cycle.

Figure 9 shows that the proposed EECACC cycle emits 32.27 kg/h of CO₂ into the air and the conventional CCACC cycle emits 33.01 kg/h. The reason is that in the proposed cycle, the mass flow rate at the compressor inlet is smaller

than the mass flow rate at the compressor inlet of CCACC because the use of an ejector in the EECACC allows for compression of a part of the refrigerant which is the secondary fluid from the ejector to the pressure of exiting the ejector.





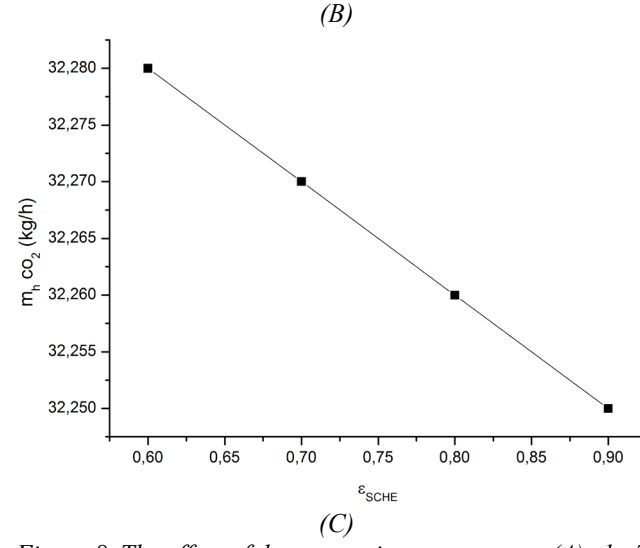


Figure 8. The effect of the generation temperature (A), the T_7 (B) and the sub cooling heat exchanger efficiency factor (C) on the hourly equivalent CO_2 mass emission

It can be concluded that the proposed cycle EECACC is more environmentally friendly because its equivalent mass emission of CO2 is lower by 2.29% than the conventional cycle.

From the point of view environmentally, the choice of the inlet temperature of absorption cycle refrigerant to cascade heat exchange should be lower possible and the subcooling heat exchanger efficiency should be the higher possible.

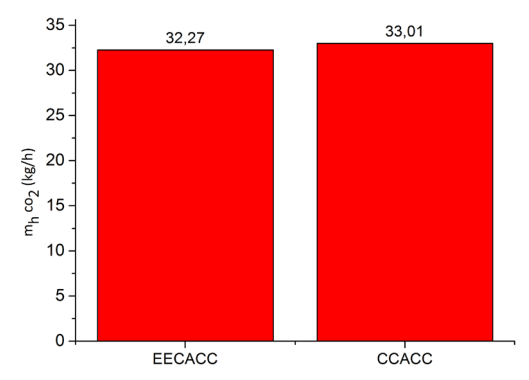


Figure 9. The comparison of equivalent CO₂ mass emission of EECACC and CCACC.

5.8 Investment Cost Analysis

Figure 10 depicts the investment cost of different components of EECACC. The almost investment cost is due to the cost of heat exchangers and the cost of heat exchanger is strongly depending to its area.

The added component the ejector and the sub cooling heat exchanger to the conventional compression absorption cascade cycle enhances in the investment cost by 3.14% in the total investment cost of EECACC.

Many recommendations can be made that the use of novel materials for heat exchangers with low prices and to develop the design of heat exchangers to enhance the global heat exchange coefficient could be diminution the investment price of EECACC.

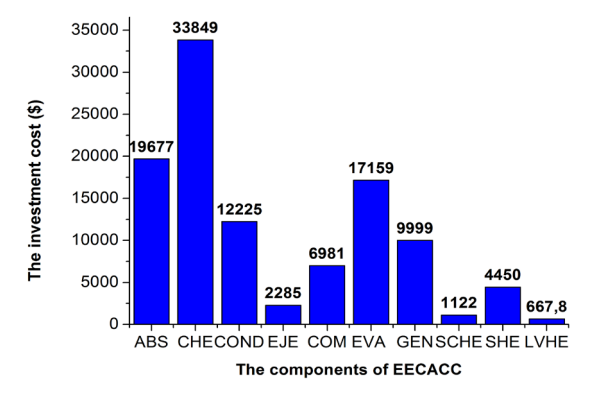


Figure 10. The investment cost of different components of ECACC.

6. Conclusion

In this work, a proposed cycle of enhanced ejector compression absorption cascade cycle is studied in different side energy, exergy, economic, and environmental. The 4E analysis of the enhanced ejector compression absorption cascaded cycle allows the conclusion of the following:

- The RE170 fluid has a higher coefficient of performance and the exergy efficiency of EECACC than 08 fluids studied with low GDP and ODP coefficients.
- The proposed cycle EECACC coefficient of performance and exergy efficiency are higher by 3.27 and 2.7 % than the coefficient of performance and the exergy efficiency

- of the conventional compression absorption cascade cycle, respectively.
- The annual cost and the hourly equivalent CO2 emission of proposed cycle are lower by 7.93 and 2.29 % than the annual cost and the hourly equivalent mass of CO2 emission of conventional compression absorption cascade cycle.
- The enhanced ejector compression absorption cascade studied reaches maximum performance at generation equation equal to 348 K.
- There is a generation temperature at which the cycle performance is in maximum, for every operating condition.
- The increasing of the cascade heat exchanger inlet temperature of the absorption cycle refrigerant from 283 to 289 K negatively affected the coefficient performance and the exergy efficiency of the EECACC by 2.36 and 9.14 %, respectively, and positively affected the annual cost and the hourly equivalent CO2 emission of the cycle by 6.97 and 24.20%, respectively
- The cascade heat exchanger inlet temperature of the absorption cycle refrigerant should be the lower possible.
- The increasing sub-cooling heat exchanger efficiency from 0.6 to 0.9 positively affected the coefficient performance and the exergy efficiency of the EECACC by 0.5 and 0.9 %, respectively, and negatively affected the annual cost and the hourly equivalent CO2 emission of the cycle by 0.76 and 0.38 %, respectively.
- The sub cooling heat exchanger efficiency should be the higher possible.
- The cycle heat exchangers like as the cascade heat exchanger, the sub-cooling heat exchanger, the absorber and the generator are responsible for almost all exergy destruction of EECACC followed by the compressor and the ejector, respectively.
- The investment cost of EECACC strongly depends on the heat exchangers and their area.
- The proposed cycle investment cost is higher by 3.14 % than the conventional compression absorption cascade cycle.
- The results obtained in this work are promoted and it is recommended to use the EECACC system for the compression absorption cascade cycle.

The future projections of research can be:

- Simulation of a new alternative refrigerant for replacement purposes.
- Develop new cycle by using double ejector for minimizing the compressor mass flow to enhance efficiency of cycle and reduce the environmental impact.

Conflict of Interest

Author approves that to the best of their knowledge; there is not any conflict of interest or common interest with an institution/organization or a person that may affect the review process of the paper.

Credit Author Statement

Billal Mebarki: Conceptualization, Methodology, Software, Data Curation, Writing- Original draft preparation, Visualization, Investigation, Validation, Writing- Reviewing and Editing.

Nomenclature

COP Coefficient of performance [-]

P	Pressure $[kPa]$
Ex_i	Exergy destruction [kW]
h	Enthalpy $[kJ/kg]$
T	Temperature [°C]
x	Mass fraction of lithium bromide $[g/kg]$
Q	Heat transfer rate $[kW]$
S	Entropy $[kJ/kg.K]$
W_{com}	Compressor work [kW]
m	Mass flow $[kg/s]$

Greek symbols

η_{ex}	Exergy efficiency [-]
ho	Mass density $[kg/m^3]$
ε	Efficiency [-]
μ	Entrainment Ratio [-]

Subscripts

0	Reference value
abs	Absorber
con	Condenser
eva	Evaporator
ev	Expansion valve
rv	Reduce pressure valve

gen	Generator
com	Compressor
ejec	Ejector
st	Separator tank

sbhex Sub cooling heat exchanger shex Solution heat exchanger chex Cascade heat exchanger

Lvhex Liquid vapor heat exchanger

i The ith chemical species

1, 2, ..., 32 The state point number

References

- [1] K. Salhi, M. Korichi, and K. M. Ramadan, "Thermodynamic and thermo-economic analysis of compression—absorption cascade refrigeration system using low-GWP HFO refrigerant powered by geothermal energy," *International Journal of Refrigeration*, vol. 94, pp. 214–229, Oct. 2018, doi: 10.1016/j.ijrefrig.2018.03.017.
- [2] M. Schulz and D. Kourkoulas, "Regulation (EU) No 517/2014 of the European Parliament and of the Council of 16 April 2014 on fluorinated greenhouse gases and repealing Regulation (EC) no 842/2006,"2014.
- [3] Y. Du, C. Chi, and X. Wang, "Energy, exergy, and economic analysis of compression-absorption cascade refrigeration cycle using different working fluids," *Energy Storage and Saving*, vol. 3, no. 2, pp. 87-95, Jun. 2024, doi: 10.1016/j.enss.2024.02.003.
- [4] M. Salek, N. Ababssi, M. Charia, and A. Boulal, "Enhancing Benefits by Rectification in the Absorption Refrigeration Systems," *International Journal of Thermodynamics*, vol. 25, no. 1, pp. 29–37, Mar. 2022, doi: 10.5541/ijot.927046.
- [5] B. Gurevich and A. Zohar, "Analytical Model for the Prediction of Performance of a Solar Driven Diffusion Absorption Cooling System," *International Journal of Thermodynamics*, vol. 24, no. 4, pp. 42–48, Dec. 2021, doi: 10.5541/ijot.929863.

- [6] Y. Maalem, Y. Tamene, and H. Madani, "Performances Investigation of the Eco-friendly Refrigerant R13I1 used as Working Fluid in the Ejector-Expansion Refrigeration Cycle," International Journal of Thermodynamics, vol. 26, no. 3, pp. 25–35, Sep. 2023, doi: 10.5541/ijot.1263939.
- [7] R. Fingas et al., "Experimental analysis of the air-towater ejector-based R290 heat pump system for domestic application," Applied Thermal Engineering, vol. 236, 2024, Jan. Art. no. 121800, 10.1016/j.applthermaleng.2023.121800.
- [8] L. Zou and J. Yu, "Performance evaluation of a solar-assisted ejector-enhanced vapor injection heat pump cycle," Solar Energy, vol. 265, Nov. 2023, Art. no. 112104, doi: 10.1016/j.solener.2023.112104.
- hybrid vapor injection cycle with subcooler and flash tank for air-source heat pumps," International Journal of Refrigeration, vol. 74, pp. 540-549, Feb. 2017, doi: 10.1016/j.ijrefrig.2016.11.024.
- [10] M. Pitarch, E. Navarro-Peris, J. Gonzálvez-Maciá, and J. M. Corberán, "Experimental study of a subcritical heat pump booster for sanitary hot water production using a subcooler in order to enhance the efficiency of the system with a natural refrigerant (R290)," International Journal of Refrigeration, vol. 73, pp. 226-234, Jan. 2017, doi: 10.1016/j.ijrefrig.2016.08.017.
- [11] M. Pitarch, E. Navarro-Peris, J. Gonzálvez-Maciá, and J. M. Corberán, "Experimental study of a heat pump with high subcooling in the condenser for sanitary hot water production," Science and Technology for the Built Environment, vol. 24, no. 1, pp. 105–114, Jan. 2018, doi: 10.1080/23744731.2017.1333366.
- [12] M. Pitarch, E. Navarro-Peris, J. Gonzálvez-Maciá, and J. M. Corberán, "Evaluation of different heat pump systems for sanitary hot water production using natural refrigerants," Applied Energy, vol. 190, pp. 911-919, Mar. 2017, doi: 10.1016/j.apenergy.2016.12.166.
- [13] C. Cimsit, I. T. Ozturk, and O. Kincay, "Thermoeconomic optimization of LiBr/H2O-R134a compression-absorption [24] J. C. V. Chinnappa, M. R. Crees, S. Srinivasa Murthy, cascade refrigeration cycle," Applied Thermal Engineering, vol. 76, pp. 105–115, Feb. 2015, 10.1016/j.applthermaleng.2014.10.094.
- [14] Z. Seyfouri and M. Ameri, "Analysis of integrated compression-absorption refrigeration systems powered by a microturbine," International Journal of Refrigeration, vol. 35, pp. 1639–1646, Sept. 2012, doi: 10.1016/j.ijrefrig.2012.04.010.
- [15] Y. Cheng, M. Wang, and J. Yu, "Thermodynamic [26] B. H. Gebreslassie, G. Guillén-Gosálbez, L. Jiménez, and analysis of a novel solar-driven booster-assisted ejector refrigeration cycle," Solar Energy, vol. 218, pp. 85-94, Apr. 2021, doi: 10.1016/j.solener.2021.02.031.
- [16] B. J. Huang, J. M. Chang, C. P. Wang, and V. A. "A 1-D Petrenko, analysis of performance," International Journal of Refrigeration, [27] A. Baghernejad and M. Yaghoubi, "Thermoeconomic vol. 22, no. 5, pp. 354–364, Aug. 1999, doi: 10.1016/S0140-7007(99)00004-3.
- [17] R. Gomri, "Investigation of the potential of application of single effect and multiple effect absorption cooling systems," Energy Conversion and Management, vol. 51,

- 1629–1636, 2010. doi: 8, pp. Aug. 10.1016/j.enconman.2009.12.039.
- [18] B. Mebarki, "Performance Investigation of Ejector Power Cooling Absorption Cycle," International Journal of Thermodynamics, vol. 26, no. 3, pp. 15-24Sep. 2023, 10.5541/ijot.1247392.
- [19] V. Jain, G. Sachdeva, S. S. Kachhwaha, and B. Patel, "Thermo-economic and environmental analyses based multi-objective optimization of vapor compressionabsorption cascaded refrigeration system using NSGA-II technique," Energy Conversion and Management, vol. 113, pp. 230–242, 2016, Apr. 10.1016/j.enconman.2016.01.056.
- [9] H. Qi, F. Liu, and J. Yu, "Performance analysis of a novel [20] Ö. Kızılkan, A. Şencan, and S. A. Kalogirou, "Thermoeconomic optimization of a LiBr absorption refrigeration system," Chemical Engineering and Processing: Process intensification, vol. 46, no. 12, pp. 1376–1384, Dec. 2007, doi: 10.1016/j.cep.2006.11.007.
 - [21] O. Caliskan, N. B. Sag, and H. K. Ersoy, "Thermodynamic, environmental, and exergoeconomic analysis of multiexpansion transcritical CO₂ supermarket refrigeration cycles in different climate regions of Türkiye," International Journal of Refrigeration, vol. 165, pp. 466-484, Sept. 2024, doi: 10.1016/j.ijrefrig.2024. 05.006.
 - [22] V. Jain, G. Sachdeva, and S. S. Kachhwaha, "Energy, exergy, economic and environmental (4E) analyses based comparative performance study and optimization of vapor compression-absorption integrated refrigeration system," Energy, vol. 91, pp. 816–832, Nov. 2015. 10.1016/j.energy.2015.08.041.
 - [23] M. Aminyavari, B. Najafi, A. Shirazi, and F. Rinaldi, "Exergetic, economic and environmental (3E) analyses, and multi-objective optimization of a CO2/NH3 cascade refrigeration system," Applied Thermal Engineering, vol. 65, no. 1–2, pp. 42–50, Apr. 2014. 10.1016/j.applthermaleng.2013.12.075.
 - and K. Srinivasan, "Solar-assisted vapor compression/absorption cascaded air-conditioning systems," Solar Energy, vol. 50, no. 5, pp. 453-458, May 1993, doi: 10.1016/0038-092X(93)90068-Y.
 - [25] C. Cimsit and I. T. Ozturk, "Analysis of compressionabsorption cascade refrigeration cycles," Applied Thermal Engineering, vol. 40, pp. 311–317, Jul. 2012, doi: 10.1016/j.applthermaleng.2012.02.035.
 - D. Boer, "Design of environmentally conscious absorption cooling systems via multi-objective optimization and life cycle assessment," Applied Energy, vol. 86, no. 9, pp. 1712–1722, Sep. 2009, doi: 10.1016/j.apenergy.2008.11.019.
 - methodology for analysis and optimization of a hybrid solar thermal power plant," International Journal of Green Energy, vol. 10, no. 6, pp. 588-609, Mar. 2013, doi: 10. 1080/15435075.2012.706672.

- [28] S. Khanmohammadi, M. Saadat-Targhi, F. W. Ahmed, and M. Afrand, "Potential of thermoelectric waste heat recovery in a combined geothermal, fuel cell and organic Rankine flash cycle (thermodynamic and economic evaluation)," *International Journal of Hydrogen Energy*, vol. 45, no. 11, pp. 6934–6948, Feb. 2020, doi: 10.1016/j.ijhydene.2019.12.113.
- [29] J. Wang, Z. (John) Zhai, Y. Jing, and C. Zhang, "Particle swarm optimization for redundant building cooling heating and power system," Applied Energy, vol. 87, no. 12, pp. 3668–3679, Dec. 2010, doi: 10.1016/j.apenergy.2010.06.021.
- [30] O. Kizilkan, S. Khanmohammadi, and M. Saadat-Targhi, "Solar based CO2 power cycle employing thermoelectric generator and absorption refrigeration: Thermodynamic assessment and multi-objective optimization," *Energy Conversion and Management*, vol. 200, Nov. 2019, Art. no. 112072, doi: 10.1016/j.enconman.2019.112072.
- [31] E. W. Lemmon, M. L. Huber, and M. O. McLinden, NIST Standard Reference Database 23: REFPROP, Version 10.0, National Institute of Standards and Technology, Gaithersburg, USA, 2018, doi: 10.18434/T4JS3C.
- [32] J.M. Calm and G.C. Hourahan, "Physical, safety, and environmental data for current and alternative refrigerants," in *23rd IIR International Congress of Refrigeration*, Prague, Czech Republic, Aug. 2011, Paper ICR11-915.

Research Article

Vol. 28 (No. 4), pp. 243-249, 2025 doi: 10.5541/ijot.1739149 Published online: December 1, 2025

The Effect of Inlet Baffle on the Skin Friction Coefficient and Turbulence Intensity in an Air-Cooled Channel

^{1*}L. N. Thanh , ²M. P. Nguyen , ³M. H. Nguyen , ¹H. S. N. Le , ¹N. H. Lai

E-mail: 1*luannt@hcmute.edu.vn

Received 10 July 2025, Revised 12 August 2025, Accepted 18 August 2025

Abstract

This study addresses the impact of an inlet baffle mounted opposite a hot surface on the properties of turbulence and flow resistance in an air-cooled channel. This study focuses on analyzing the variation in the skin friction coefficient and air turbulence intensity along the hot surface. The influence of an inclined baffle angle $\alpha=15-60^\circ$ and relative baffle length $L_n=0.625-0.875$ under the Reynolds number spectrum Re=4000-16000 was considered. Results indicated that turbulence intensity increased when the Reynolds number increased, the baffle length increased, or the inclined baffle angle decreased. The skin friction coefficient increased when the Reynolds number decreased, the baffle length increased, or the inclined baffle angle decreased. The maximum heat transfer rate occurs at $\alpha=15^\circ$, $L_n=0.875$, and Re=16000, and vice versa at $\alpha=60^\circ$, $L_n=0.625$, and Re=4000. In comparing the lowest and highest heat transfer configurations, the skin friction coefficient decreased by 77.9 %, and turbulence intensity decreased by 97 %. This means that heat transfer can be increased at the cost of higher pump power. The results of this study contribute to a more comprehensive understanding of the effect of an inlet baffle on fluid chaotic motion and flow resistance, as well as the mechanism that leads to the variation in heat transfer ability and pressure loss in the channel under the impact of the inlet baffle.

Keywords: Air-cooled channel; baffle; numerical simulation; skin friction coefficient; turbulence intensity.

1. Introduction

Enhancing heat transfer in thermal equipment is important in improving efficiency, reducing equipment size, and minimizing the impact on climate change. Therefore, many strategies have been used to increase the heat transfer rate, such as by adding baffles, adding fins, creating ribs, using nanofluid, adding an insertion, and creating dimples [1-3]. The research results have provided potential solutions for practical applications. In many fluids, air is the fluid commonly used in cooling applications. Besides advantages such as availability and simplicity in use, the disadvantage of air is its low heat transfer ability. Therefore, increasing the heat transfer rate towards the air side is a main strategy for improving cooling efficiency. The use of baffles to change flow structure is one of the methods many researchers have pointed out as having the potential to improve heat transfer rate. Yilmaz [4] experimentally studied heat transfer and pressure loss in an air-cooled channel with an inlet baffle. Results showed that the heat transfer and friction factor were 1.39-2.43 and 28.26-94.45 times higher, respectively, than with a smooth channel. Menni et al. [5] analyzed channels with multi-baffles. The results showed that heat transfer and friction factor were 3.623-5.008 and 10.829-25.412 times higher, respectively, than with the smooth channel. Ameur [6] studied air-cooled channels using an inclined baffle. Results indicated that the straight baffle yields a wider vortex

than the inclined baffle. Promvonge et al. [7] examined a channel with an arc-shaped baffle. They reported that heat transfer was enhanced, but pressure loss increased significantly. Luan et al. [8] analyzed multi-objective optimization in an air-cooled channel. They concluded that thermohydraulic performance increased with a decreasing Reynolds number, increasing baffle angle, and increasing clearance ratio. Saha et al. [9] studied channels with variable baffle positions. They reported that a turbulent airflow structure greatly affects heat transfer and pressure loss. Salhi et al. [10] investigated channels with partially inclined baffles. Results indicated that increasing the height and number of baffles enhanced heat transfer. Menni et al. [11] tested channels with S-shaped baffles. They commented that the use of baffles enhances heat transfer. Boonloi et al. [12] studied channels with V-shaped baffles. They reported that using a V-baffle increased heat transfer by 1.04-15.55 times, and friction factor increased by 1.71-112.08 times, compared to a smooth channel. Many studies that have used baffles to enhance heat transfer in air channels can be found in the literature [13]. The literature review reveals that using baffles in air-cooled channels has been a topic of interest to many authors. The results of the studies have provided valuable reports on thermohydraulic properties in channels.

Flow structure greatly affects heat transfer and pressure loss in the channel. Flow turbulence is closely related to the

*Corresponding Author Vol. 28 (No. 4) / 243

¹ Faculty of Vehicle and Energy Engineering, Ho Chi Minh City University of Technology and Education, Vietnam

² Faculty of Heat and Refrigeration Engineering, Industrial University of Ho Chi Minh City, Ho Chi Minh, Vietnam

³ Division of Mechanical Engineering, Campus in Ho Chi Minh City, University of Transport and Communications, Vietnam

Reynolds number and channel geometry. Therefore, the study on the flow and heat transfer properties is necessary for orienting the geometric shape change suitable for practical applications. Some authors have analyzed and evaluated this in previous studies [14, 15]. The researchers of [4, 8] discussed the impact of the inlet baffle on the overall heat transfer and pressure loss values in air-cooled channels. However, the chaotic motion and flow resistance properties along the hot surface have not been analyzed. Thus, this study extends the analysis of turbulence intensity and skin friction coefficient along the hot surface to elucidate the impact of the inlet baffle on fluid chaotic motion and flow resistance, to clarify the mechanism leading to the variation in heat transfer ability and pressure loss in the channel. Overall, the obtained results provide a comprehensive view of the impact of inlet baffles on flow characteristics along the hot surface, providing valuable insights for both theoretical understanding and practical applications when considering the use of an inlet baffle in an air channel.

2. Analytical Method

Figure 1 shows the computed domain with a 320 mm test section length, 80 mm channel height, 600 mm entrance section length, 300 mm exit section length, and 160 mm channel width. Geometric parameters are referenced from the research of Yilmaz [4]. Inside the channel was a baffle with an inclined angle $\alpha=15\text{--}60^\circ$ and relative length $L_n=0.625\text{--}0.875$ ($L_n=a/H$). The inlet air temperature was 300 K, and the heat flux supplied to the hot surface was 1000 W/m². Air leaving from the exit section was set up as equal to atmospheric pressure. The upper wall was set up with the adiabatic boundary condition. The no-slip condition was set up for the solid walls.

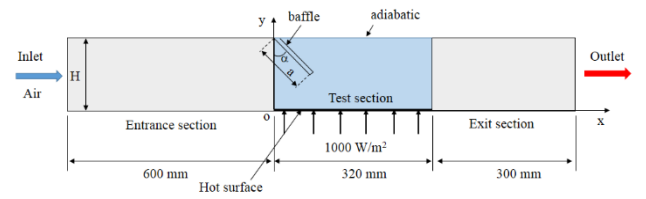


Figure 1. Computed domain.

Figure 2 shows the meshing in the computed domain with a hexahedral mesh and the creation of a five-layer mesh reinforcement. The thickness of the first layer ensures that the near-wall element spacing is approximately equal to unity. Four mesh levels were used for grid-independent tests (see Figure 3). From the results obtained, the mesh size corresponding to 169525 elements was chosen. It reduces the simulation time but still ensures the accuracy of the results.

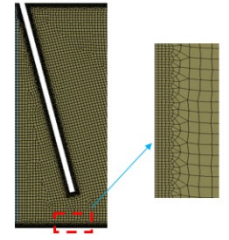


Figure 2. Mesh in the computational domain.

The difference in air temperature between the outlet and the inlet of the test section is small. To simplify the solution approach, we assume incompressible flow, steady-state heat transfer, ignore the effect of gravity, and negligible radiation heat transfer. We also assume that the air physical parameters are constant and referenced at 300 K [8]: $\rho=1.117~kg/m^3,~c_p=1007~J/kg.K,~k_a=0.0262~W/m.K,~\mu=1.857\times10^{-5}~kg/m.s.$ The standard k– ϵ turbulence model was used in the present work based on previous work [8], and its equations can also be found in the literature [16]. In this work, the residual for the equations of continuity, momentum, energy, k, and ϵ was $10^{-6}.$ The SIMPLE algorithm was used to deal with the problem of velocity and pressure coupling. Figure 4 shows the validation results based on data from the reports of Yilmaz [4]; high agreement is observed. Therefore, the simulation settings are suitable, and the results are analyzed and discussed in the next section.

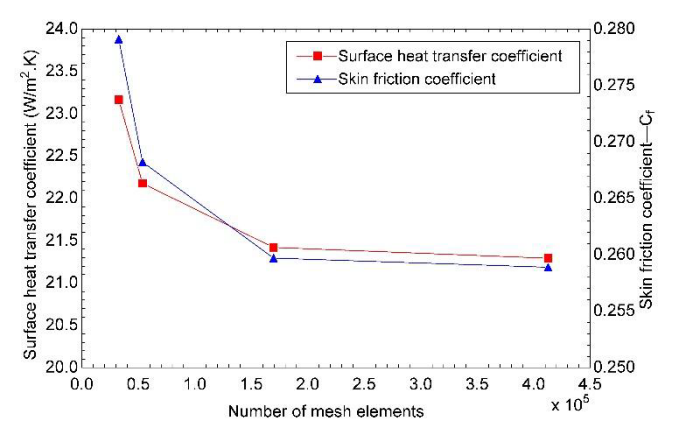


Figure 3. Grid independence test.

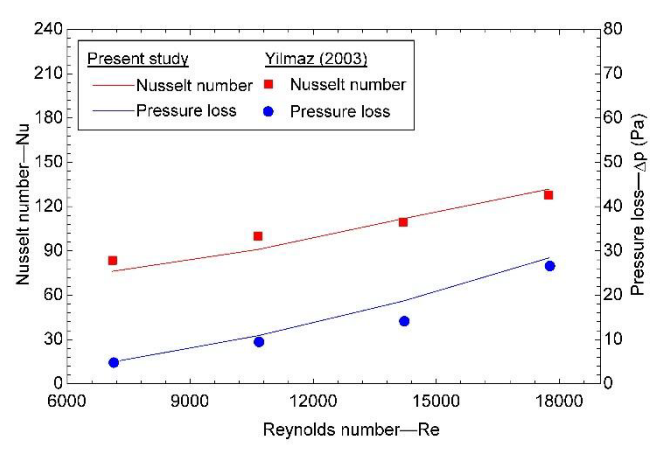


Figure 4. Validation based on the experiment of Yilmaz [4].

Under the above assumptions, the governing equations are as follows [8]:

The continuity equation:

$$\frac{\partial \left(\rho u_j\right)}{\partial x_j} = 0\tag{1}$$

The momentum equation:

$$\frac{\partial \left(\rho u_{i} u_{j}\right)}{\partial x_{j}} = -\frac{\partial p}{\partial x_{i}} + \frac{\partial}{\partial x_{j}} \left[\mu \left(\frac{\partial u_{i}}{\partial x_{j}} + \frac{\partial u_{j}}{\partial x_{i}} \right) \right] + \frac{\partial}{\partial x_{j}} \left[\mu_{i} \left(\frac{\partial u_{i}}{\partial x_{j}} + \frac{\partial u_{j}}{\partial x_{i}} \right) \right]$$
(2)

The energy equation:

$$\frac{\partial}{\partial x_j} \left(u_j \rho T \right) = \frac{\partial}{\partial x_j} \left[\left(\frac{\mu}{\Pr} + \frac{\mu_t}{\Pr_t} \right) \frac{\partial T}{\partial x_j} \right]$$
 (3)

The hydraulic diameter was calculated using the following formula [17, 18]:

$$D_h = \frac{4(HW)}{2(H+W)} \tag{4}$$

The Reynolds number was determined using the following formula [17, 18]:

$$Re = \frac{u\rho D_h}{\mu} \tag{5}$$

The turbulence intensity was computed using the formula [19]:

$$I_t = \frac{1}{u_m} \sqrt{\frac{2}{3}k} \tag{6}$$

The skin friction coefficient was expressed as follows [19, 20]:

$$C_f = \frac{\tau_{\rm w}}{\frac{1}{2}\rho u^2} \tag{7}$$

The ratio of the average temperature of the hot surface with inlet air temperature was expressed as follows:

$$T_R = \frac{T_{\rm w}}{T_{\rm c}} \tag{8}$$

3. Results and Discussion

3.1 Effect of the Reynolds number and Baffle on the Skin Friction Coefficient and Turbulence Intensity

Figure 5a shows the effect of the Reynolds number on C_f along the hot surface in the case with $\alpha = 30^{\circ}$ and $L_n = 0.75$. It can be seen that C_f decreased when the Re increased. The reason for this may be that the increase in the wall shear stress was lower than the increase in the square of reference velocity (inlet velocity) when the Re increased, resulting in a decrease in the C_f . The highest C_f was found at points X_d 0.133 for Re = 4000, $X_d = 0.129$ for Re = 8000, $X_d = 0.138$ for Re = 12000, and $X_d = 0.145$ for Re = 16000. These are locations with high differences in velocity gradient. At Re = 4000, the average C_f increased by 13.1 %, 19.9 %, and 22.9 % compared to the cases of Re = 8000, Re = 12000, and Re= 16000, respectively. The decrease in C_f with increasing Re is consistent with the trend of the decreasing friction factor with increasing Re, as previously reported [4]. Figure 5b shows the influence of the Reynolds number on the turbulence intensity of flow along the hot surface. It can be seen that increasing the Re significantly increased the It. This is because at high Re, inertial forces dominate, resulting in increased turbulence and strong energy transfer in the flow. Therefore, increasing Re is the reason for the increase in heat transfer between the hot surface and the airflow. At Re = 16000, the average turbulence intensity is 1.4 times, 2.3 times, and 4.9 times higher than at Re = 12000, Re = 8000, and Re = 4000, respectively.

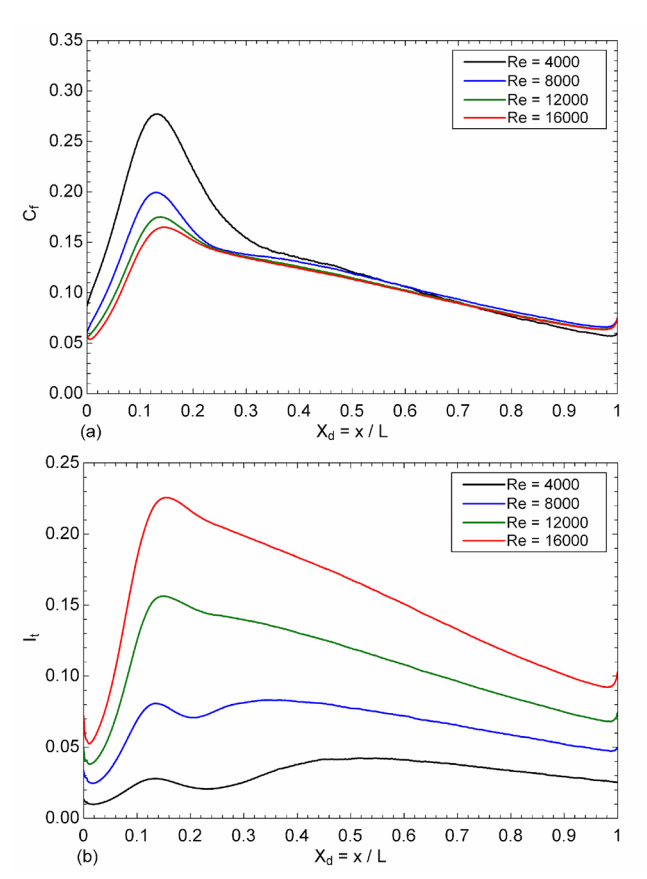
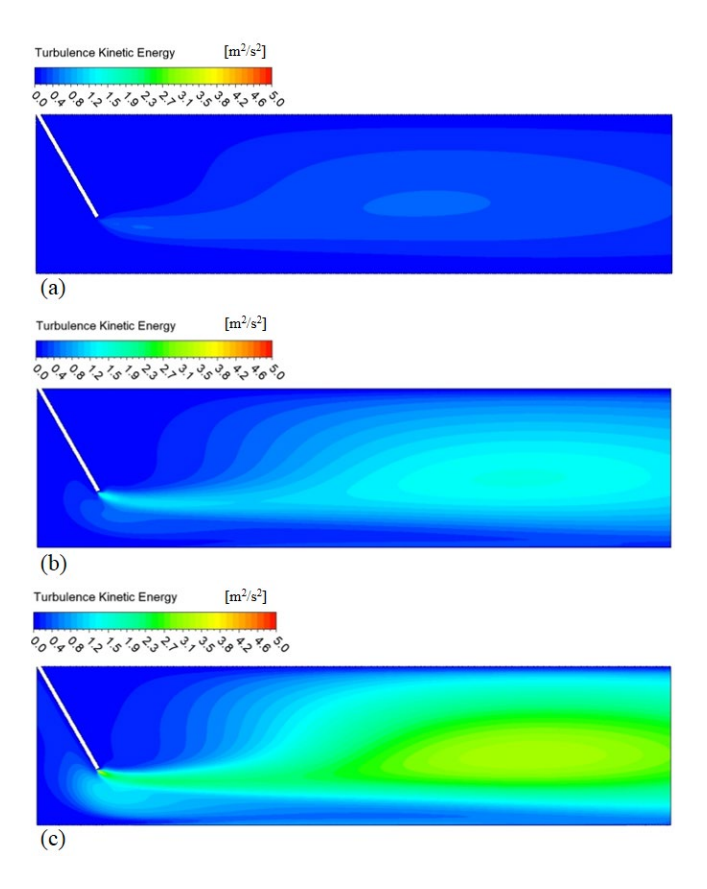


Figure 5. Effects of Reynolds number: (a) local skin friction coefficient; (b) local turbulence intensity.

Figure 6(a-d) show the turbulent kinetic energy contour in the cases under analysis. Higher turbulent kinetic energy was observed at high Reynolds number. This demonstrates that increasing the Reynolds number increases the turbulence intensity in the domain and along the hot surface, which agrees with the previous analysis.



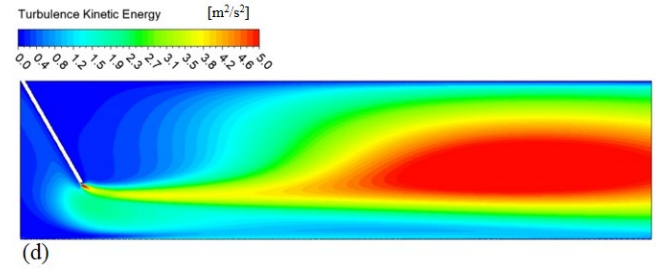


Figure 6. Turbulent kinetic energy contour with different Reynolds numbers: (a) Re = 4000; (b) Re = 8000; (c) Re = 12000; (d) Re = 16000.

Figure 7a shows the influence of baffle length on C_f along the hot surface in the case with $\alpha = 30^{\circ}$ and Re = 8000. The results show that increasing the L_n increased the C_f. This is because the air velocity after passing through the baffle suddenly increases, increasing the air-layer velocity gradient along the hot surface, leading to an increase in wall shear stress, or an increase in Cf. The longer the baffle, the higher the C_f. This means that increasing the baffle length increased the pressure loss, which is consistent with the report in the literature [4]. The average C_f at $L_n = 0.625$ decreased by 44.2 % and 72.5 % compared to the cases of $L_n = 0.75$ and $L_n =$ 0.875, respectively. Figure 7b shows the effect of baffle length on turbulence intensity along the hot surface. It can be observed that the turbulence intensity increased with increased baffle length. Increasing the baffle length increases the air velocity after passing the baffle, leading to increased turbulence and increased mixing. This increases the rate of energy transfer in the flow. Therefore, increasing the baffle length increases the heat transfer in the channel. The turbulence intensity of the shortest baffle decreased up to 69 % compared to the longest baffle.

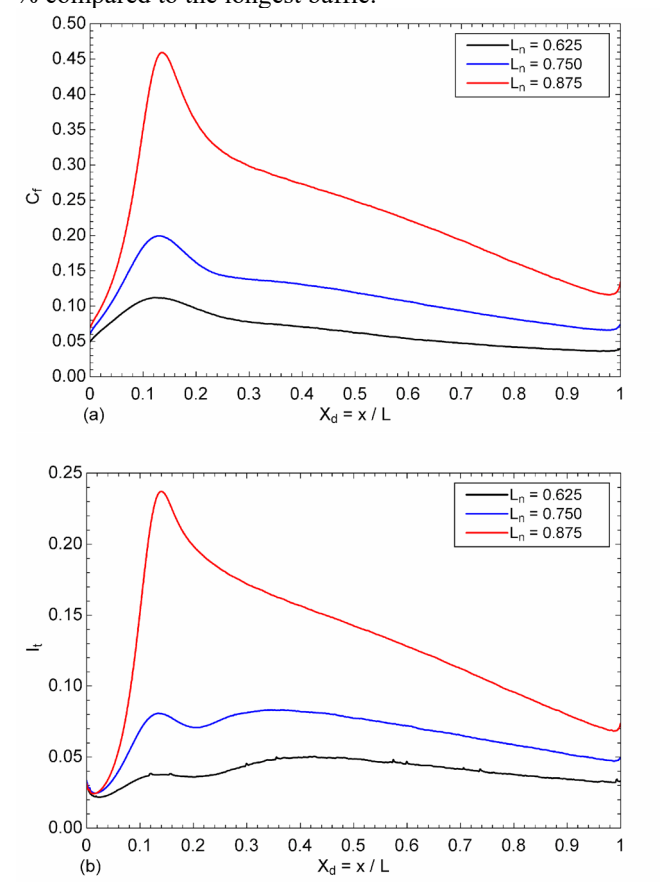


Figure 7. Effects of baffle length: (a) local skin friction coefficient; (b) local turbulence intensity.

Figure 8(a–c) show the turbulence kinetic energy contour of the case under analysis. High turbulent kinetic energy levels were observed for high L_n. This result demonstrates that increasing L_n increases the turbulence intensity in the domain and along the hot surface, which is consistent with the previous discussion on the effect of L_n. From the analysis results, it can be seen that an increased baffle length increased the skin friction coefficient and increased turbulence intensity along the hot surface. This clearly explains the motivation for increases in heat transfer and pressure loss in the channel when increasing baffle length.

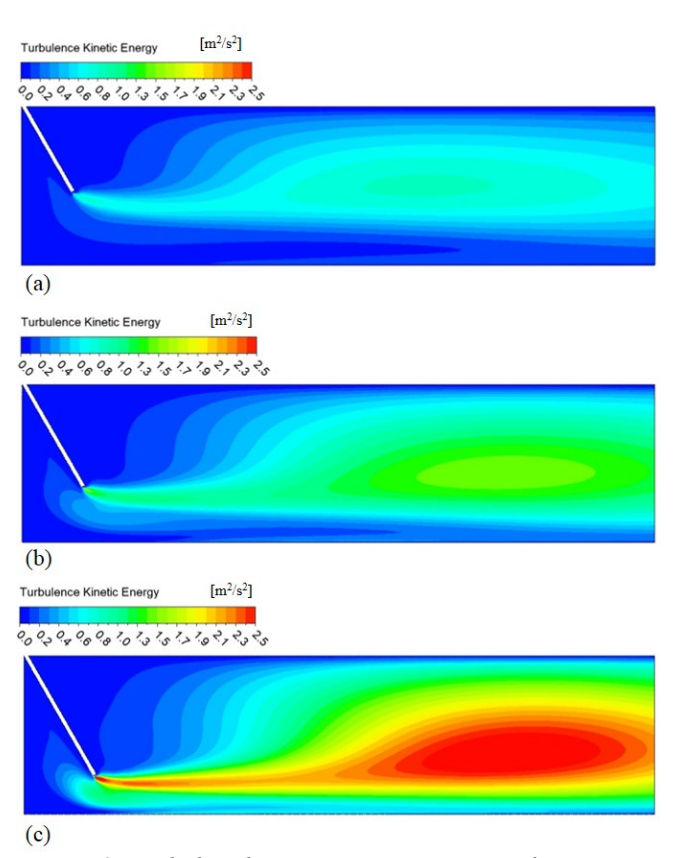


Figure 8. Turbulent kinetic energy contour with variations in L_n : (a) $L_n = 0.625$; (b) $L_n = 0.75$; (c) $L_n = 0.875$.

Figure 9a shows the effect of the inclined baffle angle on the C_f along the hot surface in the case with $L_n = 0.75$ and Re = 8000. The results indicate that a decreased inclined baffle angle results in an increased C_f. This can be explained by the fact that decreasing α leads to a decrease in the free flow cross-section, increasing the flow velocity after exiting the minimum gap between the baffle and the hot surface. This increase in velocity increases the air-layer velocity gradient along the hot plate, or in other words, it increases the wall shear stress and C_f. This means that decreasing α increased the pressure loss. The average C_f of the case with $\alpha = 60^{\circ}$ decreased by up to 88.2 % compared to the case with $\alpha = 15^{\circ}$. The effect of the inclined baffle angle on turbulence intensity is shown in Figure 9b: a decreased inclined baffle angle results in increased turbulence intensity. This is due to the increase in velocity gradient as α decreases. The increase in It explains the increase in heat transfer between the airflow and the hot surface. The average turbulence intensity at $\alpha =$ 60° decreased by 84.5 %, compared to that at $\alpha = 15^{\circ}$.

Figure 10(a-d) show the turbulence kinetic energy contour for the cases under analysis. The results indicate that a decreased inclined baffle angle increases turbulent kinetic energy in the domain. Overall, the turbulence intensity along

the hot surface increased, which is consistent with the previous analysis.

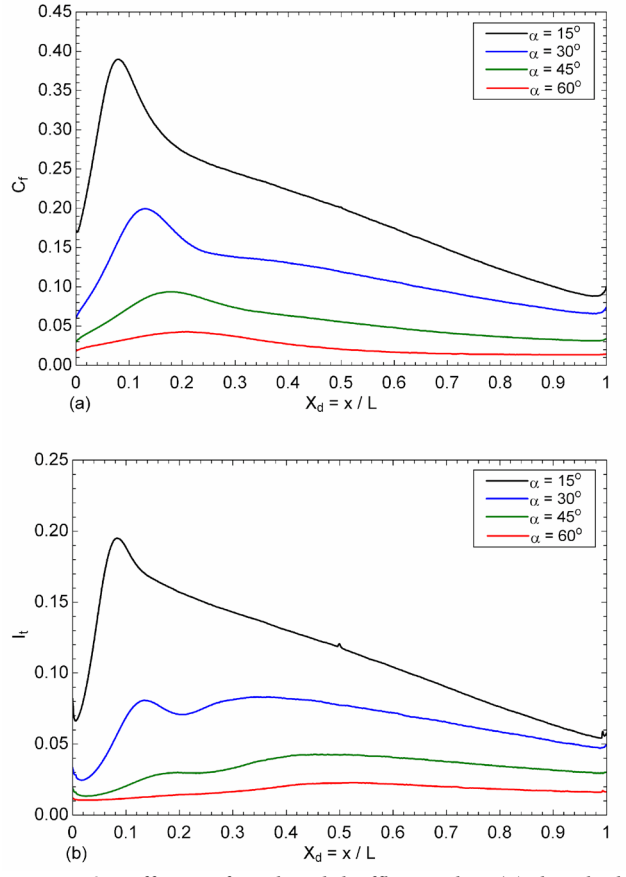
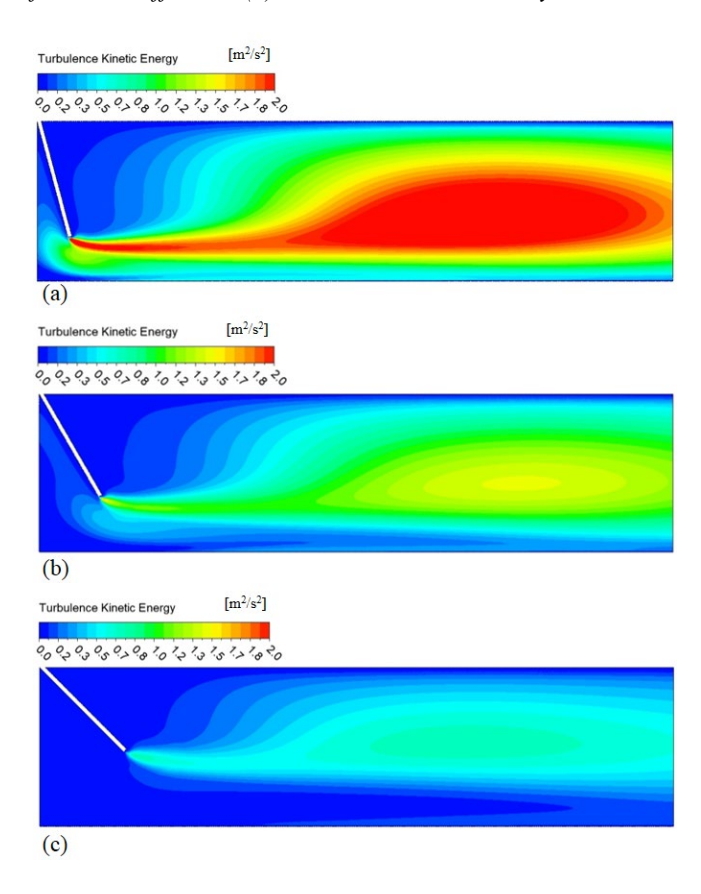


Figure 9. Effects of inclined baffle angle: (a) local skin friction coefficient; (b) local turbulence intensity.



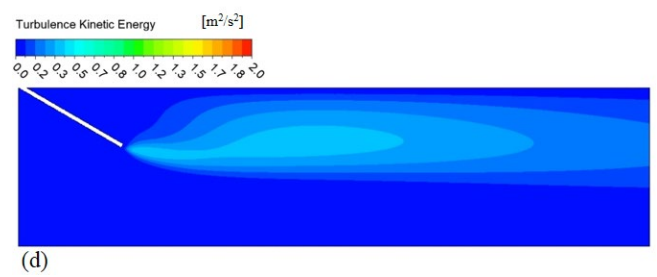
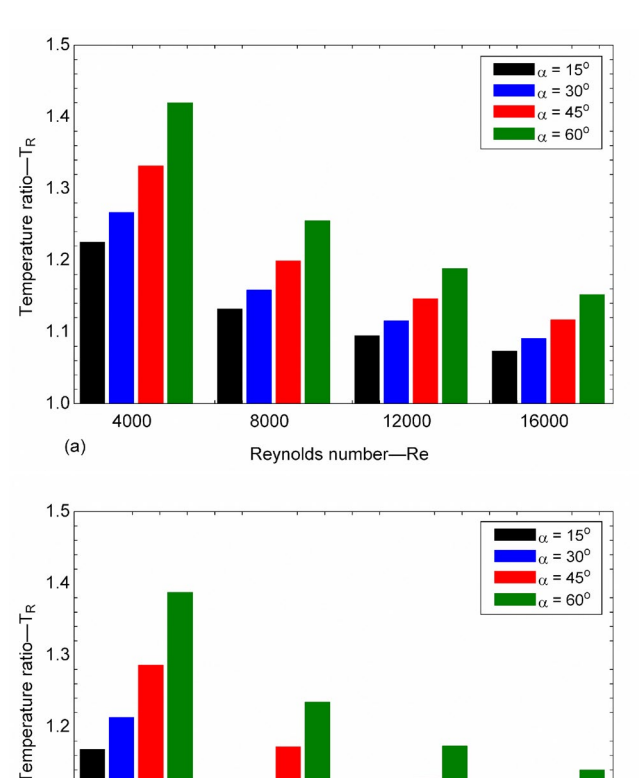


Figure 10. Turbulent kinetic energy contour with variations in α : (a) $\alpha = 15^{\circ}$; (b) $\alpha = 30^{\circ}$; (c) $\alpha = 45^{\circ}$; (d) $\alpha = 60^{\circ}$.

3.2 Effect of Baffle Use and Reynolds Number on **Average Temperature of Hot Surface**

Figure 11(a-c) show the ratio of the average temperature of the hot surface with the inlet air temperature. The results show that the configuration of $\alpha = 15^{\circ}$, $L_n = 0.875$, and Re =16000 yielded the highest heat transfer. This result is consistent with the analysis of the influence of baffle use and Reynolds number on turbulence intensity. The smallest heat transfer case corresponds to $\alpha = 60^{\circ}, \, L_n = 0.625, \, \text{and Re} =$ 4000. The $C_{\rm f}$ and $I_{\rm t}$ of the lowest heat transfer case were reduced by 77.9 % and 97 % compared to the best. This means that parameters that yield the highest heat transfer require more energy for pump power due to the large increase in flow resistance. Therefore, depending on the purpose, there is a suitable design orientation. If the purpose is to attain the highest heat transfer, the best case noted above should be considered, accepting the increased energy consumption cost. The thermohydraulic performance criteria should be considered if the goal is to obtain a balanced solution, as mentioned in previous studies [4, 8].



1.2

(b)

4000

8000

Reynolds number—Re

16000

12000

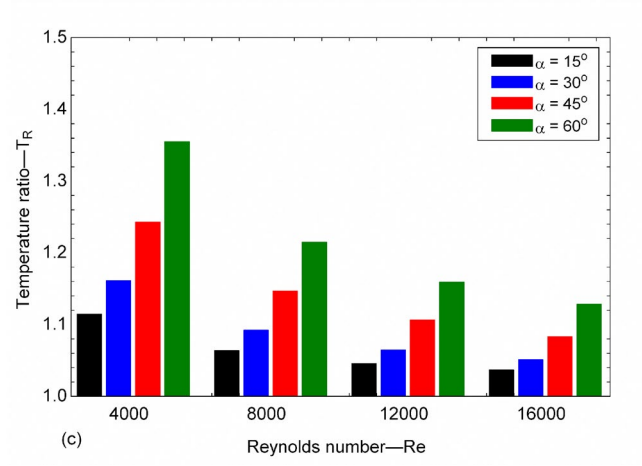


Figure 11. The ratio of the average temperature of the hot surface with inlet air temperature: (a) $L_n = 0.625$; (b) $L_n =$ 0.75; (c) $L_n = 0.875$.

4. Conclusions

The present work focuses on analyzing the effects of the inlet baffle and Reynolds number on the skin friction coefficient and turbulence intensity along the hot surface in an air-cooled channel. The influence of the inclined baffle angle, baffle length, and Reynolds number was considered. The main results of this study are the following:

- The skin friction coefficient along the hot surface increased when the Reynolds number decreased, the baffle length increased, or the inclined baffle angle decreased.
- The turbulence intensity along the hot surface increased when the Reynolds number increased, the baffle length increased, or the inclined baffle angle decreased.
- The heat transfer rate increased when the Reynolds number increased, the baffle length increased, or the inclined baffle angle decreased. The highest heat transfer rate occurs at $\alpha = 15^{\circ}$, $L_n = 0.875$, and Re = 16000, and the smallest heat transfer rate occurs at $\alpha = 60^{\circ}$, $L_n = 0.625$, and Re = 4000.
- The smallest heat transfer case has a 77.9 % reduction in the C_f and a 97 % reduction in the I_t compared to the highest heat transfer case. This means that increased heat transfer is achieved at the cost of requiring higher pump power.
- The present study examined the turbulence and flow resistance along the hot surface under the inlet baffle effect. The results show the potential use of an inlet baffle in hot surface cooling and clarify the mechanism leading to the variation in heat transfer ability and pressure loss in the channel. Future research needs to be extended to consider using multiple baffles, plastic baffles, and inlet baffles for cooling photovoltaic panels or cooling battery packs.

Acknowledgements

This research was not funded by any grant.

Conflict of Interest

Authors approve that to the best of their knowledge, there is not any conflict of interest or common interest with an institution/organization or a person that may affect the review process of the paper.

Credit Author Statement

Luan Nguyen Thanh: Conceptualization, Methodology, Software, Investigation, Visualization, Formal analysis, Writing- Reviewing and Editing. Minh Phu Nguyen: Data curation, Writing- Reviewing and Editing. Minh Ha Nguyen: Investigation, Visualization, Writing- Original draft. Hong Son Nguyen Le: Formal analysis, Visualization. Nam Hoai Lai: Software, Formal analysis.

Nomenclature

	C []
c_p	Specific heat of air $[J/kg.K]$
C_f	Skin friction coefficient [-]
D_h	Hydraulic diameter [m]
H	Channel height [<i>m</i>]
I_t	Turbulence intensity [-]
k	Turbulent kinetic energy $[m^2/s^2]$
k_a	Thermal conductivity of air $[W/m.K]$
L	Channel length (test section) [m]
L_n	Relative baffle length [-]
Nu	Nusselt number [-]
и	Inlet velocity [<i>m/s</i>]
u_m	Mean velocity [<i>m</i> / <i>s</i>]
p	Pressure $[N/m^2]$
Pr	Prandtl number [-]
Pr_t	Turbulent Prandtl number [-]
Re	Reynolds number [-]
T	Temperature [K]
W	Channel width [<i>m</i>]
X_d	Dimensionless horizontal coordinate
Greek syn	nbols

Baffle length [*m*]

α	Inclined baffle angle [o]
ρ	Density of air $[kg/m^3]$
ε	Turbulent dissipation rate $[m^2/s^3]$
$ au_{\scriptscriptstyle \mathcal{W}}$	Wall shear stress $[kg/m.s^2]$
μ	Dynamic viscosity [kg/m.s]
μ_t	Eddy viscosity [kg/m.s]
G 1	

Subscripts

i	Inlet
R	Ratio
w	Wall

References:

- [1] E. Guersoy, M. Gürdal, E. Gedik, K. Arslan, and A. Dağdeviren, "Experimental and numerical study on ferrohydrodynamic and magneto-convection Fe3O4/water ferrofluid in a sudden expansion tube with dimpled fins," Journal of the Taiwan Institute of Chemical Engineers, vol. 164, Nov. 2024, Art. no. 105676, doi: 10.1016/j.jtice.2024.105676.
- T. Alam and M.-H. Kim, "A comprehensive review on single phase heat transfer enhancement techniques in heat exchanger applications," Renewable Sustainable Energy Reviews, vol. 81, pp. 813-839, Jan. 2018, doi: 10.1016/j.rser.2017.08.060.
- [3] L. N. Thanh and M. H. Nguyen, "Heat transfer and flow characteristics in horizontal spiral coils with flat tubes and rectangular ribs: CFD and optimization," International Journal of Thermofluids, vol. 26, Mar. 2025, Art. no. 101072, doi: 10.1016/j.ijft.2025.101072.
- [4] M. Yilmaz, "The effect of inlet flow baffles on heat transfer," International Communications in Heat and Mass Transfer, vol. 30, no. 8, pp. 1169-1178, Nov. 2003, doi: 10.1016/S0735-1933(03)00182-9.
- Y. Menni, A. Azzi, and C. Zidani, "CFD simulation of thermo-aeraulic fields in a channel with multiple baffle

- plates," *Journal of Thermal Engineering*, vol. 4, no. 6, pp. 2481-2495, Sep. 2018, doi: 10.18186/thermal.465696.
- [6] H. Ameur, "Effect of the baffle inclination on the flow and thermal fields in channel heat exchangers," *Results in Engineering*, vol. 3, Sep. 2019, Art. no. 100021, doi: 10.1016/j.rineng.2019.100021.
- [7] P. Promvonge *et al.*, "Characterization of heat transfer and artificial neural networks prediction on overall performance index of a channel installed with arcshaped baffle turbulators," *Case Studies in Thermal Engineering*, vol. 26, Aug. 2021, Art. no. 101067, doi: 10.1016/j.csite.2021.101067.
- [8] N. Thanh Luan and N. Minh Phu, "Thermohydraulic Performance and Entropy Generation of Baffled Channel: Numerical Analysis and Optimization," *Journal of Thermophysics and Heat Transfer*, vol. 36, no. 2, pp. 303-313, Apr. 2022, doi: 10.2514/1.T6332.
- [9] S. Saha, P. Biswas, S. Nath, and L. Singh, "Numerical simulations of Newtonian fluid flow through a suddenly contracted rectangular channel with two different types of baffle plates," *Soft Computing*, vol. 25, no. 15, pp. 9873-9885, Aug. 2021, doi: 10.1007/s00500-020-05326-4.
- [10] J. E. Salhi, S. S. Mousavi Ajarostaghi, T. Zarrouk, M. Saffari Pour, N. Salhi, and M. Salhi, "Turbulence and thermo-flow behavior of air in a rectangular channel with partially inclined baffles," *Energy Science & Engineering*, vol. 10, no. 9, pp. 3540-3558, Sep. 2022, doi: 10.1002/ese3.1239.
- [11] Y. Menni, G. Lorenzini, R. Kumar, B. Mosavati, and S. Nekoonam, "Aerodynamic Fields inside S-Shaped Baffled-Channel Air-Heat Exchangers," *Mathematical Problems in Engineering*, vol. 2021, pp. 1-11, May 2021, doi: 10.1155/2021/6648403.
- [12] A. Boonloi and W. Jedsadaratanachai, "Effects of baffle height and baffle location on heat transfer and flow profiles in a baffled duct: a CFD analysis," *Modelling and Simulation in Engineering*, vol. 2022, pp. 1-19, Jul. 2022, doi: 10.1155/2022/3698887.

- [13] Y. Menni, A. Azzi, and A. Chamkha, "Enhancement of convective heat transfer in smooth air channels with wall-mounted obstacles in the flow path: a review," *Journal of Thermal Analysis and Calorimetry*, vol. 135, no. 4, pp. 1951-1976, Feb. 2019, doi: 10.1007/s10973-018-7268-x.
- [14] S. Sripattanapipat and P. Promvonge, "Numerical analysis of laminar heat transfer in a channel with diamond-shaped baffles," *International Communications in Heat and Mass Transfer*, vol. 36, no. 1, pp. 32-38, Jan. 2009, doi: 10.1016/j.icheatmasstransfer.2008.09.008.
- [15] Y.-T. Yang and C.-Z. Hwang, "Calculation of turbulent flow and heat transfer in a porous-baffled channel," *International Journal of Heat and Mass Transfer*, vol. 46, no. 5, pp. 771-780, Feb. 2003, doi: 10.1016/S0017-9310(02)00360-5.
- [16] R. Shaheed, A. Mohammadian, and H. Kheirkhah Gildeh, "A comparison of standard k–ε and realizable k–ε turbulence models in curved and confluent channels," *Environmental Fluid Mechanics*, vol. 19, no. 2, pp. 543-568, Apr. 2019, doi: 10.1007/s10652-018-9637-1.
- [17] O. Ghoulam, H. Talbi, K. Amghar, A.-i. Amrani, A. Charef, and I. Driouich, "Heat transfer improvement in turbulent flow using detached obstacles in heat exchanger duct," *International Journal of Thermofluids*, vol. 27, May 2025, Art. no. 101225, doi: 10.1016/j.ijft.2025.101225.
- [18] L. N. Thanh, "The influence of baffled channel for cooling hot surface: Numerical simulation and Taguchi analysis," *Case Studies in Thermal Engineering*, vol. 52, Dec. 2023, Art. no. 103646, doi: 10.1016/j.csite.2023.103646.
- [19] Ansys Fluent Theory Guide 12.0, ANSYS Inc.,, Canonsburg, PA, USA, 2012.
- [20] S. Rana, H. B. Dura, S. Bhattrai, and R. Shrestha, "Impact of baffle on forced convection heat transfer of CuO/water nanofluid in a micro-scale backward facing step channel," *Journal of Thermal Engineering*, vol. 8, no. 3, pp. 310-322, May 2022, doi: 10.18186/thermal.1107168.

Research Article

Vol. 28 (No. 4), pp. 250-255, 2025 doi: 10.5541/ijot.1714328 Published online: December 1, 2025

Cosmic Expansion Driven by Barrow Entropy

M. F. Karabat 🕑



Prof. Dr. Aziz Sancar Mardin Science and Art Center, Nur Neighborhood, 47200, Artuklu/Mardin, Turkey E-mail: mfarukkarabat@gmail.com

Received 4 June 2025, Revised 20 August 2025, Accepted 18 September 2025

Abstract

The concept of cosmic acceleration has become one of the fundamental concerns of modern cosmology. While the standard ACDM model incorporates dark energy to explain the accelerated expansion of the universe, alternative approaches are explored to understand cosmic dynamics. One such approach is Barrow entropic cosmology, which provides a generalized framework for cosmological thermodynamics by considering fractal deviations in the entropyarea relationship. In this sense, this study investigates the effects of Barrow's entropy on cosmological dynamics for the accelerating universe, focusing on modifications to the Friedmann equations. The results are compared with supernovae and CMB data based on the standard ACDM model, and provide insights into the applicability of Barrow cosmology as an alternative to dark energy. It is shown that the introduced Barrow correction term can explain the expanding universe. For Barrow parameter, which values are limited to the range $0 \le \Delta \le 1$, as Δ increases, H(z)values approach the standard at low redshifts (z < 0.5) but show significant deviations at high redshifts (z > 1).

Keywords: Barrow entropy; entropic acceleration; expanding universe.

1. Introduction

The accelerating expansion of the Universe was first revealed by distant Type Ia supernova observations [1]. Independent evidence came from the High-Z Supernova Search [2]. The cosmic microwave background further confirmed this acceleration through WMAP measurements Additional confirmation was obtained BOOMERANG observations of the CMB anisotropy [4]. The discovery of the accelerating expansion of the universe has stimulated a variety of theoretical models, most notably the ΛCDM paradigm. However, this model is based on the cosmological constant, which suffers from significant theoretical difficulties, including the vacuum energy problem. While the acceleration model of the universe is usually explained by dark energy or the cosmological constant, non-additive entropy offers an alternative perspective. Generalized entropy approaches take into account long-range gravitational interactions and complex system dynamics. Non-additive entropy, unlike classical additive entropy, can explain the expansion rate of the universe with thermodynamic principles. Such entropies are associated with the energy density and expansion of the universe, suggesting an entropic energy or entropic force without the need for dark energy. This approach makes it possible to understand the expansion of the universe through thermodynamic and fractal structures. By generalizing the holographic entropy relation to include fractal corrections, Barrow entropy provides a new way to explore cosmic acceleration without invoking dark energy. Barrow entropy is a generalization of the principles of holographic thermodynamics and was developed in cosmology to study entropy deviations from the standard Bekenstein-Hawking form. The Bekenstein-Hawking formalism shows that

gravity and thermodynamics are related [5]. After understanding the connections of gravity thermodynamics, many studies have been done. Jacobson showed that Einstein's equations can be derived from thermodynamic arguments [6]. Padmanabhan extended this approach to horizon thermodynamics and cosmology [7]. Akbar and Cai applied the first law of thermodynamics to Friedmann equations in scalar-tensor gravity [8]. Eling et al. formulated the non-equilibrium thermodynamics of spacetime [9]. In this context, the Bekenstein-Hawking formula, which states that the entropy of a black hole is proportional to its surface area, is used as a basis to understand cosmological dynamics, as it can be applied both to the apparent horizon of the Universe and to black hole horizons. However, for entropies based on Bekenstein-Hawking and Boltzmann-Gibbs (standard thermodynamics), the energy of the system is generally extensive, and the entropy is additive. On the other hand, it is known that the entropy of the whole system is not necessarily equal to the sum of the entropies of its subsystems. Therefore, this was confirmed that the standard thermodynamics theory cannot be applied and it should be generalized to non-additive systems such as gravitational systems [10]. In this context, many studies have been done based on non-extensive generalizations of entropies, especially by Tsallis and Cirto [11], Karniadakis [12] and Barrow [13]. The basic idea of Barrow entropy is to modify the entropy-temperature relationship to account for the existence of fractal structures on the horizon of the universe. Accordingly, a fractal structure for the black hole horizon was proposed by Barrow [13] inspired by the Covid-19 virus illustrations. Barrow suggested that the entropy of black holes may increase due to possible quantum gravitational effects, depending on

*Corresponding Author Vol. 28 (No. 4) / 250

changes in the horizon. On the other hand, some studies have been carried out to reveal the effects of Barrow entropy in the cosmological framework. In this context, the generalized second law of thermodynamics was investigated [14] and the holographic dark energy models (HDE) were examined by considering the apparent horizon as the thermodynamics limit [15]. Recently, a modified cosmological scenario based on Barrow entropy was presented by Saridakis [16]. In addition, many other studies in the context of HDE have been different in Pradhan and collaborators examined statefinder diagnostics within this model [17]. Bhardwaj et al. developed a statefinder hierarchy for Barrow HDE [18]. Srivastava and Sharma studied Barrow HDE with the Hubble horizon as IR cutoff [19].

In the current literature, the effects of Barrow entropy on cosmological dynamics have mostly been studied phenomenologically; however, the consistent modification of the Bekenstein–Hawking entropy together with the Einstein–Hilbert action, its impact on the Friedmann equations and its confrontation with observational data (SN Ia, CMB, H(z)) have not been thoroughly derived or systematically tested. This study addresses this gap by deriving the entropic force from Barrow entropy, incorporating it into the Friedmann framework, and comparing the resulting cosmological predictions with current observational datasets.

2. Model Development

In this section, entropic approaches are systematically derived to explain the accelerated expansion. First, the definition of Bekenstein–Hawking area law and its thermodynamic derivatives are presented (Section 2.1), followed by a demonstration of how the Barrow entropy and the Einstein–Hilbert action are modified through surface terms (Sections 2.2 and 2.3).

Bekenstein and Hawking's work first confirmed that black hole entropy is proportional to the surface area of the event horizon. This idea was later applied to the apparent horizon of the universe. The entropic force at the boundary of the Universe is derived from its entropy and temperature, and can explain both the early inflationary phase and the late accelerated expansion of the Universe. These phases are linked to the dynamics of the entropy and temperature changes at the boundary. By applying the holographic principle and extending the ideas of Bekenstein-Hawking entropy to the entire Universe, we can define entropy and temperature at the Hubble horizon. This framework generalizes the concepts of black hole thermodynamics to cosmology. This model revealed that black holes not only have classical properties such as mass, charge, and angular momentum, but also quantum properties such as information and entropy. Therefore, it also contributed to modern physics debates such as the information paradox and the holographic principle. This result is one of the points where thermodynamics, quantum mechanics and general relativity

The formula for black hole entropy, as given in [5],

$$S_{BH} = k_B \left(\frac{A_H}{4L_p^2}\right),\tag{1}$$

where, $A_H = 4\pi r_H^2$, is the surface area of the apparent horizon of the universe and the Planck length is $L_p =$

 $\sqrt{\hbar G/c^3}$. Stephen Hawking has shown that black holes have thermodynamic temperatures by emitting radiation through quantum effects. The Hawking temperature is given by [20]

$$T = \gamma \frac{\hbar H}{k_B 2\pi},\tag{2}$$

where, T is the temperature of the horizon of the universe and is closely related to the De Sitter temperature. Here γ is the non-negative free order parameter, usually $1/2 \cong \gamma$ or $3/2\pi = \gamma$, which corresponds to the parameter for the screen temperature obtained in [20].

The entropic force associated with Bekenstein-Hawking entropy can be written as:

$$S_{BH} = -T \frac{dS_{BH}}{dr_H} = -\gamma \frac{\hbar H}{k_B 2\pi} \frac{dS_{BH}}{dr_H} \left[k_B (\frac{A_H}{4L_p^2}) \right]. \tag{3}$$

For the accelerating Universe, the horizon radius is $r_H \sim c/H$ and the corresponding derivatives are given by

$$\frac{dS_{BH}}{dr_H} = \frac{dS_{BH}}{dH} \frac{dH}{dr_H}, \frac{dH}{dr_H} = -\frac{c}{r_H^2},\tag{4}$$

We have,

$$S_{BH} = -\gamma \frac{\hbar H}{k_B \pi} k_B \left(\frac{\pi c^5}{\hbar G} \right) H^{-3} \frac{c}{r_H^2}$$
 (5)

$$S_{BH} = -\gamma \frac{\hbar}{c\pi} \left(\frac{\pi c^5}{\hbar G} \right) = -\gamma \frac{c^4}{G}. \tag{6}$$

Pressure due to entropic force is

$$P_{BH} = \frac{F_{BH}}{A_H} = -\gamma \frac{c^4}{4\pi G r_H^2} \tag{7}$$

$$P_{BH} = -\frac{\gamma c^2}{4\pi G} H^2 = -\gamma \frac{2\rho_{cr}}{3} c^2, \tag{8}$$

where, $\rho_{cr} = 3H^2/8\pi G$ is the critical mass density of radiation and matter and is close to the measured negative pressure of dark energy in the form of a cosmological constant [21].

The effective pressure is

$$P_{eff} = p + p_{BH} \tag{9}$$

$$P_{eff} = p - \frac{\gamma c^2}{4\pi G} H^2. \tag{10}$$

2.2 Barrow Entropic Model

Barrow's entropy modifies [13] the standard Bekenstein-Hawking relation by introducing a fractal correction parameter for the quantum gravitational deformation, Δ , as follows:

$$S_B = k_B \left(\frac{A_H}{4L_P^2}\right)^{1 + \frac{\Delta}{2}}.\tag{11}$$

Here, Δ is deformation parameter and is constrained by the values $0 \le \Delta \le 1$. It can be clearly seen that when $\Delta = 0$, the area law is restored to the standard Bekenstein-Hawking entropy. And when $\Delta = 1$, it means that there is a maximum deviation from the Bekenstein-Hawking entropy.

The entropic force associated with Barrow's entropy can be written as:

$$F_B = -T \frac{dS_B}{dr_H}. (12)$$

Using Eq. (4) and substituting Barrow's entropy the derivative of the entropy with respect to the horizon radius r_H gives

$$F_{B} = -T \frac{dS_{B}}{dr_{H}}$$

$$= -\gamma \frac{\hbar}{k_{B}} \frac{H}{2\pi} \left[2k_{B} \left(+\frac{\Delta}{2} \right) \left(\frac{\pi c^{5}}{\hbar G} \right)^{1+\Delta/2} H^{-3-\Delta} \frac{c}{r_{H}^{2}} \right]$$
(13)

$$F_B = -\gamma \frac{(2+\Delta)c^{4+5\Delta/2}}{2G} \left(\frac{\pi}{\hbar G}\right)^{\Delta/2} H^{-\Delta}. \tag{14}$$

Pressure due to entropic force:

$$P_{B} = \frac{F_{B}}{A_{H}} = -\gamma \frac{(2+\Delta)c^{4+5\Delta/2}}{2G} \left(\frac{\pi}{\hbar G}\right)^{\Delta/2} H^{-\Delta} \frac{1}{4\pi r_{H}^{2}}$$
(15)

$$P_B = -\gamma \frac{(2+\Delta)c^{2+5\Delta/2}}{8\pi G} \left(\frac{\pi}{\hbar G}\right)^{\Delta/2} H^{2-\Delta}.$$
 (16)

The effective pressure is

$$P_{eff} = p - \gamma \frac{(2+\Delta)c^{2+5\Delta/2}}{8\pi G} \left(\frac{\pi}{\hbar G}\right)^{\Delta/2} H^{2-\Delta}.$$
 (17)

2.3 Einstein-Hilbert Action with Barrow Entropy

The acceleration of the universe, as explained in surface terms by the Einstein-Hilbert action, can be understood as a consequence of the entropy associated with the cosmological horizon. By modifying the Einstein-Hilbert action to include surface terms, the acceleration is naturally derived from the thermodynamic properties of the universe. This approach eliminates the need for dark energy and provides a new way to understand the dynamics of cosmic expansion. Barrow's framework modifies the standard Einstein-Hilbert action by introducing surface terms:

$$I = \int \left(\frac{R}{2\kappa} + L_m\right) \sqrt{-g d^4 x} + \int K \sqrt{-h} d^3 x \tag{18}$$

where, R is the curvature tensor (Ricci scalar) of the space, K is the trace of the convex curvature of the boundary, h is the metric determinant on the boundary. Here the second term on the right of the equation is the surface term. This term, which depends on the entropy $(\int K \sqrt{-h} d^3x)$, creates new terms in the Friedmann equations and is closely related to holography, the idea that the entropy of a region of space is proportional to the area of its boundary. In this case, the holographic principle suggests that the entropy of the universe is proportional to the area of the Hubble horizon. Accordingly, the entropic force driving acceleration arises from the holographic storage of information at the horizon of the universe. This is a quantum gravitational effect that arises from the thermodynamic properties of spacetime and provides an alternative explanation for cosmic acceleration. For a homogeneous and spatially flat universe, the Friedmann acceleration equation and continuity equations

without the cosmological constant are given by following equation.

(12)
$$\frac{\ddot{a}}{a} = -\frac{4\pi G}{3} \left(\rho + \frac{3P_{eff}}{c^2} \right),$$
 (19)

$$\dot{\rho} + 3\frac{\dot{a}}{a}\left(\rho + \frac{P_{eff}}{c^2}\right) = 0,$$
 (20)

where, the dot $\dot{a}/a = H$ denotes the time derivatives and a(t) is the scale factor. For the Bekenstein-Howking enropy these Eqs. (19), (20) becomes;

$$\frac{\ddot{a}}{a} = -\frac{4\pi G}{3} \left[\rho + \frac{3}{c^2} \left(p - \frac{\gamma c^2}{4\pi G} H^2 \right) \right]$$
 (21)

(14)
$$\frac{\ddot{a}}{a} = -\frac{4\pi G}{3} \left(\rho + \frac{3p}{c^2} \right) + \gamma H^2$$
 (22)

$$\dot{\rho} + 3\frac{\dot{a}}{a} \left[\rho + \frac{1}{c^2} \left(p - \frac{\gamma c^2}{4\pi G} H^2 \right) \right] = 0 \tag{23}$$

$$\dot{\rho} + 3H\left(\rho + \frac{p}{c^2}\right) = \gamma \frac{3}{4\pi G}H^3. \tag{24}$$

For the Barrow's entropy the Eqs. (19), (20) becomes:

$$\frac{\ddot{a}}{a} = -\frac{4\pi G}{3} \left[\rho + \frac{3}{c^2} \left(p - \gamma \frac{(2+\Delta)c^{2+5\Delta/2}}{8\pi G} \left(\frac{\pi}{\hbar G} \right)^{\Delta/2} H^{2-\Delta} \right) \right], \quad (25)$$

$$\frac{\ddot{a}}{a} = -\frac{4\pi G}{3} \left(\rho + \frac{3p}{c^2}\right) + \gamma \frac{(2+\Delta)c^{5\Delta/2}}{2} \left(\frac{\pi}{\hbar G}\right)^{\Delta/2} H^{2-\Delta},\tag{26}$$

$$\dot{\rho} + 3\frac{\dot{a}}{a} \left[\rho + \frac{1}{c^2} \left(p - \gamma \frac{(2+\Delta)c^{2+5\Delta/2}}{8\pi G} \left(\frac{\pi}{\hbar G} \right)^{\Delta/2} H^{2-\Delta} \right) \right] = (27)$$

$$\dot{\rho} + 3H\left(\rho + \frac{p}{c^2}\right) = \gamma \frac{3(2+\Delta)c^{5\Delta/2}}{8\pi G} \left(\frac{\pi}{\hbar G}\right)^{\Delta/2} H^{3-\Delta}.$$
 (28)

Similar results are shown in [22], [23]. Here, the second term on the right side in the Eq. (26), $\gamma ((2 + \Delta)c^{5\Delta/2}/2) (\pi/\hbar G)^{\Delta/2}H^{2-\Delta}$, is called the Barrow entropic term and allows the universe to accelerate without dark energy. This term represents the entropic contribution derived from the surface term and produces an acceleration that mimics the effects of dark energy. At late times, the matter density ρ becomes negligible and the term associated with the surface entropy becomes dominant, resulting in an accelerating expansion of the universe. Here, as can be clearly seen from Eqs. (26) and (28), the Bekenstein-Hawking entropy (22), (24) is recovered when Δ = 0. It should be recalled here that the Friedmann equation without the cosmological constant is:

$$H^2 = \frac{8\pi G}{3}\rho. \tag{29}$$

By substituting Eq. (29) and the equation of state $(p = \omega c^2 \rho)$ into Eq. (28), we obtain,

$$\frac{\dot{\rho}}{\rho} + 3(1+\omega)H = \gamma(2+\Delta)c^{5\Delta/2} \left(\frac{\pi}{\hbar G}\right)^{\Delta/2} H^{1-\Delta}$$
 (30)

After integrating Eq. (30), we get

$$\rho(a) = \left[\frac{c}{3(1+\omega)} + \left(\rho_0^{\Delta/2} - \frac{c}{3(1+\omega)} \right) a^{\frac{-3\Delta(1+\omega)}{2}} \right]^{\frac{2}{\Delta}}.$$
 (31)

where, C is defined as $C = \gamma(2 + \Delta)c^{5\Delta/2}H_0^{-\Delta}(\pi/\hbar G)^{\Delta/2}(8\pi G/3)^{-\Delta/2}$. The state parameter ω can take the values 0, 1/3 and -1 for matter-dominated, radiation-dominated and cosmological constant-dominated universes, respectively.

3. Results and Discussion

Observational data, such as distances of supernova luminosity, the cosmic microwave background (*CMB*), provide the evolution of the Hubble parameter with time (z). Type Ia supernovae is used to measure the expansion history of the universe through the luminosity distance $d_L(z)$ given by [24]:

$$d_L(z) = c(1+z) \int_0^z \frac{dz'}{H(z')},$$
(32)

where, z is the redshift defined by $1 + z = a_0/a$. For the standard ΛCDM the luminosity distance can be written [25] as

$$\begin{aligned} d_{L} &= (z; \Omega_{M}; \Omega_{\Lambda}; H_{0}) = \\ \frac{c(1+z)}{H_{0}\sqrt{|\kappa|}} sinn \{ |\Omega_{\kappa}|^{1/2} \int_{0}^{z} dz [(1+z)^{2} (1+\Omega_{m}z) - \\ z(2+z)\Omega_{\Lambda}]^{-1/2} \}, \end{aligned}$$
(33)

where, $\Omega_{\kappa}=1-\Omega_{M}-\Omega_{\Lambda}$ and sinn is equal to sinh and sin respectively when $\Omega_{\kappa}>0$, $\Omega_{\kappa}<0$. For the flat universe models (ΛCDM) we use $\Omega_{M}+\Omega_{\Lambda}=1$, neglecting the density parameter Ω_{r} for the radiation. For a homogeneous and isotropic universe, the Hubble function $H_{(Z)}$ can be written in the following form:

$$\frac{\frac{H_{(Z)}}{H_0}}{\sqrt{\Omega_m (1+z)^3 + \Omega_\Lambda + \Omega_\kappa (1+z)^2 + \Omega_r (1+z)^4}}.$$
Using this together with the Barrow entropic

Using this, together with the Barrow entropic contribution term (31) and Eq. (33), we obtain the following graphs.

The Hubble parameter has been plotted as a function of the redshift z and use $H_0 = 74 \text{ km/s/Mpc}$ and $H_0 =$ 66.6 km/a/Mpc for the supernova (SN) and CBM values, respectively. Here $\Omega_m = 0.3$ and $\Omega_{\Lambda} = 0.68$ standard values were used and we determined that the best value of γ is 0.1. In Figure 1, for small Δ ($\Delta = 0.1$) value, the models modified with Barrow entropy produced a different H(z)curve than the ΛCDM . It is shown how the difference between supernova and CMB values can be affected by the Barrow model. The Barrow model provides a different growth rate on H(z) as the redshift (z) increases. At higher redshifts (z > 1), the Barrow model differs in that the H(z)values tend to increase. This reflects how entropic effects can affect the expansion of the universe in the high-redshift regime. In Figure 2, H(z) curves are presented for some values between $\Delta = 0$ and $\Delta = 1$ in Barrow entropic cosmology. We see that at $\Delta = 0$ it is equivalent to the Standard ΛCDM model. At $\Delta > 0$ the entropic effects are added, changing the expansion rate of H(z) and at $\Delta = 1$ the maximum entropic contribution provides a noticeable increase, especially at high redshifts (z > 1). Figure 3.

compares of the luminosity distance versus redshift z with observational data for a flat cosmological model. Here, it is seen that there are significant differences in the Δ parameter at high red shifts compared to low red shifts.

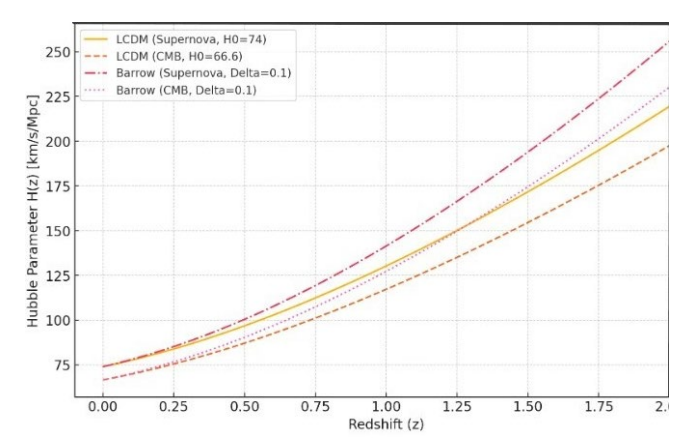


Figure 1. Comparison of H(z) models: LCDM vs Baroww entropic cosmology.

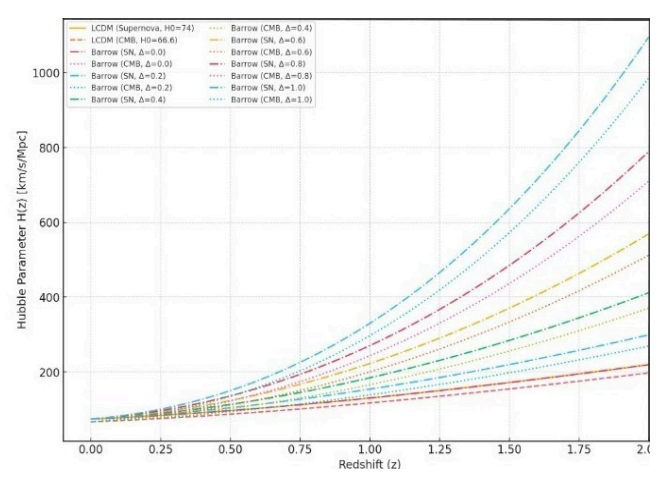


Figure 2. H(z) for $\Delta = 0$ to 1 in Barrow entropic cosmology.

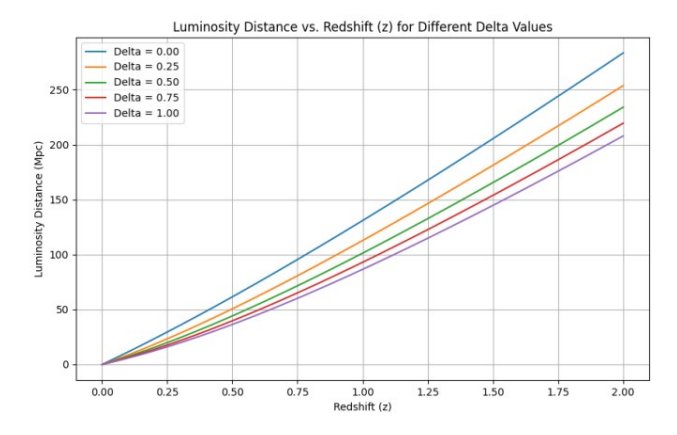


Figure 3. Luminosity distance vs. redshift (z) for different delta values.

4. Conclusion

In this study, the effects of Barrow entropic cosmology on cosmological expansion are investigated and the role of the Δ parameter on the Hubble parameter H(z) is detailed. The calculations are compared with Supernova and CMB data and are found to be compatible with both data sets. As a result of the analyses performed for Barrow parameter values limited to the range $0 \le \Delta \le 1$, it is observed that as Δ increases, the values of the Hubble parameter H(z)

approach the standard ΛCDM model at low redshifts (z < 0.5), but show significant deviations at high redshifts (z > 1). These results therefore indicate that Barrow entropy affects the cosmic expansion rate more at high redshifts. Our findings support the view that Barrow entropic cosmology offers a new approach to understanding the dynamics of cosmological acceleration and expansion of the universe and is consistent with observational data. However, more observational data are needed to determine the parameters of this model more precisely.

Conflict of Interest

Author approves that to the best of their knowledge, there is not any conflict of interest or common interest with an institution/organization or a person that may affect the review process of the paper.

Acknowledgements

The author declares that there are no acknowledgements to report.

Credit Author Statement

M. F. Karabat: Conceptualization, Methodology, Software, Data curation, writing – Original draft preparation, Visualization, Investigation, Supervision, Validation, Writing – Reviewing and Editing.

Nomenclature

utuit
Scale factor
Critical density
Energy
Pressure
Effective presure
Volume
Boltzmann constant
Gravitational constant
Planck length
Entropic force
Speed of light
Black hole horizon area
Horizon radius (Hubble horizon)
Hubble constant
Present Hubble constant
Bekenstein-Hawking entropy
Barrow entropy
Curvature tensor (Ricci scalar)
Convex curvature of the boundary
Redshift-dependent Hubble parameter
Redshift
Luminosity distance
Einstein-Hilbert action
nbols
Density parameter

References:

- [1] S. Perlmutter et al., "Discovery of a supernova explosion at half the age of the Universe," *Nature*, vol. 391, no. 6662, pp. 51–54, Jan. 1998, doi: 10.1038/34124.
- [2] B. P. Schmidt et al., "The High-Z Supernova Search: Measuring Cosmic Deceleration and Global Curvature of the Universe Using Type Ia Supernovae," *The Astrophysical Journal*, vol. 507, no. 1, pp. 46–63, Nov. 1998, doi: 10.1086/306308.
- [3] D. N. Spergel et al., "First-Year Wilkinson Microwave Anisotropy Probe (WMAP) Observations: Determination of Cosmological Parameters," *The Astrophysical Journal Supplement Series*, vol. 148, no. 1, pp. 175–194, Sep. 2003, doi: 10.1086/377226.
- [4] C. B. Netterfield et al., "A Measurement by BOOMERANG of Multiple Peaks in the Angular Power Spectrum of the Cosmic Microwave Background," *The Astrophysical Journal*, vol. 571, no. 2, pp. 604–614, Jun. 2002, doi: 10.1086/340118.
- [5] J. D. Bekenstein, "Black Holes and Entropy," *Physical Review D*, vol. 7, no. 8, pp. 2333–2346, Apr. 1973, doi:10.1103/physrevd.7.2333.
- [6] T. Jacobson, "Thermodynamics of Spacetime: The Einstein Equation of State," *Physical Review Letters*, vol. 75, no. 7, pp. 1260–1263, Aug. 1995, doi: 10.1103/physrevlett.75.1260.
- [7] T. Padmanabhan, "Gravity and the thermodynamics of horizons," *Physics Reports*, vol. 406, no. 2, pp. 49–125, Jan. 2005, doi: 10.1016/j.physrep.2004.10.003.
- [8] M. Akbar and R.-G. Cai, "Friedmann equations of FRW universe in scalar–tensor gravity, f(R) gravity and first law of thermodynamics," *Physics Letters B*, vol. 635, no. 1, pp. 7–10, Mar. 2006, doi: 10.1016/j.physletb.2006.02.035.
- [9] C. Eling, Raf Guedens, and T. Jacobson, "Non-equilibrium Thermodynamics of Spacetime," *Physical Review Letters*, vol. 96, no. 12, Mar. 2006, doi: 10.1103/physrevlett.96.121301.
- [10] M. L. Lyra and C. Tsallis, "Nonextensivity and Multifractality in Low-Dimensional Dissipative Systems," *Physical Review Letters*, vol. 80, no. 1, pp. 53–56, Jan. 1998, doi: 10.1103/physrevlett.80.53.
- [11] C. Tsallis, "Dynamical scenario for nonextensive statistical mechanics," *Physica A: Statistical Mechanics and its Applications*, vol. 340, no. 1–3, pp. 1–10, Sep. 2004, doi: https://doi.org/10.1016/j.physa.2004.03.072.
- [12] G. Kaniadakis, "Statistical mechanics in the context of special relativity," *Physical Review E*, vol. 66, no. 5, Nov. 2002, doi: 10.1103/physreve.66.056125.
- [13] J. D. Barrow, "The area of a rough black hole," *Physics Letters B*, vol. 808, Sep. 2020, Art. no. 135643, doi: 10.1016/j.physletb.2020.135643.
- [14] E. N. Saridakis, "Modified cosmology through spacetime thermodynamics and Barrow horizon entropy," *Journal of Cosmology and Astroparticle Physics*, vol. 2020, no. 07, pp. 031–031, Jul. 2020, doi: 10.1088/1475-7516/2020/07/031.

Density

ħ

ρ

γ

Reduced Planck constant

Gamma (Non-negative free order parameter)

Delta (Barrow fractal deformation parameter)

- [15] E. N. Saridakis and S. Basilakos, "The generalized second law of thermodynamics with Barrow entropy," *The European Physical Journal C*, vol. 81, no. 7, Jul. 2021, doi: 10.1140/epjc/s10052-021-09431-y.
- [16] E. N. Saridakis, "Barrow holographic dark energy," *Physical Review D*, vol. 102, no. 12, Dec. 2020, doi: 10.1103/physrevd.102.123525.
- [17] A. Pradhan, A. Dixit, and Vinod Kumar Bhardwaj, "Barrow HDE model for statefinder diagnostic in FLRW universe," *International Journal of Modern Physics*, vol. 36, no. 04, pp. 2150030–2150030, Feb. 2021, doi: 10.1142/s0217751x21500305.
- [18] V. K. Bhardwaj, A. Dixit, and A. Pradhan, "Statefinder hierarchy model for the Barrow holographic dark energy," *New Astronomy*, vol. 88, p. 101623, Oct. 2021, doi: 10.1016/j.newast.2021.101623.
- [19] S. Srivastava and U. K. Sharma, "Barrow holographic dark energy with hubble horizon as IR cutoff," *International Journal of Geometric Methods in Modern Physics*, vol. 18, no. 01, p. 2150014, Nov. 2020, doi: 10.1142/s0219887821500146.
- [20] D. A. Easson, P. H. Frampton, and G. F. Smoot, "Entropic accelerating universe," *Physics Letters B*, vol. 696, no. 3, pp. 273–277, Jan. 2011, doi: 10.1016/j.physletb.2010.12.025.
- [21] S. Weinberg, *Cosmology*. New York: Oxford university press, 2008.
- [22] M. Naeem and A. Bibi, "Accelerating universe via entropic models," *The European Physical Journal Plus*, vol. 138, no. 5, May 2023, doi: 10.1140/epjp/s13360-023-04073-3.
- [23] A. V. Kolesnichenko and M. Y. Marov, "Scenario of accelerated universe expansion under exposure to entropic forces related to with the entropies of Barrow and Tsallis-Cirto," *Mathematica Montisnigri*, vol. 50, pp. 80–103, Jan. 2021, doi: 10.20948/mathmontis-2021-50-8.
- [24] A. G. Riess et al., "Type Ia Supernova Discoveries atz> 1 from theHubble Space Telescope: Evidence for Past Deceleration and Constraints on Dark Energy Evolution," *The Astrophysical Journal*, vol. 607, no. 2, pp. 665–687, Jun. 2004, doi: 10.1086/383612.
- [25] S. Perlmutter et al., "Measurements of Ω and Λ from 42 High-Redshift Supernovae," *The Astrophysical Journal*, vol. 517, no. 2, pp. 565–586, Jun. 1999, doi: 10.1086/307221.

Research Article

Vol. 28 (No. 4), pp. 256-264, 2025 doi: 10.5541/ijot.1376509 Published online: December 1, 2025

Exergy Analysis of Cyprus International University Solar Power Plants

^{1*}M. Yilmaz , ²M. Atmaca

¹Ministry of National Education, General Directorate of Vocational and Technical Education, Turkey ²Department of Mechanical Engineering, Faculty of Technology, Marmara University, Maltepe/İstanbul, Turkey E-mail: ^{1*} mehmetyilmaz1989@hotmail.com

Received 1 April 2024, Revised 26 July 2024, Accepted 4 August 2024

Abstract

The Turkish Republic of Northern Cyprus is located in a region rich in solar energy potential, one of the renewable energy sources. Exergonomic analyzes have been carried out in recent years to determine to what extent electricity generation facilities reflect their potential. These studies, also called exergy analysis, include a series of calculations and analyzes aimed at revealing the potential that a power plant should reflect. In this study, exergy analysis of solar power plants belonging to Cyprus International University was carried out and the condition of the plants was analyzed. As a result of the analysis, it was determined that the energy efficiency of the system was 93% and the daily electricity efficiency was 12%. This value shows that the system has a good level of efficiency, considering the average efficiency of photovoltaic panels. As a result of our exergy analysis, the exergy efficiency of our system was found to be around 73%. According to this value, a large part of the usable energy is lost in our system. In order to increase these values, all universally derived methods must be reviewed and the appropriate ones must be included in the system. In this way, it is aimed to prevent global climate imbalances by increasing the amount of energy obtained from renewable energy sources in energy production, first at the Cyprus International University and then in the Turkish Republic of Northern Cyprus.

Keywords: Power plants; renewable energy; energy analysis; exergy analysis; solar energy.

1. Introduction

Non-renewable energy resources are energy resources that take a very long time to renew due to their formation. For this reason, these types of energy are called nonrenewable energy sources. Primary Energy Resources, fossil fuels such as coal, oil, natural gas and nuclear energy are non-renewable resources. Fossil resources are expected to maintain their decisive share in world primary energy production in the coming years, as they do today. It is predicted that the total share of these resources in world primary energy production will be 88.5 percent (%) in 2020. The largest share in this ratio belongs to oil [1]. Renewable energy refers to the energy source that can be available the next day in nature's own evolution [2]. Renewable energy sources have an important place for the world and our country with their renewability, minimum environmental impact, low operation and maintenance costs, national characteristics and reliable energy supply features [3]. Contemporary energy sources include solar, wind, wave, biomass, geothermal energy, hydraulic and hydrogen energy. Our country is also trying to benefit from these new energy sources. Solar cells or photovoltaics are semiconductors that convert sunlight directly into electrical energy. Photovoltaic facilities can be divided into two in terms of organization: island systems and grid-connected systems. In island Region [8]. Petela studied the exergy analysis of parabolic solar cooker. It was determined that the exergy efficiency of the system was 10 times lower [9]. Öztürk carried out a study to determine the exergy values of the annual average, highest systems, photovoltaic energy gain is adjusted according to energy need. Since photovoltaic energy production often does not equal the immediate energy needs of consumers, batteries are often used separately. In grid-connected systems, the electrical grid acts as an energy storage. Most Photovoltaic (PV) installations worldwide are operated as grid-connected facilities. Since the price paid for electricity from solar energy is higher in such facilities, the energy produced is mostly given to the general electricity grid. It is estimated that one third of Germany's energy needs will be met from photovoltaic sources by 2050 [4]. The exergy of solar radiation is the value that can be calculated depending on the relative amount of energy that can be obtained from solar energy at the highest rate [5]. In addition to the quantitative value of solar radiation, exergy analysis, which determines its qualitative value, also needs to be performed. Valuable studies on exergy analysis of solar radiation are carried out in the literature both at home and abroad. Uçkan made exergy analysis of solar radiation in Van province for the models used in the literature between 1993 and 2007 [6]. Exergy analysis has been widely used in the design, simulation and performance evaluation of energy systems

Öztürk determined the annual average, highest and lowest solar radiation exergy values for the Southeastern Anatolia and lowest solar radiation for the Mediterranean Region [10]. Öztürk stated that mapping the part of solar radiation that can be converted into useful work with exergy analysis would be useful for businesses that want to invest [11]. Kaymak

*Corresponding Author Vol. 28 (No. 4) / 256

examined the exergy analysis of wind energy system and photovoltaic cells for Istanbul climate conditions. Evaluated the feasibility of Wind- Solar hybrid systems [12]. Candau examined various exergy analysis models and determined that an exergy model based on classical thermodynamic concepts should be derived [13]. Chow studied the exergy analysis of photovoltaic panels with and without glass covers. It has been determined that a system without a glass cover will be at maximum efficiency in order to benefit from solar radiation at the maximum level, but covering the system with glass, taking into account the wind factor, prevents energy losses in terms of exergy analysis [14]. In the study conducted by Mehmet Altınkaynak, Recep Demirekin and Ali Kemal Yakut, a PV-T collector with 72 cells, single crystal silicon module cell panel and producing 190W nominal power was used for calculation to support the ground source heat pump. Energy and exergy analyzes for each element in the PV-T supported heat pump system were made with the help of the EES (Engineering Equation Solver) program. In the PV-T hybrid system used, the total electrical power is 1422 W and the total thermal power received is 4397 W. The thermal efficiency of the PV-T collector is calculated as 49.7% and the electrical efficiency is 15.2%. The efficiency contribution of the collectors to the PV-T source heat pump system was found to be 67.9%. It has been observed that as the radiation intensity increases, the total electrical power and the total received thermal power increase. Additionally, in this study, the COP of the heat pump system was calculated as 4.41. It was observed that the highest exergy destruction occurred in the condenser [15]. In the study conducted by Fatih Bayrak, a new type of finned air heated photovoltaic/thermal (PV/T) collector was designed and comparatively tested. In the experiments, natural convection (DT) and forced convection (m_1 =0.01 kg/s and m_2 =0.015 kg/s) were applied to PV/T collectors with and without fins. Thermodynamic analysis of all systems and the sustainability index (SI), which is a function of exergy efficiency, were examined. According to the results obtained, increasing the mass flow rate and integrating the fin had a positive effect on the output power, electrical energy and exergy of the PV/T system. The lowest output power in the system is 26.84W with no fins and natural convection (M1), and the highest output power is 37.40W with fins and forced convection (M6). When all PV/T collectors were compared, the highest overall exergy efficiency was the M4 collector with natural convection and fins, with 20.48%. Sustainability index (SI) values, which are a function of exergy efficiency, are higher in finned systems [16]. In the study conducted by Ömer Resuloğulları and Ali Erişen, the effects of system parameters such as absorption unit thickness, fluid flow rate and radiation intensity changes in solar energy systems were examined. It has been determined that by increasing the thickness of the absorption unit, the radiation reaching the photovoltaic module can produce electricity at higher efficiency, and by increasing the flow rate, an increase in exergy can be achieved in the system. Additionally, it has been shown that by increasing the radiation intensity, there may be heat gains in the system and therefore exergy increases based on these gains [17].

In the study conducted by Nesrin Bilgin Beyazit, Hüsamettin Bulut and Fatih Ünal, the exergy of solar radiation was analyzed for Diyarbakır province (37.55°N, 40.14°E) between 1999 and 2008. Three models were used for exergy analysis of solar radiation. According to the data

received from meteorology, the exergy efficiency of longterm solar radiation for Diyarbakır Province was evaluated by applying the 3 models used. According to the results; The exergy value of the highest long-term monthly average solar radiation was determined as 26.66 MJ/m² in the Petela and Spanner models and 27.13 MJ/m² in the Jeter model in June. The ratio of solar radiation exergy to the long-term monthly average solar radiation energy varies from 0.932 to 0.939 in both Petela and Spanner models. In the Jeter model, this ratio varies from 0.949 to 0.954. As a result of the analysis of 10year data, a correlation was developed between solar radiation and solar radiation exergy for all three models. The highest annual solar radiation value was calculated as 18.19 MJ/m² in 1999 and the lowest annual solar radiation value was calculated as 17.36 MJ/m² in 2007 [5]. In the study carried out by Erhan Kırtepe and Ali Güngör, the theoretical modeling of the solar collector that allows us to produce thermal energy from the sun was made. Different nanofluids were obtained by adding nanoparticles (Cu, CuO, Al₂O₃, TiO₂, SiO₂) at different concentration rates to the water used as the main heat transfer fluid in the solar collector. The effects of using these nanofluids at different concentration rates and different flow rates in the solar collector on the thermal and exergetic performance of the solar collector were examined. It was determined that by using the nanofluid with Cu nanoparticles at a mass flow rate of 0.048 kg/s and a concentration ratio of 0.04, there was a 1.65% decrease in the collector thermal efficiency and a 1.59% increase in the exergy efficiency compared to the case where water was used as the heat transfer fluid. As a result of the theoretical analysis, it has been determined that adding nanoparticles to water, which is the basic heat transfer fluid, increases exergy efficiency while reducing thermal efficiency and entropy production [18].

In this study, exergy analyzes of the Solar Energy Power Plants of Cyprus International University located within the borders of Nicosia, which was selected as a sample region and system, were carried out in order to provide maximum benefit from the solar energy potential of the region. It is aimed to determine the improvable aspects of the Turkish Republic of Northern Cyprus, to eliminate its deficiencies and to reach the maximum potential of the Power Plant. Although there is an energy need problem and such a solar energy potential on the island, unfortunately, there is no work yet to increase the efficiency of solar power plants. This situation expresses the regional originality of our project.

This study will enable solar power plants to approach their potential and will guide all solar energy production systems across the island. Meeting the energy needs, reducing environmental factors and obtaining maximum benefit from solar energy, which is a sustainable resource, will be worth a clog for the Turkish Republic of Northern Cyprus

2. Thermodynamic Analysis of Photovoltaic (Pv) Systems

Energy and exergy analysis of photovoltaic systems is examined within the framework of thermodynamic laws.

2.1 Energy Analysis of PV Systems

$$E_{PV} = E_{PV,electric} + E_{PV,Thermal} \tag{1}$$

The term E_{PV} represents the energy state of the system in the equilibrium state. The expression $E_{PV,electric}$ refers to the

electricity generation of the panel system, while $E_{PV,Thermal}$ denotes the lost heat energy of the panel system.

$$E_{PV,electric} = V_{oc}I_{sc} \tag{2}$$

where, V_{oc} denotes the open-circuit voltage, I_{sc} denotes the short-circuit current. The amount of heat lost by the photovoltaic system is expressed as follows.

$$E_{PV,Thermal} = h_{ca} A_C (T_C - T_a)$$
 (3)

The stable temperature of the solar cells in the system is given below.

$$4T_c^5 - 3T_aT_c^4 - T_aT_s^4 = 0 (4)$$

The amount of heat lost to the natural environment due to the effect of wind is expressed as follows.

$$h_{ca} = 2.8 + (3.0.v_r) \text{ to } 0 \le v_r \le 7 \text{ ms}^{-1}$$
 (5)

where, h_{ca} denotes the heat transfer coefficient representing the heat flow from the photovoltaic cell to the ambient environment, and v_r represents the wind speed measured in the vicinity of the PV panel.

The equilibrium state of the total energy of the photovoltaic system is shown below.

$$E_{PV} = V_{oc}I_{sc} + h_{ca}A_{c}(T_{c} - T_{a})$$

$$\tag{6}$$

In the context of engineering, efficiency is often expressed as the ratio between output and input. Energy efficiency for photovoltaic (PV) systems, on the other hand, can be defined as the ratio of the total output energy (electrical and thermal energy) to the solar energy falling on the PV surface. It is possible to express this situation as follows: "The energy efficiency of PV systems is defined as the ratio of output energy (electrical and thermal energy) to solar energy falling on the PV surface, and in general, efficiency in engineering is considered as the ratio of output to input"

$$\eta_{PV} = \frac{E_{PV}}{K_s \times A_c} = \frac{V_{oc} I_{sc} + h_{ca} A_c (T_c - T_a)}{K_s x A_c} \tag{7}$$

Here, η_{PV} represents the proportion of useful energy that can be utilized by the photovoltaic (PV) system, while K_s denotes the solar energy reaching the surface of the PV panel.

Normally, PV panels are used only in terms of generating electricity, so only the part that is converted into electrical energy is taken for efficiency. E_{PV} is the value of the energy produced by the E system during a day in Wh (Watt hours). The daily electrical yield of the PV system is given below.

$$\eta_{PV,D} = \frac{E_{PV,E}}{E_s} \tag{8}$$

where, $\eta_{PV,D}$ represents the daily electrical efficiency of the photovoltaic (PV) system, $E_{PV,E}$ denotes the amount of energy produced by the system during a day, and E_s refers to the amount of solar energy received from the sun during the same period.

2.2 Exergy Analysis of PV Systems

The electrical exergy obtained by the photovoltaic system aims to make as much of the available energy potential available as possible. The equilibrium state of exergy is given below.

$$X_{PV} = X_{PV,electric} - X_{PV,Thermal} - X_{PV-d,electric}$$
 (9)

where, $X_{PV,electric}$ represents the electrical exergy of the photovoltaic (PV) assembly, $X_{PV,Thermal}$ denotes *the* internal exergy losses within the system, and $X_{PV-D,electric}$ refers to the external exergy losses associated with thermal effects.

The internal loss of energy is a result of the natural heat flow because the insulation in the system cannot be reduced to the zero point, and the external losses are the result of the natural heat flow because the atmospheric temperature has a lower temperature than the system. The exergy losses (electrical and thermal) of the photovoltaic system are expressed as follows.

$$E_{PV,electric} = V_{oc}I_{sc} \tag{10}$$

$$X_{PV-d,electric} = V_{oc}I_{sc} - V_mI_m \tag{11}$$

$$X_{PV,Thermal} = (1 - \frac{T_a}{T_c}) \times [h_{ca} A_c (T_c - T_a)]$$
 (12)

The exergy efficiency of PV systems is calculated by the ratio of the exertion value of the PV system to the exergy value of the solar radiation incident on the PV system surface.

$$\psi_{PV} = \frac{X_{PV}}{X_{sun} \times A_c}$$

$$= \frac{\left[V_m I_m - \left(1 - \frac{T_a}{T_c}\right) \times \left(h_{ca} A_c \left(T_c - T_a\right)\right)\right]}{\left[\left(1 - \frac{T_a}{T_s}\right) \times K_s\right] A_c}$$
(13)

where, ψ_{PV} denotes the exergy efficiency of the photovoltaic (PV) system, and X_{sun} represents the exergy amount of solar radiation reaching the surface of the PV panels. This parameter is calculated straightforwardly as follows:

$$X_{sun} = \left(1 - \frac{T_a}{T_s}\right) \times K_s \tag{14}$$

$$\frac{T_s}{T_{S^*}} = 0.9562 + 0.2777 \ln\left(\frac{1}{f}\right) + 0.0511 f$$
 (15)

Here, the T_s^* value can be calculated by taking the radiation temperature from the sun Ts and the diffuse radiation reflection coefficient f [19].

3. Cyprus International University's (Ciu) Solar Power Plants

CIU's commitment to environmental awareness is known for its teaching, research, community awareness activities and supporting sustainability on campus. In this context, Cyprus International University Sustainability Program studies are carried out. The program consists of the Sustainable Energy Research Center (SERC) and the A Sustainable Campus (SC) team.

Covering an area of 14.000 m² on the northern border of the campus, it is not only the largest PV project in Northern Cyprus, but also an example of how solar panels

can be applied to different surfaces with additional installations. While solar panels in Cyprus have traditionally been installed on the roof or on the land, the panels under the current project have been installed in 5

different configurations: flat and sloping roof, façade cladding, land and car park [20].

The solar power plants of Cyprus International University established in 5 different environments and their technical characteristics are given in Table 1.

Table 1. Cyprus international university pv facilities

Photovoltaic System	Terrain	Parking	B Block	Arena	Stoneite
Commissioning Date	19/02/2016	19/02/2016	19/02/2016	31/12/2015	05/01/2016
Rated Power (kWp)	748.48	134.85	99.20	100.44	199.64
Inverters (25 kW)	30	6	4	4	8
Orientation	S	39° GD	5° GD	2° GD	21° GD
Tilt Angle	25°	6°	15°	6°	6°
Mounting Type	Floor Mounting	Car Park Roof	Flat Roof	Parking	Pitched Roof

CIU has different types of structures spread over a wide area. Solar power plants are designed to come to the appropriate places of these structures. Although the sketch given in Figure 1 creates the idea that all the power plants are together, in fact these places are not next to each other but are located in different locations.

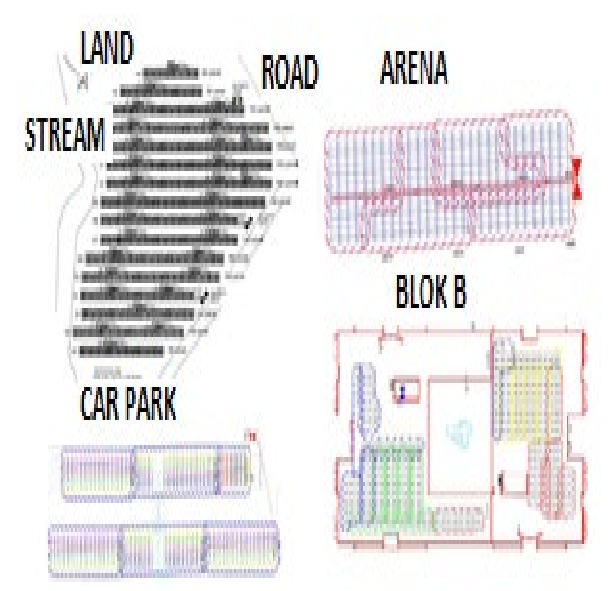


Figure 1. CIU pv plants.

The land installation is the one with the highest number of panels among the regions. It has 2408 panels. It meets most of the energy produced. Figure 2 shows the setup.



Figure 2. CIU land solar installation.

The technical values of the land installation are given in Table 2.

Table 2. Ciu land solar information.

Parameters	CIU Land
Rated Power (kWp)	746.48
Orientation	S
Tilt Angle	25°

The number of panels in the region built on the roofs of the parking lot is 435. Due to the fact that the air temperature is too high, the roof paints of the vehicles are damaged. Therefore, indoor and shaded parking lots are of great importance. The installation of the parking lot has contributed to the multifunctional use of the roof that provides shade for vehicles. Figure 3 shows the parking setup.



Figure 3. CIU car park spp (solar power plant) installation.

The technical values of the parking lot installation are given in Table 3.

Table 3. CIU parking spp information

1 00000 01 010	partition spp injointation
Parameters	Carport Parking
Rated Power (kWp)	134.85
Orientation	39° GD
Tilt Angle	6°

There are 320 panels in the B block roof installation. It is the installation with the fewest panels among the zones. Figure 4 shows the B block roof installation.



Figure 4. CIU block b roof solar installation.

Table 4. CIU block b roof spp information.

Parameters	Block B Roof	
Rated Power (kWp)	99.20	
Orientation	5° GD	
Tilt Angle	15°	

CIU arena setup takes its name from CIU arena sports complex. It has 324 panels. After the construction of the sports complex, it was built on the roof of the parking lot, which was located right next to it. Figure 5 shows the CIU arena setup.



Figure 5. CIU arena solar installation.

The technical values of the CIU arena installation are given in Table 5.

Table 5.CIU arena spp information.

- more ever a more app vigoriment					
Parameters	CIU Arena				
Rated Power (kWp)	100.44				
Orientation	2° GD				
Tilt Angle	6°				

Stoneite installation is installed on a pitched roof. It is the installation with the highest number of panels after the land installation. It has 644 panels. It is shown in Figure 6.



Figure 6. Stoneite solar installation.

The technical values of the installation of Stoneite SPP are given in Table 6.

Table 6. Stoneite spp information.

Parameters	Stoneite Pitched Roof
Rated Power (kWp)	199.64
Orientation	21° GD
Tilt Angle	6°

CIU, which was the first university in the Republic of Northern Cyprus to be included in the UI GreenMetrics world university rankings in 2018, has become the 111th most sustainable university in the world according to the 2021 UI GreenMetrics world ranking [20].

3.1 Energy and Exergy Analysis of Solar Power Plants of Cyprus International University

CIU Solar Power Plants are located at different points in the region where the university was established. Due to the fact that these points are far from each other and the variability of the factors that are active is not high, some values to be used in the calculations will be accepted as the same and analyzes will be made.

3.1.1 CIU SPP Energy Analysis

The energy balance of the PV system is as follows. All calculations are based on the daily time frame. Units are accordingly specified in Watt hours (Wh).

$$E_{PV} = E_{PV,electric} + E_{PV,Thermal} \tag{16}$$

The term E_{PV} represents the energy state of the system in the equilibrium state. The expression $E_{PV,electric}$ refers to the electricity generation of the panel system, while $E_{PV,Thermal}$ denotes the lost heat energy of the panel system.

$$E_{PV.electric} = V_{oc}I_{sc} \tag{17}$$

 V_{oc} (Open Circuit Voltage) is the maximum voltage that can be obtained from a solar cell and occurs at zero current. When no load is connected to the solar panel, it is the voltage value measured with an avometer from both ends. Isc (Short Circuit Current) is the maximum current read at the ends of the panel when the voltage is zero. The values to be used below are taken from the performance analysis study of PV plants carried out by the CIU Sustainable Energy Research Center.

$$E_{PV,elec.} = V_{oc}I_{sc} = (45.6)x(8.99) = 409.944 \text{ Wh}$$
 (18)

where, $V_{oc} = 45.6 V$ and $I_{sc} = 8.99 A$.

The amount of heat lost to the natural environment due to the effect of wind is expressed as follows [19].

$$E_{PV.Thermal} = hca Ac (Tc - Ta)$$
 (19)

The stable temperature of the solar cells in the system is given below [21].

$$4T_c^5 - 3T_aT_c^4 - T_aT_s^4 = 0 (20)$$

The average panel surface temperature, $T_{c,CIU}$, was provided by the CIU staff who supported the study. The average ambient temperature, $T_{a,CIU}$, corresponds to the annual mean temperature of the Nicosia region. After substituting these values into the equation, the solar radiation temperature in the region, $T_{s,CIU}$ was determined. These values were used in subsequent calculations. $T_{c,CIU}=44.3^{\circ}C=317.45~K$ (average panel surface temperature),

 $T_{a,CIU} = 19^{\circ}C = 292.15 K$ (average ambient temperature), $T_{s,CIU} = 345 K$ (solar radiation temperature in the region).

The heat transport coefficient during the amount of heat lost to the natural environment due to the effect of the wind is expressed as follows [22].

$$h_{ca} = 2.8 + (3.0.v_r) \text{ to } 0 \le v_r \le 7 \text{ ms} - 1$$
 (21)

where, v_r is the wind speed measured on the panel. For Northern Cyprus this value is 2.8 m/s. This value has been accepted as the annual average wind speed of the region where the panels are located and the value determined by the meteorological department of the Republic of Northern Cyprus has been used [22].

$$h_{ca} = 2.8 + (3.0x2.8) = 11.2 \text{ W/m}^2\text{K}$$
 (22)

The dimensions required for the Ac panel surface area were taken from the performance analysis study of PV plants carried out by the CIU Sustainable Energy Research Center, where the Ac panel surface area was calculated as $1.97x0.99 m = 1.95 m^2$

$$E_{PV,Thermal} = h_{ca} A_C (T_C - T_a)$$

= 11.2 x 1.95 x(317.45 - 292.15) (23)

The equilibrium state of the total energy of the photovoltaic system is shown below.

$$E_{PV} = V_{oc}I_{sc} + h_{ca}A_{c}(T_{c} - T_{a})$$
 (24)

$$E_{PV} = 409.944 + 552.552 = 962.496 \,\text{Wh}$$
 (25)

A value of 409.944 ($E_{PV,electric}$) indicates the electrical energy production of the PV system, and a value of 552.552 ($E_{PV,Thermal}$) refers to the heat losses of the PV system. A value of 962.496 (E_{PV}) refers to the energy balance of the PV system.

In the context of engineering, efficiency is often expressed as the ratio between output and input. Energy efficiency for photovoltaic (PV) systems, on the other hand, can be defined as the ratio of the total output energy (electrical and thermal energy) to the solar energy falling on the PV surface. It is possible to express this situation as follows: "The energy efficiency of PV systems is defined as the ratio of output energy (electrical and thermal energy) to solar energy falling on the PV surface, and in general, efficiency in engineering is considered as the ratio of output to input". This value was used by taking the accepted value from the CIU staff in their past studies.

$$\eta_{PV} = \frac{E_{PV}}{K_s x A_c} = \frac{V_{oc} I_{sc} + h_{ca} A_c (T_c - T_a)}{K_s x A_c}$$
(26)

where, η_{PV} represents the proportion of useful energy that can be utilized by the photovoltaic (PV) system, while K_s denotes the solar energy reaching the surface of the PV panel ($K_s = 533.03 \text{ Wh/m}^2$).

$$\eta_{PV} = \frac{962.496}{533.03 \times 1.95} = 0.926 = 0.93 \tag{27}$$

As a result of the analyzes carried out within the scope of TRNC CIU PV systems, it has been observed that almost 58% of the energy delivered to the panels by the sun is converted into thermal energy, which is a different type of

energy, during the journey and becomes useless. It has been determined in many previous studies that this level of thermal energy in PV systems both reduces the life of the system and negatively affects the energy production efficiency. The ratio of the thermal energy and the total Electrical energy obtained to the total amount of radiation energy provided by the sun has been determined to be at the level of 93% of the efficiency of the PV system. However, in this calculation, heat energy is also included in the scope of energy accepted as output. If a calculation is made in such a way that heat energy is not included in the scope of the output, it has been determined that the efficiency of the PV system is around 39%. While determining the 58% and 39% values specified here, 552.552 (E_{PV,Thermal}) and 409.944 $(E_{PV,electric})$ values calculated with the formulas were used. The value of K_s was used by taking the value accepted in the past studies from the CIU staff.

Normally, PV panels are used only in terms of generating electricity, so only the part that is converted into electrical energy is taken for efficiency. E_{PV} is the value of the energy produced by the E system during a day in Wh (Watt hours). The daily electrical yield of the PV system is given below.

$$\eta_{PV,D} = \frac{E_{PV,E}}{E_c} \tag{28}$$

where, $\eta_{PV,D}$ represents the daily electrical efficiency of the photovoltaic (PV) system, $E_{PV,E}$ denotes the amount of energy produced by the system during a day (115 Wh), and E_s refers to the amount of solar energy received from the sun during the same period (946 Wh).

$$\eta_{PV,D} = \frac{E_{PV,E}}{E_s} = \frac{115}{946} = 0.12$$
(29)

As a result of the calculations made with the monthly production quantities continuously recorded by CIU, E_{PV} was found to be the value corresponding to the average daily production value. The E_s value was used by taking the value accepted by the CIU Sustainable Energy Research Center in its studies.

3.1.2 CIU SPP Exergy Analysis

The electrical exergy obtained by the photovoltaic system aims to make as much of the available energy potential available as possible. The equilibrium state of exergy is given below.

$$X_{PV} = X_{PV,electric} - X_{PV,Thermal} - X_{PV-d,electric}$$
 (30)

where, $X_{PV,electric}$ represents the electrical exergy of the photovoltaic (PV) assembly, $X_{PV,Thermal}$ denotes *the* internal exergy losses within the system, and $X_{PV-D,electric}$ refers to the external exergy losses associated with thermal effects.

The internal loss of energy is a result of the natural heat flow because the insulation in the system cannot be reduced to the zero point, and the external losses are the result of the natural heat flow because the atmospheric temperature has a lower temperature than the system. The exergy losses (electrical and thermal) of the photovoltaic system are expressed as follows.

$$E_{PV,electric} = V_{oc}I_{sc} \tag{31}$$

$$E_{PV,electric} = V_{oc}I_{sc} = (45.6)x(8.99) = 409.944 \text{ Wh}$$
 (32)

$$X_{PV-d,electric} = V_{oc}I_{sc} - V_mI_m \tag{33}$$

where, $V_m = 36.3 \text{ V}$ and $I_m = 8.53 \text{ A}$.

$$X_{PV-d,electric} = (45.6)x(8.99) - (36.3)x(8.53)$$

= 100.305 Wh

The V_m value used in equation 3 expresses the voltage of the system during maximum power, and the I_m value expresses the current of the system during maximum power. These values were taken from the performance analysis study of PV plants carried out by the CIU Sustainable Energy Research Center.

The values of $(Tc)_{ciu}$ and $(Ta)_{ciu}$ used in the equation below express the average panel surface temperature of the system and the average environmental temperature of the region, respectively. External exerge losses due to heat $X_{PV.Thermal}$ are obtained by the following formula.

$$X_{PV,Thermal} = \left\{ \left[1 - \frac{(T_a)_{ciu}}{(T_c)_{ciu}} \right] x \left[h_{ca} A_c \left(T_{c_{ciu}} - T_{a_{ciu}} \right) \right] \right\}$$
(35)

$$X_{PV,Thermal} = \left(1 - \frac{292.15}{317.45}\right) \times (552.552) = 44.2 \text{ Wh}$$
 (36)

The exergy efficiency of PV systems is calculated by the ratio of the exertion value of the PV system to the exergy value of the solar radiation incident on the PV system surface, where $X_{PV,Thermal} = 44.2 \text{ Wh}$ represents the thermal exergy of the photovoltaic system.

$$\psi_{PV} = \frac{X_{PV}}{X_{sun} \times A_c}$$

$$= \frac{\left\{ V_m I_m - \left[1 - \frac{(T_a)_{ciu}}{(T_c)_{ciu}} \right] \times \left[h_{ca} A_c ((T_c)_{ciu} - (T_a)_{ciu}) \right] \right\}}{\left\{ \left[1 - \frac{(T_a)_{ciu}}{(T_c)_{ciu}} \right] \times I_s \right\} \times A_c}$$
(37)

where, ψ_{PV} denotes the exergy efficiency of the photovoltaic (PV) system, and X_{sun} represents the exergy amount of solar radiation reaching the surface of the PV panels. This parameter is calculated straightforwardly as follows:

$$X_{sun} = \left(1 - \frac{(Ta)ciu}{T_{c^*}}\right) \times K_s \tag{38}$$

$$\frac{T_s}{T_{s^*}} = 0.9562 + 0.2777 \ln\left(\frac{1}{f}\right) + 0.0511 f \tag{39}$$

In the calculations, the solar radiant temperature was taken as $T_s = 5777 \text{ K}$, while the reference temperature of the system was determined as $T_s^* = 446.71$. The diffuse radiation coefficient in the region (f) was considered to be between 260 and 270.

$$X_{sun} = \left(1 - \frac{(292.15)}{(446.71)}\right) \times 533.0 = 184.42 \,\text{Wh}$$
 (40)

$$\psi_{PV} = \frac{x_{PV}}{x_{sun} \times A_c} = \frac{(36.3) \times (8.53) - (0.080) \times (552.552)}{(184.42) \times (1.95)}$$
(41)

The parameter ψ_{PV} was calculated using Equation (41), and $\psi_{PV} = 0.73$ was found to be an approximate value.

When calculating the exergy efficiency of the PV system, x_{sun} , that is, the exergy value of the solar radiation coming to the panel surface, is needed. The $T_s *$ value used in the

calculation of this value refers to the sum of the radiation temperature of the sun directly reaching the region and the radiation temperature caused by the effect of diffuse radiation. While finding this value, the solar radiation temperature acting on the system in the region is obtained based on the effects of solar radiation temperature and diffuse radiation coefficient. As a result, the exergy efficiency of the PV system was found to be 73%. The f value, which is specified as the diffuse radiation coefficient, refers to the radiation that arises from the reflection of the rays coming from the sun through the clouds.

4. Conclusion and Recommendations

With our studies on CIU solar power plants, it has been determined that the energy efficiency of the system is 93% and the daily electricity efficiency is 12%. This value shows that the system has a good level of efficiency, considering the average efficiency of photovoltaic panels. The concept of exergy, defined as the 'usable part' of energy or the part that can be converted into another form of energy, is also very important for photovoltaic panels. As a result of our exergy analysis, the exergy efficiency of our system was found to be around 73%. According to this value, a large part of the usable energy is lost in our system. It is of great importance for Turkish Republic of Northern Cyprus, which has difficulties in meeting its energy needs, to be able to use its solar energy potential at the maximum level.

In the study conducted by Mehmet Altınkaynak, Recep Demirekin and Ali Kemal Yakut, the electrical efficiency of the system was calculated as 15.2%. In our study, we see that this value is around 12%. There are few studies in the literature that directly analyze the exergy efficiency of solar panels. However, considering these studies, the values we achieved in our study are quite acceptable. Due to the location of the Turkish Republic of Northern Cyprus, solar radiation is quite high. This increases the efficiency of the panels. We see that the exergy and energy efficiencies are at very high levels along with the measures taken to increase the efficiency of the installed solar panels.

The data that allows these values to be obtained was obtained by using the average of the values measured in the past. Therefore, average efficiency values were calculated not by following the process, but by determining an average reference point. That's why we haven't formed a chain of values that changes over time. The value we found represents the values that should be considered average in a process.

If we need to evaluate the findings obtained, the efficiency of our power plant has not yet reached the optimum level according to the solar radiation potential of the Turkish Republic of Northern Cyprus. Getting maximum efficiency is of great importance in meeting the energy needs of the island. Therefore, suggestions and studies should be made in terms of development to increase efficiency. If the desired goals are achieved after the recommendations and studies, this work will be an example for all other solar power plants on the island. This exemplary work will be disseminated and energy efficiency will be increased throughout the country. Since the Turkish Republic of Northern Cyprus is an island country, it is very important to use local resources efficiently. In this sense, it is very important to carry out these studies. Therefore, in order to increase these values, all universally derived methods must be reviewed and the appropriate ones must be included in the system. Some of these methods will be presented as suggestions below.

CIU Solar power plants are currently high efficiency plants. In order to contribute to the sustainability level of these efficiencies, some suggestions can be put into practice. These;

- ❖ When measuring the panel temperature, the best measurement point that can represent the panel is the panel center. Taking sustainable measures to keep the panel temperature at maximum efficiency will contribute to the average efficiency of our system.
- ❖ The slope of a correctly calculated panel allows more sunshine time, which increases efficiency. In the light of this information, the development of panels whose slopes can be improved can be achieved. In addition, panel slopes are effective in better absorption of radiation and reducing reflection losses.
- ❖ Wind, which contributes more to the efficiency in roof applications, contributes less to the points close to the ground. Utilizing artificial or natural wind energy according to the installation method and region will contribute to increasing panel efficiency.
- ❖ Studies that can keep the panel temperature under control according to the maximum useful radiation value will contribute to increasing the panel efficiency.
- ❖ In order to minimize the shading effect of CIU Solar power plants, the environmental conditions will be examined at regular intervals and measures will be taken against the factors that may create shading.
- ❖ The effect of cleaning will prevent losses due to dusting and maintain efficiency.
- ❖ Maximum Power Point Tracking system method is a control mechanism that detects the point where the power obtained from the panel is at its highest level. Radiation, Temperature, Panel slope, Panel aging and structural features can change this point. This mechanism evaluates the panel variables and changes the reference of the power converter so that the power peaks. With the activation of this mechanism in CIU solar power plants, the output power will be increased by 25-30% compared to the power obtained without control
- ❖ With the hot spot effect, cell temperatures can reach very high levels and completely deteriorate. Today, bridging diodes are widely used to avoid this effect. After the analysis of this situation in CIU SPP power plants, bridging diodes can be used at necessary points. With this study, panel efficiency will be maintained in a stable manner.
- ❖ By evaluating the options according to each region and installation, and adding the appropriate cooling system to the system, an increase in panel efficiency can be achieved.
- ❖ By making analyzes on the power plants, the panels that remain at the extreme points and whose efficiency can be increased with the solar tracking system can be determined and solar tracking systems can be installed specifically for these panels.
- ❖ By choosing the most suitable conductor in CIU SPP power plants, energy production will be protected from decreases. The condition of the conductors used in the system should be analyzed in periods to be determined, and if they lose their function, sustainability should be ensured by making changes.
- ❖ Panels operating at different DC currents in SPP cause incompatibility between each other. This incompatibility creates losses on the system. In order to eliminate incompatibility problems, panels with maximum power point currents close to each other can be positioned together. This situation can be analyzed at CIU SPP power plants, and

this can be used at appropriate points and losses can be reduced

Feasibility studies were carried out very carefully before the installations of CIU SPP power plants. The improvement of the existing system and the transformation of developments into modern systems are also constantly monitored. CIU continues to provide all kinds of support for the solution of the energy crisis, which is also a problem throughout the TRNC, as well as being very sensitive to renewable energy and sustainable environment issues within its own structure. The October 2022 'Renewable Energy Summit' symposium and the April 2023 'Energy Crisis in the TRNC' panel are some of the recent studies for the solution of the energy problem in the TRNC. With this energy crisis, it is of great importance to carry out efficiency studies at every point in energy production. Researching efficiency studies at every point and applying them where necessary will be a very important factor contributing to the solution of the energy crisis. This crisis can be overcome by the fact that every private and legal entity in the TRNC, both in private and in general, acts together on this issue, such as CIU.

Acknowledgment

For this study, I would like to thank Cyprus International University for providing all kinds of support for the exergy analysis of solar power plants.

Conflict of Interest

The author declares that there is no conflict of interest regarding the publication of this paper.

Credit Author Statement

Mehmet Yılmaz: Conceptualization, Methodology, Software, Validation, Formal analysis, Investigation, Resources, Data Curation, Writing- Original draft, Visualization Mustafa Atmaca: Conceptualization, Methodology, Software, Validation, Formal analysis, Investigation, Resources, Data Curation, Writing- Original draft, Visualization, Supervision

Nomenclature

SI

SPP

Nomencl	ature
%	Percentage
A_c	Solar panel area $[m^2]$
CIU	Cyprus International University
COP	Conference of the Parties
E_{PV}	Energy state of the system in equilibrium [Wh]
$E_{PV,E}$	Amount of energy produced during a day [Wh]
$E_{PV,electric}$	Electricity generation of the panel system [Wh]
$E_{PV,thermal}$	Lost heat energy of the panel system [Wh]
E	Amount of solar energy received from the sun
E_s	during a day [Wh]
f	Diffuse radiation reflection coefficient $[W/m^2]$
h_{ca}	Heat transfer coefficient from the photovoltaic
n_{ca}	cell to the ambient air $[W/m^2 \cdot K]$
I_m	Current at maximum power [A]
I_{sc}	Short-circuit current [A]
K_s	Solar energy reaching the PV surface [Wh]
PV	Photovoltaic
SC	Sustainable Campus
SERC	Sustainable Energy Research Center

Sustainability Index

Solar Power Plant

 T_s Solar radiation temperature [5777 K] TRNC Turkish Republic of Northern Cyprus

 V_{m} Voltage at maximum power [V]

 V_{oc} Open-circuit voltage [V] $X_{PV d,electric}$ Internal exergy losses [Wh]

Electrical exergy of the photovoltaic assembly $X_{PV,electric}$

[Wh]

 $X_{PV,thermal}$ External exergy losses [Wh]

Exergy amount of solar radiation reaching the X_{sun}

PV panels [Wh]

Greek symbols

Energy efficiency Exergy efficiency η_{II}

Useful energy rate of the PV system that can be

 η_{PV}

Daily electrical efficiency of the PV system $\eta_{PV.D}$

Wind speed around the panel [m/s]Exergy efficiency of the PV system ψ_{PV}

References:

- [1] U. Örgen, "Sustainable energy policies in the context of environmental security in Turkey," Ph.D. dissertation, Inst. of Social Sci., Ankara Univ., Ankara, Turkey, 2006.
- [2] S. Turan, "Renewable energy sources," Konya, Turkey, Res. Rep., 2006.
- [3] A. Ş. Haskök, "Evaluation of the situation of Turkey's current energy resources," M.S. thesis, Inst. of Sci., Eskisehir Osmangazi Univ., Eskisehir, Turkey, 2005.
- [4] K. A. Anıl, "Determination of the production potential of solar power plants in Turkey in terms of energy and exergy efficiency," M.S. thesis, Dept. of Energy Systems Engineering, Istanbul Aydın University, Istanbul, Turkey, 2016.
- [5] N. İ. Beyazıt, H. Bulut and F. Ünal, "Exergy analysis of long-term solar radiation for Diyarbakır Province," Harran Univ. Eng. J., vol. 4, no. 2, pp. 1-6, 2019. Available: https://dergipark.org.tr/tr/download/article-file/776854
- [6] İ. Uçkan, "Long-term exergy analysis of solar radiation for Van Province," Politeknik Dergisi, vol. 20, no. 3, pp. 579-584, 2017.
- [7] A. Hepbasli, "A key review on exergetic analysis and assessment of renewable energy resources for a sustainable future, Renew. Sustain. Energy Rev., vol. 12, no. 3, pp. 593-661, Apr. 2008, doi: 10.1016/j.rser.2006.10.001.
- [8] M. Öztürk, A. Hepbaslı, C. Akdeniz, H. Bulut, A. Ş. Duran, and M. Kacıra, "Investigation of solar radiation exergy for the Southeastern Anatolia region," in Proc. GAP V Eng. Congr., Sanliurfa, Turkey, Apr. 26-28, 2006.
- [9] R. Petela, "Exergy analysis of solar cylindricalparabolic cooker," Sol. Energy, vol. 79, no. 3, pp. 221-233, Sep. 2005, doi: 10.1016/j.solener.2004.12.001.
- [10] H. H. Öztürk, "Experimental determination of energy and exergy efficiency of the solar parabolic-cooker," Sol. Energy, vol. 77, no. 1, pp. 67-71, 2004, doi: 10.1016/j.solener.2004.03.006.

- [11] M. Öztürk, A. Elbir, and N. Özek, "Exergy analysis of solar radiation to the Mediterranean region," in Proc. 6th Int. Adv. Technol. Symp. (IATS'11), Elazig, Turkey, May 2011.
- [12] M. K. Kaymak, "Modeling and exergy analysis of wind and solar systems in Istanbul climate conditions," M.S. thesis, Istanbul Tech. Univ., Istanbul, Turkey, 2011.
- [13] Y. Candau, "On the exergy of radiation," Sol. Energy, vol. 75, no. 3, pp. 241–247, 2003, doi: 10.1016/j.solener.2003.07.012.
- [14] T. T. Chow, G. Pei, K. F. Fong, Z. Lin, A. L. S. Chan, and J. Ji, "Energy and exergy analysis of photovoltaicthermal collector with and without glass cover," Appl. Energy, vol. 86, no. 3, pp. 310-316, Mar. 2009, doi: 10.1016/j.apenergy.2008.04.016.
- [15] M. Altınkaynak, R. Demirekin, and A. K. Yakut, "Energy and exergy analysis of a PV-T collectorsourced heat pump system," NÖHÜ Müh. Bilim. Derg., vol. 10, no. 2, pp. 753–762, 2021, doi: 10.28948/ngumuh.693384.
- [16] F. Bayrak, "Sustainability index and thermodynamic analysis of porous fin added air-heated PV/T collector," Int. J. Pure Appl. Sci., vol. 7, no. 3, pp. 419-428, Dec. 2021, doi: 10.29132/ijpas.931021.
- [17] Ö. Resuloğulları and A. Erişen, "Energy and exergy analysis of PV/T systems with concentrated integrated radiative decoupling," Int. J. Eng. Res. Dev., vol. 14, no. 1, pp. 32–45, 2022, doi: 10.29137/umagd.1196884.
- [18] E. Kırtepe and A. Güngör, "Theoretical modeling of the solar collector using nanofluid and energy and exergy performance at different operating conditions," Tesisat Müh. Derg., no. 184, pp. 21–28, May–Jun. 2021.
- [19] Z. Çelik and H. S. Çelik, "Parameters affecting the exergic efficiency of PV/T systems and hybrid system design with water heater," EJONS Int. J. Math. Eng. Nat. Sci., vol. 3, pp. 107–119, 2018.
- [20] Cyprus International University, "Official Website," Accessed: Mar. 2023. [Online]. Available: https://www.ciu.edu.tr/tr
- [21] TRNC Meteorology Department, "Cyprus Climate Information," Accessed: Mar. 2023. [Online]. Available: http://kktcmeteor.org/meteorolojibilgi/kibris-iklimi.
- [22] TRNC Meteorology Department, "Climate Characteristics of Northern Cyprus." Accessed: Mar. [Online]. Available: 2023 http://kktcmeteor.org/meteorolojibilgi/kibricyclimi.

Research Article

Vol. 28 (No. 4), pp. 265-278, 2025 doi: 10.5541/ijot.1652943 Published online: December 1, 2025

Enhanced Prosumer Energy Management Using Modified Social Group Optimization for Cost-Effective and Sustainable Energy Utilization

¹*S. Singh , ¹R. Bhasker

¹ Department of Electrical Engineering, Faculty of Electrical Engineering & Technology (UNSIET), VBS Purvanchal University, Jaunpur, UP, India E-mail: *shwetasingh.singh334@gmail.com

Received 8 March 2025, Revised 25 September 2025, Accepted 3 November 2025

Abstract

Effective energy management in prosumer communities is significant for optimizing renewable energy usage and cutting down costs. The research develops an optimization framework to analyze the impact of scaling up photovoltaic (PV) generation and demand on self-consumption, storage utilization, and grid interaction. A linear programming approach can be used to minimize total energy costs by optimizing energy purchases, storage operation, and grid sales. Additionally, the Modified Social Group Optimization (MSGO) algorithm improves the optimization efficiency, taking into account the variations in demand, storage restriction, and the limits of grid exchanges. Simulation results show that by increasing PV generation, self-consumption and energy export are maximized, while high demand requires efficient storage and thus large reliance on grids. The system generates 182.58 kW PV energy and the consumption of 343.20 kW requires import of 262.80 kW. The storage systems manage surplus power 109.23 kW; of that stored, 72.63 kW is released during low solar periods. Economically, contribution of PV sales reaches €41.29, and that of storage adds up to €18.45, resulting in partial offsetting of total costs amounting to €340. Findings highlight that proper scaling of PV and managing demand could enhance energy efficiency as well as reduce dependence on the grid while unlocking better economic returns, thus making this framework a very advantageous tool in making sustainable energy plans for prosumer communities.

Keywords: Energy cost optimization; modified social group optimization; prosumer energy management; renewable energy utilization; smart grids; social group optimization.

1. Introduction

Gradually but steadily, the energy landscape is changing from totally centralized to more decentralized architectures in the context of distributed energy resources (DERs) adoption and the growing emergence of prosumers, which are entities acting as energy consumers and producers. Unlike conventional consumers, who rely solely on centralized generation plants, prosumers actively use markets through generating meters, storing, and consuming electricity, thereby decentralizing energy generation. This shift fosters more resilience, security, and self-sufficiency within the grid while reducing dependency on fossil fuel powers [1].

Improvements in smart meters, battery storage systems, and bidirectional communication networks allow prosumers to use energy more efficiently in real-time. This has not only reduced energy costs but has also enabled renewable energy integration, and thus a cleaner, more sustainable energy ecosystem. In many cases, the optimal utilization of prosumer energy resources requires quite sophisticated optimization techniques, balancing generation, storage, and consumption.

1.2 Significance of Photovoltaic (PV) Generation in Sustainable Energy Management

Solar resource photovoltaic (PV) generation is one of the renewables promising or apt solutions for prosumers at present. Increasingly lower cost of solar panels, coupled with government support programs and net metering policies, induces the ever-accelerating PV adoption worldwide [2]. Integration of PV systems allows prosumers to create their power and use it, instead of supplementing it with the traditional grid. This technology substantially lowers energy expenses, mitigates the carbon footprint, and enhances sustainability levels.

However, PV generation remains sparse, and in a nutshell, it depends on solar radiation, which is variable due to varying weather patterns, geographical locational differences, and seasonal changes occurring. Such variations pose threats toward balancing a stable supply-demand profile of electricity. This situation thus poses a necessity for effective energy storage and scheduling mechanisms for optimal utilization of PV-generated electricity.

1.3 Challenges in Optimizing Prosumer Energy Management

Uncertainty in PV generation: Solar power output differs due to environmental factors such as cloud cover, shading, and seasonal variations; hence, accurate energy planning becomes tough [3].

*Corresponding Author Vol. 28 (No. 4) / 265

Demand variations: The load demand varies over time because of the dynamic behavior of customers with respect to different appliances and systems at different times of the day.

Storage limitations: batteries are commonly employed for energy storage, but their limited capacity, degradation with time, and high cost require efficient strategy, on how and when to charge and discharge them [4].

Bidirectional energy flow: Prosumers can either inject their excess energy into the grid or withdraw power whenever they require it, hence needing dynamic pricing models and smart trading of energy.

1.4 Need for Efficient Optimization Techniques

Conventional methods that rely on rules and heuristics for energy scheduling are unable to address some non-linear, high-dimensional, and uncertain energy systems. Machine learning and AI techniques promise to do much better, albeit they often require enormous datasets and do not guarantee the real-time computational efficiency required for energy management.

Some metaheuristics like Particle Swarm Optimization (PSO), Genetic Algorithm (GA), and Social Group Optimization (SGO) have been widely applied for the optimization of prosumer energy [5]. However, their slow convergence, premature stagnation, and difficulty to adapt to dynamic energy environments are now the major problems. To address these issues, this research presents the Modified Social Group Optimization (MSGO), which modifies the conventional SGO algorithm to improve convergence, adaptability, and computational efficiency in prosumer energy management with PV generation.

1.5 Research Gap & Contribution

Existing Optimization Methods and Their Limitations

This shows that energy management techniques of prosumer energy optimization have been extensively investigated. Swarm intelligence-based Particle Swarm Optimization (PSO), a popular technique, has been widely used for energy scheduling; however, its main drawbacks are that it often gets stuck in local optima and has slow convergence in immensely complicated Mult objective problems. Being another evolutionary algorithm, the Genetic Algorithm (GA) traverses the solution space rapidly; however, it suffers from high computational complexity and longer execution times [6]. A relatively new optimization algorithm that imitates social groups' interactions during problem-solving known as Social Group Optimization (SGO) has been fairly new in showings its bright results across many optimization tests. The weak point of SGO, however, is its less efficient exploration-exploitation balance, which, as a result, reduces convergence in a more dynamic energy landscape.

There is thus a need for an optimization technique that would combine computational expediency with robustness in terms of handling dynamic energy environments. This study thus seeks to bridge the gap by proposing the Modified Social Group Optimization (MSGO) algorithm, which integrates adaptive learning mechanisms, dynamic weight adjustments, and a hybrid mutation strategy toward improving performance.

1.6 Introduction of Modified Social Group Optimization (MSGO)

It has modified the SGO algorithm by adding adaptive parameters-which increase the efficiency and speed of convergence-to create the MSGO algorithm. Unlike standard SGO, which relies on a fixed interaction model, the MSGO algorithm dynamically adjusts the learning rates and weighting factors to meet real-time energy demand and generation conditions [7]. This makes the algorithm capable of exploring a wider solution space avoiding premature convergence. MSGO is suitable for prosumer energy management for handling uncertainties in PV generation storage optimization of batteries charge schedule efficiently. Furthermore, real-time decision-making regarding energy consumption optimizes the cost with self-sufficiency. This adaptiveness between cost minimization and self-sufficiency enables more reliable and efficient improvement provisions in MSGO. The embedded improvements result in discovery toward a productive and effective framework for optimization of energy production with consumption through storage in prosumer smart grids [8, 9].

1.7 Key Contributions of This Work

A new framework of energy management is presented in this study using the Modified Social Group Optimization (MSGO) algorithm to maximize the energy utilization of prosumers from PV-integrated smart grids. The dynamic energy scheduling model differs from the conventional static optimization as it adjusts according to battery storage limits, grid interaction policies, and dynamic pricing schemes. The MSGO algorithm is tested in many operational scenarios so far under which energy storage and trade costs are reduced while the effectiveness in grid stability improved. Besides being faster in convergence and less in price than what PSO, GA, and Standard SGO determined, MSGO also uses renewables better, a use-case ideal in smart grids.

2. Literature Survey

2.1 Prosumer Energy Management (PEM) and Optimization Approaches

In the study by Gomez-Gonzalez et al. (2021) and Yang et al. (2022) [11], PEM is said to optimize the consumption, storage, and generation of energy. In other words, prosumers need to resolve supply and demand optimally while considering the increasing trend of distributed RESs such as PV and wind systems. Also, some advanced energy storage methods include BESS and HESS to promote renewable integration. Demand-side management techniques enabling further optimization of energy consumption include load shifting and dynamic pricing. Metaheuristic techniques-GA, PSO, ACO, and SGO-are used to increase the efficiency of PEM through cost minimization and reliability of energy supply [12].

2.2 Social Group Optimization (SGO) and Its Limitations

Ghasemnejad et al. (2024) [13] highlights the efficient application of the SGO algorithm when applied in the complex energy scheduling problems, involving the modeling of interactions inside social groups to find. In that way, it shows potential for application in the field of prosumer energy management due to its great adaptability to dynamic energy environments. Despite the beauty of the algorithm from the conceptual point of view, several principal drawbacks exist. These issues concern slow convergence speed and confinement to local optima, especially in high-dimensional search spaces. At the same

time, the scalability problem arises when it is applied to large energy networks with multiple prosumers and storage units, limiting its suitability for full-scale complex optimization problems [13].

2.3 Modifications in MSGO for Improved Energy Optimization

To overcome the drawbacks of the classical Social Group Optimization (SGO), these authors developed the so-called Modified Social Group Optimization (MSGO) techniques to strike a fine balance between good exploitation and analysis of the search workspace. There are adaptive learning schemes, mutation operators, and hybrid metaheuristic frameworks introduced by Sharma et al. (2024) and Mohammadi et al. (2022) to considerably augment the convergence speed and, by and large, to avoid the entrapment in a local optimum [14, 15].

In regard to demonstrating its capacity to do so, the MSGO solution achieves energy demand anticipation while reducing operating costs, enhancing self-sufficiency, and optimizing load distribution. Secchi et al. (2021) used MSGO for battery storage sizing toward economically viable self-sufficiency [16]. Wu et al. (2025) integrated transmission congestion and carbon emission constraints into energy management models, further extending MSGO with improved grid interaction [17]. Such works confirm the superiority of the MSGO that traditional methods of optimization have conferred on renewable energy prosumer networks, making it a very robust tool for the optimization of storage, energy trading, and demand-side management under dynamic electricity markets.

While MSGO does improve the classical SGO, it also achieves competitive results against recent approaches like TLBO, NSGA-II, and DE-based variants. Naik et al. (2020) as well as Reddy & Narayana (2022) extended MSGO to electric vehicle energy systems and economic dispatch problems, validating its adaptability. Unlike PSO or GA, MSGO manages a better exploration-exploitation trade-off, particularly in complex multimodal problems like dynamic energy management.

In recent times, the MSGO algorithm has seen application in various energy-oriented domains. Reddy and Narayana (2022) used it as a multi-strategy ensemble for electric vehicle energy optimization, whereas Naik et al. (2020) employed MSGO for short-term hydrothermal scheduling [18, 19]. These works stand as testament to the robustness of MSGO in handling constraints existing in the energy domain in real life, thus supporting its application in prosumer energy management.

3. Problem Formulation

3.1 Prosumer Energy Management Model

Because of the growing integration of renewable energy, prosumers have emerged: people who generate and use power, chiefly by means of photovoltaic (PV) systems. Within such a context, the development of an economic and environmental benefit-enhanced optimization energy management model becomes necessary. The model presented here optimally describes supply and demand, in so doing taking storage and grid interactivity into account. To this end, the model proposes minimizing electricity expenses by optimizing the energy mix, thus deciding when to use self-generated PV power, store energy, or trade with the grid. Self-consumption is prioritized as much as possible, to avoid reliance on fossil-fuel-based power. This renders an energy

management approach that is viable, economical, and sustainable for prosumer communities.

3.2 Mathematical Formulation

An energy management model has been defined as an optimization problem with an objective function and associated constraints.

Objective Function: The aim should be to minimize the overall costs attributed to energy grid purchases and the operation costs of the battery, compensated through additional energy selling on the grid. The cost function is represented by [18]:

$$\min J = \sum_{t=1}^{T} \left| P_{grid}(t) \cdot C_{grid}(t) - P_{sell}(t) \cdot R_{sell}(t) + C_{battery}(t) + C_{demand\ response}(t) \right|$$
(1)

where: $P_{grid}(t)$ is the energy purchased from the grid at time t, $C_{grid}(t)$ is the dynamic price per unit of electricity from the grid, $P_{sell}(t)$ is the energy sold back to the grid, $R_{sell}(t)$ is the revenue earned per unit of energy sold, $C_{battery}(t)$ is the cost of charging and discharging the battery, and $C_{demand\ response}(t)$ is the cost associated with load shifting.

The self-consumption of power generated by photovoltaic (PV) systems can be used as a good indicator when examining the cost of credit in photovoltaics in the solar energy business if the power system installation costs are also known.

Decision Variables: The optimization model determines the following decision variables:

- $P_{grid}(t)$ is power drawn from the grid at each time step,
- P_{sell}(t) is power sold to the grid from PV generation or battery storage.
- $P_{PV}(t)$ is power generated by the PV system.
- $P_{bat,charge}(t)$, $P_{bat,discharge}(t)$ are battery charging and discharging power.
- $P_{demand}(t)$ is power demand of the system at each time step.
- SOC(t) is state of charge of the battery at each time step. System Constraints: Power Balance Constraint [19]:

$$\begin{split} P_{grid}(t) + P_{PV}(t) + P_{bat, \ dicharge}(t) &= P_{demand}(t) + \\ P_{bat, charge}(t) + P_{sell}(t) \end{split} \tag{2}$$

It assures generation and purchase of total power equal to the whole demand including power supply and sales.

Grid Stability Constraints: Power grids must not be overburdened, and the exchange of power energy shall be limited within admissible limits so as to avoid violation fees and service interruptions. [20].

$$P_{grid}^{min} \le P_{grid}(t) \le P_{grid}^{max} \tag{3}$$

where, P_{grid}^{min} and P_{grid}^{max} are the minimum and maximum allowable grid power exchanges.

Also, great swings in the power demand should be checked for frequency stability. Let P_{arid} be the grid power:

$$\left| P_{grid}(t) - P_{grid}(t-1) \right| \le \Delta P_{grid}^{max} \tag{4}$$

where, ΔP_{grid}^{max} is the maximum allowable change in grid power per time step.

Battery Operational Constraints: In each time step, the battery's state of charge (SoC) changes due to the charging and discharging processes [21]:

$$SOC_{min} \le SOC(t) \le SOC_{max}$$
 (5)

Ensures that the battery's state of charge SOC(t) at any time t remains within the permissible range, SOC(t) is the State of charge of the battery at time t (in kWh or %), SOC_{min} denotes as Minimum allowable SOC to avoid deep discharge (typically 10–20%), and SOC_{max} as Maximum allowable SOC to avoid overcharging (typically 90–100%).

Maintaining the SOC within this range extends battery life and ensures safety.

$$P_{bat,charge}(t) \le C_{bat,max}, P_{bat,discharge}(t) \le D_{bat,max}$$
 (6)

These constraints ensure that the battery charging **power** $P_{bat,charge}(t)$ and discharging power $P_{bat,discharge}(t)$ at time t do not exceed their respective maximum capacities: $P_{bat,charge}(t)$ denotes as Charging power applied to the battery at time t (in kW), $P_{bat,discharge}(t)$ as Power discharged from the battery at time t (in kW), $C_{bat,max}$ as Maximum charging power limit of the battery (in kW), and $D_{bat,max}$ denotes as Maximum discharging power limit of the battery (in kW).

These constraints help protect the battery from excessive charging or discharging rates, ensuring optimal performance and longevity.

The battery is limited by its charging capacity and charge/discharge pulse power limits.

Battery Degradation and Lifespan Constraints: More and more charge-discharge cycles may wear down batteries all the more swiftly. To coincide with the worsened battery condition, depth of discharge (DoD) and number of charge-discharge cycles must be reduced [22]:

$$SOC_{min} + \Delta SOC_{safe} \le SOC(t) \le SOC_{max} - \Delta SOC_{safe}$$
 (7)

where ΔSOC_{safe} is a safety margin to prevent excessive charge/discharge.

Battery power variations also can be limited:

$$|P_{bat, charge}(t) - P_{bat, charge}(t-1)| \le \Delta P_{bat}^{max}$$
 (8)

$$|P_{bat, discharge}(t) - P_{bat, discharge}(t-1)| \le \Delta P_{bat}^{max}$$
 (9)

where, ΔP_{bat}^{max} limits the rate of change in battery power.

Energy Trading Constraint [23]:

$$P_{sell}(t) \le P_{PV}(t) - P_{demand}(t)$$
 if $P_{PV}(t) > P_{demand}(t)$ (10)

where, $P_{sell}(t)$ defined as Power exported to the grid at time t (in kW), $P_{PV}(t)$ as Power generated by the PV system at time t (in kW), and $P_{demand}(t)$ denotes as Power consumed by the prosumer (load demand) at time t (in kW).

This ensures that only surplus PV energy is sold to the grid.

Demand Response Constraints [24]:

 $P_{demand\ shifted}(t) \le P_{demand}(t)$ for $t \in peak\ hours$ (11)

$$\sum_{t=1}^{T} P_{demand,shifted}(t) = \sum_{t=1}^{T} P_{demand,original}(t)$$
 (12)

where, $P_{demand,original}(t)$ defined as original prosumer demand at time t (kW). $P_{demand,shifted}(t)$ as Demand after shifting to minimize peak-hour consumption (kW). And $t \in peak\ hours$ denotes Time intervals where electricity tariffs are higher. T as Total number of time intervals in the scheduling horizon (e.g., 24 for hourly scheduling over a day).

The premise of load shifting is that the shifting of load does not change net energy consumption but shifts that consumption to time periods in which the energy price is lower.

Dynamic Pricing Constraints: Demand-and-supply mechanisms and market links determine electricity prices from time to time. Therefore, power transactions (in terms of grid purchases or sales) should be optimized to suit market conditions that are price favorable [25].

$$P_{grid}(t) \le P_{grid}^{max} \quad if \ C_{grid}(t) \le C_{grid}^{avg}$$
 (13)

$$P_{sell}(t) \le P_{PV}(t) - P_{demand}(t)$$
 if $R_{sell}(t) \ge R_{sell}^{avg}$ (14)

where, C_{grid}^{avg} is the average grid price over a given period and R_{sell}^{avg} is the average selling price over a given period.

Such restraints ascertain that energy dealings come about at their optimal cost-benefit points.

PV Scaling Factor Constraints [26]:

$$P_{PV.\ scaled}(t) = m_S \cdot P_{PV.\ original}(t) \tag{15}$$

$$P_{demand, scaled}(t) = m_D \cdot P_{demand, original}(t)$$
 (16)

where m_S and m_D are multiplicative scaling factors applied to PV generation and demand, respectively.

Incorporating Emission Reduction: The total grid energy purchase carbon emissions can be expressed as [27]:

$$E_{CO_2} = \sum_{t=1}^{T} P_{grid}(t) \cdot \gamma \tag{17}$$

where γ is the grid emission factor (kg CO₂ per kWh). The objective function can be extended to penalize emissions:

$$J' = J + \lambda_{CO_2} E_{CO_2} \tag{18}$$

where, λ_{CO_2} is the cost penalty per unit of CO₂ emissions.

PV Generation Uncertainty Modeling: To account for the inherent uncertainty in solar photovoltaic (PV) output due to variable weather conditions, we extended our simulation model by incorporating stochastic PV generation profiles. A Monte Carlo simulation approach was adopted to generate multiple irradiance scenarios reflecting real-world variability. Historical irradiance data from the NREL OpenEI solar database was used to generate 100 distinct weather scenarios for a 24-hour period, including clear-sky, partly cloudy, and overcast conditions.

For each scenario, the corresponding PV output $P_{PV}(t)$ was computed using:

$$P_{PV}(t) = \eta \cdot A \cdot G_t(t) \tag{19}$$

where η is the PV efficiency, A is the panel area, and $G_t(t)$ is the solar irradiance (W/m²) at time t, randomly sampled from the irradiance distribution.

The Modified Social Group Optimization (MSGO) algorithm was then run for each irradiance scenario

independently, and the expected value of the key performance indicators (energy cost, renewable utilization, battery cycling) was calculated:

$$\mathbb{E}[f(x)] = \frac{1}{N} \sum_{i=1}^{N} f_i(x)$$
 (20)

where, N = 100 is the number of Monte Carlo trials and $f_i(x)$ is the objective value for the i^{th} scenario.

This approach allows for evaluating the robustness of the optimization framework under realistic PV uncertainty, ensuring that the scheduling solution remains effective across a broad range of environmental conditions.

4. Modified Social Group Optimization (MSGO) Approach

4.1 Overview of Social Group Optimization (SGO) Algorithm

Social Group Optimization (SGO) refers to the population-based metaheuristics evolution from cooperative behaviors found in groups of animals and human beings. This method is also incorporated in a leader-follower paradigm, which involves moving the individuals according to a leader and their association with other members. Furthermore, such social activities or interactions are the basis for the exchange of information and decision-making, finally culminating in the optimized solution.

The position of an individual at iteration t + 1 is updated mathematically as follows [29]:

$$X_i^{t+1} = X_i^t + \lambda_1 (X_i^t - X_i^t) + \lambda_2 (X_{rand}^t - X_i^t)$$
 (21)

where, X_i^t represents the position of the ithi th ith agent at iteration t, X_L^t is the leader's position, and X_{rand}^t is a randomly chosen individual's position. The parameters λ_1 and λ_2 control the influence of the leader and peer agents.

The conventional SGO algorithm is effective but slow in convergence and prone to local optimal. The Modified Social Group Optimization (MSGO) algorithm offers the adaptive learning mechanism, dynamic weight adjustment, and hybrid mutation strategies to overcome these issues.

Unlike standard SGO, MSGO integrates a timedependent learning rate and combines exploration (via Gaussian mutation) with exploitation (via introspection learning). This hybrid strategy reduces premature convergence and improves adaptability to dynamic constraints.

4.2 Enhancements in MSGO

MSGO's foremost new feature is its adaptive learning mechanism, which allows the learning rate to be adjusted dynamically, hence balancing exploration and exploitation. The learning rate α changes over iterations according to [30]:

$$\alpha_t = \alpha_{max} - \left(\frac{t}{T}\right)(\alpha_{max} - \alpha_{min}) \tag{22}$$

where α_{max} and α_{min} are the initial and final learning rates, and T is the total number of iterations. This allows the algorithm to explore more in the initial stages and refine solutions in later stages.

The second improvement is that dynamic weight adjustment increases the balance between intensification and diversification. The weight factor W_t is adjusted dynamically, as indicated by [31]:

$$W_t = W_{max} - \frac{t}{T}(W_{max} - W_{min})$$
 (23)

where, W_{max} and W_{min} define the range of weight values. This ensures that the algorithm transitions smoothly from exploration to exploitation, leading to better convergence.

An additional hybrid mutation strategy is introduced for this application in order to avert premature convergence. This mutation process perturbs the stagnant agents' positions so that they might escape the local optima. The mutation is defined using [32]:

$$X_i^{t+1} = X_i^t + \beta(X_U - X_L) \cdot rand(-1, 1)$$
 (24)

where, β is a mutation factor, and X_U , X_L represent upper and lower bounds of the search space.

4.3 Algorithm Workflow for Energy Management

Energy scheduling is achieved by including energy balance, limitations in battery storage, and grid import/export constraints in the MSGO algorithm. The optimization scheme has a stepwise process.

The initial phase defines the search space, including decision variables such as energy generation, storage, and grid transactions. A population of candidate solutions is randomly initialized, and the leader is identified based on the objective function, which minimizes total energy costs and maximizes renewable energy utilization. During position updates, each agent refines its energy scheduling decision through the improved MSGO equations. Constraint handling techniques guarantee the feasibility of the solutions, particularly regarding limits of battery charge and grid export thresholds [33]. The mutation and refinement phase introduce diversity by perturbing certain agents' positions. This requirement is necessary in order to escape the local optima of the algorithm and further improves the global search efficiency.

The algorithm continues iterating until some convergence criteria are met, e.g., reaching a certain number of iterations or not improving the solution quality at a minimal level. In the final output, an optimized energy schedule is provided, specifying how the renewable energy is allocated along with battery use and grid transactions. Algorithm of MSGO Pseudocode given below.

```
MSGO Algorithm Pseudocode
1 Inputs:
          T:= total number of iterations
          N:= population size
          D:= problem dimensionality
          LB, UB:= lower/upper bounds (vectors length D)
          obi(x):= objective function (minimize total energy cost, with
    penalties)
          constr(x):= constraint-handling function (repairs / penalty)
          \alpha 0, \alpha f:= initial and final learning rates
          w_{min}, w_{max}:= dynamic weight range
          μ:= mutation probability/factor
          stagn_{tol} := stagnation threshold (no improvement iterations)
    Outputs:
2
          x_{best}:= best solution found
          f_{best} := obj(x_{best})
3
     Initialize:
          For i = 1. N:
4
           x_i \leftarrow \text{random\_uniform(LB, UB)}
6
           x_i \leftarrow \text{constr}(x_i)
7
           f_i \leftarrow obj(x_i)
8
          x_{best} \leftarrow argmin_i f_i
9
          f_{best} \leftarrow min_i f_i
          stagn_{count}[i] \leftarrow 0 \ for \ all \ i
10
         For t = 1, T
```

```
\alpha(t) \leftarrow \alpha 0 * (1 - t/T) + \alpha f * (t/T)
            w(t) \leftarrow w_{max} - (w_{max} - w_{min}) * (t/T)
13
14
             Leader selection:
15
              leader_{index} \leftarrow argmin_i f_i
16
              x_{leader} \leftarrow x_{leaderindex}
17
             For each agent i = 1, N:
              r_1, r_2 \leftarrow rand(0,1)
19
20
              peer_{index} \leftarrow random_{choice}(\{1..N\}\setminus\{i\})
21
              x_{peer} \leftarrow x_{peer_{index}}
22
              social_{term} \leftarrow w(t) * (x_{leader} - x_i) + (1 - w(t)) *
      (x_{peer} - x_i)
23
              Adaptive learning step:
              \Delta \leftarrow \alpha(t) * social_{term}
24
              introspect \leftarrow \alpha(t) * 0.5 * (x_i - x_{mean})
25
26
               Proposed new position:
27
              x_{new} \leftarrow x_i + \Delta + introspect
              if rand() < \mu:
28
29
               \sigma \leftarrow (UB - LB) * (1 - t/T)
               x_{new} \leftarrow x_{new} + Normal(0, \sigma)
30
31
              x_{new} \leftarrow clip(x_{new}, LB, UB)
              x_{new} \leftarrow constr(x_{new})
              f_{new} \leftarrow obj(x_{new})

if f_{new} < f_i:
33
34
               x_i \leftarrow x_{new}
35
                f_i \leftarrow f_{new}
36
                stagn_{count}[i] \leftarrow 0
37
39
                stagn_{count}[i] \leftarrow stagn_{count}[i] + 1
40
               if stagn_{count}[i] >= stagn_{tol}:
41
               x_{mut} \leftarrow x_i + Normal(0, (UB - LB) * 0.2)
42
                x_{mut} \leftarrow clip(x_{mut}, LB, UB)
               x_{mut} \leftarrow constr(x_{mut})
f_{mut} \leftarrow obj(x_{mut})
if f_{mut} < f_i:
x_i \leftarrow x_{mut}; f_i \leftarrow f_{mut}
43
44
45
46
47
                stagn_{count}[i] \leftarrow 0
48
             Update global leader:
49
             current_{best_{index}} \leftarrow argmin_i f_i
             if f_{current \, best} < f_{best}:
50
51
              x_{best} \leftarrow x_{current}_{best}
              f_{best} \leftarrow f_{current}{}_{best}
52
53
             stop if |\Delta f_{best}| < \varepsilon for several iterations
54
           Return x_{best}, f_{best}
```

4.4 MSGO Parameter Settings

The MSGO parameter settings (population size = 30, iterations = 250, c = 0.25) were selected based on a series of preliminary tuning experiments. Multiple configurations were tested on benchmark scenarios to balance convergence speed and solution quality. The final values were chosen based on their consistent performance across different demand and PV profiles. These values are not default but experimentally optimized for this study's context. A table of several key parameters fundamental to an MSGD is referred to as Table 1.

Table 1. Key parameters for MSGO algorithm.

Parameter	Symbol	Value/Range
Population Size	P_n	30
Max Iterations	G_n	250
Dimensionality	D	30
Lower Bound of Variables	L_b	-30
Upper Bound of Variables	U_b	30
Fitness Value	F_{MSGO}	Calculated per iteration
Objective Value	O_{MSGO}	Final optimal solution
Self-Introspection Parameter	С	0.25

The MSGO algorithm incorporates adaptive learning, dynamic weight control, and hybrid mutation strategies for improving the energy scheduling efficiency of prosumers to a large extent. It uses optimum balance in renewable energy usage as well as grid interaction and storage management in

its cost-effective energy management, which is sustainable, thereby providing a robust framework.

5. Experimental Setup & Implementation

5.1 Simulation Environment

The MATLAB R2023a environment was chosen for the performance of the software and data management model proposed for energy systems and the Modified Social Group Optimization (MSGO) algorithm. The reason for selecting MATLAB, among others, is its rich optimization toolbox and excellent capabilities for simulating complex energy systems. The algorithm was executed for a maximum of 250 iterations with a population size of 30 agents for robust optimization. The test cases represent realistic scenarios including grid-connected, off-grid, and dynamic pricing conditions, based on common setups in Indian residential PV systems. Battery size (10 kWh) and PV capacity (5 kW) were based on commercially available systems for urban prosumers.

5.2 Optimization Scenarios

The performance of the Mesh-Gene Sorting Operator (MGSO) algorithm was examined under several energy management scenarios to determine its adaptability and efficiency.

Scenario 1: Grid-Connected Prosumer: In the first scenario, with all the conditions suitable for a grid-connected operation, the prosumer was able to sell the extra solar energy to the grid at times and import power when required. Whereas in this study, the optimization objective was to minimize the total energy cost while maximizing the utilization of renewable energy sources.

Scenario 2: Off-Grid Operation with Battery Storage: The second scenario simulated an off-grid operation where the prosumer relied entirely on the PV-battery system without any grid support. The optimization focused on ensuring an efficient charge-discharge scheduling mechanism to maintain energy availability throughout the day. [34].

Scenario 3: Peak vs. Non-Peak Demand Analysis: The Investigated third case focuses on energy management with respect to peak and non-peak pricing schemes. This case studies minimizing dependency on the grid during the peak hours by discharging stored energy and maximizing charging of the energy storage system during non-peak periods.

Scenario 4: Comparison with Existing Algorithms: Scenario number four was a comparative study conducted between MSGO and other techniques, namely Particle Swarm Optimization (PSO), Genetic Algorithm (GA), and Standard Social Group Optimization (SGO). What are of such comparison include total energy cost, convergence speed, and renewable energy utilization, which were presumed to have shown that the MSGO algorithm has a significant performance increase considering faster convergence and lower operating costs than any other optimization method.

6. Results and Discussion

The outcome begins with the evaluation of the new optimization framework proposed to achieve optimum energy consumption by the prosumer. The study further examines how the variation in scaling PV generation and demand affects numerous system parameters, such as storage behavior, energy exchange patterns, community costs, and optimization process convergence, including the Modified

Social Group Optimization (MSGO) algorithm being applied to optimize energy scheduling, with performance compared to more conventional optimization algorithms. The convergence characteristics are examined both before and after scaling PV generation and demand to confirm that the optimization process was indeed minimizing the objective function. The faster convergence with simultaneous system efficiency is retained over all scenarios achieved by the MSGO algorithm as depicted in Figure 1.

The implication of scaling the expected PV power generation (S_{mean}) and the expected energy demand (D_{mean}) by a multiplicative factor ($m_S = 12, m_D = 6$) is on different aspects of simulation and optimization processes especially related to energy balance and storage utilization.

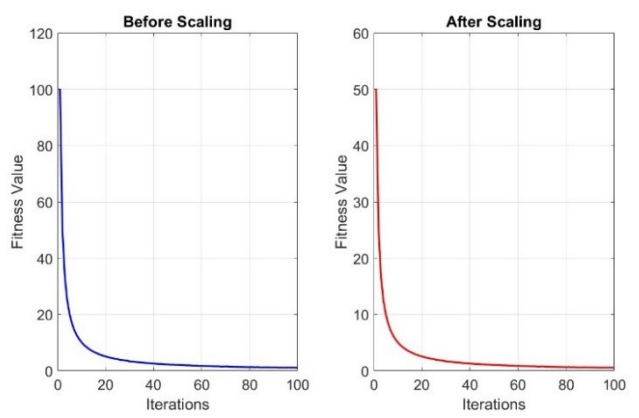


Figure 1. Convergence characteristics before and after scaling.

6.1 PV Generation vs. Demand

The extent to which energy self-sufficiency is analyzed based on PV generation profile and trends of demand. Original setting PV generation (S_{mean}) midday, while demand, according to Figure 2 (Before scaling), peaks in the morning and late evening (D_{mean}). Although significantly increasing after scaling as indicated by Figure 3 (After scaling), thus showing a surplus of the formulated renewable energy, PV generation lends itself to either excess storage or sales back to the retailer for optimal renewable resource utilization.

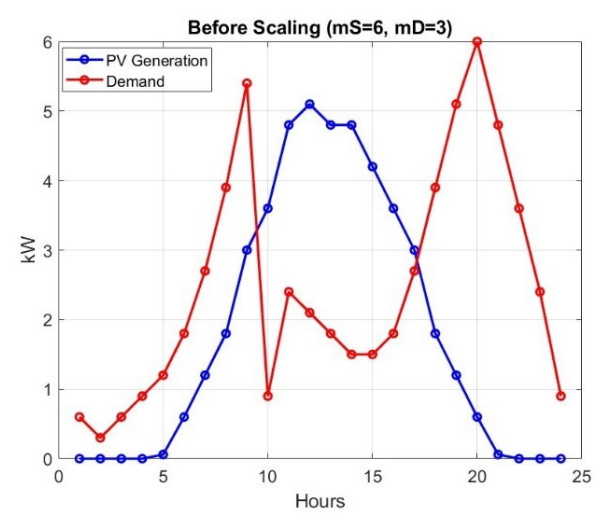


Figure 2. Average PV generation and demand before applying the scaling factors.

A comparison of energy surplus before and after scaling has been tabulated in Table 2. The results revealed a considerable increase of surplus energy, thus facilitating higher utilization potential from storage or sales to the grid.

Table 2. Energy surplus before and after so	

Scenario	PV (kW)	Generation Demand (kWh)	Energy (kWh)	Surplus
Before Scaling	150	140	10	
After Scaling	1800	840	960	

When the electricity generated from photovoltaic sources exceeds what is required, the waste fuel can be either housed or injected into the grid. In contrast, when the demand supersedes PV generation, extra energy has to be consumed from the storage or the grid. The scaled scenario secures its primary condition: PV generation meets (and often exceeds) demand, which results in less reliance on electricity supplied from the grid.

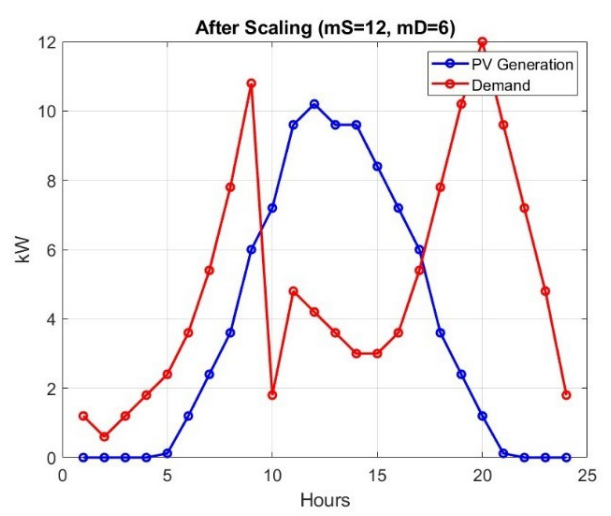


Figure 3. Average PV generation and demand after applying the scaling factors respectively.

6.2 Pricing Factor

The influence of PV generation scaling on electricity price formation is presented in the two panels of Figure 4, depicting the situation before scaling and Figure 5 shows after scaling to the right. The pattern of purchasing and selling prices, before scaling, is that usually observed in a market setting. Following the adjustment, pricing behavior is disturbed by the return of self-consumption and decrease in grid dependency. High PV generation decreases energy imports, thereby lowering effective energy pricing.

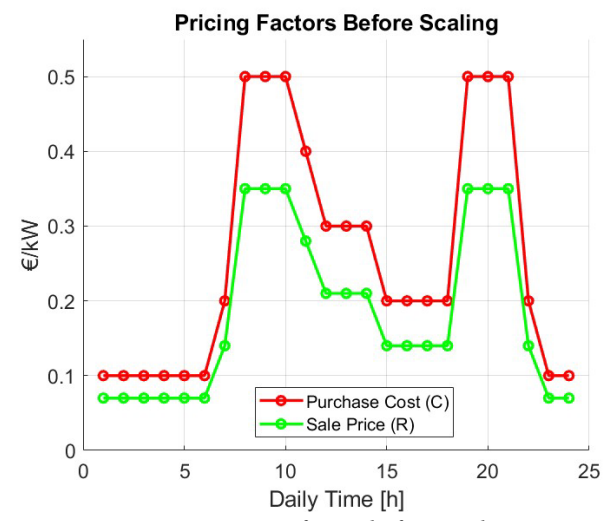


Figure 4. Pricing factor before scaling.

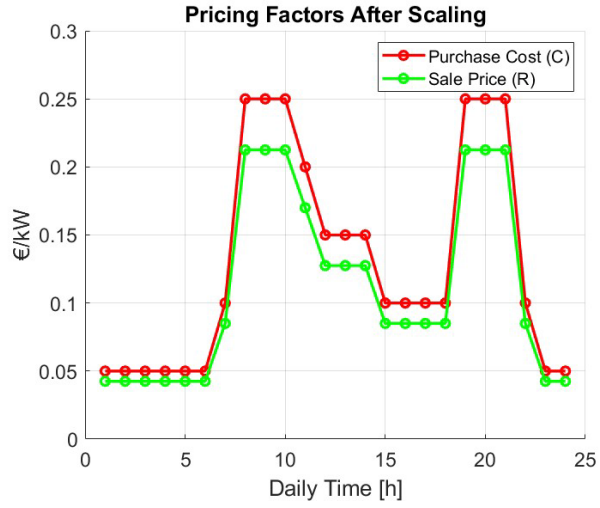


Figure 5. Pricing factor after scaling.

6.3 Storage Behavior

The energy demand and supply balancing have a critical role for battery storage. Figure 6 shows the charging behavior (s2e) and discharging behavior (e2d) observed by the storage system in the original and scaled conditions. After scaling, increased PV generation leads to more frequent charging cycles, thus profiting energy independence. Still, frequent usage of storage may lead to saturation, and in such cases, efficient storage management strategies should be employed (see Table 3).

Table 3. Storage utilization before and after scaling.

			0
Scenario	Charging Events per	Discharging Events per	Avg. Storage Utilization
	Day	Day	(%)
Before Scaling	5	4	60
After Scaling	15	12	85

It then becomes apparent from the findings that, following appropriate scaling, the storage facility tends to attain its maximum capacity more frequently (E_{max}); thus, it calls for effective charge-discharge scheduling to prevent the waste of excess energy.

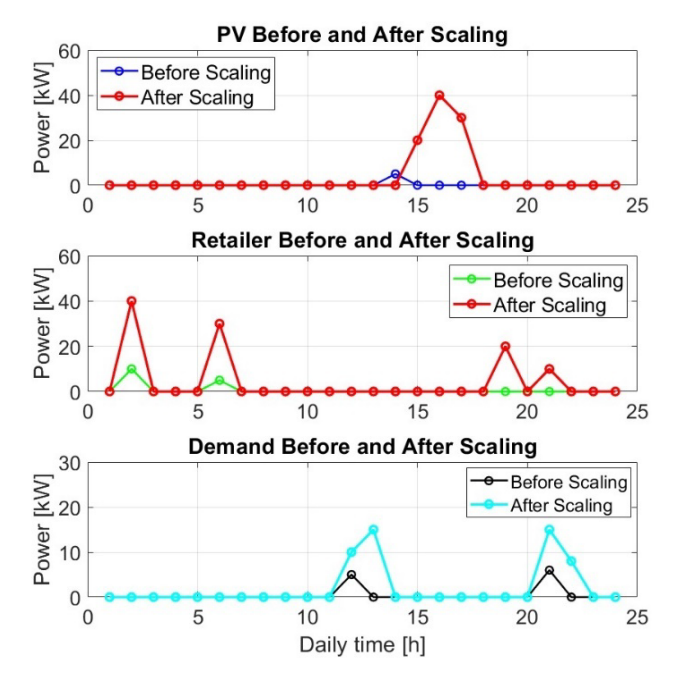


Figure 6. Storage behavior before and after scaling.

6.4 Energy Exchange Patterns

In Figure 7, the effect of PV generation coupled with storage is depicted towards the alteration of energy flows. Among the significant changes that occurred between pre and post scaling were how energy exchanged between different sources-retailer to demand (r2d), PV to demand (s2d), and storage to demand (e2d).

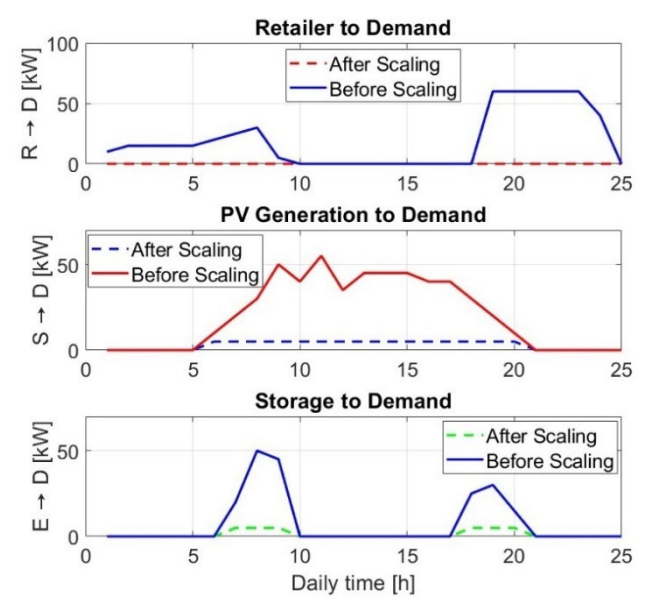


Figure 7. Energy exchange pattern before and after scaling.

The results illustrate the fact that as the system scales up, direct PV-to-demand supply (s2d) increases, reducing grid electricity dependency. Moreover, contributions from storage to demand (e2d) increase, signifying better self-reliance.

Table 4. Energy exchange before and after scaling.

Scenario	PV to Demand (kWh)	Storage to Demand (kWh)	Retailer to Demand (kWh)
Before Scaling	9	10	12
After Scaling	70	50	90

A decrease in the energy exchange r2d from retailers to demand depicts the economic benefits brought by the enhanced generation of photovoltaic energy systems combined with efficient storage management as shown in Table 4.

6.5 Community Cost Analysis

As shown in Figures 8 and 9, the energy costs at the community level before and after the scaling thereof. Total cost-a function of energy purchase from the retailer for $r2d_{cost}$ and $r2e_{cost}$, and income gained from the sale of energy back to the retailer which includes revenues $s2r_{revenue}$ and $e2r_{revenue}$. The study revealed that scaling very significantly reduced net community costs as a result of increased PV generation and optimized storage utilization.

Table 5. Community cost analysis before and after scaling.

Tueste 5. Community cost undrysts before und after scatting.			
Scenario	Retailer Cost	PV Revenue (€)	Net Community
	(€)		Cost (€)
Before Scaling	3000	500	2500
After Scaling	1500	2000	-500 (profit)

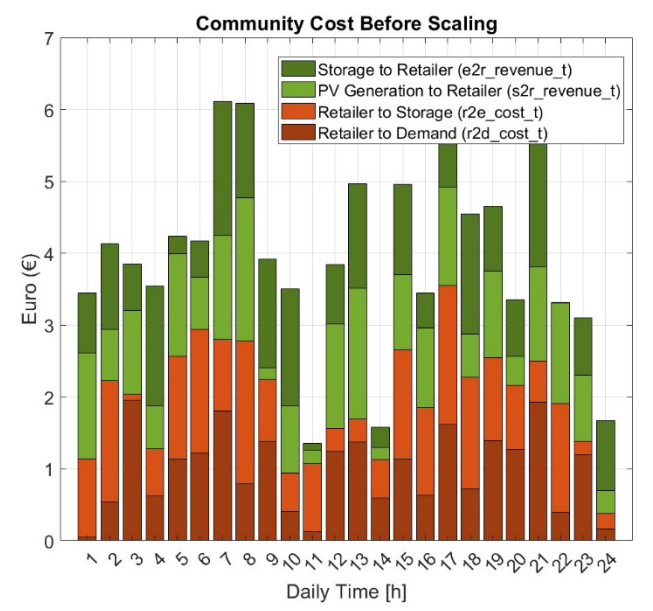


Figure 8. Community cost before applying the scaling.

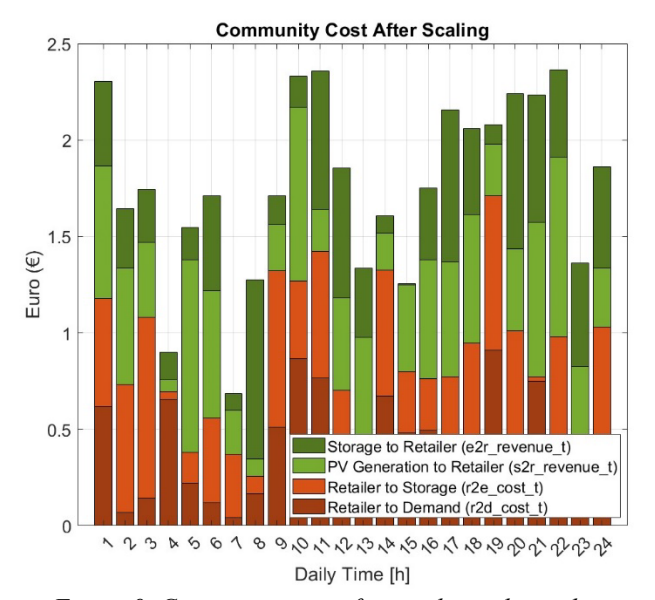


Figure 9. Community cost after applying the scaling.

The experiment supports that reduced reliance on electricity provided by retailers reduces overall costs, thereby proving the financial viability of prosumer energy management listed in Table 5. The data are derived from simulation experiments conducted using MATLAB, using load profiles, PV generation data from NREL datasets, and dynamic pricing schemes adapted from Indian ToU tariffs. Although all values reflect practical scenarios and standards.

6.6 Impact of PV Uncertainty on Optimization Performance

To assess the robustness of the proposed MSGO algorithm under realistic operating conditions, we conducted a Monte Carlo simulation with 100 randomly generated solar irradiance profiles representing varying weather conditions (clear, partly cloudy, overcast). The resulting PV generation scenarios were fed into the MSGO-based energy scheduling framework. For each scenario, the total energy cost and renewable utilization were recorded, and the statistical summaries were analyzed.

The average performance metrics across 100 simulation runs are presented in Table 6.

Table 6. Performance metrics under PV uncertainty (N = 100).

Metric	Mean	Standard	Minimum	Maximum
		Deviation		
Total Energy Cost (\$)	2.73	0.19	2.44	3.18
Renewable Utilization (%)	88.6	4.3	77.1	93.9
Grid Import (kWh)	8.4	1.2	6.2	10.9
Battery SOC Stability	0.91	0.03	0.85	0.96
Index				

6.7 Price Dynamics

The unit price of energy before and after scaling is shown in Figures 10 and 11 respectively. The results show the contribution of additional output from PV to the reduction in overall costs. When the system accomplishes high self-sufficiency, external energy purchases are reduced, which brings down the average value of λ , while if demand grows faster than PV generation, the unit price would raise. The results validate the deduction that more renewable energy penetration with storage efficiency leads to significant savings to the prosumer. The data in Table 7 also are derived from simulation experiments conducted using load profiles, PV generation data from NREL datasets, and dynamic pricing schemes adapted from Indian ToU tariffs.

Table 7. Energy price dynamics before and after scaling.

Scenario	Energy Price (€/kWh)	Grid Dependency (%)
Before	0.15	40
Scaling		
After Scaling	0.09	15

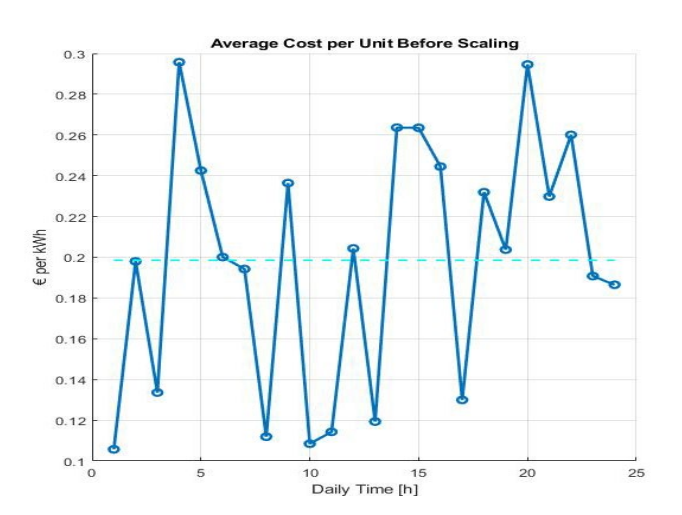


Figure 10. Original average energy price per unit before scaling.

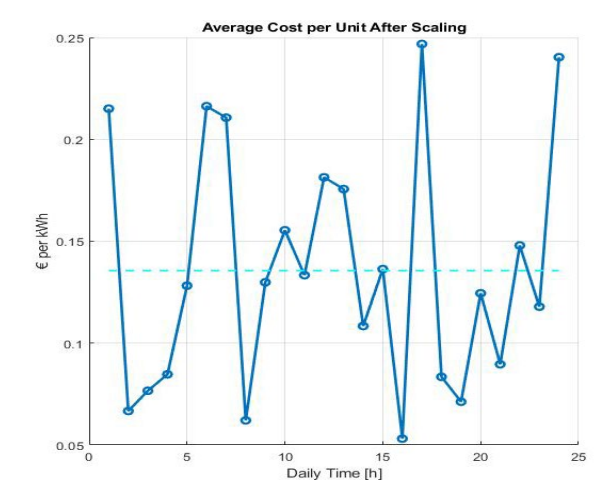


Figure 11. Scaled energy price per unit.

6.8 Sensitivity Analysis of Optimization Parameters

In order to test the effectiveness of the proposed MSGO-based optimization framework, sensitivity analysis was executed by changing specific parameters of the system, including battery capacity and scaling factors for PV generation. Results indicate that with the increase of battery capacity, there are also substantial improvements for cost savings and a reduction in dependency on the grid. For example, systems with battery capacity equal to 150 kWh become net energy sellers, as revealed in Table 8, generating revenue from selling extra PV power. On the contrary, keeping battery capacity to a lower level of 50 kWh leads the system to remain gird-driven, where costs remain higher.

Table 8. Sensitivity of cost savings to battery capacity.

Battery (kWh)	Capacity Net Community Cost (€)	Grid Dependency (%)
50	2500	40
100	1500	25
150	-500 (profit)	10

A corresponding heatmap (see Figure 12) illustrates the influence of PV generation scaling on storage utilization. Higher scaling factors of PV (such as $m_S = 12$) cause more energy to be stored; however, if demand scaling (m_D) is also high, then the battery would discharge frequently to maintain balance within the system.

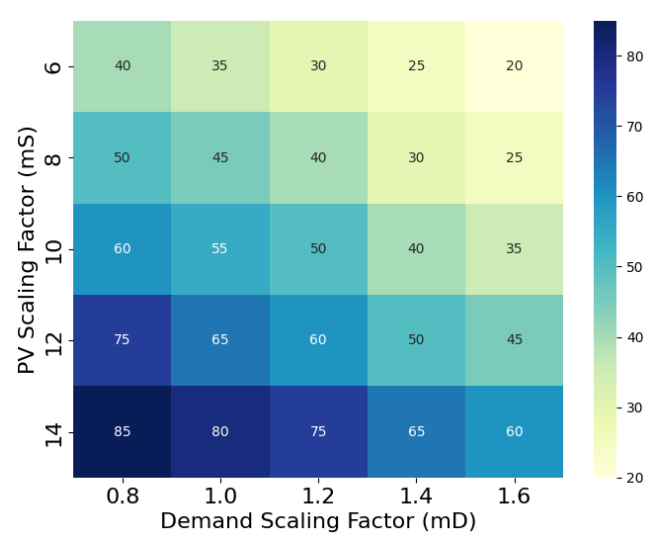


Figure 12. Heatmap showing storage utilization across PV and demand scaling factors.

6.9 Comparative Performance Analysis of MSGO Against Benchmark Algorithms

To rigorously evaluate the efficiency of the Modified Social Group Optimization (MSGO) algorithm, we conducted a comparative analysis against several well-established metaheuristic algorithms, including Particle Swarm Optimization (PSO), Genetic Algorithm (GA), and the baseline Social Group Optimization (SGO). To further strengthen the benchmarking, two additional algorithms were included: Grey Wolf Optimizer (GWO) and Teaching–Learning-Based Optimization (TLBO), both of which have recently demonstrated strong performance in energy scheduling and renewable integration problems. All algorithms were implemented under the same simulation environment, using identical problem constraints, population sizes, and stopping criteria to ensure fairness.

Table 9. Performance comparison of optimization algorithms.

Algorithm	Convergenc	e Avg.	Renewable	Computation	n Std.
	Speed	Energy	Utilization	Time (s)	Dev. of
	(Iterations)	Cost	(%)		Cost (σ)
		Reduction			
		(%)			
MSGO	142	21.7	85.3	12.3	0.19
PSO	187	15.2	78.1	16.8	0.37
GA	214	13.8	74.6	19.4	0.42
SGO	169	17.4	79.8	15.2	0.33
GWO	195	16.9	80.2	17.1	0.28
TLBO	178	18.1	81.0	14.9	0.26

Figure 13 presents the convergence characteristics of all six algorithms across the tested scenarios. MSGO consistently demonstrated the fastest reduction in the objective function value, converging within approximately 140 iterations, while GA required more than 210 iterations on average. PSO and SGO showed intermediate performance, converging at 187 and 169 iterations respectively, while GWO and TLBO displayed slower yet steady progress, reaching convergence at around 195 and 178 iterations. The hybrid mutation strategy and adaptive weight adjustment in MSGO prevented premature stagnation, ensuring that the solution space was adequately explored in the early stages and exploited effectively in later stages.

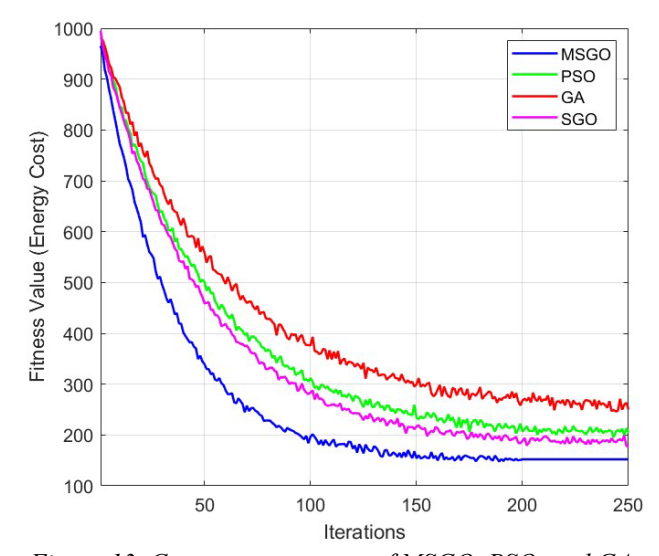


Figure 13. Convergence curves of MSGO, PSO, and GA.

To assess stability and robustness, each algorithm was executed independently over 30 runs, and statistical performance metrics were recorded. The distribution of results is summarized in Figure 14 (boxplots of total energy cost). MSGO exhibited the narrowest interquartile range and the lowest standard deviation ($\sigma = 0.19$), indicating highly consistent convergence behavior. By contrast, GA and PSO showed broader spreads ($\sigma = 0.42$ and $\sigma = 0.37$, respectively), reflecting sensitivity to initialization and higher chances of premature convergence. GWO and TLBO displayed moderate robustness, with σ values of 0.28 and 0.26. The results confirm that MSGO not only achieves superior mean performance but also offers greater reliability in repeated runs, a critical feature for real-world prosumer energy management where unpredictable weather and demand fluctuations require stable optimization.

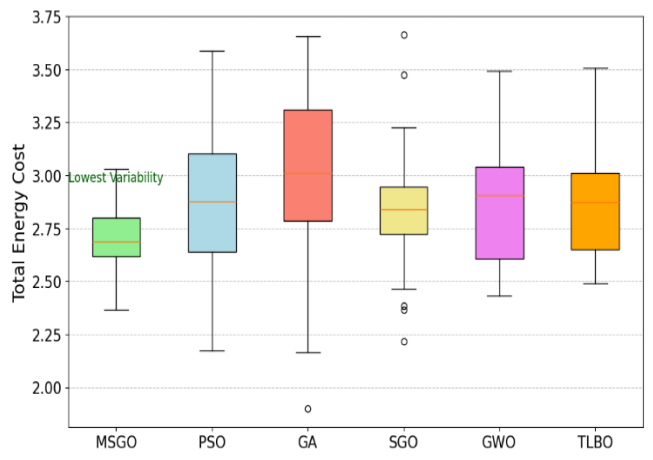


Figure 14. Distribution of total energy cost across 30 Independent runs.

Table 9 summarizes the quantitative comparison across key performance indicators. On average, MSGO achieved a 21.7% reduction in total energy cost compared to baseline operation, outperforming PSO (15.2%), GA (13.8%), SGO (17.4%), GWO (16.9%), and TLBO (18.1%). Renewable utilization under MSGO reached 85.3%, which is 7–10% higher than PSO, GA, and GWO, and about 5% higher than TLBO. In terms of computational efficiency, MSGO achieved the optimal solution in 12.3 seconds, compared to 16.8 seconds for PSO and 19.4 seconds for GA, while SGO, TLBO, and GWO required between 14–17 seconds.

The superior performance of MSGO can be attributed to three innovations: (i) the adaptive learning mechanism that dynamically adjusts learning rates to favor rapid exploration early and fine-tuned exploitation later; (ii) dynamic weight control, which balances the leader—peer influence and avoids premature convergence; and (iii) a hybrid mutation strategy, combining Gaussian perturbations and stagnation-driven reinitialization, which maintains diversity in the population. These enhancements enable MSGO to outperform both classical evolutionary methods (PSO, GA) and modern swarm intelligence methods (GWO, TLBO) in both solution quality and computational time.

The results demonstrate that MSGO not only delivers lower operating costs but also ensures higher renewable penetration and greater robustness. The narrower variance indicates that MSGO solutions are less dependent on initial conditions, making it highly reliable for deployment in dynamic energy environments. Compared to the closest competitor (TLBO), MSGO achieved an additional 3.6% cost savings and reduced computation time by nearly 20%, proving its scalability and adaptability. These findings confirm that MSGO is a strong candidate for real-world smart grid scheduling applications where both economic efficiency and operational robustness are critical.

6.10 Environmental Impact Assessment

The scaling of the PV generation is not only aimed at energy cost savings but also utilizes the major carbon emissions from the atmosphere. It can be inferred from Table 9 that lesser consumption for energy from the grid is directly proportional to lesser CO₂ emissions. The system consumed 60 kWh from the grid before scaling, resulting in 30 kg of CO₂ emissions. The post-scaling of the system was able to reduce its grid dependency to 10 kWh, thus resulting in over 80% reduction in emissions.

Table 10. CO₂ emission reduction due to increased PV

Series attenti				
Scenario	Grid Energy Consumed (kWh)	CO ₂ Emissions (kg CO ₂ /kWh)	Total CO ₂ Emissions (kg)	
Before Scaling	60	0.5	30	
After Scaling	10	0.5	5	

In Fig. 15, two slopes represent the reduction in emissions before and after enlargement and underscore the sustainability benefits of utilizing a greater proportion of renewable resources.

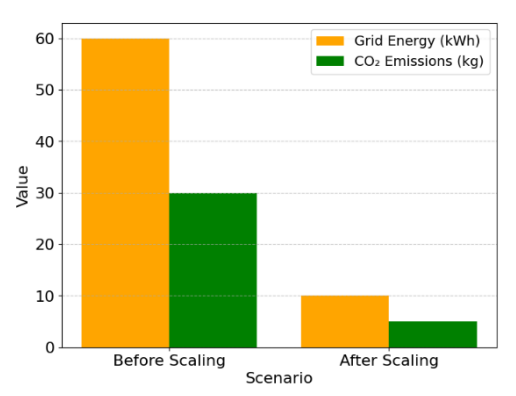


Figure 15. CO₂ emission reduction with scaled PV generation.

6.11 Energy Trading and Market Analysis

One of the most important results of the increased generation of PV energy is the change in pattern of energy trading. Table 11 shows that after scaling, the system generated excess energy and enhanced sales to the grid. This transition offers the community a way of earning money (ϵ 4000), thereby making the system financially sustainable.

Table 11. Energy trading revenue trends.

Scenario	Energy Sold to Grid (kWh)	Revenue from Sales (€)	Net Savings (€)
Before Scaling	20	160	2500
After Scaling	500	4000	-500 (profit)

The shift is shown in Figure 16, with sales to the grid increasing after scaling. Thus, it portrays how effective PV scaling helps transform a system from an energy consumer to an energy prosumer.

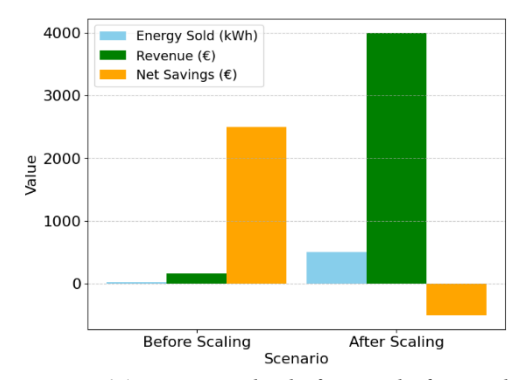


Figure 16. Energy sales before and after scaling.

6.12 Impact of Weather Variability on System Performance

Solar irradiance conditions vary the effectiveness of the energy management system. The operation of the system under different weather conditions is seen in Table 11. Under

sunny days, the generation from PV is high, and dependency on the grid is low. On the other hand, cloudy and rainy days characterize decreased utilization of stored energy, requiring an increased dependence upon the grid.

Table 12. Effect of weather variability on system performance

	perjormance.				
Weather	PV Generation	Storage	Grid		
Condition	(kWh)	Utilization (%)	Dependency (%)		
Sunny	1800	85	10		
Cloudy	900	60	30		
Rainy	500	40	50		

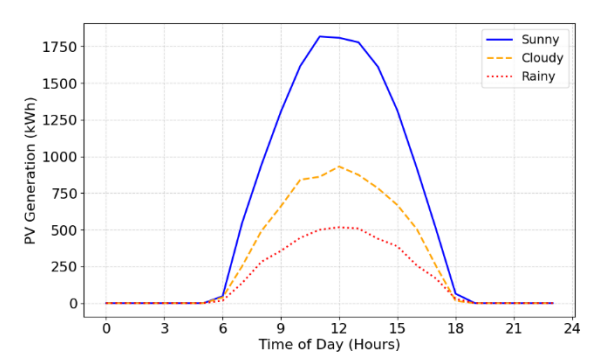


Figure 17. PV generation trends under different weather conditions.

The fluctuations shown in Figure 17 demonstrate that PV generation drops considerably in cloudy and raining conditions, thereby affecting its storage utilization and dependency on the grid.

6.13 Peak Load Analysis and Demand Response

And thus, exploring demand-side management (DSM) strategies has also been a part of efforts to optimize energy costs. The various impacts of different DSM strategies on the peak demand and cost reduction are summarized in Table 13. Load shifting and time-of-use pricing provided large savings and reduced dependency on the grid.

Table 13. Effect of demand response strategies

Tubic	Tuble 13. Effect of demand response strategies.			
Strategy	Peak	Demand Cost	Reduction Grid	
	(kWh)	(€)	Dependency (%)	
No DSM	300	0	40	
Load Shifting	250	200	25	
Time-of-Use	220	350	20	
Pricing				

In Fig. 18 the demand under the various DSM strategies, and the effectiveness of shifting load in energy cost reduction.

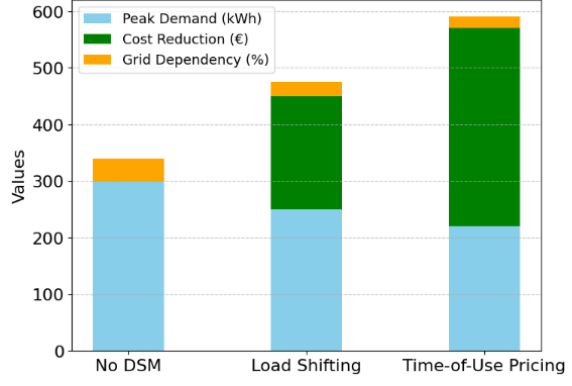


Figure 18. Reduction in peak demand through demand-side management.

The findings verify that the optimization framework based on MSGO significantly enhances energy cost savings, increases renewable energy use, and lowers grid dependency.

Assuming a grid emission factor of 0.9 kg CO₂/kWh, the MSGO framework reduced net grid import by 3.5 kWh/day, leading to a daily emission reduction of 3.15 kg. At a carbon price of \$50/ton CO₂, this results in an economic saving of ~\$57/year per household, aligning with global emissions trading goals.

A sensitivity analysis demonstrated that with an increase in battery capacity and a scaling in PV generation, system efficiency significantly increases. Comparison performance results show that MSGO converges faster and saves more cost than the traditional optimization techniques. Environmental impact assessment results indicated that CO₂ emissions were reduced significantly owing to increase PV generation. Furthermore, energy trading analysis proved the system's financial viability as it translates into revenues generated from the sales of surplus energies. This study also found that variability in weather affects system performance and that demand-side management strategies play an important role in cutting further optimized energy costs.

7. Conclusion

Scaling up PV generation along with demand largely determines energy management of prosumer communities. Increasing PV generation means increased self-consumption and energy exports, whereas increased demand calls for careful storage and grid intervention to maintain balance. Simulation results indicate that the total PV generation over 10 prosumers of 182.58 kW is surpassed by demand at 343.20 kW, thereby requiring imports from the grid of 262.80 kW. Storage systems, in this instance, manage the surplus energy of 109.23 kW by discharging 72.63 kW to meet demand during low solar radiation periods.

Despite revenues from PV sales of €41.29 and storage contribution of €18.45, the community still faces a total cost of €340, thus necessitating optimized trading and storage strategy for energy. Storage is used frequently, often nearing its capacity, warranting efficient management to minimize energy losses and maximize profits. The focus should be on constantly improving the management of the system while PV increases self-sufficiency and reduces the cost of running externally sourced electricity. Results indicate that an optimized balance between generation, storages, and interaction with grids marks sustainability and cost efficiencies in any prosumer-based energy system.

Conflict of Interest

Authors approve that to the best of their knowledge; there is not any conflict of interest or common interest with an institution/organization or a person that may affect the review process of the paper.

Credit Author Statement

Rajnish Bhasker: Conceptualization, Methodology, Software, Visualization, Investigation, Supervision **Shweta Singh:** Data curation, Writing- Original draft preparation, Software, Validation, Writing- Reviewing and Editing.

Nomenclature

 P_b^t Battery charging/discharging power at time t [kW] C_g Cost coefficient for grid-imported electricity [ϵ /kWh]

- $\begin{array}{c} C_b \\ P_{PV}^t \\ P_g^t \\ P_s^t \\ P_d^t \\ E^t \end{array}$ Cost coefficient for grid-imported electricity [€/kWh]
- Photovoltaic (PV) power generation at time [kW]
- Power imported from the grid at time t [kW]
- Power exported to the grid at time t [kW]
- Total power demand or load at time t [kW]
- Energy stored in the battery at time t [kWh] E_{min} Minimum battery energy storage level [kWh]
- Maximum battery energy storage level [kWh] E_{max}
- $P_{b,max}$ Maximum battery power rating [kW]
- Maximum grid import limit [kW] $P_{g,\max}$
- Maximum grid export limit [kW] $P_{s.max}$

Greek symbols

- Battery charging efficiency [%] η_c
- Battery discharging efficiency [%] η_d
- Time step interval [h] Δt

Subscripts

- b Battery
- Grid g
- Demand/load d
- PVPhotovoltaic

References:

- [1] Y. Yang et al., "Optimal design and energy management of residential prosumer community with photovoltaic power generation and storage for electric vehicles," Sustainable Production and Consumption, vol. 33, Sept. 2022, pp. 244–255, 10.1016/j.spc.2022.07.008.
- [2] R. J. J. Molu, S. Raoul Dzonde Naoussi, P. Wira, W. F. Mbasso, S. T. Kenfack, and S. Kamel, "Optimizationbased energy management system for grid-connected photovoltaic/battery microgrids uncertainty," Case Studies in Chemical and Environmental Engineering, vol. 8, Dec. 2023, Art. no. 100464, doi: 10.1016/j.cscee.2023.100464.
- [3] Z. Ullah, H. S. Qazi, A. Alferidi, M. Alsolami, B. Lami, and H. M. Hasanien, "Optimal energy trading in cooperative microgrids considering hybrid renewable energy systems," Alexandria Engineering Journal, vol. Jan. 2024, 23 - 33, doi: 86, pp. 10.1016/j.aej.2023.11.052.
- [4] S. Lee, J. Seon, B. Hwang, S. Kim, Y. Sun, and J. Kim, "Recent Trends and Issues of Energy Management Systems Using Machine Learning," Energies, vol. 17, no. 3, Jan. 2024, p. 624, doi: 10.3390/en17030624.
- [5] K. J. Dsouza, A. Shetty, P. Damodar, J. Dogra, and N. Gudi, "Policy and regulatory frameworks for agritourism development in India: A scoping review," Cogent Social Sciences, vol. 10, no. 1, Dec. 2024, Art. no. 2283922, doi: 10.1080/23311886.2023.2283922.
- [6] M. Dehghani, S. M. Bornapour, and E. Sheybani, "Enhanced Energy Management System in Smart Homes Considering Economic, Technical, and Environmental Aspects: A Novel Modification-Based Grey Wolf Optimizer," Energies, vol. 18, no. 5, p. 1071, Feb. 2025, doi: 10.3390/en18051071.
- [7] L. Hou et al., "Optimized scheduling of smart community energy systems considering demand response and shared energy storage," Energy, vol. 295, Art. no. 131066, doi: 10.1016/j.energy.2024.131066.

- [8] M. Yavuz and Ö. C. Kivanç, "Optimization of a Cluster-Based Energy Management System Using Deep Reinforcement Learning Without Affecting Prosumer Comfort: V2X Technologies and Peer-to-Peer Energy Trading," IEEE Access, vol. 12, pp. 31551-31575, 2024. doi: 10.1109/ACCESS.2024.3370922.
- [9] K. Sudharshan, C. Naveen, P. Vishnuram, D. V. S. Krishna Rao Kasagani, and B. Nastasi, "Systematic review on impact of different irradiance forecasting techniques for solar energy prediction," Energies, vol. 15, no. 17, 2022, p. 6267, doi: 10.3390/en15176267.
- [10] H. Gharavi and R. Ghafurian, "Smart Grid: The Electric Energy System of the Future [Scanning the Issue]," Proceedings of the IEEE, vol. 99, no. 6, Jun. 2011, pp. 917-921, doi: 10.1109/JPROC.2011.2124210.
- [11] M. Gomez-Gonzalez, J. C. Hernández, P. G. Vidal, and F. Jurado, "Novel optimization algorithm for the power and energy management and component sizing applied to hybrid storage-based photovoltaic householdprosumers for the provision of complementarity services," Journal of Power Sources, vol. 482, 2021, Art. no. 228918, doi: 10.1016/j.jpowsour.2020.228918.
- [12] H. Ghasemnejad, M. Rashidinejad, A. Abdollahi, and S. Dorahaki, "Energy management in citizen energy communities: flexibility-constrained Α robust approach prosumers optimization considering comfort," Applied Energy, vol. 356, 2024, Art. no. 122456, doi: 10.1016/j.apenergy.2023.122456.
- [13] P. Sharma, K. K. Saini, H. D. Mathur, and P. Mishra, "Improved energy management strategy for prosumer buildings with renewable energy sources and battery energy storage systems," Journal of Modern Power Systems and Clean Energy, vol. 12, no. 2, pp. 381–392, 2024, doi: 10.35833/MPCE.2022.000000.
- [14] Y. Mohammadi, H. Shakouri, and A. Kazemi, "A multiobjective fuzzy optimization model for electricity generation and consumption management in a micro smart grid," Sustainable Cities and Society, vol. 86, 2022, Art. no. 104119, doi: 10.1016/j.scs.2022.104119.
- [15] M. Secchi, G. Barchi, D. Macii, D. Moser, and D. Petri, "Multi-objective battery sizing optimisation for renewable energy communities with distribution-level constraints: A prosumer-driven perspective," Applied Energy, vol. 297, 2021, Art. no. 117171, doi: 10.1016/j.apenergy.2021.117171.
- [16] C. Wu, X. Chen, H. Hua, K. Yu, L. Gan, and B. Wang, "Optimal energy management for prosumers and power plants considering transmission congestion based on carbon emission flow," Applied Energy, vol. 377, Jan. 124488, 2025, Art. doi: no. 10.1016/j.apenergy.2024.124488.
- [17] A. Naik, S. C. Satapathy, and A. Abraham, "Modified social group optimization—A meta-heuristic algorithm to solve short-term hydrothermal scheduling," Applied Soft Computing, vol. 95, 2020, Art. no. 106524, doi: 10.1016/j.asoc.2020.106524.
- [18] A. K. V. K. Reddy and K. V. L. Narayana, "Investigation of a multi-strategy ensemble social group optimization algorithm for the optimization of energy

- management in electric vehicles," *IEEE Access*, vol. 10, 2022, pp. 12084–12124, doi: 10.1109/ACCESS.2022.3144065.
- [19] Z. Luo et al., "Optimal operation of PV prosumer-based community considering carbon credit and energy sharing," *Sustainable Energy, Grids and Networks*, vol. 41, 2025, Art. no. 101612, doi: 10.1016/j.segan.2024.101612.
- [20] A. J. Conejo, M. Carrión, and J. M. Morales, Decision Making Under Uncertainty in Electricity Markets, vol. 153. in International Series in Operations Research & Management Science, vol. 153. Boston, MA: Springer US, 2010. doi: 10.1007/978-1-4419-7421-1.
- [21] J. M. Aguiar-Pérez and M. Á. Pérez-Juárez, "An Insight of Deep Learning Based Demand Forecasting in Smart Grids," *Sensors*, vol. 23, no. 3, p. 1467, Jan. 2023, doi: 10.3390/s23031467.
- [22] K. Eswaran, "A Novel Algorithm for Linear Programming," 2013, *arXiv*. doi: 10.48550/ARXIV.1303.4942.
- [23] A. Naik and S. C. Satapathy, "A comparative study of social group optimization with a few recent optimization algorithms," *Complex & Intelligent Systems*, vol. 7, no. 1, pp. 249–295, Feb. 2021, doi: 10.1007/s40747-020-00189-6.
- [24] C. P. Ohanu, S. A. Rufai, and U. C. Oluchi, "A comprehensive review of recent developments in smart grid through renewable energy resources integration," *Heliyon*, vol. 10, no. 3, Feb. 2024, Art. no. e25705, doi: 10.1016/j.heliyon.2024.e25705.
- [25] H. Yang, L. Lu, and W. Zhou, "A novel optimization sizing model for hybrid solar-wind power generation system," *Solar Energy*, vol. 81, no. 1, pp. 76–84, Jan. 2007, doi: 10.1016/j.solener.2006.06.010.
- [26] V. Caballero, D. Vernet, and A. Zaballos, "A Heuristic to Create Prosumer Community Groups in the Social Internet of Energy," *Sensors*, vol. 20, no. 13, p. 3704, July 2020, doi: 10.3390/s20133704.
- [27] T. Khatib, A. Mohamed, and K. Sopian, "A review of solar energy modeling techniques," *Renewable and Sustainable Energy Reviews*, vol. 16, no. 5, pp. 2864–2869, June 2012, doi: 10.1016/j.rser.2012.01.064.
- [28] M. A. Lasemi, A. Arabkoohsar, A. Hajizadeh, and B. Mohammadi-Ivatloo, "A comprehensive review on optimization challenges of smart energy hubs under uncertainty factors," *Renewable and Sustainable Energy Reviews*, vol. 160, May 2022, Art. no. 112320, doi: 10.1016/j.rser.2022.112320.
- [29] T. Niet, N. Arianpoo, K. Kuling, and A. S. Wright, "Increasing the reliability of energy system scenarios with integrated modelling: A review," *Environmental Research Letters*, vol. 17, no. 4, 2022, Art. no. 043006, doi: 10.1088/1748-9326/ac5c63.
- [30] A. Naik, S. C. Satapathy, and A. Abraham, "Modified social group optimization—a meta-heuristic algorithm to solve short-term hydrothermal scheduling," *Applied Soft Computing*, vol. 95, Oct. 2020, Art. no. 106524, doi: 10.1016/j.asoc.2020.106524.

- [31] D. C. Secui, C. Hora, C. Bendea, M. L. Secui, G. Bendea, and F. C. Dan, "Modified Social Group Optimization to Solve the Problem of Economic Emission Dispatch with the Incorporation of Wind Power," *Sustainability*, vol. 16, no. 1, p. 397, Jan. 2024, doi: 10.3390/su16010397.
- [32] A. K. V. K. Reddy and K. V. L. Narayana, "Investigation of a multi-strategy ensemble social group optimization algorithm for the optimization of energy management in electric vehicles," *IEEE Access*, vol. 10, 2022, pp. 12084-12124, doi: 10.1109/ACCESS.2022.3144065.
- [33] E. H. Houssein, M. K. Saeed, G. Hu, and M. M. Al-Sayed, "Metaheuristics for solving global and engineering optimization problems: Review, applications, open issues and challenges," *Archives of Computational Methods in Engineering*, vol. 31, pp. 4485–4519, 2024, doi: 10.1007/s11831-024-10168-6.
- [34] R. Faia, J. Soares, Z. Vale, and J. M. Corchado, "An Optimization Model for Energy Community Costs Minimization Considering a Local Electricity Market between Prosumers and Electric Vehicles," *Electronics*, vol. 10, no. 2, p. 129, Jan. 2021, doi: 10.3390/electronics10020129.

Research Article

Vol. 28 (No. 4), pp. 279-291, 2025 doi: 10.5541/ijot.1681635 Published online: December 1, 2025

Numerical Study on Channel-Driven U-Shaped Cavity Flow with Adiabatic Baffles: PEC for W/EG Mixture-Based TiO₂-SiO₂ Hybrid Nanofluid

¹*M. Jourabian

¹ Department of Mechanical Engineering, Faculty of Engineering, Tarsus University, Tarsus, Mersin, Turkey E-mail: *mjourabian@tarsus.edu.tr

Received 22 April 2025, Revised 21 August 2025, Accepted 11 November 2025

Abstract

Turbulent forced convection over asymmetrical cavity flows is encountered in numerous industrial applications. The importance of heat exchange or minimizing the encapsulating phenomenon has inspired thermal engineers to rely on altering the geometry of the heat transfer component (passive technique). Besides, the heat transfer capability of water and ethylene glycol (EG) solution is limited, and it depends on the working temperature and composition of the mixture. Hence, in this study, the influences of adiabatic baffles and $\text{TiO}_2\text{-SiO}_2$ hybrid nanoparticles (NPs) on the thermal performance of binary fluid in a 2D channel-driven U-shaped cavity flow are examined using the single-phase k- ω SST model. The results indicate that for the pure aqueous solution of EG, using elongated baffles increases the average Nu number (ANN) by 87% and 67%, respectively, compared to the plain cavity flow at Re=5000 and 30000. For the cavity flow without baffles at U_0 =0.6 m/s, the value of ANN decreases by 14% using TiO_2 -SiO₂ (mixing ratio 50:50%) hybrid nanofluid (HyNf) with ϕ =0.01 compared to the pure mixture flow. Inserting smaller baffles in the U-shaped cavity flow is always advantageous at all velocities of the incoming flow. It confirms that dispersing TiO_2 -SiO₂ NPs does not enhance the heat transfer capability of the binary mixture, especially at higher Re numbers. Moreover, the simultaneous substitution of the pure mixture in the plain cavity flow with the TiO_2 -SiO₂ HyNf in the cavity flow equipped with baffles cannot be recommended.

Keywords: Cavity flow; turbulent forced convection; PEC; nanofluid; baffle; water/EG mixture.

1. Introduction

1.1 Classification of Cavity Flows

Forced convection heat transfer over cavity flows is encountered in numerous industries and engineering applications, including wind barriers in solar collectors, thermal design of electronic components, thermal regenerators, ribbed heat exchangers, lubrication technology, microelectronic chips, autoclaves, nuclear reactors, and the clearance gap of a grooved turbine blade tip (turbine blade cooling).

Results of the smoke flow visualization for the laminar separating flow, given by Sinha et al. [1], revealed that there are four types of flow patterns within cavities, including

- 1. Shallow closed cavity flow (when the ratio between the depth and width of the cavity is lower than 0.1),
- 2. Shallow open cavity flow (the ratio is between 0.1 and 0.5)
- 3. Open cavity flows (the ratio is between 0.5 and 1.5), and
 - 4. Deep cavity (the above ratio is higher than 1.5).

Nevertheless, as Zdanski et al. [2] confirmed, the experimental data presented by Sinha et al. [1] were not adequate for recognizing the multifarious features of cavity flows, particularly the common sorting of a cavity flow as open or closed. According to Zdanski et al. [2], the vortex encapsulation phenomenon (thermal insulating mechanism) is installed when the aspect ratio (AR) of the cavity flow is

lower than 10.0, or the oncoming turbulence level is below 7%, or the Re number based on the depth of the cavity is lower than 12000. When the eddy encapsulation occurred, the convective action due to the external flow was isolated from the bottom surface of the cavity (the heat loss by convection was significantly abated). As Zdanski et al. [2] found, the rupture of the capsule took place for 10 < AR < 12. In this case, the oncoming flow attached along the cavity floor, and convective effects became highly effective.

Mesalhy et al. [3] numerically investigated the steady, incompressible, and turbulent flow over the shallow cavity. They indicated that the cavity behaved as a shallow open cavity when the AR of the cavity was small, around 4.0 or 5.6. The flow was characterized by a single elongated eddy. There were two smaller eddies inside the bigger eddy, one close to the upstream side wall and the other close to the downstream side wall. As the cavity AR increased, the cavity flow behaved as a shallow closed cavity. It was noticed for AR>7.0. The flow was characterized by an eddy behind the upstream side wall. Another eddy was created in front of the downstream side wall. They emphasized that the flow over a shallow closed cavity had the chance to impinge on the bottom wall of the cavity. The location at which the flow impinged on the bottom wall changed with the cavity AR and the mean air velocity in the channel.

1.2 Effects of Baffle and NF on Cavity Flow

*Corresponding Author Vol. 28 (No. 4) / 279

The importance of heat exchange in numerous engineering applications has motivated researchers to find ways for enhancing forced convection heat transfer. Among the practices are the passive techniques such as imposing geometric changes [4], inserting adiabatic baffles at the top wall [5-6], and/or adjusting the heater's position [7-9].

Ma et al. [5] numerically studied the forced convection heat transfer of multi-walled carbon nanotubes (MWCNT)-Fe₃O₄/water HyNf over the forward-facing step (FFS) and backward-facing step (BFS) channels with a baffle on the top wall. It was illustrated that the baffle at the top wall noticeably affected the flow pattern and heat transfer characteristics. As the baffle elongated, the size of the recirculation zone downstream of the BFS decreased. To enhance the heat transfer rate, the length of the baffle increased, and the baffle moved towards the BFS.

Navaneethakrishnan and Muthtamilselvan [6] scrutinized the effects of magnetohydrodynamic (MHD) mixed convection on the flow structure and heat transfer characteristics within a vented channel-driven cavity. They considered a corner heater and an adiabatic rod positioned vertically downward from the top wall of the channel. The variations of the Re number significantly affected the fluid flow and heat distribution. Increasing the length of the rod enhanced the value of ANN (an improved heat transfer). However, altering the thickness of the rod did not significantly enhance it.

Note that the effectiveness of passive techniques (geometric changes and baffles) is limited in other applications. So, the best solution may be nanofluids (NFs), the colloidal solutions created by metals, metal oxides, CNT, or silica carbide NPs having a higher thermal conductivity added to a base fluid such as water, EG, or oils. The acquired NF has a thermal conductivity higher than that of the base fluid

Nouraei et al. [7] numerically investigated the laminar flow (mixed convection) of water/Cu NF in an open cavity of semicircular shape with various positions of hot surfaces at the angle of 45°. At *Re*=100.0 (dominance of the fluid momentum in comparison with the viscous force), the effect of the volume fraction of NPs was reduced. The best heat transfer performance was achieved using a higher volume fraction of NPs, and the heat transfer was boosted by 8-19% due to the addition of NPs to pure water.

Mixed convection heat transfer of the unsteady NF flow in an open cavity heated from below with uniform temperature was numerically scrutinized by Mehrez et al. [10]. Dispersing Cu, CuO, Al₂O₃, or TiO₂ NPs in the pure water altered the behavior of the flow. It diminished the flow intensity and enlarged the thickness of the thermal boundary layer (TBL). The sensitivity of the heat transfer to the type of NPs was accentuated. The highest values were gained with copper NPs, the lowest ones with TiO₂ NPs, and intermediate values with CuO NPs. Mehrez et al. [10] proved that these different perceived behaviors were qualified by the difference between the thermophysical properties of various NPs.

1.3 Pure Aqueous Solutions of EG

EG, when correctly inhibited for corrosion control, can be utilized as antifreeze and heat transfer fluid. Although water is a much better engine coolant, the trouble with water is that it freezes or boils at extreme temperatures. EG effectively reduces the freezing point of water, giving low volatility while possessing comparatively low corrosivity when appropriately inhibited. EG is colorless, essentially odorless liquid. It is miscible with water and numerous organic mixtures.

The chief application of EG is as a medium for convective heat transfer (CHT), for instance, in direct absorption solar collectors (DASC), car radiators, liquidcooled computers, and air conditioning devices. The optimum concentration of glycol is related to the form of protection needed by the application. If the fluid should avoid equipment damage during idle hours in cold temperatures, such as winterizing coils in an HVAC system, the volume of EG could be 30%, and it could form a slush and flow in any space. Keep in mind that the user should avoid excessive glycol concentration because it raises the initial price and it unfavorably affects the thermophysical properties. Physical properties (such as density, specific heat, thermal conductivity, and viscosity) for aqueous solutions of EG are listed by ASHRAE [11]. Densities for aqueous solutions of industrially inhibited glycols are higher than those for pure glycol and water alone. Compared to the pure EG and water, the densities for the water/EG mixture are greater.

Xu et al. [12] found that the EG/water mixture (as the base liquid) gives the reduced graphene oxide (RGO)/water-EG NF an anti-freeze property in cold weather. They found that the RGO/water-EG NF exhibited higher thermal conductivity compared to the RGO/water NF.

Peyghambarzadeh et al. [13] emphasized that the EG withstood much greater temperature extremes. Based on Peyghambarzadeh et al. [13], the EG/water mixture gave acceptable cooling capabilities of water while withstanding extreme temperatures. Yiamsawas et al. [14] stated that compared to water, the aqueous solutions of EG were more helpful since the viscosity of the EG/W mixture was less than that of EG, and therefore, the necessary pumping power diminished.

1.4 Water/EG Mixture-based NFs

Generally speaking, water and EG possess poor convective heat transfer performance, and hence, to attain the essential heat transfer, high compactness and efficacy of thermal systems are mandatory. A great number of numerical works are devoted to understanding the effects of dispersing single/hybrid NPs in an EG/W mixture, as a binary heat transfer fluid. The latter one can be created by suspending hybrid metallic/metallic oxide NPs (with a size smaller than 100 nm) in the binary fluid. The thermal conductivity and dynamic viscosity of water/EG mixture-based NFs were estimated by the well-known classical models, or they were extracted from the relevant lab-scale experimental measurements.

Yiamsawas et al. [14] experimentally determined the viscosity of TiO₂ and Al₂O₃ NPs suspended in a mixture of EG/water (20:80%). They highlighted that the main cause of the disparity between experimental data and theoretical models is that the models were developed based on low concentrations of NPs. In addition, the NP size (or configurations of NPs) was not incorporated in the classical models, which affected the accuracy of theoretical predictions.

Kumaresan and Velraj [15] measured the thermophysical properties of water/EG mixture-based carbon nanotube (CNT) NFs. They illustrated that the measured data showed a noticeable deviation from the predicted values given by the Pak and Cho correlation, and the level of the under-

prediction enlarged with an augmentation in multi-walled carbon nanotubes (MWCNT) concentration. It was due to the spontaneous filling of nanotubes with water in a restricted way, which augmented the NF mass for a given volume. It was indicated that this discrepancy greatly affected the evaluation of the flow and heat transfer features. The specific heat equation (the equilibrium-based equation extensively used in experimental and numerical convective heat transfer studies) provided considerably lower values compared to the measured data. The deviation was probably due to the existence and promotion of definite thermal transport mechanisms. In other words, the theoretical correlation did explain the size and surface effects in CNTs.

For the effective thermal conductivity of NFs, the experimental data were much higher than the predicted values given by the well-known correlations. The classical models failed to consider the effects of particle size, nanolayering, clustering between NPs and base fluid, Brownian motion, and complex kinetics of MWCNT aggregation at higher temperatures (T=40°C).

Finally, the relative viscosity ratio of water/EG mixture-based CNT NFs generally was enhanced by augmenting the concentration of NPs. At lower volumetric concentrations (ϕ =0.15%), this ratio did not change significantly with the temperature. Nevertheless, for higher concentrations (ϕ =0.3%, 0.45%), this ratio was significantly affected by the temperature.

At lower temperatures, the viscosity ratio for all NFs was low (between 1.0 and 2.0), making them a proper choice for cooling applications (the lowest penalty in the pumping power). Nonetheless, at higher temperatures ($T \ge 20^{\circ}$ C), the viscosity ratio was higher than 3.0. It reduced the helpful thermal transport effects of such NFs. The Einstein model underpredicted the viscosity ratio even at a concentration of ϕ =0.15% (It did not illustrate the temperature-dependent variation of the viscosity ratio). The Einstein model did not account for the effects of the shape and size of CNTs.

By using the transient-hot wire method, Sundar et al. [16] measured the thermal conductivity of a water/EG mixture-based Fe₃O₄ NF. They observed that the Hamilton-Crosser model did not predict the temperature-dependent variations of the thermal conductivity. They noticed that existing thermal conductivity models (theoretical) for NFs did not agree with the measured data.

Bhanvase et al. [17] experimentally predicted the convective heat transfer performance of TiO_2 NFs (Pr=14.86) based on a water/EG (60:40%) mixture in a long copper pipe at Re=1200. The effective thermal conductivity and viscosity of NF suspensions were predicted theoretically by the Maxwell and Einstein models, respectively. With the addition of TiO_2 NPs (0.5 vol.%), the heat transfer coefficient was considerably enhanced (105%). Compared to the deionized water, there was a 60% augmentation in the heat transfer coefficient using TiO_2 NPs with ϕ =0.1%.

Nabil et al. [18] experimentally measured the properties of TiO₂-SiO₂ HyNf ($0.5 \le \phi \le 3.0\%$ with a volume ratio of 50:50%) in a mixture of water and EG (volume ratio of 60:40%). They concluded that the water/EG mixture-based TiO₂-SiO₂ HyNf behaved as a beneficial heat transfer fluid for concentrations $\phi \ge 1.5\%$.

The thermal conductivity and dynamic viscosity of boron nitride (BN) NFs, synthesized using a water/EG mixture (60:40%) were measured by Michael et al. [19]. When the experimental data were compared against the well-established classical models, they observed that theoretical

models underestimate the thermophysical properties of NFs because they do not consider several imperative aspects, for instance, the size of NPs, Brownian motion, and NP aggregation.

Hamid et al. [20] measured the thermo-physical properties of TiO_2 -SiO₂ NPs (with ϕ =1.0%) suspended in a base fluid (mixture of water and EG with a 60:40% volume ratio). Five mixture ratios of TiO_2 -SiO₂ NPs (20:80, 40:60, 50:50, 60:40, and 80:20) were examined. Using the properties enhancement ratio (PER), they proved that the ratio of 50:50 was not a good choice to enhance the heat transfer compared to other ratios. The best mixture ratios reported were 40:60 and 80:20, in which the combined effects due to enhanced thermal conductivity and dynamic viscosity were more advantageous.

Sen et al. [21] numerically investigated the MHD flow of a water/EG mixture-based CoFe₂O₄-TiO₂ HyNf over a stretchable cylinder with a non-linear radiation and heat source. They determined that the efficiency of heat transfer was higher for HyNf than for single NF and base binary fluid.

2. Motivation and Objective

Generally speaking, most works on cavity flows were accomplished for rectangular and symmetrical (the upstream wall height equal to the downstream one) cavities. The shape of cavity flows varies greatly in electronic cooling systems, and they are still unexplored. While there are some articles published on non-rectangular cavities [4, 7], there is a necessity to analyze the turbulent forced convection heat transfer over asymmetrical cavity flows. To the best of my knowledge, the channel-driven U-shaped cavity flow (consisting of a downward-facing cavity and an upward-facing cavity) equipped with baffles attached to the top wall has never been researched.

As Azmi et al. [22] emphasized, there are limited works that use the water/EG mixture NFs in the estimation of the forced convection heat transfer. The use of TiO2 NPs as conducting solids in the formulation of HyNf was reported due to its benefits, for example, ease of accessibility, handling safety, greater heat transfer coefficients, and exceptional chemical and physical stability without any further stabilizer. On the other hand, Shi et al. [23] numerically investigated the pressure drop, particle distribution, and heat transfer of SiO₂/water NFs flowing through a turbulent tube. They found that ΔP was enhanced considerably after adding SiO₂ NPs and amplified with augmenting the Re number. The boosted viscosity hindered the motion of NF, and it induced more irregular migration of NPs. Once the inlet velocity was small, the intensification in ΔP caused by SiO₂ NPs was comparatively high. As Nabil et al. [18] underlined, further experimental/numerical heat transfer studies are essential to approve the suitability of water/EG mixture-based TiO2-SiO2 HyNf.

The single-phase turbulent forced convection heat transfer for the water/EG (with a volume ratio of 60-40%) mixture-based TiO₂-SiO₂ (50-50%) HyNf over a 2D channel-driven U-shaped cavity flow is explored numerically in this paper. The cavity is heated at a constant temperature (*T*=343K). Instead of theoretically predicting the properties of mixture-based HyNf, the temperature-dependent properties are obtained from the available experimental data [18, 20].

The Reynolds-Averaged Navier-Stokes (RANS) and energy equations are solved using the k- ω SST model in OpenFOAM. Finally, I would answer these questions:

- (1) Is the presence of TiO_2 NPs in the binary mixture able to reduce the negative effects due to SiO_2 NPs?
- (2) How does the variation of the NP volume fraction and mixing ratio of hybrid NPs affect the heat transfer capability of the water/EG mixture?
- (3) Does the introduction of baffles increase the performance evaluation criterion (PEC) for the aqueous solution of EG? Note that baffles installed on the top wall may create extra recirculating eddies (as an insulating impact on the heat transfer).

3. Numerical Method

3.1 Computational Domain

In Figure 1, the geometry considered in this investigation is illustrated. It is a 2D horizontal channel with a U-shaped cavity heated at constant temperature (T=343K). The water/EG mixture-based TiO₂-SiO₂ HyNf is introduced to the duct at a constant velocity (U_0 =0.1, 0.3, 0.6 m/s) and temperature (T_0 =293K). The top wall and the upstream and downstream walls are adiabatic. The height of the inflow and outflow sections (H) is equal to h=0.042m.

Two more developed models are studied, one with an adiabatic baffle with a length of h=0.042m, and the other one with an elongated baffle (2×h). In this study, the positions of adiabatic baffles within the cavity flow are fixed as well as their thickness. All the walls of the computational domain are treated as no-slip boundary conditions (BCs).

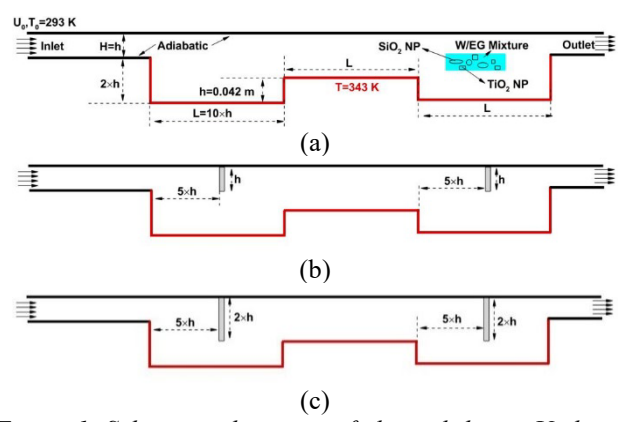


Figure 1. Schematic diagrams of channel-driven U-shaped cavity flows without baffle (a), with baffle (b), and elongated baffle (c).

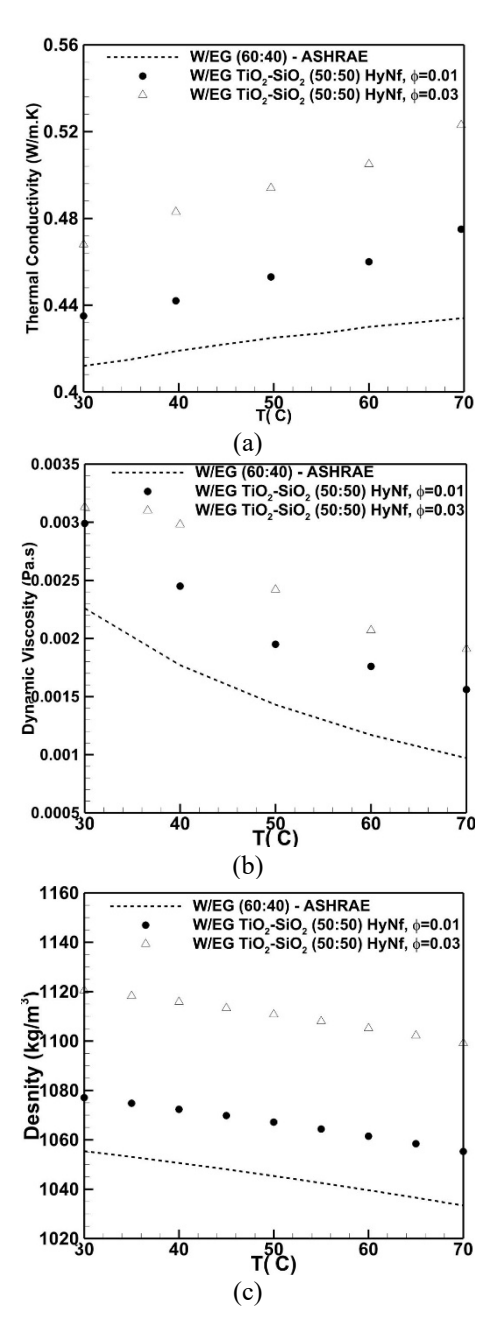
The incoming water/EG (with a volume ratio of 60-40%) mixture flow (with Pr_b =19.20 at T=303K) is 2D, steady-state, turbulent, fully developed, and incompressible. Considering the analysis of heat transfer in high Re number flows, the forced convection is assumed to be prevailing, and hence, the natural convection is disregarded. The working fluids are assumed to be single-phase and Newtonian fluids. The thermophysical properties of pure binary fluid and HyNf are defined as a function of temperature and NP volume fraction.

3.2 Thermophysical Properties of HyNf

In the present study, to get a clear understanding of the effects of hybrid NPs on the thermal performance of the binary mixture, the lab-scale experimental data of thermal conductivity and dynamic viscosity given by [18, 20] are implemented.

In Figure 2, the thermophysical properties for aqueous solutions of EG dispersed with TiO₂-SiO₂ hybrid NPs are given. Nabil et al. [18] measured the thermal conductivity

and dynamic viscosity of TiO2-SiO2 HyNf in a water/EG mixture (for concentrations $0.5 \le \phi \le 3.0\%$ and temperatures 30≤T≤80°C) using KD2 Pro Thermal Properties Analyser and Brookfield LVDV III Ultra Rheometer, respectively. The average diameters for TiO₂ and SiO₂ NPs were equal to 30-50nm and 22nm, respectively. The densities for TiO₂ and SiO₂ NPs were equal to 4230 and 2220 kg/m3, respectively. They studied HyNf in a base fluid mixture of distilled water and EG with a volume ratio of 60:40%. The HyNf was prepared by mixing both single NFs by a 50:50% (TiO2:SiO2) volume ratio. The TiO2-SiO2 HyNf were subjected to the process of mixing by using a magnetic stirrer and sonification. They validated the thermal conductivity and dynamic viscosity measurements of water/EG (60:40) mixture against ASHRAE [11]. Regarding the thermal conductivity of the aqueous solution of EG, the maximum deviation was found to be 1.6% (the measurement was reliable). The viscosity data were also in good agreement with the data from ASHRAE [11]. It showed that the dynamic viscosity declined with the increase of temperature.



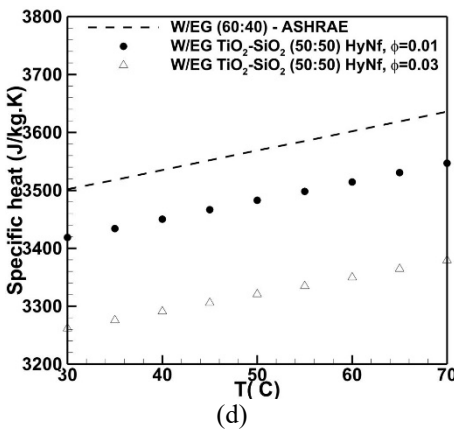


Figure 2. Thermal conductivity (a), dynamic viscosity (b), density (c), and specific heat (d) for aqueous solutions of EG with/without TiO₂-SiO₂ hybrid NPs.

The thermal conductivity of water/EG mixture-based TiO2-SiO2 HyNf improved with increasing concentration and temperature. Compared to the pure mixture, the maximum enhancement (22.8%) was found at a concentration of ϕ =3.0% and a temperature of T=80°C. The collision of hybrid NPs occurred at a higher rate at higher temperatures, thus transporting more kinetic energy and resulting in improved thermal conductivity. The higher concentration of HyNf and the greater number of NPs dispersed in the base mixture resulted in the augmentation of the surface-to-volume ratio and collisions between NPs. This effect was also due to the Brownian motion of NPs in the base fluid. The dynamic viscosity of HyNF was higher than the base mixture, and it amplified with the NP concentration. It was due to the augmentation in the fluid internal shear stress when hybrid NPs were added to the base mixture.

At higher concentrations (ϕ =3.0%), the enhancement in dynamic viscosity concerning NP concentration was much higher than the base mixture. The interaction between hybrid NPs and base fluid (water/EG) also contributed to the greater augmentation compared to single NF. The viscosity of HyNF followed the base mixture trend, which diminished with the increment of the temperature. The intermolecular interactions between molecules became weaker when the temperature rises, and therefore, reducing the dynamic viscosity. The viscosity ratio was enhanced with the rising NP concentration. Nevertheless, it was slightly changed with temperature (small fluctuations).

The lowest average value of the relative viscosity (with a percentage increase of 25.9%) was obtained for ϕ =0.5%. Besides, the highest average value of the relative viscosity (with a 62.5% increment) was achieved for ϕ =3.0%. The maximum value of the relative viscosity was observed for ϕ =3.0% at a temperature of T=80°C. In general, the relative viscosity within the present range of ϕ and temperature increased from 21.3% to 80.0% compared to the mixture. The fluctuation of the relative viscosity in the temperature range (30°C \leq T<80°C) was not well understood. Nonetheless, this outcome was due to the difference in structure and thickness of the diffused fluid layers around NPs in the base mixture, which influenced the effective concentration and viscosity of the suspension.

The effective density and heat capacity of water/EG mixture-based TiO₂-SiO₂ HyNf at a reference temperature were acquired via the following expressions:

$$\rho_{hnf} = (1.0 - \phi)\rho_{bf} + \phi\rho_{hnp} \tag{1}$$

$$\left(\rho c_p\right)_{hnf} = (1.0 - \phi)\left(\rho c_p\right)_{hf} + \phi\left(\rho c_p\right)_{hnn} \tag{2}$$

3.3 Governing Equations

The single-phase turbulent forced convection heat transfer of HyNf is solved by the Reynolds-Averaged Navier-Stokes (RANS) equations. The time-averaged velocity, pressure, and temperature fields are resolved. The Reynolds stresses are estimated by the eddy viscosity models. These models apply the turbulent viscosity for relating the turbulent stresses and heat fluxes to the mean strain rate. Furthermore, the radiation heat transfer and heat generation are assumed to be insignificant.

Regarding the above assumptions, the time-averaged mass, momentum, and energy conservation equations can be written as [24-27],

$$\frac{\partial \bar{u}}{\partial x} + \frac{\partial \bar{v}}{\partial y} = 0 \tag{3}$$

$$\rho_{hnf}\left(\bar{u}\,\frac{\partial\bar{u}}{\partial x}+\bar{v}\,\frac{\partial\bar{u}}{\partial y}\right)=-\frac{\partial\bar{v}}{\partial x}+\left[\left(\mu_{hnf}+\mu_{t}\right)\left(\frac{\partial^{2}\bar{u}}{\partial x^{2}}+\frac{\partial^{2}\bar{u}}{\partial y^{2}}\right)\right]\ (4)$$

$$\rho_{hnf}\left(\bar{u}\frac{\partial\bar{v}}{\partial x} + \bar{v}\frac{\partial\bar{v}}{\partial y}\right) = -\frac{\partial\bar{v}}{\partial y} + \left[\left(\mu_{hnf} + \mu_{t}\right)\left(\frac{\partial^{2}\bar{v}}{\partial x^{2}} + \frac{\partial^{2}\bar{v}}{\partial y^{2}}\right)\right] \tag{5}$$

$$\begin{split} \rho_{hnf} \left(c_p \right)_{hnf} \left(\overline{u} \, \frac{\partial \overline{T}}{\partial x} + \overline{v} \, \frac{\partial \overline{T}}{\partial y} \right) &= \left(k_{hnf} \, + \right. \\ \left. \frac{\left(c_p \right)_{hnf} \times \mu_t}{Pr_t} \right) \left(\frac{\partial^2 \overline{T}}{\partial x^2} + \frac{\partial^2 \overline{T}}{\partial y^2} \right) \end{split} \tag{6}$$

3.4 Turbulence Modeling

The standard SST $k-\omega$ model [28-29] utilizes the effectiveness of Wilcox $k-\omega$ and $k-\epsilon$ models at favorable regimes (near solid walls and in the freestream).

As Araujo and Rezende [30] emphasized, the SST k- ω model (as a RANS turbulence model) is recommended for cases with adverse pressure gradient and flow separation. This model presents a better treatment in the near-wall regions compared to other RANS models.

Sekrani et al. [31] clarified that the SST k- ω model gave the most precise estimates for both the Nu number and the friction factor.

Jehad et al. [32] analyzed the turbulent flow over the BFS with three turbulence models called the standard k- ϵ , realizable k- ϵ and SST k- ω . They found that the SST k- ω model exhibited a satisfactory agreement against experimental data given by [33] in terms of the size of the reattachment zone.

Nevertheless, interestingly, the SST k- ω model performs poorly in calculating the turbulence intensity and shear stress in the recirculation region (underestimating the eddy viscosity compared to experimental data).

In OpenFOAM package [34], the production limiter is added in the standard SST k- ω model. In OpenFOAM, the transport equations for the turbulent kinetic energy (TKE) and specific dissipation rate are given as [35-36]:

$$\frac{\partial}{\partial x_i}(\rho k u_i) = \frac{\partial}{\partial x_i} \left[(\mu + \sigma_k \mu_t) \frac{\partial k}{\partial x_i} \right] + P_k - \beta^* \rho k \omega \tag{7}$$

$$\frac{\partial}{\partial x_{i}}(\rho\omega u_{i}) = \frac{\partial}{\partial x_{i}}\left[(\mu + \sigma_{\omega}\mu_{t}).\frac{\partial\omega}{\partial x_{i}}\right] + \frac{\gamma\rho}{\mu_{t}}P_{k} - \beta\rho\omega^{2} + 2(1 - F_{1})\frac{\rho\sigma_{\omega 2}}{\omega}\frac{\partial k}{\partial x_{i}}\frac{\partial\omega}{\partial x_{i}}$$
(8)

$$P_{k} = \tau_{ij} \frac{\partial u_{i}}{\partial x_{i}} = \left[\mu_{t} \left(2S_{ij} - \frac{2}{3} \frac{\partial u_{k}}{\partial x_{k}} \delta_{ij} \right) - \frac{2}{3} \rho k \delta_{ij} \right] \frac{\partial u_{i}}{\partial x_{i}}$$
(9)

$$F_1 = \tan h(\Phi_1^4), \qquad F_2 = \tan h(\Phi_2^2)$$
 (10)

$$\Phi_{1} = min \left[max \left(\frac{\sqrt{k}}{\beta^{*} \omega y}, \frac{500 \mu}{\rho y^{2} \omega} \right), \frac{4\rho \sigma_{\omega 2} k}{CD_{k\omega} y^{2}} \right]$$
 (11)

$$CD_{k\omega} = max \left(2\rho \frac{\sigma_{\omega 2}}{\omega} \frac{\partial k}{\partial x_i} \frac{\partial \omega}{\partial x_i}, 10^{-10} \right)$$
 (12)

$$\Phi_2 = max\left(\frac{2\sqrt{k}}{\beta^*\omega y}, \frac{500\nu}{y^2\omega}\right) \tag{13}$$

$$\mu_t = \frac{\rho a_1 k}{\max(a_1 \omega, F_2 S)}, \quad S = \sqrt{S_{ij} S_{ij}}, \quad S_{ij} = \frac{1}{2} \left(\frac{\partial u_i}{\partial x_j} + \frac{\partial u_j}{\partial x_i} \right) \quad (14)$$

The empirical constant χ is evaluated based on,

$$\chi = \chi_1 F_1 + \chi_2 (1 - F_1) \tag{15}$$

Keep in mind that χ_1 and χ_2 are extracted from k-ω and k-ε models, respectively. Also, all is a constant and estimated experimentally (0.31), F_2 is the blending (damping) function. The values of constants for the SST k-ω model were provided by Torabi et al. [24].

4. Flow and Heat Transfer Characteristics

In this study, the inlet channel height-based Re number is defined as,

$$Re = \frac{\rho_{hnf} \times U_0 \times H}{\mu_{hnf}} \tag{16}$$

The surface Nu number on the heated surfaces and ANN along the cavity walls are calculated to present the convective performance of coolant,

$$Nu = \frac{h_{hnf} \times H}{k_{hf}} \tag{17}$$

$$ANN_{cavity\ flow} = ANN_{BFS1} + ANN_{BFS2} + ANN_{FFS1} + \\ ANN_{FFS2} + ANN_{lowerwall1} + ANN_{lowerwall2} + \\ ANN_{lowerwall3}$$
 (18)

For the single-phase turbulent forced convection flow, the friction factor is estimated by,

$$f = \frac{2\Delta P}{\rho_{hnf} \times U_0^2} \times \frac{H}{(3 \times L)} \tag{19}$$

The FOM is characterized as the ratio between Mouromtseff (*Mo*) numbers of HyNF and pure mixture as,

$$FOM = \frac{Mo_{hnf}}{Mo_{bf}} = \frac{\rho_{hnf}^{0.8} k_{hnf}^{0.6} c_{p,hnf}^{0.4}}{\mu_{hnf}^{0.4}} \times \frac{\mu_{bf}^{0.4}}{\rho_{bf}^{0.8} k_{bf}^{0.6} c_{p,bf}^{0.4}}$$
(20)

In this study, the PEC_{baffle} and PEC_{hnf} characterizes the influences of adiabatic baffles and concentration of HyNf, respectively.

Keep in mind that *PEC*_{tot} designates the ratio of the Nu number of HyNf in U-shaped cavity flow equipped with baffles to that of the pure mixture (binary fluid) in the U-shaped cavity flow without baffles divided by the ratio of the

friction factor of HyNf in the cavity flow with baffles to that of the pure mixture in the cavity flow without baffles,

$$PEC_{baffle} = \frac{\frac{Nu_{baffle}}{Nu_{no\ baffle}}|_{\phi = const}}{\left[\frac{f_{baffle}}{f_{no\ baffle}}\right]_{\phi = const}^{\frac{1}{3}}}$$

$$\phi = const$$
(21)

$$PEC_{hnf} = \frac{\frac{Nu_{hnf}}{Nu_{bf}}\Big|_{baffle,no\ baffle}}{\left[\frac{f_{hnf}}{f_{bf}}\right]^{\frac{1}{3}}}\Big|_{baffle,no\ baffle}$$
(22)

$$PEC_{tot} = \frac{\frac{Nu_{hnf,baffle}}{Nu_{bf,no\ baffle}}}{\left[\frac{f_{hnf,baffle}}{f_{bf,no\ baffle}}\right]^{\frac{1}{3}}}$$
(23)

It must be emphasized that when $PEC_{np}>1.0$, the HyNf is preferred compared to the pure base mixture in U-shaped cavity flows with/without adiabatic baffles.

5. Numerical Result and Discussion5.1 Grid Independence and Solution

All 2D numerical simulations have been performed on a desktop PC with a CPU Intel(R) Core i5, 2.9 GHz, and 24.00 GB of RAM. The aforementioned governing equations and the turbulence model are solved via the open-source code OpenFOAM. It is a free-source CFD package providing C++ codes. The existing computational modules permit the user to accomplish the desired objectives effectively. The library blockMeshDict is used to create the mesh, and the solver buoyantSimpleFoam is applied in simulations.

In the object file fvSolution, the values for the residualControl and relaxationFactors are equal to 10^{-7} and 0.4, respectively. Additionally, in the object file fvSchemes, divSchemes is selected as bounded Gauss upwind. At the walls including the downward-facing cavity and an upward-facing cavity, wall functions are used for each turbulence variable. For the TKE, kqRWallFunction is applied. It is a zero-gradient BC. For the specific dissipation rate, omegaWallFunction is used.

For the pure aqueous solution of EG in the cavity flow without baffles at Re=5000, three mesh sizes (excluding the inlet and outlet regions) with the mesh refinement close to cavity walls are selected: 23360, 52560, and 118260. For the mesh size equal to 52560, the SIMPLE solution converges in 55696 iterations, and the execution time is approximately 37.06 hours. After performing command foamLog, the final values for U_x and U_y are 6.91×10^{-9} and 9.75×10^{-8} , respectively. Besides, the maximum value of y^+ for the three lower walls and steps (FFS or BFS) is equal to 3.61×10^{-2} and 1.73, respectively.

As the mesh size enlarges from 23360 to 52560, the total ANN increases by 1.69%. When the fine grid is applied, the value of total ANN decreases by 0.84% compared to the medium size of the mesh. Also, the values of Nu_{max} on the first and third floors of the cavity reduce by 1.3% and 7%, respectively. However, the execution time is enhanced by more than 60%. So, the medium size of the grid is selected for the computational domain in this paper. The mesh refinement study was performed after a careful examination

of the large eddy simulation (LES) findings of the turbulent flow over a BFS given by Akselvoll and Moin [37]. Mesh refinements close to solid walls were visualized in my previous work [38].

5.2 Model Validation

Xie and Xi [39] investigated the geometry effect (changeable bottom wall length and step height) on fluid flow and heat transfer characteristics over a single backwardforward facing pair at Re=700 using the direct numerical simulation (DNS). The temperature of the bottom wall is constant (T_h =313K), while the walls of the horizontal channel are thermally insulated. The air flow (Pr=0.71) at the inflow opening was fully developed for U (as the streamwise velocity) with a uniform temperature (T_0 =283K). The number of computational cells in the cavity flow is equal to 36000. To validate the time-mean surface Nu number (SNN) along the bottom wall inside the cavity, the following case is selected: the inlet channel height is equal to the step height h=0.015m, and the bottom wall length is fixed as 14×h. An acceptable agreement between the present results and the ones given by [39] is obtained in Figure 3.

Abdellahoum et al. [40] and Abdellahoum and Mataoui [41] numerically evaluated the turbulent forced convection of various NFs (consisting of Cu, CuO, Ag, and Al₂O₃ NPs with $0.0 \le \phi \le 0.2$ in water) over a heated shallow cavity in a horizontal channel at $4 \times 10^4 \le Re \le 10^5$.

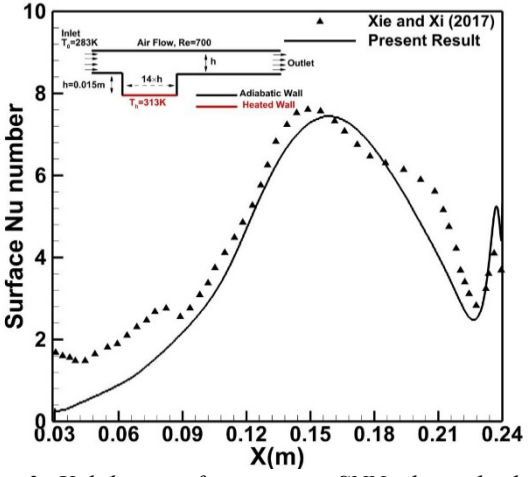


Figure 3. Validation of time-mean SNN along the bottom wall of cavity for the air flow against Xie and Xi [39].

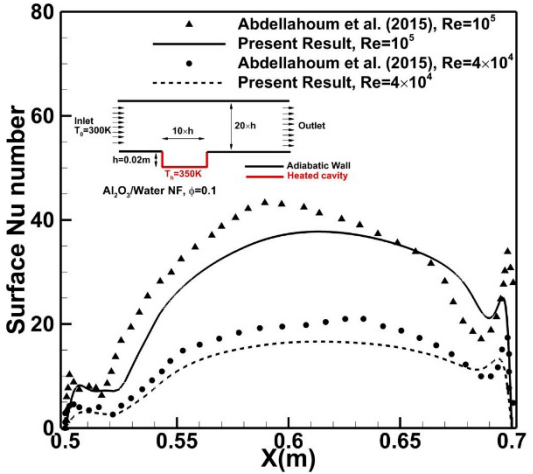


Figure 4. Validation of SNN along the bottom surface of cavity for the single NF flow against Abdellahoum et al. [40].

In Figure 4, the 2D computational domain as the second validation case is illustrated. The length of the upstream section is equal to $25 \times h$, and the length of the horizontal channel in the downstream section and the height of the channel (in the vertical direction) is equal to $55 \times h$ and $20 \times h$, respectively. The aspect ratio (AR_c) between the width and height of the rectangular cavity is equal to 10.0, and hence, the elongated cavity is a backward/forward-facing step pair. The cavity walls are heated at a constant temperature T_h =350K while the other walls are adiabatic. At the inlet of the computational domain, fixed values are enforced as velocity components U= U_0 , V=0, and ambient temperature (T_0 =300K).

For the closure of governing equations of fluid flow and heat transfer, the SST k- ω model in the single-phase framework was implemented. The thermophysical properties of all NFs were presumed to be fixed, and they are given in Table 1 for Al₂O₃/water NF. The dynamic viscosity and thermal conductivity of NFs (as a dilute suspension of small spherical particles in a base fluid) were calculated using the Brinkman and Maxwell-Garnett (MG) models, respectively. The effective density and heat capacity of NFs were acquired at a reference temperature using the Pak and Cho correlation and thermal equilibrium model, respectively.

Table 1. Thermophysical properties of alumina/water NF with $\phi = 0.1$ ($Pr_{rr} = 5.6$).

Property	Value	
Specific heat [j/kg.K]	3131.89828	
Density [kg/m³]	1294.39	
Dynamic viscosity [kg/m.s]	0.00130525	
Thermal conductivity [W/m.K]	0.80725567	

In Figure 4, the value of SNN along the cavity bottom is compared against [40-41], and a satisfactory agreement is achieved. The mesh size in the cavity flow is equal to 19200. It confirms that the increase of Re number enhances the heat transfer for ϕ =0.1. Abdellahoum and Mataoui [41] also emphasized that the increment of NP volume fraction improved the heat transfer (the sum of average Nu number on heated surfaces) moderately and linearly. Unfortunately, researchers [40-41] did not examine how the theoretical values for the NF thermophysical properties may affect the accuracy of numerical results.

5.3 Aqueous Solutions of EG Without Hybrid NPs

The investigation of the effects of adiabatic baffles on the fluid dynamics and heat transfer is of great importance in various engineering domains. The presence of baffles in cavity flows may modify the flow structures significantly. As revealed by Ma et al. [5], when the length of adiabatic baffles augments, the size of the recirculation region downstream of the BFS diminishes.

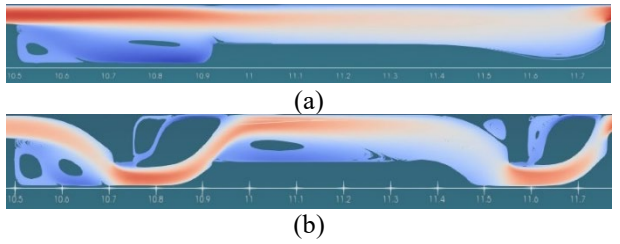


Figure 5. Streamlines for the pure mixture in the cavity flow without baffles (a), with elongated baffles (b)

In Figure 5, for the pure binary fluid flow at U_0 =0.1 m/s, the streamlines in the cavity flow with/without elongated baffles are given.

In the absence of any baffles, a main clockwise recirculating eddy and a secondary counterclockwise one at the left bottom corner are created over the first floor of the cavity. The presence of baffles plays a crucial role in minimizing the encapsulating phenomenon [2]. Baffles may direct the cold fluid throughout the beneath of the U-shaped cavity (inner cavity region).

Adding baffles maximizes the interaction between the incoming fluid flow and cavity walls while reducing the sizes of both recirculating eddies. Additionally, the above arrangement of baffles generates one recirculating eddy (as a negative outcome) over the middle floor of the cavity. The turbulent flow passing over the first trailing edge of the U-shaped cavity impinges on the top wall. As confirmed by Mesalhy et al. [3], this eddy creates an insulation effect on the heat transfer from the second floor of the U-shaped cavity.

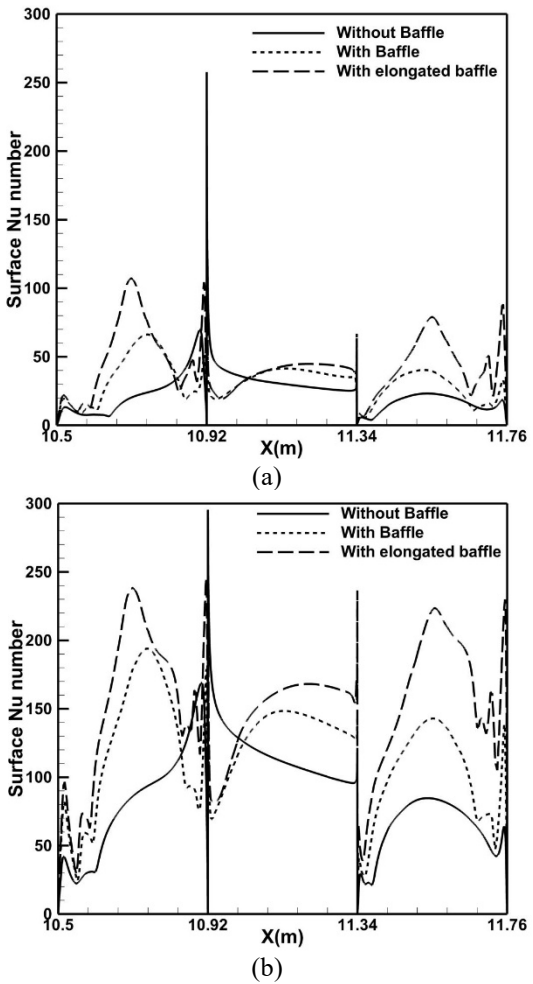


Figure 6. Effect of adiabatic baffles on the value of SNN over bottom walls for the pure mixture (without hybrid NPs) at $U_0=0.1$ m/s (a), and $U_0=0.6$ m/s (b).

In Figure 6, for the pure mixture, the effects of adiabatic baffles and Re number on the SNN at the cavity floors are illustrated. Consistent with Zdanski et al. [2], for low Re numbers, the heat dissipation by the convection from the cavity floor is possibly low. Increasing the Re number promotes the cooling system (mixing of hot and cold fluids) and enhances the heat dissipation.

As indicated by Zdanski et al. [42], most of the heat flux (89%) coming from the cavity floor is pumped by the turbulent diffusion. It is influential on the mechanism of the heat transfer at the cavity floor. When adiabatic baffles are installed, the impact of the externally cold binary fluid on the cavity dynamics increases significantly, and the value of SNN enhances. The distribution of the SNN shows that the peak values of the heat flux at the cavity floor are intensified due to the presence of baffles.

As can be detected, the presence of baffles considerably enhances the SNN over two floors of the U-shaped cavity. However, due to the redirected flow over the first trailing edge of the cavity, the SNN over the middle floor is initially decreased compared to the case without adiabatic baffles.

For the pure mixture, the variations of ANN with the Re number are displayed in Figure 7a. At Re=5000, adding baffles with a length equal to h=0.042m enhances the value of ANN by 47% compared to the case without baffles. At Re=30000, due to the presence of these baffles, the value of ANN augments by 35%. At Re=5000 and 30000, using elongated baffles (with a length equal to 2×h) increases the value of ANN by 87% and 67%, respectively, in contrast to the case without baffles.

As Navaneethakrishnan and Muthtamilselvan [6] discussed, using baffles with a shorter length engenders a lesser disturbance compared to elongated baffles. Hence, the mainstream channel flow is less affected, and the fluid mixing is diminished, resulting in lower heat transfer rates. When elongated baffles are introduced, the channel flow is further forced downward toward the cavity floor, and hence, the fluid mixing is boosted.

As can be seen, when the Re number increases, the presence of adiabatic baffles becomes less effective in improving the heat transfer capability of the binary fluid.

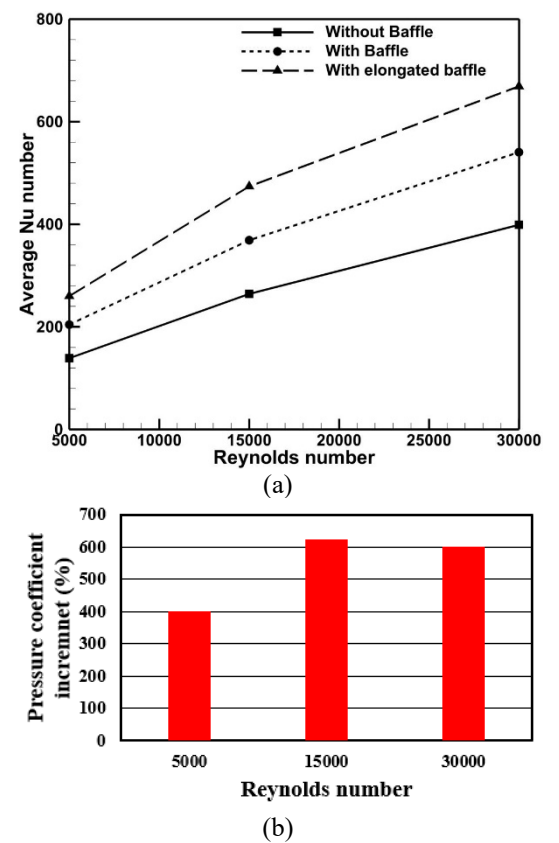


Figure 7. Variations of the ANN with the Re number for the pure binary fluid (a) and percentage of pressure coefficient increment due to the presence of elongated baffles (b).

The pressure coefficient in the horizontal channel-driven U-shaped cavity flow is defined as,

$$C_{p,hnf} = 2.0 \times (P_{inlet,ave} - P_{outlet,ave})$$

$$P_{inlet,ave} = \frac{1}{H} \times \int_{0}^{H} P_{inlet} dy \quad P_{outlet,ave}$$

$$= \frac{1}{H} \times \int_{0}^{H} P_{outlet} dy$$

$$(25)$$

Interestingly, Figure 7b corroborates that adding elongated baffles to the top wall significantly augments the pressure coefficient compared to the plain U-shaped cavity flow (without baffle) particularly at higher *Re* number.

5.4 Effect of NP Concentration and Mixing Ratio

The effects of the NP concentration on the value of ANN along all cavity walls are provided in Figure 8. Dispersing hybrid NPs with ϕ =0.01 in the binary mixture reduces the value of ANN. The heat transfer capability of the U-shaped cavity flow is weakened.

For example, at U_0 =0.6 m/s, in the absence of baffles, the value of ANN declines by 14% using TiO_2 - SiO_2 (mixing ratio 50:50%) HyNf with ϕ =0.01 compared to the pure mixture. It implies that HyNf with a mixing ratio of 50:50% is not a good heat transfer fluid, and it is contrary to the outcome reported by Nabil et al. [18]. Adding more NPs (ϕ =0.03) weakens the heat transfer capability of the binary mixture insignificantly (around 5%) compared to the case with ϕ =0.01.

According to Mehrez et al. [10], adding NPs to the pure mixture alters the flow behavior (reducing the flow intensity) and enlarges the thickness of TBL. More importantly, it is observed that the unfavorable effect due to dispersing NPs (reduction of ANN) intensifies as the incoming flow becomes more turbulent.

For the pure mixture and HyNf, the variations of the PEC_{baffle} with the reference velocity (velocity of the incoming flow) are included in Figure 9.

Adding smaller baffles to the top side of the cavity flow is always advantageous ($PEC_{baffle} > 1.0$) at all reference velocities. However, the substitution of the plain cavity flow with the cavity equipped with elongated baffles is only recommended at lower inlet velocity (0.1).

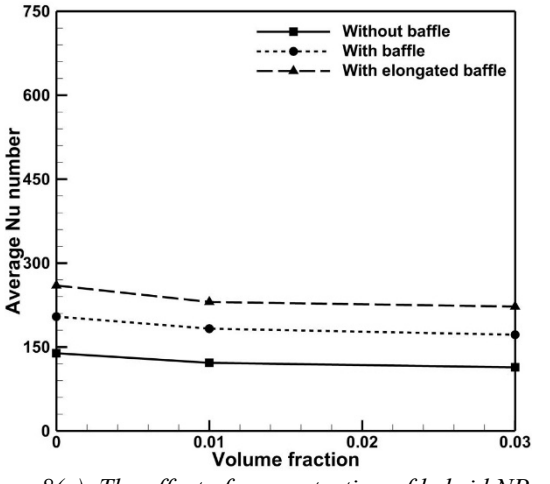


Figure 8(a). The effect of concentration of hybrid NPs on the ANN along all cavity walls at U_0 =0.1 m/s.

The negative impact (pressure drop penalty) due to elongated baffles exceeds the positive effect (improved convection) at higher Re numbers. For the cavity flow with/without baffles, the effects of hybrid NPs on the thermo-hydrodynamic performance (represented by PEC_{nf}) of the system are shown in Figure 10. It is realized that for $0.01 \le \phi \le 0.03$, the addition of hybrid TiO₂-SiO₂ NPs with the mixing ratio 50:50% is not beneficial.

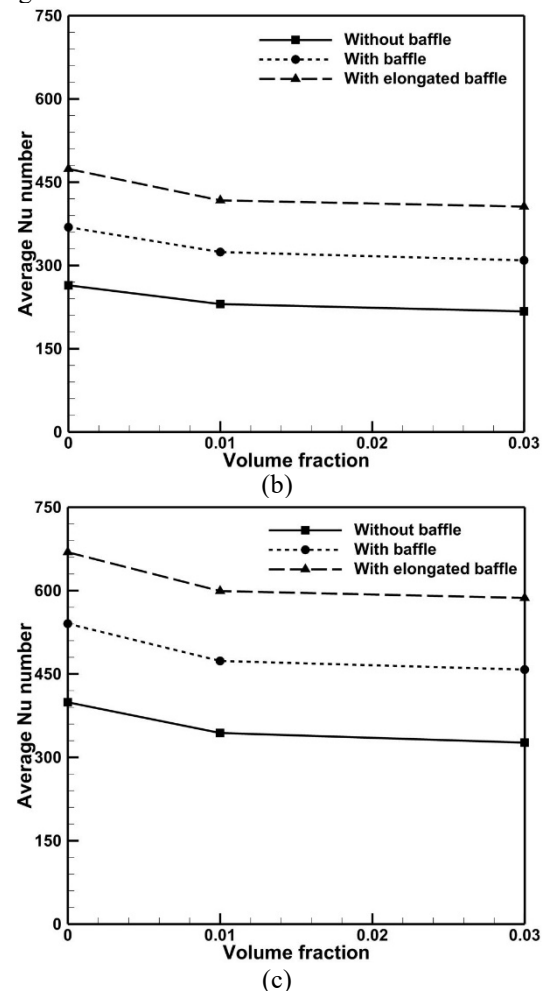


Figure 8. The effect of concentration of hybrid NPs on the ANN along all cavity walls at U_0 =0.3 m/s (b), and U_0 =0.6 m/s (c).

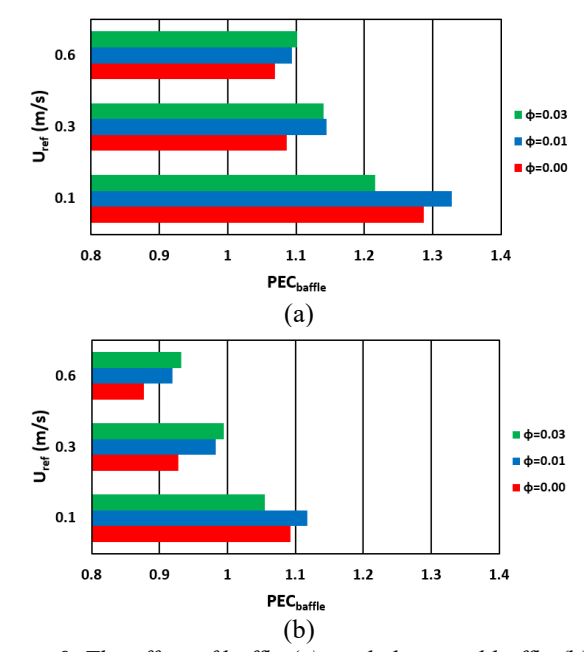


Figure 9. The effect of baffle (a), and elongated baffle (b) on the thermo-hydrodynamic performance of the cavity flow filled with pure mixture or HyNf.

Hamid et al. [20] stressed that the mixing ratio of 20:80% or 80:20% for hybrid NPs induces a PER less than 5.0, where the integrated augmentations in k and μ has more benefits in comparison with the equal ratio (50:50%). The performances of unequal ratios, such as 20:80% or 80:20% are evaluated in Table 2 in terms of the temperature-dependent figure-of-merit (FOM).

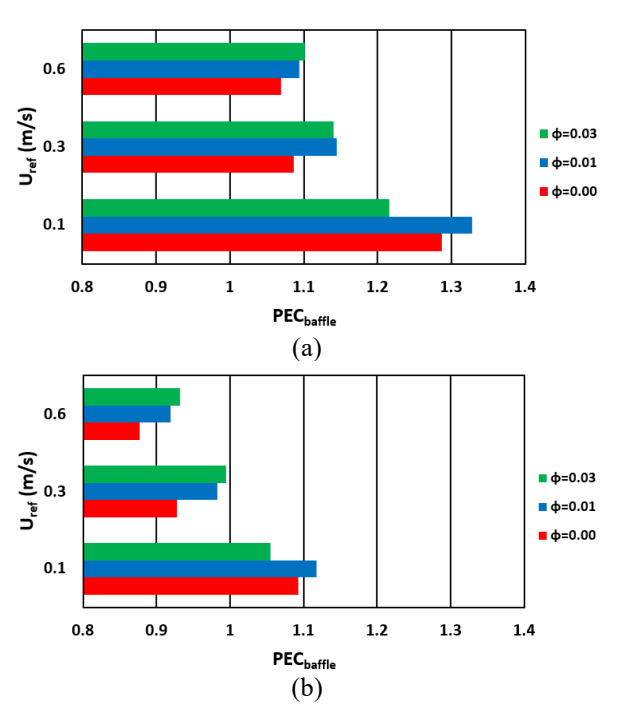


Figure 10. Replacement of the pure base fluid with HyNf at concentrations ϕ =0.01 (a), and ϕ =0.03 (b) in cavity flows with/without baffles.

Based on Hamid et al. [20], the mixing ratio of 20:80% gives the maximum enhancement of thermal conductivity (16%), whereas the ratio of 80:20% gives the least augmentation for the dynamic viscosity compared to other ratios.

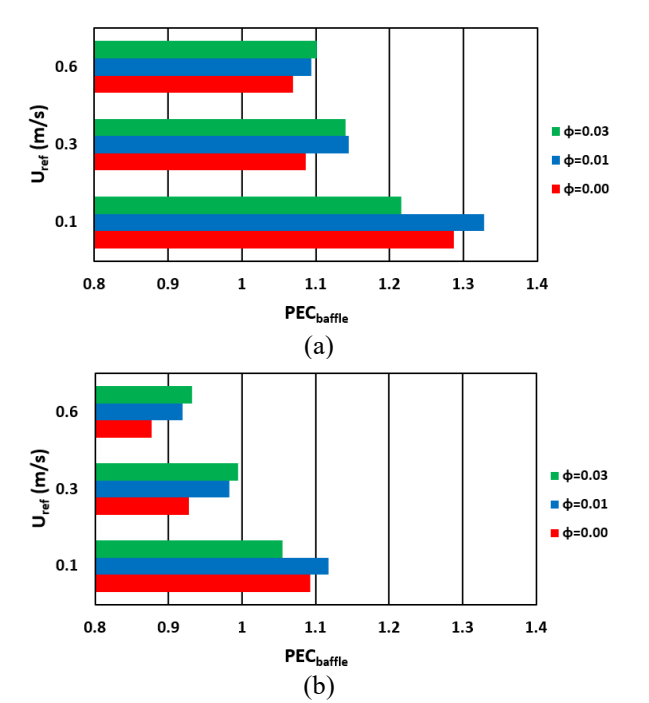


Figure 11. Variations of PEC_{tot} at various reference velocities.

I confirm that adding TiO₂-SiO₂ hybrid NPs (with unequal ratio) does not improve the heat transfer capability of the binary mixture. Minimizing the pressure drop through the trade-off between the shortcomings and benefits of individual NPs is not achieved here.

Table 2. Temperature-dependent variations of FOM for various mixing ratios of hybrid NPs at ϕ =0.01.

Temperature (K)	TiO ₂ -SiO ₂ (20:80%)	TiO ₂ -SiO ₂ (80:20%)
303	1.00	1.006
313	0.980	0.985
323	0.995	0.986
333	0.941	0.987
343	0.915	0.954

The outcomes of this investigation recommend some strategies for the thermal design of electronic devices where two adjacent cavities with asymmetrical walls [39] exist.

6. Conclusion

The heat transfer capability of the water/EG mixture in a 2D channel-driven U-shaped cavity flow, including a downward-facing cavity and an upward-facing cavity was assessed. Only the single-phase forced convection heat transfer was evaluated (the effect of natural convection within the shallow cavity was insignificant). The thermophysical properties for the aqueous solution of EG and HyNf are temperature-dependent. The available measurement data was used to acquire precise input property values in order to assess the thermal performance of HyNf. It was found that,

- (1) For the pure aqueous solution of EG, adding baffles significantly minimized the encapsulating phenomenon and enhanced the heat dissipation while it generated one recirculating eddy (as a negative outcome) over the middle floor of the cavity.
- (2) The more the velocity of the incoming flow increased, the less the presence of baffles became beneficial.
- (3) The substitution of the plain U-shaped cavity flow with the one equipped with elongated baffles was only permitted at a lower Re number.
- (4) The thermo-hydraulic performance of aqueous solution of EG was not enhanced in the presence of hybrid TiO₂-SiO₂ NPs (with equal/unequal ratio of 50:50%) in the aforementioned asymmetrical cavity flow.
- (5) Minimizing the pressure drop through the trade-off between the shortcomings and benefits of individual NPs in the binary fluid (water/EG solution) was not achieved.

Conflict of Interest

Dr. Mahmoud Jourabian approves that to the best of his knowledge, there is not any conflict of interest or common interest with an institution/organization or a person that may affect the review process of the paper.

Credit Author Statement

Mahmoud Jourabian: Writing - Original draft, Writing-Reviewing and Editing, Visualization, Conceptualization, Methodology, Software.

Nomenclature

 c_p Specific heat $[J/kg \cdot K]$ C_p Pressure coefficient $[N/m^2]$ F_1, F_2 Blending functions

f Friction factor

- H Inlet height [m]
- h Height of middle floor [m]
- k Turbulent kinetic energy $[m^2 \cdot s^{-2}]$
- k Thermal Conductivity $[Wm^{-1}K^{-1}]$
- L Length of cavity floor [m]
- Mo Mouromtseff number
- Nu Nusselt number
- P Pressure $[N/m^2]$
- Pr Prandtl number
- *Re* Reynolds number
- S_{ij} Strain rate tensor $[s^{-1}]$
- T Temperature [K]
- u, v Streamwise and vertical velocities [m/s]
- \bar{u} , \bar{v} Time-averaged velocities [m/s]
- U_0 Velocity of incoming flow [m/s]
- x, y Streamwise and vertical distance [m]
- y^+ Nondimensional distance from the wall

Greek symbols

- δ_{ij} Kronecker delta
- μ Dynamic viscosity [kg/ms]
- ν Kinematic viscosity $[m^2/s]$
- ρ Density $[kg/m^3]$
- ϕ Volume fraction of NPs
- $\chi_1 \chi_2$ Empirical constants
- ω Specific dissipation rate [s^{-1}]

Subscripts

- bf Base fluid
- nf Nanofluid
- *hnf* Hybrid nanofluid
- t Turbulent
- tot Total
- *i* Direction
- ave Average

Abbreviations

- ANN Average Nusselt number
- BC Boundary condition
- BFS Backward facing step
- BL Boundary layer
- CHT Convective heat transfer
- CNT Carbon nanotube
- DASC Direct absorption solar collectors
- DNS Direct numerical simulation
- EG Ethylene glycol
- FFS Forward facing step
- FOM Figure-of-merit
- HyNf Hybrid nanofluid
- LES Large eddy simulation
- MHD Magnetohydrodynamic MWCNT Multi-walled carbon nanotubes
- NF Nanofluid
- NP Nanoparticles
- PEC Performance evaluation criterion

References:

- [1] S. N. Sinha, A. K. Gupta, and M. M. Oberai, "Laminar separating flow over backsteps and cavities, Part ii: cavities," *AIAA Journal*, vol. 20, no. 3, pp. 370-375, Mar. 1982, doi: 10.2514/3.7918.
- [2] P. S. B. Zdanski, M. A. Ortega, and N. G. C. R. Fico, "Numerical study of the flow over shallow cavities," *Computers & Fluids*, vol. 32, no. 7, pp. 953-974, Aug. 2003, doi: 10.1016/S0045-7930(02)00067-1.

- [3] O. Mesalhy, S. S. A. Aziz, M. M. El-Sayed, "Flow and heat transfer over shallow cavities," *International Journal of Thermal Sciences*, vol. 49, no. 3, pp. 514-521, Mar. 2010, doi: 10.1016/j.ijthermalsci.2009.09.007.
- [4] C. Ozalp, A. Pinarbasi, and B. Sahin, "Experimental measurement of flow past cavities of different shapes," *Experimental Thermal and Fluid Science*, vol. 34, no. 5, pp. 505-515, July 2010, doi: 10.1016/j.expthermflusci.2009.11.003.
- [5] Y. Ma, R. Mohebbi, M. M. Rashidi, Z. Yang, and Y. Fang, "Baffle and geometry effects on nanofluid forced convection over forward- and backward-facing steps channel by means of lattice Boltzmann method," *Physica A: Statistical Mechanics and its Applications*, vol. 554, Sept. 2020, Art. no. 124696, doi: 10.1016/j.physa.2020.124696.
- [6] V. Navaneethakrishnan and M. Muthtamilselvan, "Thermal analysis of magnetohydrodynamic mixed convection in vented channel-driven cavity with corner heater: influence of adiabatic rod and flow parameters," *Journal of Thermal Analysis and Calorimetry*, vol. 149, no. 11, pp. 5755–5770, June 2024, doi: 10.1007/s10973-024-13117-4
- [7] S. Nouraei et al., "Heat transfer and entropy analysis for nanofluid flow in a semi-circular open cavity under mixed convection," Alexandria Engineering Journal, vol. 64, pp. 309–334, Feb. 2023, doi: 10.1016/j.aej.2022.09.007
- [8] S.M. Aminossadati, and B. Ghasemi, "A numerical study of mixed convection in a horizontal channel with a discrete heat source in an open cavity," *European Journal of Mechanics B/Fluids*, vol. 28, no. 4, pp. 590-598, 2009, doi: 10.1016/j.euromechflu.2009.01.001.
- [9] O. Manca, S. Nardini, K. Khanafer, and K. Vafai, "Effect of heated wall position on mixed convection in a channel with an open cavity," *Numerical Heat Transfer, Part A: Applications*, vol. 43, no. 3, pp. 259-282, 2003, doi: 10.1080/10407780307310.
- [10] Z. Mehrez, M. Bouterra, A.E. Cafsi, and A. Belghith, "Heat transfer and entropy generation analysis of nanofluids flow in an open cavity," *Computers & Fluids*, vol. 88, pp. 363-373, Dec. 2013, doi: 10.1016/j.compfluid.2013.09.026.
- [11] ASHRAE Handbook Fundamentals (SI Edition), American Society of Heating, Refrigerating and Air-Conditioning Engineers, Inc., Atlanta, 2009.
- [12] X. Xu, C. Xu, J. Liu, X. Fang, and Z. Zhang, "A direct absorption solar collector based on a water-ethylene glycol based nanofluid with anti-freeze property and excellent dispersion stability," *Renewable Energy*, vol. 133, pp. 760-769, Apr. 2019, doi: 10.1016/j.renene.2018.10.073.
- [13] S. M. Peyghambarzadeh, S. H. Hashemabadi, S.M. Hoseini, and M. S. Jamnani, "Experimental study of heat transfer enhancement using water/ethylene glycol based nanofluids as a new coolant for car radiators," *International Communications in Heat and Mass Transfer*, vol. 38, no. 9, pp. 1283-1290, Nov. 2011, doi: 10.1016/j.icheatmasstransfer.2011.07.001.

- [14] T. Yiamsawas, O. Mahian, A. S. Dalkilic, S. Kaewnai, and S. Wongwises, "Experimental studies on the viscosity of TiO₂ and Al₂O₃ nanoparticles suspended in a mixture of ethylene glycol and water for high temperature applications," *Applied Energy*, vol. 111, pp. 40-45, Nov. 2013, doi: 10.1016/j.apenergy.2013.04.068.
- [15] V. Kumaresan, and R. Velraj, "Experimental investigation of the thermo-physical properties of water-ethylene glycol mixture based CNT nanofluids," *Thermochimica Acta*, vol. 545, 180-186, Oct. 2012. doi: 10.1016/j.tca.2012.07.017.
- [16] L. S. Sundar, M. K. Singh, and A. C. Sousa, "Thermal conductivity of ethylene glycol and water mixture based Fe₃O₄ nanofluid," *International Communications in Heat and Mass Transfer*, vol. 49, pp. 17-24, Dec. 2013, doi: 10.1016/j.icheatmasstransfer.2013.08.026.
- [17] B. A. Bhanvase, M. R. Sarode, L. A. Putterwar, A. K. A., M. P. Deosarkar, and S. H. Sonawane, "Intensification of convective heat transfer in water/ethylene glycol-based nanofluids containing TiO₂ nanoparticles," *Chemical Engineering and Processing: Process Intensification*, vol. 82, pp. 123-131, Aug. 2014, doi: 10.1016/j.cep.2014.06.009.
- [18] M. F. Nabil, W. H. Azmi, K. A. Hamid, R. Mamat, and F. Y. Hagos, "An experimental study on the thermal conductivity and dynamic viscosity of TiO₂-SiO₂ nanofluids in water: ethylene glycol mixture," *International Communications in Heat and Mass Transfer*, vol. 86, pp. 181-189, Aug. 2017, doi: 10.1016/j.icheatmasstransfer.2017.05.024.
- [19] M. Michael, A. Zagabathuni, S. Ghosh, and S. K. Pabi, "Thermo-physical properties of pure ethylene glycol and water—ethylene glycol mixture-based boron nitride nanofluids: an experimental investigation," *Journal of Thermal Analysis and Calorimetry*, vol. 137, no. 2, pp. 369-380, 2019, doi: 10.1007/s10973-018-7965-5.
- [20] K. A. Hamid, W. H. Azmi, M. F. Nabil, R. Mamat, and K. V. Sharma, "Experimental investigation of thermal conductivity and dynamic viscosity on nanoparticle mixture ratios of TiO₂-SiO₂ nanofluids," *International Journal of Heat and Mass Transfer*, vol. 116, pp. 1143-1152, Jan. 2018, doi: 10.1016/j.ijheatmasstransfer.2017.09.087.
- [21] S. S. S. Sen, R. Mahato, S. Shaw, and M. Das, "Simulation of entropy and heat and mass transfer in Water-EG based hybrid nanoliquid flow with MHD and nonlinear radiation," *Numerical Heat Transfer, Part A: Applications*, vol. 85, no. 19, pp. 3253–3267, Oct. 2024, doi: 10.1080/10407782.2023.2233736.
- [22] W. H. Azmi, K. A. Hamid, N. A. Usri, R. Mamat, and K. V. Sharma, "Heat transfer augmentation of ethylene glycol: water nanofluids and applications A review," *International Communications in Heat and Mass Transfer*, vol. 75, pp. 13–23, July 2016, doi: 10.1016/j.icheatmasstransfer.2016.03.018.
- [23] R. Shi, J. Lin, and H. Yang, "Particle Distribution and Heat Transfer of SiO2/Water Nanofluid in the Turbulent Tube Flow," *Nanomaterials*, vol. 12, no. 16, p. 2803, Aug. 2022, doi: 10.3390/nano12162803.

- [24] M. Torabi, M. Torabi, M. E. Yazdi, and G. P. Peterson, "Fluid flow, heat transfer and entropy generation analyses of turbulent forced convection through isotropic porous media using RANS models," *International Journal of Heat and Mass Transfer*, vol. 132, pp. 443–461, Apr. 2019, doi: 10.1016/j.ijheatmasstransfer.2018.12.020.
- [25] F. Iachachene, Z. Haddad, M. Arıcı, M. Jamei, and A. Mataoui, "Turbulent forced convective flow in a conical diffuser: Hybrid and single nanofluids," *Engineering Analysis with Boundary Elements*, vol. 148, pp. 205–219, Mar. 2023, doi: 10.1016/j.enganabound.2022.12.027.
- [26] N. Al-Zurfi, A. Alhusseny, and A. Nasser, "Effect of rotation on forced convection in wavy wall channels," *International Journal of Heat and Mass Transfer*, vol. 149, Mar. 2020, Art. no. 119177, doi: 10.1016/j.ijheatmasstransfer.2019.119177.
- [27] Md. S. Shuvo, T. H. Ruvo, and S. Saha, "Characteristics of turbulent forced convective nanofluid flow and heat transfer in a 2D axisymmetric corrugated pipe," *Thermal Science and Engineering Progress*, vol. 41, June 2023, Art. no. 101838, doi: 10.1016/j.tsep.2023.101838.
- [28] F.R. Menter, "Two-equation eddy-viscosity turbulence models for engineering applications," *AIAA Journal*, vol. 32, no. 8, pp. 1598-1605, Aug. 1994, doi: 10.2514/3.12149.
- [29] A. Hellsten, "Some improvements in Menter's k-omega SST turbulence model," in 29th AIAA, Fluid Dynamics Conference, Albuquerque, NM, U.S.A.: American Institute of Aeronautics and Astronautics, June 1998. doi: 10.2514/6.1998-2554
- [30] P. Pires Araujo and A. L. Tenório Rezende, "Comparison of Turbulence Models in the Flow over a Backward Facing Step," *IJOER*, vol. 3, no. 11, pp. 88–93, Nov. 2017, doi: 10.25125/engineering-journal-IJOER-NOV-2017-19.
- [31] G. Sekrani, S. Poncet, and P. Proulx, "Modeling of convective turbulent heat transfer of water-based Al 2 O 3 nanofluids in an uniformly heated pipe," *Chemical Engineering Science*, vol. 176, pp. 205–219, Feb. 2018, doi: 10.1016/j.ces.2017.10.044.
- [32] D. G. Jehad, G. A. Hashim, A. K. Zarzoor, and C. S. Nor Azwadi, "Numerical study of turbulent flow over backward-facing step with different turbulence models," *Journal of Advanced Research Design*, vol. 4, no. 1, pp. 20-27, 2015.
- [33] J. Kim, S.J. Kline, and J.P. Johnston, "Investigation of a reattaching turbulent shear layer: flow over a backward-facing step," *Journal of Fluids Engineering*, vol. 102, no. 3, pp. 302-308, Sep. 1980, doi: 10.1115/1.3240686.
- [34] "OpenFOAM | Free CFD Software | The OpenFOAM Foundation." Accessed: Nov. 17, 2025. [Online]. Available: https://openfoam.org/
- [35] E. YousefiMiab, S. Baheri Islami, and R. Gharraei, "Feasibility assessment of using nanofluids in shell and tube heat exchanger of gas pressure reducing stations

- through a new developed OpenFOAM solver," *International Journal of Heat and Fluid Flow*, vol. 96, Aug. 2022, Art. no. 108985, doi: 10.1016/j.ijheatfluidflow.2022.108985.
- [36] A. Safari, M. Saffar-Avval, and E. Amani, "Numerical investigation of turbulent forced convection flow of nano fluid in curved and helical pipe using fourequation model," *Powder Technology*, vol. 328, pp. 47-53, Apr. 2018, doi: 10.1016/j.powtec.2018.01.025.
- [37] K. Akselvoll, and P. Moin, "Large-eddy simulation of turbulent confined coannular jets," *Journal of Fluid Mechanics*, vol. 315, pp. 387-411, May 1996, doi: 10.1017/S0022112096002479.
- [38] M. Jourabian, and M. Raeesi, "Turbulent forced convection flow of water-based nanofluids with temperature-dependent properties over backward-facing step channel with upwardly deflected downstream wall," *Numerical Heat Transfer, Part A: Applications*, vol. 86, no. 7, pp. 2125-2154, Apr. 2025, doi: 10.1080/10407782.2023.2287541.
- [39] W. A. Xie, and G. N. Xi, "Geometry effect on flow fluctuation and heat transfer in unsteady forced convection over backward and forward facing steps," *Energy*, vol. 132, pp. 49-56, Aug. 2017, doi: 10.1016/j.energy.2017.05.072.
- [40] C. Abdellahoum, A. Mataoui, and H. F. Oztop, "Turbulent forced convection of nanofluid over a heated shallow cavity in a duct," *Powder Technology*, vol. 277, pp. 126-134, June 2015, doi: 10.1016/j.powtec.2015.02.048.
- [41] C. Abdellahoum, and A. Mataoui, "Numerical analysis of turbulent forced convection of nanofluid flow over a heated shallow cavity," *Heat Transfer Asian Research*, vol. 45, no. 5, pp. 434-450, July 2016, doi: 10.1002/htj.21170.
- [42] P. S. B. Zdanski, M. A. Ortega, and N. G. C. R. Fico, "Heat transfer studies in the flow over shallow cavities," *Journal of Heat Transfer*, vol. 127, no.7, pp. 699-712, July 2005, doi: 10.1115/1.1924630.
- [43] D. Cornu, L. Keirsbulck, F. Kerhervé, F. Aloui, M. Lippert, "On the vortex dynamics of shear-driven deep cavity flows with asymmetrical walls," *Canadian Journal of Physics*, vol. 94, no. 12, pp. 1344-1352, Dec. 2016, doi:10.1139/cjp-2016-0305.

Research Article

Vol. 28 (No. 4), pp. 292-295, 2025 doi: 10.5541/ijot.1754041 Published online: December 1, 2025

How Much Labor Was Lost in the US During the Covid-19 Pandemic

¹*M. Özilgen 🗓

¹Department of Food Engineering, Yeditepe University, 34755, Istanbul, Turkey E-mail: ¹*mozilgen@yeditepe.edu.tr

Received 30 July 2025, Revised 22 October 2025, Accepted 11 November 2025

Abstract

The US National Center for Health Statistics published the ages of patients who died in the US during the pandemic, as well as the numbers of false-negative and false-positive PCR tests. Assessment of the data showed that roughly 33.9×10^9 J of work power is lost. A cyclist may do 3,709 kJ, a weight lifter may do 3,950 kJ, a rugby player may do 3,716 kJ, and a golfer may do 2,413 kJ of work in a day. Therefore, the total loss of work potential during the pandemic would be equivalent to the work power utilized by an elite athlete biker in $91x10^5$ days, a weight lifter in $85x10^5$ days, a rugby player in $91x10^5$ days, and a golfer in $15x10^6$ days. The disease transmission rate and the reliability of the data may be substantially different in different countries and age groups; therefore, this may lead to different global work power loss results.

Keywords: Loss of work power; COVID-19 PCR test; discordant results; false negative results; false positive results.

1. Introduction

The COVID-19 (SARS-CoV-2) pandemic (also known as the coronavirus pandemic) began in China in December 2019. It invaded the other areas of Asia and then the other parts of the world in early 2020. The WHO declared the end of the PHEIC (Public Health Emergency of International Concern) for COVID-19 on 5 May 2023. It is difficult to know exactly how many people have died because of this pandemic, because many people who die while infected with SARS-CoV-2 have never been tested for it, and do not enter the official totals. Conversely, some people whose deaths have been attributed to COVID-19 had other ailments that might have led to their deaths in a similar timeframe anyway. The beginning and end of the pandemics are not well-defined and differ according to the definition used. The polymerase chain reaction (PCR) test is employed to diagnose the presence of the actual genetic material of a virus or its fragments in the body of a person. A PCR test is done with a sample collected by a health care professional from the nose and mouth of the suspected patient. A COVID-19 diagnostic test result could be positive or negative [1]. A positive result means that the alleged person currently has an active infection; therefore, appropriate measures must be taken to avoid spreading the virus to others, but there is also a possibility of having false positive results. A negative result means that the suspected subject likely does not have an infection with the COVID-19 virus. But a false-negative test result could happen depending on the timing and quality of the test sample. A false positive outcome (also referred to as a type I error) occurs when a health service worker obtains a positive result when it is negative. A false positive result, also known as a type II error, is an incorrect warning [2]. A false negative warning is claiming that something is false when it is true. Yilmaz et al [3] calculated the energetic and exergetic costs of the COVID-19 infection on the patient. In

a different publication, Yilmaz et al [3] argued that to continue living a healthy life, energy supplied by metabolism must be adequate to meet the expenses of the life processes. Circulation of the blood, respiration of air, excretion of urine and other end products of metabolism, movement, growth, nutrition, nervous and endocrine control systems are collectively referred to as the life processes in the scientific literature: they represent the expenses incurred through the distribution of appropriate levels of energy for each of them. If the metabolism of a person provides sufficient energy to support his or her life processes, that person may be considered a "healthy" individual. Inflammation of the lung tissue distracts this process, and depending on the deficiency of the oxygen supply, as a result, ATP production via metabolic activity will decrease. ATP is the energy transfer currency of the cells and is produced in the metabolism in two stages:

Reaction (1) happens in the cytoplasm,

$$Gluc + 2Pi + 2ADP + 2NAD \rightarrow 2PYR + 2ATP + 2NADH + 2H_2O$$
 (1)

and reaction (2) happens in the mitochondria:

$$\begin{array}{l} 2PYR \ + \ O_2 \ + \ 28ADP \ + \ 28Pi \ + \ 2NADH \ \rightarrow \\ 28ATP \ + \ 2NAD \ + \ 6CO_2 \ + \ 24H_2O \end{array} \tag{2}$$

As it is seen here, it is expected to produce two moles of ATP from one mole of glucose through reaction 1 and twenty-eight moles of ATP from two moles of PYR (pyruvate). PYR, which is produced in the cytoplasm, is then delivered to mitochondria for further processing in the tricarboxylic acid cycle and electron transport chain. When we look at reactions 1 and 2, we see that less than 10% of the total ATP is produced in the cytoplasm, and more than 90%

*Corresponding Author Vol. 28 (No. 4) / 292

is produced in the mitochondria. In addition to serving as part of the cellular energy generation, the tricarboxylic acid cycle also serves to produce intermediaries for chemical synthesis in the cells. In the life processes of the pregnant mice, Semerciöz et al [4] found that 27.8% of the metabolites are taken by the tricarboxylic acid cycle to construct the cellular components. ATP is delivered to the locations of the cell where energy is desirable. It is hydrolyzed by reaction (3) to yield ADP and organic phosphate, and in this process, 30.5 kJ/mol ATP of energy may be produced:

$$ATP + H_2O \rightarrow ADP + Pi + H^+ \tag{3}$$

Chemical reactions, which require energy to happen, occur simultaneously with reaction (3), since they would not happen otherwise. When aerobic respiration, as explained by reaction (2), cannot occur, because of the absence of sufficient oxygen delivery to the muscles, a fraction of pyruvic acid is taken away from the metabolism after being converted into lactic acid. In general, lactic acid accumulates in the muscle cells when sufficient oxygen is not supplied to the muscles during excessive exercise. Lactic acid buildup is noticed as pain in the case of COVID-19.

COVID-19 makes it very hard to deliver the energy demanded for the life processes, because of the shortage of O2. COVID-19 patients may be placed in a respiratory unit, where higher oxygen pressures are provided to compensate for the increased resistance to oxygen delivery in the lungs [2]. In the respiratory unit, the pressure of oxygen cannot exceed three times the partial pressure of oxygen of the air; otherwise, the lungs may be damaged. The impact of the COVID-19 disease may be assessed in five levels. At the highest impact, patients may be found positive, but recover without any symptoms or clinical signs. COVID-19 patients, who have the most severe symptoms, may have difficulty in respiration, experience malfunctioning organs, and shock. Patients who experience severe symptoms are usually provided with an elevated level of oxygen supply, up to 300% of the partial pressure of oxygen in the air.

Less than 25-27% of the energy obtained from the food can be used for external or internal work performance [5, 6], and almost 75 % is delivered out from the body as heat during the metabolic events [7]. In case of natural death, Kuddusi [8] suggested that the lifespan-entropy-generationlimit was 11,404 kJ/K kg, and then the people were passing away. The relationship between aging and the calories of food is calculated according to metabolic activity. The diet is expected to provide sufficient or more energy for metabolism [9]. This oxidative stress, in turn, is required to intensify the telomere attrition, which has been linked to aging in many creatures, including mice and humans. An elevated rate of metabolism causes an elevated level of entropy generation and suggests correlations that can be helpful in future aging studies. Öngel et al [9] studied the results of telomere length-regulated entropic assessment with four different diets, indicating that women live longer than men. Faster shortening of the telomere lengths in men was the major reason for this estimation. The Mediterranean diet includes foods with anti-oxidative outcomes, and people who are on this diet are subject to slower telomere attrition since they are exposed to less oxidative damage. The Western diet (American diet) is composed mainly of concentrated grains, salt, sugar, saturated lipids, and processed meat are associated with increased cancer risk and chronic diseases. Vegan diets are among the widespread

contemporary would have 112 and 86 years of lifespan, on the women and men would have 108 and 85 years of lifespan, 108 and 85 years of lifespan, on the ketogenic diet, women and men may have 110 and 80 years of lifespan and on the vegan diet, women and men may have 99 and 88 years of lifespan; with the average lifespan of 95 years.

The exergy method of calculations was also used in references [10-15], and they may be helpful to gain a comprehensive understanding of the subject.

2. Materials and Methods

The data [16] were obtained from the US National Center for Health Statistics (NCHS), which operates under the Centers for Disease Control and Prevention, a principal agency of the US Federal Statistical System, at Hyattsville, Maryland, and presented in the initial two columns of Table 1. Data describing the weight of the people were adapted from the National Center for

3. Results and Discussion

Table 1. Calculation of the loss of work power.

Age of the patients (years)	Calculation of the work power lost due to the deaths of the people	Work power lost (J)
0-17	(1,516 children died) (35 kg/child) (309.5 K) (65 years until retirement) (1/0.26 work performed with consumption of 1 J of nutrients)	6.10 x 10 ⁹
18-29	(6,870 people died) (65 kg/person) (309.5 K) [65-(18+29)/2] (years until retirement) (1/0.26 work performed with consumption of 1 J of nutrients)	3.40 x 10 ⁹
30-39	(42,627 people died) (65 kg/person) (309.5 K) [65-(30+39)/2] (years until retirement) (1/0.26 work performed with consumption of 1 J of nutrients)	1.55 x 10 ⁹
40-49	(45,627 people died) (65 kg/person) (309.5 K) [65-(30+39)/2] (years until retirement) (1/0.26 work performed with consumption of 1 J of nutrients)	1.66 x 10 ⁹
50-64	(200,067people died) (65 kg/person) (309.5 K) [65-(50+64)/2] (years until retirement) (1/0.26 work performed with consumption of 1 J of nutrients)	1.38 x 10 ¹⁰
65-74		
75-84	These people have already retired and do not perform any work of commercial value	
85 years old and over		
18-29	Work power loss due to the false negative test results by the 18-29- year-old university students	7.4 x 10 ⁹
18-29	Work power loss due to the false positive test results by the 18-29-year-old university students	1.3 x 10 ⁵
TO	OTAL WORK POWER LOSS	33.9 x 10 ⁹

The first row explains that in the 0 to 17-year age group, 1,516 children died. If the average weight of these children were 35 kg/child, at 309.5 K (37 °C), they would have 65

years until retirement, and perform 1/0.26 of work with consumption of 1 J of nutrients. The following rows were constructed by following a similar technique. The work power was based on the number of people; on the other hand, productivity depends on the skills of the people and how they use them. The work power was considered in Table 1, not the productivity. The physical/energetic work capacity depends only on the number of people in the labor market.

A graphical description of the COVID-19 disease on the body of a person is presented in Figure 1.

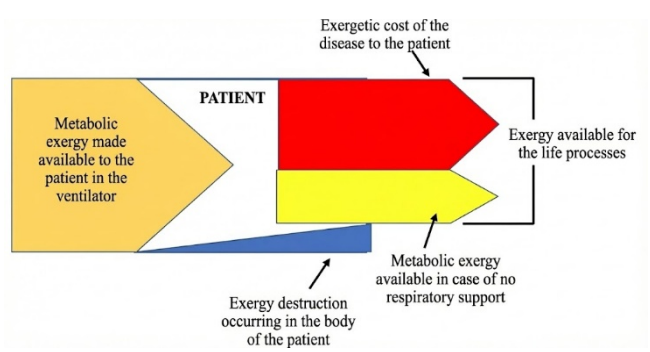


Figure 1. Graphical description of the COVID-19 disease in the body of a person.

The diseased person was assumed to be taken to a ventilator. The exergetic cost of the inefficient metabolism is described with the red arrow, and the patient's remaining metabolic activity is described with the yellow arrow. The blue fraction of the figure describes the exergy destruction in the body of the patient.

Jarvis and Kelley [18], after performing different modeling studies, concluded that one false negative may lead to approximately 2.25 inoculations. If we should consider that the virus was spread between the 18-29 years old university students, we may calculate the work power lass as = (1,025 false negatives) (2.25 number spread by false negatives) (65 kg/person) (309.5 K) [65-(18+29)/2] (years until retirement) (1/0.26 work performed with consumption of 1 J of nutrients) = 7.4×10^9 J.

If we should focus on the effect of the false positives on the 18-29 years old university students and they isolate themselves for two weeks we may calculate the work power loss as = (447 false positives) (65 kg/person) (309.5 K) (14 days/365 days) (1/0.26 work performed with consumption of 1 J of nutrients) = 1.3×10^5 J

When we add up these numbers, we may estimate that approximately 33.9x10⁹ J of work power is lost during the pandemic in the US. Yildiz et al [19] estimated that a cyclist may do 3,709 kJ, a weight lifter may do 3,950 kJ, a rugby player may do 3,716 kJ, and a golfer may do 2,413 kJ of work per day. Therefore, the total loss of work potential during the pandemic would correspond to the work power utilized by an elite athlete biker in 91x10⁵ days, a weight lifter in 85x10⁵ days, a rugby player in 91x10⁵ days, and a golfer in 15x10⁶ days.

4. Conclusion

The number of people who died in the US during the pandemic, their ages, and accounts of false negative and false positive PCR tests are available in the publications of the US National Center for Health Statistics. Analysis of the data showed that approximately 33.9x10⁹ J of work power was lost. A cyclist may do 3,709 kJ, a weight lifter may do 3,950 kJ, a rugby player may do 3,716 kJ, and a golfer may do

2,413 kJ of work in a day. Therefore, the total loss of work potential during the pandemic would be equivalent to the work power utilized by an elite athlete biker in 91x10⁵ days, a weight lifter in 85x10⁵ days, a rugby player in 91x10⁵ days, and a golfer in 15x10⁶ days. The inoculation rate and the reliability of the data may vary substantially across different countries and age groups; therefore, this may lead to significantly different work power loss results.

Conflict of Interest

Author approves that to the best of their knowledge, there is not any conflict of interest or common interest with an institution/organization or a person that may affect the review process of the paper.

Credit Author Statement

M. Özilgen: Conceptualization, Writing- Reviewing and Editing, Visualization, Investigation

Nomenclature

ADP Adenosine diphosphate ATP Adenosine tri phosphate

References:

- [1] "COVID-19 diagnostic testing." Accessed: Dec. 19, 2025. [Online]. Available: https://www.mayoclinic.org/tests-procedures/covid-19-diagnostic-test/about/pac-20488900.
- [2] M. Ozilgen, Handbook of Food Process Modeling and Statistical Quality Control, 2nd ed. Boca Raton: CRC Press, 2011. doi: 10.1201/b10833.
- [3] B. Yilmaz, S. Ercan, S. Akduman, and M. Özilgen, "Energetic and exergetic costs of COVID-19 infection on the body of a patient," *International Journal of Exergy*, vol. 32, no. 3, p. 314, 2020, doi: 10.1504/IJEX.2020.108602.
- [4] A. S. Semerciöz, B. Yılmaz, and M. Özilgen, "Thermodynamic assessment of allocation of energy and exergy of the nutrients for the life processes during pregnancy," *British Journal of Nutrition*, vol. 124, no. 7, pp. 742–753, Oct. 2020, doi: 10.1017/S0007114520001646.
- [5] L. Sherwood, *Human physiology: from cells to systems*, 9th ed. Boston: Cengage learning, 2016.
- [6] J. E. Hall and A. C. Guyton, Guyton and Hall textbook of medical physiology, 13th edition. in Student consult. Philadelphia, PA, USA: Elsevier, 2016.
- [7] P. G. Kopelman, "Obesity as a medical problem," *Nature*, vol. 404, no. 6778, pp. 635–643, Apr. 2000, doi: 10.1038/35007508.
- [8] L. Kuddusi, "Thermodynamics and life span estimation," *Energy*, vol. 80, pp. 227–238, Feb. 2015, doi: 10.1016/j.energy.2014.11.065.
- [9] M. E. Öngel, C. Yıldız, C. Akpınaroğlu, B. Yilmaz, and M. Özilgen, "Why women may live longer than men do? A telomere-length regulated and diet-based entropic assessment," *Clinical Nutrition*, vol. 40, no. 3, pp. 1186–1191, Mar. 2021, doi: 10.1016/j.clnu.2020.07.030.

- [10] E. Turgut and U. Yardımcı, "Detailed evaluation of a heat exchanger in terms of effectiveness and second law," *Journal of Turbulence*, vol. 23, no. 9–10, pp. 515–547, Oct. 2022, doi: 10.1080/14685248.2022.2134571.
- [11] A. Tiktaş, H. Gunerhan, A. Hepbasli, and E. Açıkkalp, "Exergy-based techno-economic and environmental assessments of a proposed integrated solar powered electricity generation system along with novel prioritization method and performance indices," *Process Safety and Environmental Protection*, vol. 178, pp. 396–413, Oct. 2023, doi: 10.1016/j.psep.2023.08.048.
- [12] A. Tiktas, H. Gunerhan, and A. Hepbasli, "Exergoeconomic optimization of a proposed novel combined solar powered electricity and high-capacity cooling load production system for economical and potent generation via utilization of low-grade waste heat source," *Thermal Science and Engineering Progress*, vol. 55, Oct. 2024, Art. no. 102976, doi: 10.1016/j.tsep.2024.102976.
- [13] A. Elkihel, A. Bakdid, Y. Elkihel, and H. Gziri, "Optimization of Energy Consumption of a Thermal Installation Based on the Energy Management System EnMS," in *Advanced Technologies for Humanity*, vol. 110, Cham: Springer International Publishing, 2022, pp. 311–319. doi: 10.1007/978-3-030-94188-8_29.
- [14] A. Tiktas, H. Gunerhan, A. Hepbasli, and E. Açıkkalp, "Extended exergy analysis of a novel integrated absorptional cooling system design without utilization of generator for economical and robust provision of higher cooling demands," *Energy Conversion and Management*, vol. 307, May 2024, Art. no. 118350, doi: 10.1016/j.enconman.2024.118350.
- [15] A. Tiktas, A. Hepbasli, and H. Gunerhan, "Achieving ultra-high coefficient of performance in a novel solar-assisted trigeneration system integrating absorption and Rankine cycles," *Energy Conversion and Management*, vol. 346, p. 120415, Dec. 2025, doi: 10.1016/j.enconman.2025.120415.
- [16] "COVID-19 Provisional Counts Weekly Updates by Select Demographic and Geographic Characteristics." Accessed: Mar. 11, 2023. [Online]. Available: https://www.cdc.gov/nchs/nvss/vsrr/covid_weekly/index.htm.
- [17] "Anthropometric Reference Data for Children and Adults: United States, 2015–2018." Accessed: Sep. 20, 2025. [Online]. Available: https://www.cdc.gov/nchs/data/series/sr_03/sr03-046-508.pdf
- [18] K. F. Jarvis and J. B. Kelley, "Temporal Dynamics of Viral Load and False negative Rate Influence the Levels of Testing Necessary to Combat COVID19 Spread," Aug. 14, 2020. doi: 10.1101/2020.08.12.20173831.
- [19] C. Yildiz, M. E. Öngel, B. Yilmaz, and M. Özilgen, "Diet-dependent entropic assessment of athletes' lifespan," *Journal of Nutritional Science*, vol. 10, p. e83, 2021, doi: 10.1017/jns.2021.78.

Research Article

Vol. 28 (No. 4), pp. 296-307, 2025 doi: 10.5541/ijot.1684430 Published online: December 1, 2025

Comparative Study on The Effect of Oxygen-Enriched Air on Combustion of a Spark Ignition Engine Fuelled with Methanol and Ethanol

*1 Nidhi

¹ Department of Mechanical Engineering, Galgotias University, Greater Noida, Uttar Pradesh, India E-mail: *nidhi.tevatia@gmail.com

Received 26 April 2025, Revised 12 June 2025, Accepted 3 November 2025

Abstract

An experimental investigation was carried out on a single-cylinder four-stroke spark-ignition engine fuelled with methanol (M100) and ethanol (E100) to study the effect of oxygen enrichment on combustion characteristics of the engine. The experiments were carried out at base compression ratio 9.8 and the results were compared at higher compression ratio 10.6. The compression ratio was increased by decreasing the clearance volume from the cylinder head. The engine was operated at the maximum torque (4.5 Nm at 3600 rpm) achieved with M100 fuel and the results were compared for both the fuels at the same torque. The results indicate that with oxygen enrichment at the increased compression ratio, in-cylinder peak pressure increased significantly by 34.7% with M100 and 8.4% with E100 compared to base gasoline. The rate of pressure rise increased by 2.7 times with M100 and by 20% with E100. Due to high peak pressure, heat release rate, and rate of pressure rise, the combustion duration decreased significantly with both fuels. The cycle-to-cycle variation in indicated mean effective pressure decreased to 1.48% with E100 and M100. A notable outcome of the study was that the effect of oxygen enrichment was more prominent in methanol combustion than with ethanol at both compression ratios with greater effect at higher CR.

Keywords: Methanol; ethanol; combustion; IC engine; oxygen-enriched air.

1. Introduction

The utilisation of petroleum-based conventional fuels for transportation is a source of global problems including energy security, global warming, and poor local air quality. The transportation sector consumes 95% of the energy from gasoline and diesel [1]. Conventional fossil fuels are limited while the energy demand is rising rapidly. It is projected that coal reserves are available till 2112 and will be the only fossil fuel remaining after 2042. Oil and gas would have been diminished by that time [2]. The challenges of energy security and better climatic conditions have paved the path for the utilisation of alternative fuels such as ethanol and methanol in the transport sector. Ethanol and methanol are produced through well-established methods of biomass fermentation and coal gasification respectively. The physicochemical properties of the alcohol fuels including high flame velocity, high octane number, and low carbon to hydrogen ratio are suitable for their application in high compression ratio spark ignition (SI) engines. Most of the research work with ethanol and methanol fuels has been conducted with various blends of gasoline. The blending ratio of alcohol fuels with gasoline can be varied from 5% to 90% by volume. Various authors including, Tian et al. [3], and Pourkhesalian et al. [4] have reported that blends of alcohols (ethanol, methanol, and butanol) and gasoline improve the performance and decrease the emissions of carbonmonoxide (CO), hydrocarbon (HC), and oxides of nitrogen (NOx) from the engine.

High compression ratio and oxygen-enriched air for combustion are existing techniques to further enhance the performance of an alcohol-fuelled engine. The superior knock resistance of ethanol and methanol fuels allows for their application at a high compression ratio [5-9]. Awad et al. [10] reviewed the extensive literature on the impact of increasing compression ratio on performance, combustion, and emissions of the engine fuelled with oxygenated fuels such as alcohols and ethers. They reported that engine performance improved at high compression ratio (CR) and emissions of CO and carbondioxide (CO₂) decreased due to oxygen present in the fuels. High CR increased the flame speed and extended the air-fuel ratio and thus increasing the efficiency of the engine. Sakthivel et al. [11] reported that increasing the CR of the engine increased the peak pressure and heat release rate (HRR) in a motorcycle fuelled with E30 (ethanol gasoline blend). Balki and Sayin [12] reported that with the increase of CR, brake thermal efficiency (BTE) of the engine increased by 3.6% and 4.5% due to an increase in cylinder pressure which resulted in more work done by the piston. Prasad et al. [13] reported an increase in peak cylinder pressure with an increased compression ratio. Wouters et al. [14] reported that knock was not observed even at CR of 20.6 with methanol. In addition Gong et al., [15] Celik et al. [16], and Zhou et al. [17] reported the improvement of combustion, fuel economy, and emissions in engines fuelled with ethanol and methanol fuels at a high compression ratio.

The application of oxygen-enriched air to improve performance and control the emissions in an IC engine is a widely accepted method. Li et al. [18] reported that peak

*Corresponding Author Vol. 28 (No. 4) / 296

pressure and heat release increased with oxygen enrichment in an LPG fuelled SI engine. Emissions of CO and HC decreased and NOx increased due to high peak temperature and the presence of more oxygen during oxygen-enriched air. Caton [19] reported that increased cylinder pressure and temperature due to oxygen enrichment resulted in heat loss and decreased the thermal efficiency of the engine while emissions of NOx increased drastically. Seers et al. [20] reported that oxygen-enriched air resulted in fast flame propagation due to increased laminar flame speed and high initial mixture temperature during ignition timing in a SI engine. Nidhi and Subramanian [21] concluded a significant improvement in BTE of the engine and a reduction in CO and HC emissions from the engine. In addition, authors including Jeevahan et al. [22], Maxwell et al. [23], Quader [24], Kajitani et al. [25], and Poola et al. [26] reported that utilisation of oxygen-enriched air for combustion was beneficial to decrease the emissions from the engine.

The oxygen enrichment at increased compression ratio is a novel way to improve the combustion quality which would result in high thermal efficiency of the engine along with ultra-low emissions in ethanol and methanol fuelled SI engines. This experimental investigation was carried out at base and increased compression ratio to notice the effect of oxygen enrichment with two fuels ethanol and methanol. However, the literature survey indicates the studies on oxygen enrichment with conventional fuels such as gasoline and few studies are available with alcohol fuels. The literature survey does not indicate research work at increased compression ratio. This paper exclusively discusses the effect of oxygen enriched air on combustion characteristics of a SI engine including heat release rate, peak pressure, rate of pressure rise, combustion duration and coefficient of variance in IMEP in detail fuelled with two alcohol fuels.

2. Methodology

Maximum Brake Torque (MBT) timing for the study is the spark timing at which brake thermal efficiency of the engine is maximum. MBT timing for base gasoline, M100, and E100 fuels are determined experimentally. With M100, the maximum torque achieved was 4.5 Nm at 3600 rpm. The results obtained with methanol are compared with ethanol and BS-VI gasoline (base gasoline). The physicochemical properties of the fuels are given in Table 6. The engine characteristics are studied at the base condition with the fuels, then by oxygen enrichment (OE) at the base compression ratio of 9.8:1. Afterward, the compression ratio (CR) of the engine was increased to 10.6 and finally, oxygen enrichment was carried out at the increased compression ratio. For oxygen enrichment, the flow of oxygen was kept at maximum with both the fuels. The oxygen was injected into the intake manifold continuously (Figure 1). The enrichment level achieved was 30-40% (by mass) at the maximum torque condition. It was calculated as the percentage of oxygen supplied externally to oxygen present in the airflow. Since the maximum gas flow rate could not be changed due to which OE with M100 and E100 was not equal and lay in the range of 30-40%. With M100, it varied between 35-38% at both the compression ratios. The maximum oxygen flow rate is 0.22 g/s with the injector and it was obtained at 0.75 bar pressure beyond which the injector would close. The oxygen was injected into the intake manifold continuously. The maximum flow of oxygen from the injector was determined after several experimental trails. The working principle of the gas flowmeter is Coriolis with a maximum measurement error of \pm 0.5%. The gas is 99.9% pure in a high-pressure cylinder.

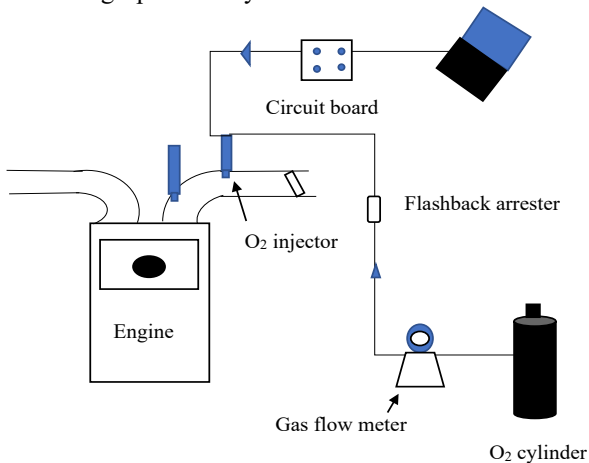


Figure 1. Oxygen enrichment method.

The compression ratio was increased by decreasing the clearance volume of the engine head [27] (Eq. (1)). It was performed by removing one layer from the gasket (fitted between head and liner) which was originally a pack of three layers as shown in Figure 2. Removing more than one layer could lead to the piston touching the head. Therefore, the removal of more than one layer was not carried out.

$$CR = 1 + \frac{V_{swept}}{V_{clearance}} \tag{1}$$

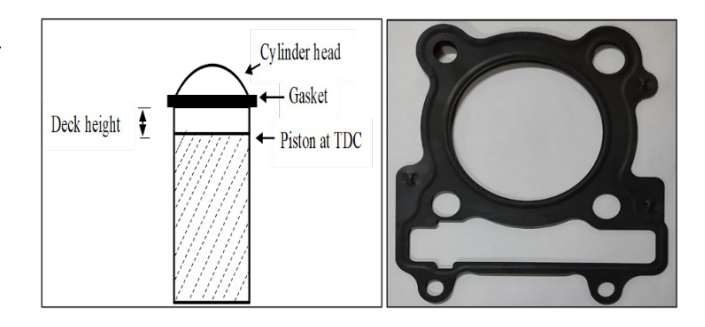


Figure 2. Schematic view of cylinder head with gasket and the original gasket.

Figure 2 shows the schematic view of cylinder head with gasket and the original gasket. Eqd. (2)-(5) were used for the calculation of the compression ratio. The original gasket of 1.3 mm thickness was replaced with thickness of 0.8mm (Figure 2). As a result, the volume of the gasket decreased which decreased the clearance volume of the engine head, thus compression ratio increased to 10.6:1. Swept volume (V_s) was calculated using Eq. (3). The calculated value is 249.32 cm³. *V_{crevice}* was measured by filling water inside the cylinder head. The calculated value is 19 cm³. The deck height is 0.8 mm given by the manufacturer which is used in Eq. (4) to calculate clearance gap height. The calculated gasket volume is 3.44 cm³ with thickness 0.8 mm. The increased compression ratio is 10.6:1.

$$V_C = V_{gasket} + V_{clearance gap} + V_{crevice}$$
 (2)

Swept volume
$$V_s = \frac{\pi}{4}B^2 \times L \tag{3}$$

$$\frac{\pi}{4}B^2 \times deck \ height \tag{4}$$

Volume of metal gasket

 $\frac{\pi}{4}B^2 \times \text{clearance gasket thickness} \tag{5}$

2.1 Experimental Details

The experiments were conducted on a single-cylinder four-stroke spark ignition engine having port injection. Valve timing diagram of the engine is given in Figure 3. The details of the engine are given in Table 1. The schematic layout of the experimental setup is given in Figure 4. An eddy current water-cooled dynamometer was used for applying load on the engine. The data was acquired at the maximum torque (4.5 Nm at 3600 rpm) achieved with methanol (M100) and compared with E100 at the base compression ratio. The throttle was fully opened at maximum torque point with methanol. The intake pressure for the condition was 1 bar. The volumetric efficiency of the engine was 83%. The MBT with M100 and E100 was 45 bTDC while with base gasoline it was 42 bTDC. MBT timings were found after several repeated experiments. Although methanol and ethanol have higher flame velocities than gasoline, their strong charge-cooling effect due to higher latent heat of vaporization and larger fuel mass requirement necessitates slightly earlier ignition to achieve the optimal cylinder pressure phasing.

Table 1. Engine specifications.

Table 1. Engine specifications.			
Engine	Single cylinder, four- stroke air-cooled		
Cylinder bore	74 mm		
Stroke	58 mm		
Compression ratio	9.8:1		
Swept Volume	250 сс		
Length of connecting rod	112 mm		
Lubrication	Forced		
Fuel injection	Port type		
Max. power output @ 8000 rpm	20 to 25 H.P		
Max. torque output @ 6000 rpm	18 to 20 Nm		

The equivalence ratio was stoichiometric for the fuels. It was controlled through a lambda sensor fitted to the exhaust side of the engine. An open ECU was used for controlling spark timing and equivalence ratio. A flashback arrester was used to control backfire propagation during oxygen enrichment. The uncertainty, sensitivity and other specifications of the instruments including air flow meter, fuel flow meter, dynamometer, crank angle encoder, pressure sensor and combustion analyser are given in Table 2 to 5. The fuel flow rate and oxygen gas flow rate were measured with a Coriolis principle-based flowmeters. Thermal based air flowmeter was used for measuring the air flow rate. The engine was run for 20-25 minutes to get it stabilized before storing the data. The data for in-cylinder pressure and corresponding crank angle was acquired using a piezoelectric-based pressure sensor fitted in the engine head and an optical-based crank angle encoder fitted on the dynamometer side. The pressure theta data was acquired

using AVL Indicom software, version 2.1. To study cycle to cycle variations in pressure, 500 cycles were acquired for analysis.

Table 2. Specifications of air flow meter.

S. No.	Parameter	Values/description
1	Make	Endress+Hauser (EH)
2	Measuring principle	Thermal mass flow
3	Operating temperature range	0-500C
4	Accuracy	+-1.5%

Table 3. Specifications of fuel flow meter.

S. No.	Parameter	Values/description
1	Make and Model	Rheonik, RHM015L
2	Working Principle	Coriolis
3	Temperature range	-20 to 1200C
4	Mass flow uncertainty	< 0.10%

Table 4. Specifications of dynamometer.

S. No.	Parameter	Values/description
1	Make and Model	Technomech, TME -50 (7.5 kW)
2	Туре	Eddy Current Water- Cooled Dynamometer
3	Maximum Power	37 kW
4	Maximum Torque	100 Nm
5	Cooling Media	Water
6	Direction of rotation	Bi – directional

Table 5. Specifications of crank angle encoder, pressure sensor and combustion analyser.

S. No.	Parameter	Values/description
1	Combustion Analyser Make and Model	AVL, IndiMicro 602TM
2	Linearity	±0.01% FS
3	Input Range (Piezo)	Up to 14,400 pC
4	Angle Encoder Make and Model	AVL, Angle encoder 366C
5	Engine speed measuring range	0-20,000 rpm
6	Resolution	0.5 CA.
7	Crank angle Signal	720 crank angles
8	Pressure Sensor Make and Model	AVL, GH15D
9	Working Principle	Piezoelectric Pressure Sensor
10	Sensitivity	19 pC/bar
11	Measuring Range	0-250 bar

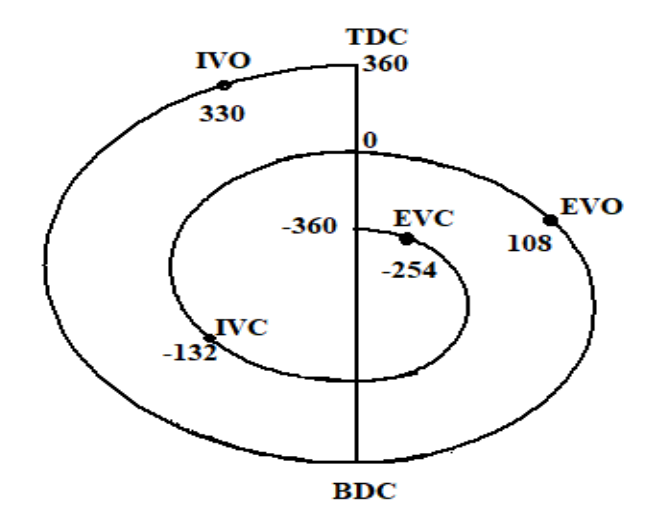


Figure 3. Valve timings of the engine.

Table 6. Physicochemical properties of ethanol, methanol and gasoline [12, 28, 29].

Properties	Gasoline	Methanol	Ethanol
Composition	>C ₈	СН ₃ ОН	C ₂ H ₅ OH
Carbon (% mass)	86	37.48	52.14
Hydrogen (%mass)	14	12.58	13.13
Oxygen (% mass)	0	50	34.7
Density STP, kg/m3	740	790	790
Dynamic viscosity (200C, mPa)	0.6	0.57	1.2
RON Research octane number (min.)	95	109	109
MON Motor octane number (min.)	85	92	98
Flash point (0C)	-45	11	14
Auto ignition temperature (0C)	465-743	738	698
Boiling point (0C)	25-215	65	79
Latent heat of vaporisation (kJ/kg)	180-350	1100	838
Low calorific value (MJ/kg)	43	20	26.95
Adiabatic flame temperature (K)	2275	2143	2193
Minimum ignition energy in air (mJ)	0.25	0.14	0.23
Quenching distance (mm)	2	1.85	1.65
Flame speed (cm/s)	28	52	39
Stoichiometric air/fuel ratio	14.5	6.5	9

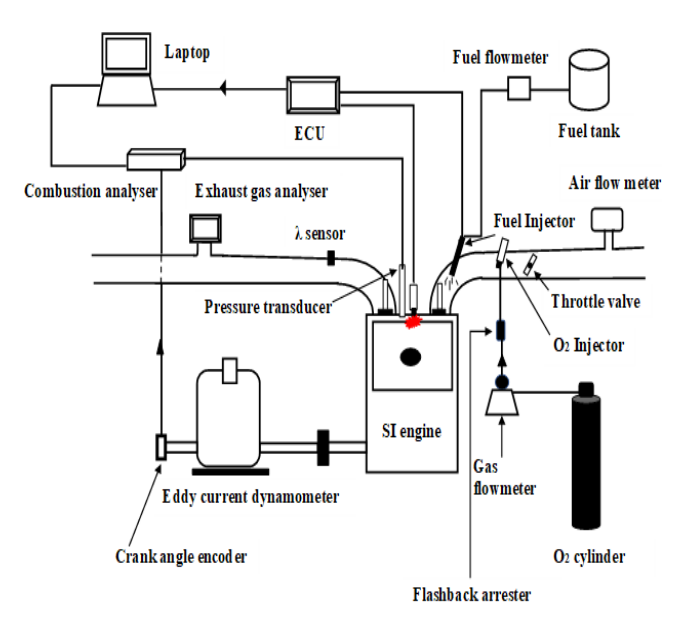


Figure 4. Experimental setup.

2.2 Mathematical Relations Used for Calculation

The net heat release rate (Q) was calculated using the first law of thermodynamics as given in Eq. (6) [27].

$$\frac{dQ}{d\theta} = \frac{\gamma}{\gamma - 1} P \frac{dV}{d\theta} + \frac{1}{\gamma - 1} V \frac{dP}{d\theta}$$
 (6)

where P, V, γ , and θ represent the in-cylinder pressure (pascal), instantaneous cylinder volume (m³), the ratio of specific heats, and the crank angle, respectively. The rate of pressure rise is calculated using Eq. (7). The ignition delay (ID) was calculated by using Eq. (8). The combustion duration (CD) was calculated by using Eq. (9).

$$\frac{dP}{d\theta} = P_i - P_{i-1} \tag{7}$$

where P_i is the pressure at a crank angle

$$ID = \int_{Spark}^{SOC} d\theta$$
 (8)

$$CD = \int_{SOC}^{EOC} d\theta \tag{9}$$

where, SOC- Start of combustion (crank angle (C.A) at which 10% of the maximum cumulative heat is released), EOC- End of combustion (C.A at which 90% of the maximum cumulative heat is released), ID- Crank angle duration of ignition timing and SOC, CD- Crank angle duration between SOC and EOC.

Net indicated mean effective pressure (IMEP $_{net}$) is calculated by Eq. (10).

IMEPnet =
$$\int_{-360}^{+360} PdV$$
 (10)

Coefficient of variance (COV) in $IMEP_{net}$ was calculated by Eq. (11).

$$COV_{IMEPnet} = \frac{\sigma_{IMEP_{net}}}{\mu_{IMEP_{net}}} \times 100\% \tag{11}$$

3. Results and Discussion

3.1 Variation of Peak Pressure and Its Crank Angle Position

With oxygen enrichment, peak pressure (P_{max}) increased by 56.5% with M100 and by 17.6% with E100 compared to base gasoline (Figure 5). The position of P_{max} shifted to 6 deg aTDC and 18 deg aTDC with M100 and E100 which was 23 aTDC with base gasoline. The distinct separation of the methanol curve in the in-cylinder pressure graph is primarily attributed to methanol's significantly higher laminar flame speed compared to both gasoline and ethanol. This characteristic leads to faster combustion and a more rapid pressure rise within the cylinder. Consequently, the spark timing for methanol was advanced closer to TDC to optimize peak pressure timing, resulting in a noticeably different pressure trace.

Various comparative studies confirm that P_{max} is higher with M100 than E100 [30-32]. The generation of OH radicals is more with M100 than E100 and gasoline. M100 does not contain carbon to carbon bond as found in E100. Inherently, the flame speed of M100 is greater than E100 and gasoline which is further enhanced due to oxygen enrichment [33]. The effect of oxygen enrichment was thus, more prominent with M100 than with E100. The combustion efficiency with methanol is higher than ethanol since number of intermediate products formed during its combustion are less than ethanol which adds to lower irreversibility and improved combustion [34].

Due to oxygen enrichment (OE) of intake air, the amount of nitrogen decreased which has higher specific heat (1.03 kJ/kg-K at 300 K, 1.21 kJ/kg-K at 1300 K) than oxygen (0.9 kJ/kg-K and 1.12 kJ/kg-K at 1300 K). When the nitrogen percentage decreases, the in-cylinder temperature increases. The high in-cylinder temperature promotes a faster rate of the chemical reaction. The oxygen helps in the generation of OH radicals which promotes the chain propagation of chemical reactions.

At a high compression ratio, P_{max} increased by 8% with both M100 and E100 compared to their values at base CR as shown Figure 6. The position of P_{max} shifted closer to TDC compared to the base compression ratio. The gain in peak pressure and shift in crank angle position can be attributed to the thermodynamic effects of higher compression ratios, which inherently raise the temperature and pressure of the intake charge during the compression stroke. These elevated thermodynamic conditions significantly enhance the flame propagation speed. The laminar flame speed is known to be a function of the initial pressure, temperature, and density of the unburned air-fuel mixture; thus, increased pressure and temperature at higher CR directly contribute to faster combustion kinetics [11].

For alcohol-based fuels such as M100 and E100, which already exhibit high flame speeds due to their oxygenated molecular structures and lower hydrocarbon chain lengths, the increase in CR further amplifies this behavior. Consequently, the combustion process becomes more rapid and complete, resulting in a steeper pressure rise and a higher peak pressure. This also causes the peak pressure to occur earlier in the cycle (closer to TDC), improving thermal

efficiency but potentially increasing the mechanical and thermal loads on engine components.

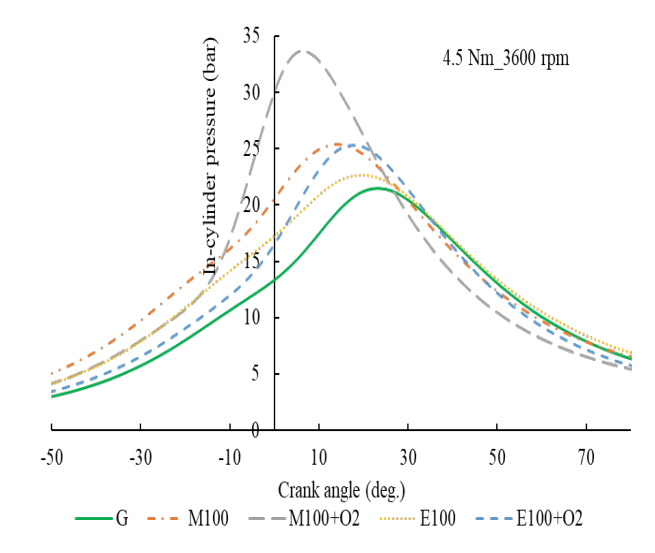


Figure 5. In-cylinder pressure variation with crank angle at base compression ratio with both fuels.

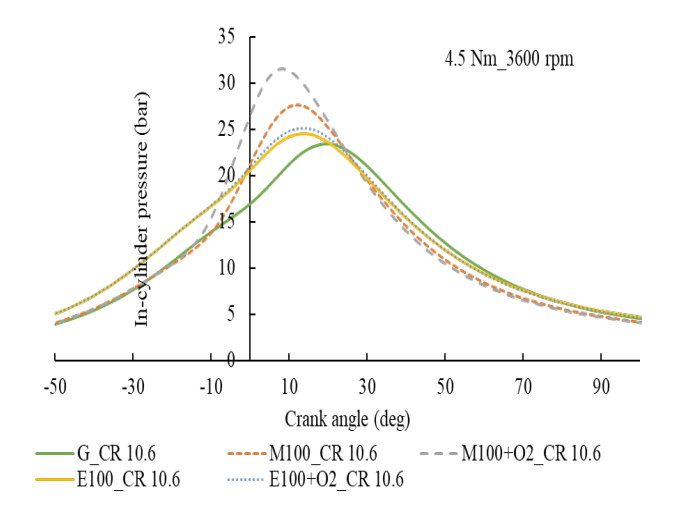


Figure 6. In-cylinder pressure with M100 and E100 at 4.5 Nm, 3600 rpm at 10.6 CR.

With oxygen enrichment at high CR (Figure 7), P_{max} increased by 34.7% and 8.4% with M100 and E100 compared to base gasoline. The position of P_{max} was 8 aTDC with M100 and 14 aTDC with E100. Eqs. (12) and (13) [21] show that with an increasing amount of oxygen, the rate of chemical reaction could be enhanced during the combustion of fuel. This is the famous Arrhenius Equation which indicates the temperature dependency of reaction rates.

Fuel + oxygen/air
$$\rightarrow$$
 products (12)

$$R_{r} = Ae^{\frac{-E_{a}}{RT}}[Fuel]^{a}[Oxygen]^{b}$$
 (13)

where A is the Arrhenius constant, Ea is the activation energy, R is the universal gas constant and T is the absolute temperature of the reaction.

With the added benefit of high CR, high temperature and pressure of reactants improve the growth of flame kernel and increase the flame propagation speed [35]. These factors result in better combustion with oxygen enrichment at high CR. At elevated CRs, the end-of-compression temperature and pressure rise significantly due to increased isentropic

compression work. This enhances the pre-flame reactions, facilitates autoignition, and supports the rapid growth of the flame kernel. A higher initial pressure also increases the density of the mixture, which according to laminar flame speed theory, increases the flame propagation speed due to the enhanced molecular collision frequency and reduced mean free path. Furthermore, oxygen enrichment increases the local oxygen availability in the flame front, leading to intensified exothermic reactions and a steeper pressure rise during the premixed combustion phase.

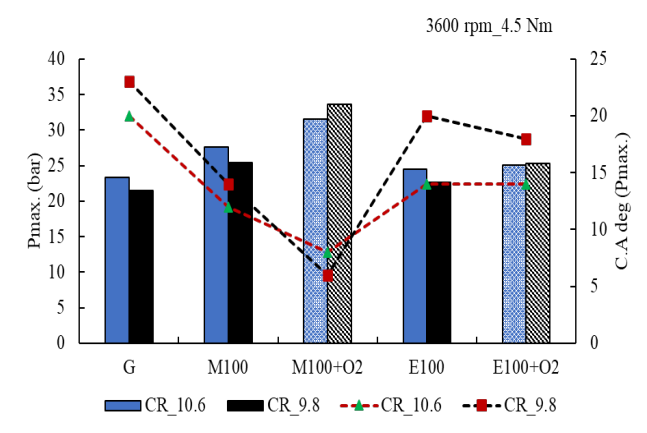


Figure 7. Comparison of P_{max} and corresponding crank angle with M100 and E100 at 4.5 Nm, 3600 rpm at different conditions.

3.2 Variation of Heat Release Rate (HRR), Combustion Duration, and Ignition Delay

With oxygen enrichment, max. HRR increased by more than 92.2% with M100 and by 65.4% with E100 compared to base gasoline. Combustion duration (CD) shortened by 35.8% with M100 and 28.2% with E100 compared to base gasoline. Furthermore, ignition delay (ID) shortened by 32% with M100 and was comparable to base gasoline in E100 (Figure 9).

M100 and E100 are neat (homogeneous) substances with a single boiling point. Gasoline does not behave like alcohol as it consists of different hydrocarbons. It has higher T90 (90% evaporation corresponding to the temperature) than alcohol fuels. Therefore, some fraction needs a high temperature for combustion. With oxygen enrichment, the flame speed and burning rate of charge are more pronounced since in-cylinder pressure and temperature are higher. It enhanced the HRR even better with M100 and E100 taking the added advantage of their lower boiling points. Figure 10 shows the cumulative heat release with both fuels at increased CR.

With a high heat release rate, the burning speed of charge is enhanced which shortened the CD with alcohol fuels. ID depends on the latent heat of vaporisation. When cylinder temperature is higher due to oxygen enrichment, alcohol fuels might evaporate quickly, thus shortening the ignition delay period. Overall, the effect of oxygen enrichment was more significant with M100 than with E100 as discussed previously.

At high compression ratio, max. HRR increased by 3% with M100 compared to base CR and was similar to base CR with E100. CD shortened by 20% with M100 and 2.7% with E100 compared to their respective values at base CR. ID decreased by 11.1% with M100 and by 9.8% with E100 compared to base CR. The CD and ID shortened by 8% and 12.2% at high CR compared to base CR.

At high CR, residual gases are lower and turbulence is more. As a result, rapid charge burning resulted in a shortened combustion duration and ignition delay with M100 and E100 compared to the values at the base compression ratio. The effect of increased CR is more significant with M100 and E100 than with gasoline for obvious reasons of their physico-chemical properties.

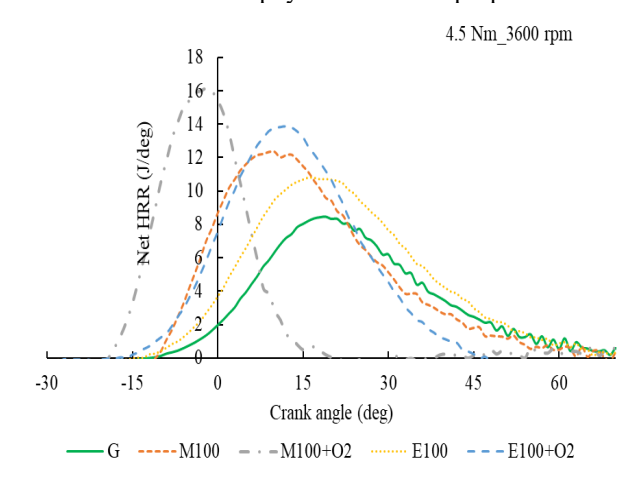


Figure 8. Net heat release rate with M100 and E100 at 4.5 Nm, 3600 rpm at both CRs.

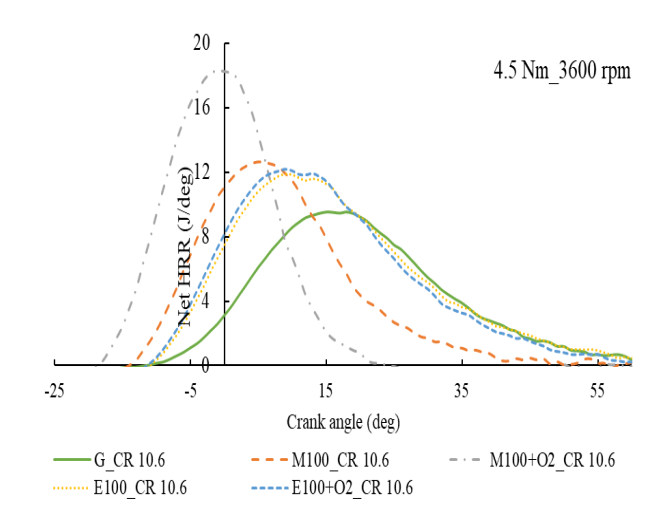


Figure 9. Net heat release rate with both fuels at 10.6 CR.

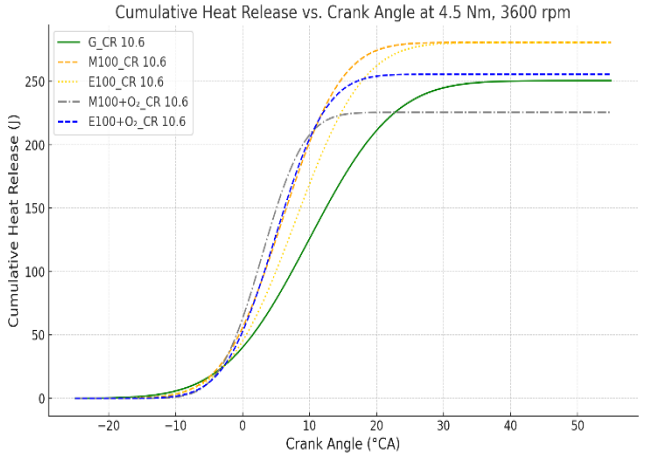


Figure 10. Cumulative heat release with both fuels at 10.6 CR.

With oxygen enrichment at high CR, max. HRR doubled with M100 and increased by 35.4% with E100 compared to base gasoline at high CR as shown in Figure 9. ID decreased by 32% with M100 compared to base gasoline at high CR

and by 10% with E100. CD shortened by 45.9% with M100 and by 8.1% with E100 compared to base gasoline at higher CR. The cumulative heat release (CHR) curves at 4.5 Nm and 3600 rpm shown in Figure 9 depicts that methanol (M100) and ethanol (E100) exhibit faster and earlier combustion compared to gasoline, due to their higher laminar flame speeds and oxygen content. Among all, methanol with oxygen enrichment (M100+O2) shows the steepest and earliest rise in CHR, indicating highly reactive and concentrated combustion. Ethanol with oxygen (E100+O₂) also shows enhanced combustion, though slightly less aggressive than methanol. In contrast, gasoline shows a delayed and broader CHR profile due to slower combustion kinetics. The leftward shift of CHR curves with oxygen enrichment confirms improved combustion phasing, which can enhance thermal efficiency if appropriately controlled.

Oxygen enrichment and high compression ratio both improve the combustion by enhancing flame propagation which contributes to shorter combustion duration [36]. Due to the rapid rate of reaction, the ignition delay period shortened with M100 and E100. With the high cylinder temperature, the vaporisation of E100 and M100 might also improve which could help to shorten ignition delay. Maximum HRR values for M100 are better than E100 because of the better combustion rate (Figure 11). It is well indicated through its high P_{max} and high max. ROPR values. Similar study from the literature reports that with oxyfuel combustion, at higher compression ratio the ignition delay shorten significantly with the improvement of cylinder pressure and fuel economy in a dual fuel spark ignition engine [37]. After most of the combustion is complete for fast-burning fuels (especially with oxygen enrichment), the remaining HRR signal is small in magnitude and more susceptible to signal noise. This is the reason of waveform pattern visible at the end of HRR curve. In addition to this, SI engines, especially under low load, exhibit cycle-to-cycle variation due to turbulence and fuel-air mixing dynamics. This is discussed in the subsequent section.

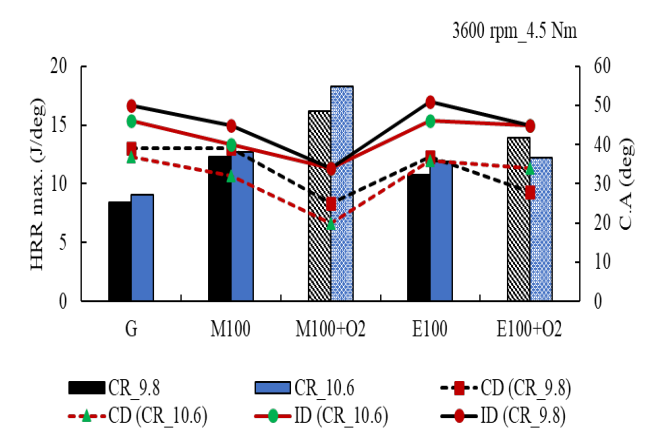


Figure 11. Comparison of max. HRR, combustion duration, and ignition delay with M100 and E100 at different conditions at 4.5 Nm, 3600 rpm.

3.3 Variation of Maximum (Rate of Pressure Rise) ROPR And Its Crank Angle Position

OE increased the max. ROPR by more than 2.5 times with M100 and 40.8% with E100 compared to base gasoline (Figure 12). The positions shifted much closer to TDC. With M100 and E100, it was 4 deg bTDC and 4 deg aTDC.

Max. ROPR was higher with M100 than with either base gasoline and E100. ROPR depends on various factors such as flame speed, turbulence inside the cylinder, the calorific value of the fuel, latent heat of vaporisation, and oxygen content [38-40]. High calorific value and turbulence result in high ROPR. The calorific values of M100 and E100 are lower than gasoline. Their flame speed and oxygen content ensure better and complete combustion which results in a high rate of pressure rise. Furthermore, methanol is a highly reactive fuel. All these factors increased the rate of pressure rise with M100. These factors would dominate the effect of its lower calorific value which could have decreased the ROPR. In the case of E100, the flame speed is not as high as M100 causing low ROPR. In addition to this, E100 breaks into triatomic molecules having high specific heat which lowers the in-cylinder temperature, and thus the rate of pressure rise could decrease. Since OE results in enhanced flame speed and combustion rate, ROPR would increase. More oxygen helps in the proper mixing of air and fuel and improves the combustion hence rate of pressure rise could increase.

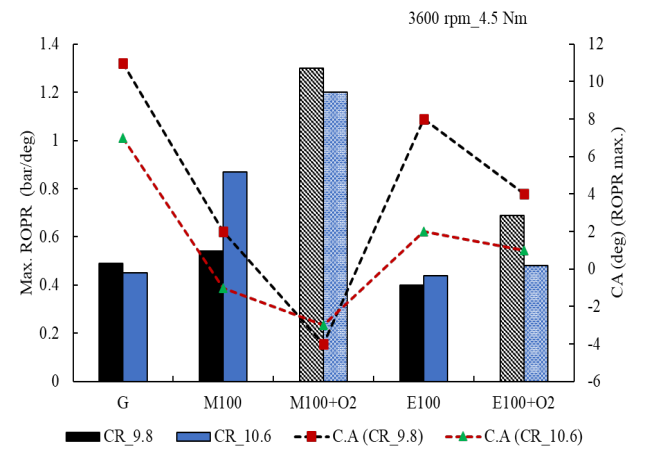


Figure 12. Comparison of max. ROPR with M100 and E100 at different conditions.

At high compression ratio, max. ROPR increased by 61% to 0.87 bar/deg with M100. With E100, it increased by 10%. At high CR, the positions were -1(bTDC) and 2 deg (aTDC) with M100 and E100. A high compression ratio increases the temperature as well as turbulence in the cylinder. As a result, the rate of heat release is improved which increased the maximum rate of pressure rise with alcohol fuels. Compared to gasoline, max. ROPR with E100 was slightly less at high CR. The low calorific value might lead to the generation of a low rate of pressure. It is clear from the values of peak pressure with E100 also, which is higher than gasoline but not at the level of M100. In this context, the fact that the reactivity of methanol is higher than E100, cannot be ignored.

With OE at high CR, max. ROPR with M100 increased by 2.7 times and with E100 by 20% compared to base gasoline. The corresponding crank angle positions advanced by 5 and 7 deg with M100 and E100. The positions were -3 (bTDC) and 1 deg (aTDC) with OE at high CR which was 7 deg (aTDC) with base gasoline. The degree of constant volume combustion is thus enhanced with OE at high CR.

In this method, the individual effect of OE and increased compression ratio is combined and in combination, the effect is more pronounced. With OE, the generation of active radicals such as OH, O, H etc. is more which caused rapid heat release, and thus the rate of pressure rise increases. In

addition, the turbulence level increases, and residual gas fraction decreases at high CR. All these factors contribute to high in-cylinder temperature and high rate of pressure rise.

3.4 Cycle-To-Cycle Variations in Imepnet

Figure 13 and 14 show the COV in IMEP with M100 and E100 fuels. The COV_{IMEP net} decreased from 2.38% to 1.97% with M100 and from 3.8% to 2.98% with E100 with oxygen enrichment (Figure 15). It should be noted that the experiments were conducted using an older dynamometer setup, which may have contributed to higher apparent frictional losses and deviations between IMEP and brake mean effective pressure values (BMEP). However, this does not affect the reliability of the comparative results and the observed trends between ethanol, methanol, and gasoline. Oxygen enrichment reduces the cyclic fluctuations in initial flame formation [35]. It implies that flame development and flame propagation are improved with oxygen enrichment resulting in better combustion. Therefore, cycle-to-cycle variations decreased with M100 and E100.

A lean mixture, incomplete combustion, low flame speed, and less ignition intensity are some of the factors which contribute to the cycle-to-cycle variations during combustion in SI engines [41]. The burning rate of charge inside the cylinder is influenced by variations in gas motion, amount of air, fuel, recycled exhaust gas, residual gases, and mixture composition near the spark plug. These factors depend on engine design and operating parameters and affect the cyclic variations [42].

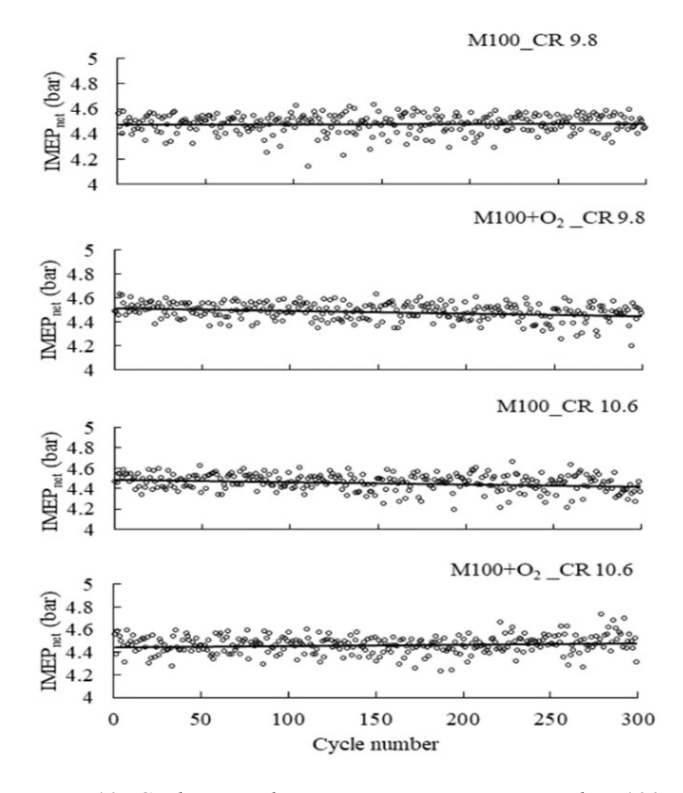


Figure 13. Cycle-to-cycle variations in IMEPnet with M100 at various conditions.

With the increase of compression ratio, the turbulence intensity increases, and cylinder pressure and temperature both increases. Squish intensity increase and combustion duration decrease at high CR. It improves flame kernel growth and thus flame propagation. As a result of this, the COV_{IMEP} decreased with M100 and E100 to 1.67%. With the increase in compression ratio, the cycle-to-cycle variations

decrease due to engine operation at high temperatures. The amount of residual gases decreases at high CR. The amount of residual gases change in every cycle. The decrease in their fraction and increase of turbulence and flame speed at high CR results in the decrease of the cycle-to-cycle variations.

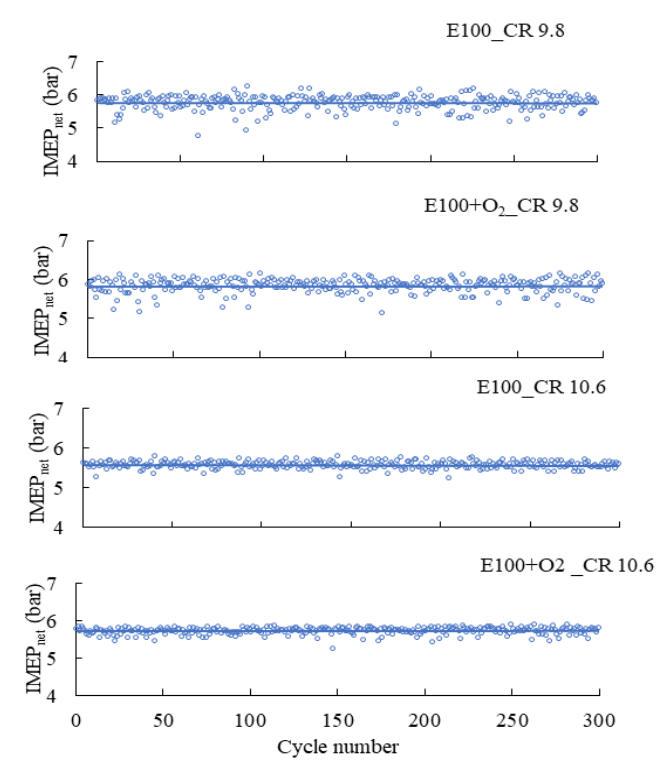


Figure 14. Cycle-to-cycle variations in IMEPnet with E100 at various conditions.

With the combined effect of high compression ratio and oxygen enrichment, the turbulence is dominant further with the additional factor of a decrease in residual gases. High amounts of residual gases hinder the formation of the flame kernel and thus flame development and propagation become difficult. Due to improved combustion, the COV_{IMEP} decreased to 1.48% with M100 and E100. With oxygen enrichment, the mixture formation of air and fuel is improved. The in-cylinder temperature increases and combustion become better. The quality of heat increases which enhances the work output. The flame speed increases and the combustion is completed in less time. All these factors contribute to a decrease in cyclic variations in IMEP. With oxygen enrichment at high compression ratio, the effect is cumulative and cyclic variations decreased further.

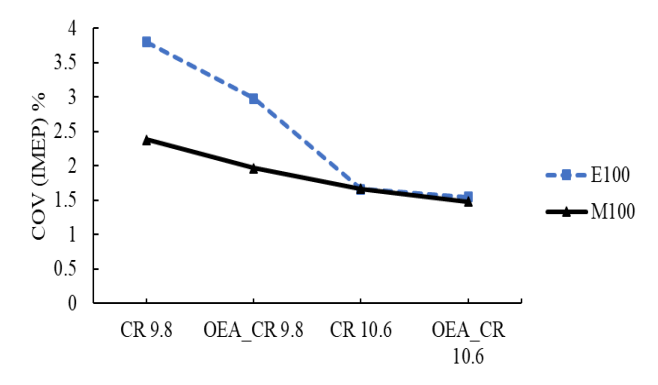


Figure 15. COV_{IMEP} net with M100 and E100 at various conditions.

It is also observed from the figure that at the base condition the COV was less with M100 than with E100. It is due to better combustion with M100 on account of its high laminar flame speed, more oxygen content, and lean burning ability. The high flame diffusivity helps in the formation of a homogenous air-fuel mixture and thus promotes better combustion with M100. In addition to this, the formation of OH radicals is also higher with M100 which is helpful in flame propagation.

3.5 Summary of Discussion

The summary of results and discussion section is tabulated in Table 7. All experimental data in Table 2 are reported at a constant torque of 4.5 Nm, which corresponds to the maximum torque achievable with methanol (M100) under the tested conditions. This torque value was selected as a reference point to ensure a fair and consistent comparison of the combustion and performance characteristics of different fuels under identical load conditions. Evaluating the fuels at the same operating torque eliminates variability due to load differences and isolates the effect of fuel properties, allowing for a more accurate assessment of their performance across various combustion parameters.

Symbol indication: "↑↑↑"- drastic increase, "↑↑"- significant increase, "↑"- moderate increase, "--" - comparable to base gasoline, "↓↓↓"- drastic decrease, "↓↓"- significant decrease, "↓"- moderate decrease

Table 7. Summary of discussion with M100 and E100 fuels.

Parameter	M100 (max. torque)	E100 (lower torque)
Peak cylinder pressure	↑↑↑ ↑ ↑↑	↑ ↑
Max. HRR	↑↑↑ ↑ ↑↑↑	1-↑↑ 2 3-↑↑
Max. ROPR	↑↑↑ ↑↑ ↑↑↑	↑↑ ↑
Combustion duration	↓	↓↓ ↓
Ignition delay	↓↓ ↓ ↓↓	 ↓ ↓

4. Conclusions

Experiments were conducted on a single-cylinder fourstroke spark-ignition engine fuelled with methanol and ethanol to study the combustion characteristics using oxygen-enriched air and increased compression ratio. The important points that emerged from the study are given below:

The P_{max} increased drastically by 56.5% with M100 and by 17.6% with E100 compared to the base gasoline. It increased further significantly with oxygen enrichment at increased compression ratio. The increase in peak pressure was higher with M100 due to its high flame speed, more oxygen content and high reactivity than E100.

The maximum heat release rate increased by more than 92.2% with M100 and by 65.4% with E100 due to oxygen enrichment. High rate of heat release caused the fast burning of fuel and shorten the combustion duration and ignition

delay. Combustion duration shortened by 35.8% with M100 and 28.2% with E100.

Due to oxygen enrichment, the combustion improved resulting in high rate of pressure rise with M100 and E100. The maximum rate of pressure rise increased by 2.5 times with M100 and 40.8% with E100 compared to base gasoline at the base compression ratio. The trend was similar at increased compression ratio and with oxygen enrichment at increased CR.

With oxygen enrichment, the combustion parameters including $P_{\text{max}},$ HRR, and ROPR improved resulting in a decreased cycle-to-cycle to variations. The COVIMEP net decreased from 2.38% to 1.97% with M100 and from 3.8% to 2.98% with E100 with oxygen enrichment.

The effect of oxygen enrichment was more prominent with M100 than E100 at both the compression ratios. The effect was greater at higher compression ratio than the base.

In future work, it's important to explore emissions performance under oxygen-enriched conditions to better understand environmental impacts alongside efficiency gains. Investigating knock tendency, combustion stability over extended cycles, and using advanced diagnostics like optical imaging can offer deeper insights into flame behaviour and in-cylinder dynamics. Studying fuel blends and applying CFD and chemical kinetics modelling could further support optimization. Finally, long-term durability testing is recommended to evaluate the practical feasibility of using oxygen-enriched air with alcohol fuels in real engine applications.

Acknowledgement

Author is thankful to *the Engine and Unconventional Fuels Laboratory, IIT Delhi* where experimental work was carried out during doctoral work under the supervision of Prof. Dr. K. A. Subramanian.

Conflict of Interest

The author approves that to the best of knowledge; there is not any conflict of interest or common interest with an institution/organization or a person that may affect the review process of the paper.

Credit Author Statement

Nidhi: Data Analysis and Interpretation, Writing

Nomenclature

Spark Ignition
Compression Ratio
Internal Combustion
Methanol (100%)
Ethanol (100%)
Methanol blend with X% of gasoline
Ethanol blend with X% of gasoline
Brake Mean Effective Pressure
Brake Specific Fuel Consumption
Indicated Mean Effective Pressure
Coefficient of Variance
Brake Thermal Efficiency
Pressure Volume Curve
Volumetric Efficiency
Carbonmonoxide
Hydrocarbon
Nitrogen oxides
Peak pressure [bar]

ROPR Rate of Pressure Rise
HRR Heat Release Rate [J/deg.]
(a/b) TDC After/Before Top Dead Centre

OEAOxygen Enriched AirOEOxygen EnrichmentCDCombustion Duration

BS Bharat Stage C.A Crank Angle

 $V_{crevice}$ Crevice volume of cylinder [m³] V_{swept} Swept volume of cylinder [m³] $V_{clearance}$ Clearance volume of cylinder [m³] $V_{clearance\ gap}$ Volume of clearance gap [m³]

B Cylinder bore [mm]
L Cylinder length [mm]
P In-cylinder pressure [bar]
V Instantaneous volume [m³]
γ Ratio of specific heats

Orank angle

References:

- [1] E. Lindstad, T. Ø. Ask, P. Cariou, G. S. Eskeland and A. Rialland, "Wide use of renewable energy in transport," *Transportation Research Part D: Transport and Environment*, vol. 119, June 2023, Art. no. 103713, doi: 10.1016/j.trd.2023.103713.
- [2] S. Shafiee and E. Topal, "When will fossil fuel reserves be diminished?," *Energy Policy*, vol. 37, no. 1, pp. 181–189, Jan. 2009, doi: 10.1016/j.enpol.2008.08.016.
- [3] Z. Tian, X. Zhen, Y. Wang, D. Liu, and X. Li, "Comparative study on combustion and emission characteristics of methanol, ethanol and butanol fuel in TISI engine," *Fuel*, vol. 259, Jan. 2020, Art. no. 116199, doi: 10.1016/j.fuel.2019.116199.
- [4] A. M. Pourkhesalian, A. H. Shamekhi, and F. Salimi, "Alternative fuel and gasoline in an SI engine: A comparative study of performance and emissions characteristics," *Fuel*, vol. 89, no. 5, pp. 1056–1063, May 2010, doi: 10.1016/j.fuel.2009.11.025.
- [5] Y. Li, X.-S. Bai, M. Tunér, H. G. Im, and B. Johansson, "Investigation on a high-stratified direct injection spark ignition (DISI) engine fueled with methanol under a high compression ratio," *Applied Thermal Engineering*, vol. 148, pp. 352–362, Feb. 2019, doi: 10.1016/j.applthermaleng.2018.11.065.
- [6] X. Li, X. Zhen, Y. Wang, and Z. Tian, "Numerical comparative study on performance and emissions characteristics fueled with methanol, ethanol and methane in high compression spark ignition engine," *Energy*, vol. 254, Sept. 2022, Art. no. 124374, doi: 10.1016/j.energy.2022.124374.
- [7] X. Li, X. Zhen, S. Xu, Y. Wang, D. Liu, and Z. Tian, "Numerical comparative study on knocking combustion of high compression ratio spark ignition engine fueled with methanol, ethanol and methane based on detailed chemical kinetics," *Fuel*, vol. 306, Dec. 2021, Art. no. 121615, doi: 10.1016/j.fuel.2021.121615.
- [8] Q. Duan, X. Yin, X. Wang, H. Kou, and K. Zeng, "Experimental study of knock combustion and direct injection on knock suppression in a high compression

- ratio methanol engine," *Fuel*, vol. 311, Mar. 2022, Art. no. 122505, doi: 10.1016/j.fuel.2021.122505.
- [9] T. G. Leone et al., "The Effect of Compression Ratio, Fuel Octane Rating, and Ethanol Content on Spark-Ignition Engine Efficiency," Environ. Sci. Technol., vol. 49, no. 18, pp. 10778–10789, Sept. 2015, doi: 10.1021/acs.est.5b01420.
- [10] O. I. Awad, R. Mamat, M. M. Noor, T. K. Ibrahim, I. M. Yusri, and A. F. Yusop, "The impacts of compression ratio on the performance and emissions of ice powered by oxygenated fuels: A review," *Journal of the Energy Institute*, vol. 91, no. 1, pp. 19–32, Feb. 2018, doi: 10.1016/j.joei.2016.09.003.
- [11] P. Sakthivel, K. A. Subramanian, and R. Mathai, "Effects of different compression ratios and spark timings on performance and emissions of a two-wheeler with 30% ethanol-gasoline blend (E30)," *Fuel*, vol. 277, May 2020, Art. no. 118113 doi: 10.1016/j.fuel.2020.118113.
- [12] M. K. Balki and C. Sayin, "The effect of compression ratio on the performance, emissions and combustion of an SI (spark ignition) engine fueled with pure ethanol, methanol and unleaded gasoline," *Energy*, vol. 71, pp. 194–201, July 2014, doi: 10.1016/j.energy.2014.04.074.
- [13] B. S. Nuthan Prasad, J. K. Pandey, and G. N. Kumar, "Impact of changing compression ratio on engine characteristics of an SI engine fueled with equi-volume blend of methanol and gasoline," *Energy*, vol. 191, Jan. 2020, Art. no. 116605, doi: 10.1016/j.energy.2019.116605.
- [14] C. Wouters, P. Burkardt, and S. Pischinger, "Limits of compression ratio in spark-ignition combustion with methanol," *International Journal of Engine Research*, vol. 23, no. 5, pp. 793–803, May 2022, doi: 10.1177/14680874211043390.
- [15] C. Gong, F. Liu, J. Sun, and K. Wang, "Effect of compression ratio on performance and emissions of a stratified-charge DISI (direct injection spark ignition) methanol engine," *Energy*, vol. 96, pp. 166–175, Feb. 2016, doi: 10.1016/j.energy.2015.12.062.
- [16] M. B. Çelik, B. Özdalyan, and F. Alkan, "The use of pure methanol as fuel at high compression ratio in a single cylinder gasoline engine," *Fuel*, vol. 90, no. 4, pp. 1591–1598, Apr. 2011, doi: 10.1016/j.fuel.2010.10.035.
- [17] Y. Zhou *et al.*, "Potential of compression ratio and exhaust gas dilution on improving combustion and nitrogen oxides emission performance on a PFI engine fueled with methanol," *Fuel*, vol. 323, Sept. 2022, Art. no. 124197, doi: 10.1016/j.fuel.2022.124197.
- [18] L. Li, D. Qiu, and Z. Liu, "The Characteristic of Transient HC Emissions of the First Firing Cycle During Cold Start on an LPG SI Engine," Toronto, Canada, Oct. 2006, doi: 10.4271/2006-01-3403.
- [19] J. A. Caton, "The Effects of Oxygen Enrichment of Combustion Air for Spark-Ignition Engines Using a Thermodynamic Cycle Simulation," in ASME 2005 Internal Combustion Engine Division Spring Technical

- *Conference*, Chicago, Illinois, USA: ASMEDC, pp. 135–147, Jan. 2005, doi: 10.1115/ICES2005-1006.
- [20] P. Seers, F. Foucher, and C. Mounaïm-Rousselle, "Influence of O₂ -enriched intake air with CO₂ dilution on the combustion process of an optically accessible spark-ignition engine," *International Journal of Engine Research*, vol. 14, no. 1, pp. 34–44, Feb. 2013, doi: 10.1177/1468087412442122.
- [21] Nidhi and K. A. Subramanian, "Experimental investigation on effects of oxygen enriched air on performance, combustion and emission characteristics of a methanol fuelled spark ignition engine," *Applied Thermal Engineering*, vol. 147, pp. 501–508, Jan. 2019, doi: 10.1016/j.applthermaleng.2018.10.066.
- [22] J. Jeevahan, A. Poovannan, V. Sriram, R. B. Durai Raj, G. Maghwaran, and G. Britto Joseph, "Effect of intake air oxygen enrichment for improving engine performance and emissions control in diesel engine," *International Journal of Ambient Energy*, vol. 40, no. 1, pp. 96–100, Jan. 2019, doi: 10.1080/01430750.2017.1372811.
- [23] T. T. Maxwell, V. Setty, J. C. Jones, and R. Narayan, "The Effect of Oxygen Enriched Air on the Performance and Emissions of an Internal Combustion Engines," Philadelphia, Pennsylvania, United States, Oct. 1993, Art. no. 932804. doi: 10.4271/932804.
- [24] A. A. Quader, "Exhaust Emissions and Performance of a Spark Ignition Engine Using Oxygen Enriched Intake Air," *Combustion Science and Technology*, vol. 19, no. 1–2, pp. 81–86, Nov. 1978, doi: 10.1080/00102207808946869.
- [25] S. Kajitani, N. Sawa, T. McComiskey, and K. T. Rhee, "A Spark Ignition Engine Operated by Oxygen Enriched Air," San Francisco, California, United States, Oct. 1992, Art. no. 922174. doi: 10.4271/922174.
- [26] R. B. Poola, H. K. Ng, R. R. Sekar, J. H. Baudino, and C. P. Colucci, "Utilizing Intake-Air Oxygen-Enrichment Technology to Reduce Cold-Phase Emissions," Toronto, Canada, Oct. 1995, Art. no. 952420. doi: 10.4271/952420.
- [27] J. Heywood, *Internal Combustion Engine Fundamentals 2E*, 2nd edition. New York, N.Y: McGraw-Hill Education, 2019.
- [28] S. Verhelst, J. W. Turner, L. Sileghem, and J. Vancoillie, "Methanol as a fuel for internal combustion engines," *Progress in Energy and Combustion Science*, vol. 70, pp. 43–88, Jan. 2019, doi: 10.1016/j.pecs.2018.10.001.
- [29] H. Köten, Y. Karagöz, and Ö. Balcı, "Effect of different levels of ethanol addition on performance, emission, and combustion characteristics of a gasoline engine," *Advances in Mechanical Engineering*, vol. 12, no. 7, July 2020, Art. no. 1687814020943356, doi: 10.1177/1687814020943356.
- [30] X. Li, X. Zhen, Y. Wang, and Z. Tian, "Numerical comparative study on performance and emissions characteristics fueled with methanol, ethanol and methane in high compression spark ignition engine,"

- *Energy*, vol. 254, Sept. 2022, Art. no. 124374, doi: 10.1016/j.energy.2022.124374.
- [31] V. Ya. Basevich, S. M. Kogarko, and G. A. Furman, "The reaction of methanol with atomic oxygen," *Russ Chem Bull*, vol. 24, no. 5, pp. 948–952, May 1975, doi: 10.1007/BF00922939.
- [32] P. Geng, H. Zhang, and S. Yang, "Experimental investigation on the combustion and particulate matter (PM) emissions from a port-fuel injection (PFI) gasoline engine fueled with methanol–ultralow sulfur gasoline blends," *Fuel*, vol. 145, pp. 221–227, Apr. 2015, doi: 10.1016/j.fuel.2014.12.067.
- [33] X. Cai, J. Wang, W. Zhang, Y. Xie, M. Zhang, and Z. Huang, "Effects of oxygen enrichment on laminar burning velocities and Markstein lengths of CH4/O2/N2 flames at elevated pressures," *Fuel*, vol. 184, pp. 466–473, Nov. 2016, doi: 10.1016/j.fuel.2016.07.011.
- [34] S. M. Sarathy, P. Oßwald, N. Hansen, and K. Kohse-Höinghaus, "Alcohol combustion chemistry," *Progress in Energy and Combustion Science*, vol. 44, pp. 40–102, Oct. 2014, doi: 10.1016/j.pecs.2014.04.003.
- [35] X. Zhang, Y. Duan, R. Zhang, H. Wei, and L. Chen, "Optical study of oxygen enrichment on methane combustion characteristics under high compression-ratio conditions," *Fuel*, vol. 328, Nov. 2022, Art. no. 125251, doi: 10.1016/j.fuel.2022.125251.
- [36] D. N. Assanis, R. B. Poola, R. Sekar, and G. R. Cataldi, "Study of Using Oxygen-Enriched Combustion Air for Locomotive Diesel Engines," *Journal of Engineering for Gas Turbines and Power*, vol. 123, no. 1, pp. 157–166, Jan. 2001, doi: 10.1115/1.1290590.
- [37] X. Li *et al.*, "Exploring the effects of compression ratio and initial flame kernel radius on combustion characteristics and fuel economy of a dual-fuel spark ignition engine under oxy-fuel combustion mode," *Fuel*, vol. 385, Apr. 2025, Art. no. 134098, doi: 10.1016/j.fuel.2024.134098.
- [38] J. Skřínský, "Measurement and Calculation of Explosion Pressure for Hydroxyl Substituted Hydrocarbons Mixture," MATEC Web Conf., vol. 168, p. 06006, 2018, doi: 10.1051/matecconf/201816806006.
- [39] Z. H. Huang *et al.*, "Combustion characteristics and heat release analysis of a compression ignition engine operating on a diesel/methanol blend," *Proceedings of the Institution of Mechanical Engineers, Part D: Journal of Automobile Engineering*, vol. 218, no. 9, pp. 1011–1024, Sept. 2004, doi: 10.1243/0954407041856818.
- [40] Z. Chen, J. Deng, H. Zhen, C. Wang, and L. Wang, "Experimental Investigation of Hydrous Ethanol Gasoline on Engine Noise, Cyclic Variations and Combustion Characteristics," *Energies*, vol. 15, no. 5, p. 1760, Feb. 2022, doi: 10.3390/en15051760.
- [41] M. Ghaderi Masouleh, K. Keskinen, O. Kaario, H. Kahila, S. Karimkashi, and V. Vuorinen, "Modeling cycle-to-cycle variations in spark ignited combustion engines by scale-resolving simulations for different

- engine speeds," *Applied Energy*, vol. 250, pp. 801–820, Sept. 2019, doi: 10.1016/j.apenergy.2019.03.198.
- [42] J. Zheng, Z. Huang, J. Wang, B. Wang, D. Ning, and Y. Zhang, "Effect of compression ratio on Cycle-by-
- Cycle variations in a natural gas direct injection engine," Energy & Fuels, vol. 23, no. 11, pp. 5357–5366, Nov. 2009, doi: 10.1021/ef900651p.

Review Article

Vol. 28 (No. 4), pp. 308-319, 2025 doi: 10.5541/ijot.1729632 Published online: December 1, 2025

Performance, Emissions, Optimization of Ammonia and Biodiesel Utilization in Compression Ignition Diesel Engines: A Review

¹*D. H. T. Prasetiyo, ¹A. Sanata, ²G. A. Rahardi, ³A. Muhammad

¹Department of Mechanical Engineering, Faculty of Engineering, University of Jember, Indonesia ²Department of Electrical Engineering, Faculty of Engineering, University of Jember, Indonesia ³Department of Mechanical Engineering, Faculty of Engineering and Informatics, University of Panca Marga, Indonesia E-mail: ^{1*} dani.hari@unej.ac.id

Received 1 July 2025, Revised 12 October 2025, Accepted 19 November 2025

Abstract

The global energy crisis and decarbonization demands emphasize the need for low-carbon fuels that remain compatible with conventional diesel engines. Ammonia and biodiesel have emerged as complementary candidates for compression ignition engine applications. This article summarizes 56 publications discussing engine performance, emission characteristics, and optimization strategies for their use, both separately and in dual-fuel configurations. The study results show that a blend of 40% ammonia and 60% biodiesel can increase thermal efficiency by up to 21.3%, decrease specific fuel consumption by 4.06%, and reduce CO₂ emissions by 6.6% compared to pure diesel. A dual injection strategy with a timing of 25° BTDC proved effective in shortening the ignition delay and increasing heat release. Predictive approaches based on Artificial Neural Network (ANN) and Response Surface Method (RSM) also demonstrated high accuracy (R² > 0.99). However, significant technical challenges remain, particularly increased NOx emissions, ammonia slip, and N₂O formation. This study confirms the potential of ammonia—biodiesel as a transition fuel towards a low-carbon energy system, requiring the implementation of emission control technologies, precision injection engineering, and adaptive combustion strategies. Open research areas include long-term durability testing, performance in multi-cylinder engines under transient conditions, and the development of a multi-objective optimization algorithm based on the integration of ANN, RSM, and evolutionary methods.

Keywords: Biodiesel; ammonia; compression ignition engines; exhaust emissions; dual-fuel combustion.

1. Introduction

The global environmental crisis is increasingly fueled by reliance on fossil fuels, which are a major contributor to CO₂ emissions and accelerated global warming [1]. Diesel engines, despite their high thermal efficiency, remain a significant source of CO₂, NO_x, and harmful particulate emissions [2]. This phenomenon is not only an ecological threat but also a multidimensional pressure trigger for the modern energy and transportation system to undergo comprehensive reforms. This situation emphasizes the urgency of a transition to low-carbon fuels that can be integrated without requiring major changes to existing engine technology.

Ammonia (NH₃) is currently gaining attention as a potential carbon-free fuel candidate for internal combustion engines [3]. Its advantages include relatively high volumetric energy density, the availability of large-scale production lines based on renewable energy, and compatibility with existing distribution infrastructure [4]. In practical applications, ammonia is often configured with hydrocarbon fuels such as diesel or biodiesel in dual-fuel systems to overcome its limitations in ignition and flame stability [5], [6]. This naturally presents limitations in the form of high autoignition temperatures, low flame stability, and potential

 NO_x and ammonia slip emissions, making it a major implementation challenge [7].

Biodiesel, derived from biomass sources such as vegetable oils and animal fats, offers chemical characteristics that make it an attractive alternative energy source. Biodiesel, derived from vegetable oils and animal fats, offers complementary characteristics to ammonia. Its internal oxygen content supports more complete combustion, while its high cetane number accelerates reaction initiation [8]. However, biodiesel has drawbacks such as high viscosity, the potential for increased NO_x emissions, and corrosive effects on fuel injection systems.

Experimental and simulation studies have shown that ammonia-biodiesel blends have the potential to reduce carbon emissions without compromising engine performance [9]. Adjusting the injection strategy and blend ratio are key factors in optimizing combustion efficiency. Innovations such as multi-stage injection, in-situ hydrogen reforming, and artificial intelligence (ANN) and response surface method (RSM)-based approaches have proven promising in extending the operational range of dual-fuel systems [10]. Previous research also reported that the addition of 10% to 30% biodiesel increases ignition delay, peak cylinder pressure, and heat release rate, thus affecting the thermal dynamics of the combustion chamber [11].

*Corresponding Author Vol. 28 (No. 4) / 308

Considering the urgency of the energy transition and the need for low-carbon fuel solutions that are compatible with existing engine technology, this article aims to present a comprehensive scientific review of the use of ammonia and biodiesel in Compression Ignition (CI) diesel engines. The study focuses on fuel characteristics, their effects on engine performance and emissions, and the effectiveness of ANN and RSM-based optimization strategies. The study's main contributions are identifying research gaps, mapping emerging technological approaches, and offering technical policy directions to encourage the development of feasible and sustainable low-carbon dual-fuel systems.

2. Materials and Methods

This article is structured as a systematic literature review focusing on the utilization of ammonia and biodiesel in compression ignition diesel engines. The method used not only maps and classifies scientific sources but also conducts a thematic synthesis to identify trends, challenges, and development directions for dual-fuel systems. A schematic of the study methodology is shown in Figure 1.



Figure 1. Review methodology scheme.

The study is structured progressively. The initial section describes the basic characteristics of ammonia and biodiesel, followed by a discussion of dual-fuel strategies and their effects on engine performance. The analysis is then expanded to include key exhaust emissions, predictive modeling-based optimization strategies, and a critical evaluation of research gaps and technology development prospects. Literature sources were obtained from the ScienceDirect, IEEE Xplore, SpringerLink, and MDPI databases using the following keyword combinations: "ammonia fuel" OR "NH3 combustion," "biodiesel," "diesel engine" OR "compression ignition engine," "emissions" OR "performance," and "dual fuel" OR "co-combustion." The search process yielded over 300 articles. After screening based on title and abstract, 103 articles were selected, and 56 articles were retained as the primary sources for the analysis in Figure 2.

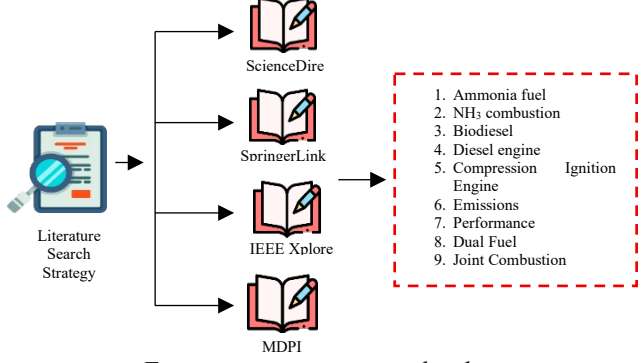


Figure 2. Literature search scheme.

Inclusion criteria included: (1) publication between 2015-2025, (2) focus on the utilization of ammonia, biodiesel, or their combination in CI diesel engines, and (3) use of experimental, numerical, or review approaches with data on performance, thermal efficiency, emissions, and fuel injection strategies. Conversely, articles that discussed ammonia outside the context of CI engines, were available only as abstracts, or did not present empirical data were excluded from the analysis. This selection approach ensured that the studies remained relevant to current technological developments and representative of research needs. The selected articles were classified into four main categories: (1) fuel physicochemical characteristics, (2) engine performance, (3) exhaust emission profiles, and (4) optimization strategies and predictive modeling (Figure 3). classification allowed for a structured comprehensive discussion of the technical and environmental implications of the ammonia-biodiesel dualfuel system.

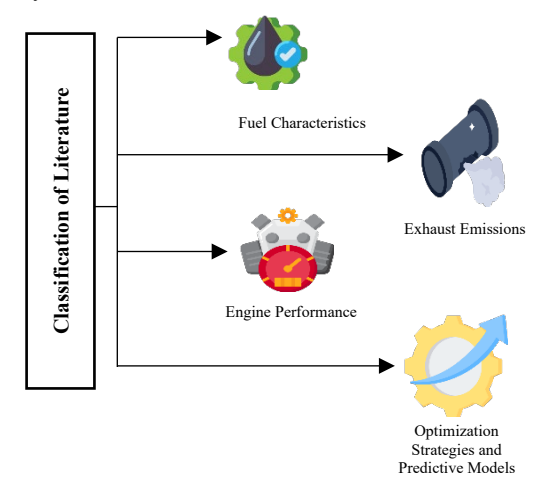


Figure 3. Main categories of research focus.

Data analysis was performed by examining operational parameters such as injection pressure, ignition timing, fuel mixture ratio, and combustion chamber temperature. Results from various studies were compared to identify consistent patterns, such as the relationship between ammonia—biodiesel mixture ratio and specific fuel consumption (BSFC), thermal efficiency, and emission characteristics. A synthesis of the results is presented within a thematic discussion framework visualized in Figure 4, allowing for objective generalizations and identifying future research directions.

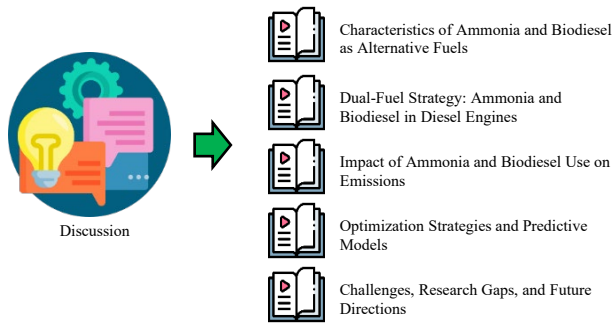


Figure 4. Discussion of journal article review results.

3. Results And Discussion

This section presents a thematic synthesis of key findings related to the utilization of ammonia and biodiesel in dualfuel systems for compression ignition diesel engines. An analysis of 56 experimental and numerical studies categorizes the results into four main aspects: (1) physicochemical characteristics of the fuel, (2) effects on combustion and engine performance, (3) impact on exhaust emissions, and (4) predictive model-based optimization strategies. Each aspect is comparatively evaluated based on operational variables, including mixture ratio, injection pressure, ignition timing, and injection pattern. This synthesis not only summarizes experimental trends but also assesses the effectiveness of the technologies and highlights research gaps that require further study.

3.1 Characteristics of Ammonia and Biodiesel as Alternative Fuels

The physicochemical properties of ammonia and biodiesel determine their suitability as alternative fuels, particularly in dual-fuel compression ignition systems that rely on flame stability, combustion rate, energy density, and emission profiles [12]. Ammonia offers the advantage of being a carbon-free fuel with a high octane rating and infrastructure compatibility, but is limited by its low energy density (18.6 MJ/kg) and high autoignition temperature (~650 °C), which prolongs ignition delay and increases the risk of NO_x and residual NH₃ emissions [13], [14], [15], [16], [17].

In contrast, biodiesel (FAME) offers a high cetane number (50–60) and an oxygen content of 10–12%, accelerating initial ignition and reducing CO, HC, and particulate emissions [18, 19], although it has the potential to increase NO_x due to its high combustion temperature [20]. The synergy of both fuels has been shown to be thermally and environmentally effective: biodiesel accelerates the formation of reactive radicals (OH, CH₃O) that favor ammonia decomposition, improving flame stability and combustion efficiency while reducing carbon emissions [21]. Dimitriou and Javaid [22], reported that configurations with ammonia energy fractions up to 95% maintained efficiency, as long as injection parameters and ignition timing were optimized.

3.2 Dual Fuel Strategy between Ammonia and Biodiesel in Diesel Engine

A dual-fuel strategy in diesel engines offers an efficient decarbonization solution, utilizing ammonia as a carbon-free fuel and biodiesel as a high-cetane pilot fuel [23]. This configuration can reduce fossil fuel consumption and GHG emissions without major engine modifications. In pilot injection mode, ammonia is supplied through the intake manifold, while biodiesel is injected directly into the combustion chamber to trigger ignition. Biodiesel shortens the ammonia ignition delay (~650°C, cetane number <10) by forming reactive radicals that accelerate thermal decomposition [24], [25], [26].

Alternatively, direct dual injection schemes using staged or differential injection techniques allow precise control of the mixture ratio, ignition timing, heat distribution, and cylinder pressure, resulting in increased efficiency and reduced emissions [25], [26], [27], [28]. The integration of in-situ reforming has also been shown to thermally generate hydrogen, accelerating combustion kinetics and reducing NH₃ and N₂O emissions [29]. The effectiveness of this configuration is measured through the Ammonia Energy Share (AES). Studies show that AES of 40–70% is suitable for partial loads [30], [31]; while AES of 60–80% is optimal for medium to high loads with significant CO₂ reduction.

AES >80% is only stable if supported by multi-stage injection, peak temperature cooling (e.g., via EGR), or insitu reforming. For example, the A40 configuration (40% ammonia, 60% citronella biodiesel) successfully reduced CO₂ emissions [32], and energy replacement of up to 69.4% with ammonia has been achieved without compromising engine stability [30]. On the other hand, low AES configurations such as D/B/N7.5 (7.5% ammonia) were reported to improve thermal efficiency (BTE) and reduce specific fuel consumption (BSFC) [33]. Schematic diagram of dual injection and ammonia—diesel/biodiesel fuel flow in a diesel engine in Figure 5.

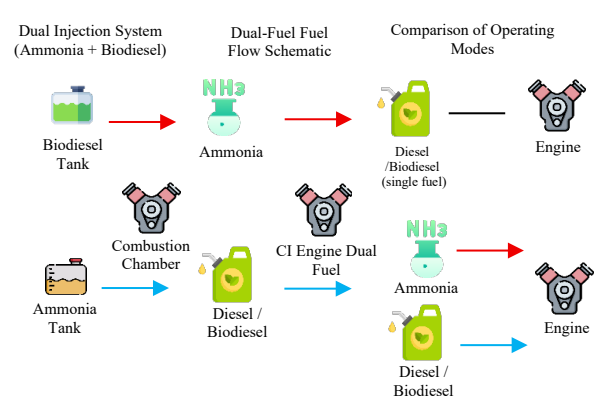


Figure 5. Schematic diagram of dual injection and ammonia–diesel/biodiesel fuel flow.

3.2.1 Combustion and Engine Performance

The ammonia and biodiesel dual-fuel configuration exhibits complex combustion dynamics but offers significant potential for improving diesel engine efficiency. As shown in Figure 6, ammonia serves as the primary fuel, while biodiesel acts as a pilot fuel, promoting early ignition due to its high cetane number and combustion stability. This combination is designed to overcome ignition delays caused by ammonia's high autoignition temperature (~650°C) and low cetane number. The classification of the impact of using a dual fuel configuration of ammonia and biodiesel can be seen in Figure 6.

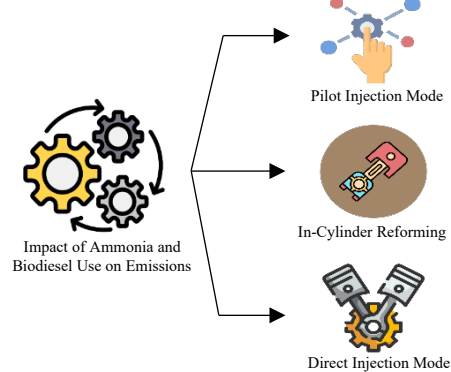


Figure 6. Dual-fuel configuration of ammonia and biodiesel.

Two approaches are commonly used: (1) intake fumigation and DI biodiesel, where ammonia is routed through the manifold and biodiesel is injected directly; and (2) dual direct injection (DDI) with staged or differential modes, which allows precise control of ignition delay, heat release rate (HRR), SOI, and injection pressure. The DDI configuration has been shown to regulate heat distribution, maintain flame stability at high AES, and reduce NO_x emissions [30], [34]. Nadimi et al. [30], showed that substitution of up to 69.4% biodiesel with ammonia

maintained BTE. Similar results were reported by Elkelawy et al. [34], who noted an increase in BTE from 20.5% to 23.5% and a decrease in BSFC from 455.56 g/kWh to 391.08 g/kWh using a blend of ammonia hydroxide and diesel. This correlation supports the importance of precise injection timing to optimize premixed combustion and prevent excessive heat release early in the cycle.

The ammonia-biodiesel ratio significantly affects HRR. A high biodiesel fraction accelerates ignition, while ammonia dominance without an adequate injection strategy risks causing a cylinder pressure spike [35]. Cheng et al. [36] emphasized that the stability of a dual-fuel system is highly dependent on the duration of the pilot fuel chemical delay. A study by Uyumaz et al. [37] also highlighted the potential of biodiesel from poppy seed oil as a non-food alternative with competitive thermal performance and reduced particulate emissions.

The addition of ammonia-water (25%) to diesel fuel has also been reported to affect combustion kinetics: ignition delay increases and combustion duration is prolonged, but HRR remains high and flame stability remains within operational limits [38]. Temizer and Cihan [39] showed that the addition of 3-6% hydrogen to canola biodiesel blends (B10, B20) increases peak pressure and combustion homogeneity, with the best performance achieved with B20 and 6% H₂. AVL-FIRE simulations support these findings. A study by Ince et al. [40] showed that B10 in a singlecylinder diesel engine increases power and torque and reduces BSFC by up to 17.54% compared to pure diesel (D100). However, the high oxygen content of B10 and B20 also increases NO_x and CO₂, highlighting a trade-off between efficiency and emissions, necessitating further optimization strategies.

Summary of Experimental Findings:

- B10 and B20 blends increase in-cylinder pressure compared to D100.
- Ignition delay in ammonia-biodiesel blends is shortened by higher biodiesel fractions, especially at low loads
- Thermal efficiency tends to decrease with higher biodiesel fractions due to the lower calorific value.

3.2.2 Dual Fuel Experimental Study

A series of experimental studies confirmed the effectiveness of an ammonia-biodiesel dual-fuel system in improving diesel engine performance and efficiency. Ramalingam et al. [38] reported that a blend of 40% ammonia with 60% biodiesel not only increased thermal efficiency by 5.4%, but also reduced NO_x emissions by 17%, CO₂ by 6.6%, and smoke by 9.8%. These findings highlight the synergy between the two fuels in reducing emissions without compromising engine performance. Similar results were reported by Elkelawy et al. [33], who demonstrated a 21.26% increase in thermal efficiency across five blends, accompanied by a 4.06% decrease in specific fuel consumption (BSFC), and significant reductions in NO_x and CO emissions compared to conventional diesel. Nadimi et al. [41] explored higher ammonia ratios, up to 84% of total energy, and found that engine stability was maintained. However, a spike in NO_x emissions was recorded when inadequate emission controls were not in place. These findings align with Cheng et al. [36], who emphasized that pilot injection timing is crucial to prevent pressure surges and excessive heat release, especially in premixed combustion modes. An additional study by Ramalingam et al., [38] showed that the use of a 25% ammonia-water blend in diesel fuel prolonged the ignition delay and combustion duration, although the HRR remained high and efficiency was not significantly degraded. This suggests that combustion dynamics can remain manageable as long as the blend characteristics are properly controlled. Temizer and Cihan [39] evaluated the addition of hydrogen (3-6%) to canola biodiesel blends (B10 and B20), and found increased peak pressure, more homogeneous mixture distribution, and the highest combustion stability in B20 + 6% H₂. These findings were confirmed by CFD simulations using AVL-FIRE. Meanwhile, İnce et al., [40] reported that the use of B10 in a single-cylinder diesel engine resulted in increased torque and power, as well as a 17.54% reduction in BSFC compared to D100. The use of B10 and B20 also reduced smoke opacity, although this resulted in increased NO_x and CO₂ emissions due to the high oxygen content in biodiesel. These findings highlight the trade-off between thermal efficiency and emissions, which requires further optimization of combustion strategies. Summary of the results of the experimental study of biodiesel and its mixtures in diesel engines can be seen in Table 1.

Table 1. Summary of experimental study results of biodiesel and its blends in diesel engines.

Engine Type and Operating Conditions	Fuel Type / Mixture Ratio	Focus and Parameters	Results	Ref.
Diesel engine, dual fuel mode	40% ammonia and 60% biodiesel	Efficiency and emissions	Efficiency up 5.4%; NOx emissions down 17%; CO ₂ down 6.6%; smoke down 9.8%.	[38]
Diesel engine with five mixture variations	Ammonia-biodiesel vs. pure diesel	Efficiency, fuel consumption, emissions	Efficiency increased by 21.26%; fuel consumption decreased by 4.06%; NO _x and CO were lower than pure diesel.	[33]
Diesel engine, stability test	84% NH ₃ and 16% biodiesel	Stability and emissions	Stable operation maintained; NO _x increased without aftertreatment	[41]
Diesel engine, pilot injection strategy	Ammonia and biodiesel	Combustion process	Injection timing critical to avoid excessive heat release and peak pressure	[36]
Diesel engine with ammonia-water-diesel blend	25% ammonia, air and diesel fuel	Combustion characteristics	Longer ignition delay; extended combustion duration; high HRR maintained	[38]
Direct-injection diesel + AVL-FIRE simulation	B10 and B20 biodiesel canola as well as 3%–6% hydrogen	Performance and combustion	Peak pressure and heat release rate increase; fuel distribution is more even; B20 and 6% H ₂ provide the most stable flame and highest efficiency.	[39]
Single-cylinder, 4-stroke, air-cooled diesel	D100, B10, B20	Power, torque, fuel consumption, emissions	B10 increases power, torque, and reduces fuel consumption by 17.54%; B10 and B20 reduce smoke, but increase NO_x and CO_2 .	[40]

3.3 Impact of Ammonia and Biodiesel Use on Emissions

Exhaust emission analysis is a fundamental component in assessing the technical, environmental, and sustainable feasibility of using alternative fuels in compression ignition engines. Conventional diesel engines generally produce emissions consisting of CO₂, NO_x, hydrocarbons (HC), carbon monoxide (CO), and significant amounts of particulate matter. Partial or complete substitution of diesel with ammonia or biodiesel results in changes in combustion characteristics that directly impact these emission patterns.

Ammonia is known as a carbon-free fuel; however, its complex combustion kinetics often result in ammonia slip (incompletely burned NH₃) and the formation of nitrous oxide (N₂O), both reactive pollutants that contribute to air quality degradation and increased global warming potential [31]. On the other hand, biodiesel through its natural oxygen content can reduce CO_2 and particulate matter emissions when used in diesel engines. However, various studies consistently show that both ammonia and biodiesel have a tendency to increase NO_x formation through thermal and NO-prompt mechanisms.

These findings indicate that the assumption regarding the potential of these two fuels to balance each other's environmental impacts has not been fully proven. In fact, their simultaneous use has the potential to increase the production of reactive nitrogen compounds, necessitating a more comprehensive emissions control strategy. Therefore, the implementation of a decarbonization pathway based on an ammonia-biodiesel blend must be accompanied by the implementation of NO_x mitigation technologies, such as selective catalytic reduction (SCR), exhaust gas recirculation (EGR), or intelligent control-based combustion parameter optimization.

To provide a more systematic analytical overview, the emissions evaluation in this study is classified into several main groups: CO₂, CO and HC, NO_x, NH₃ slip, N₂O, and particulates/soot. The reduction magnitude of each parameter is calculated using Equation (1), while the interaction between the variables is visualized in Figure 7. This relationship pattern demonstrates a clear trade-off between reducing carbon emissions and increasing nitrogen oxide components, particularly under oxygen-rich combustion conditions and high peak temperatures.

Reduction (%) =
$$\frac{X_{\text{diesel}} - X_{\text{blend}}}{X_{\text{diesel}}} \times 100\%$$
 (1)

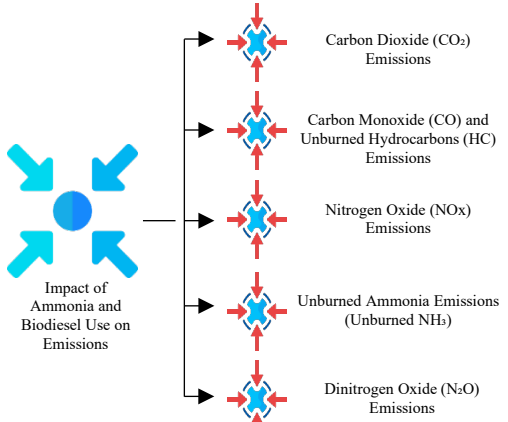


Figure 7. Impact of ammonia and viouseses use on emissions.

3.3.1 Carbon Dioxide (CO2) Emissions

As a carbon-free compound, ammonia does not produce CO₂ during combustion, unlike conventional fossil fuels such as diesel. This characteristic makes ammonia one of the most promising candidates for decarbonization strategies for the transportation sector, maritime industry, and internal combustion engine-based power plants [42]. In dual-fuel configurations, the use of ammonia has consistently been reported to reduce CO₂ emissions without decreasing thermal efficiency; some studies even indicate increased efficiency due to the more stable reactivity of the mixture.

Ramalingam et al. [32] found that the magnitude of CO₂ reduction is influenced by the ammonia energy share (AES), injection strategy, and engine operating conditions. For example, an A40 blend consisting of 40% ammonia and 60% citronella biodiesel in a low-temperature combustion engine configuration based on RCCI can reduce CO₂ emissions by up to 6.6% compared to pure diesel. Meanwhile, in large-scale maritime engine applications, the application of incylinder reforming gas recirculation (IRGR) techniques has been reported to reduce CO₂ emissions by up to 97% [29]. In theoretical scenarios, the use of pure ammonia has the potential to completely eliminate CO₂ emissions, although strict control of NO_x emissions is required [43], [44]. A comparison of research results related to CO₂ reduction is shown in Table 2.

Table 2. Results of comparison of carbon dioxide emissions

Tuble 2. Results of comparison of curbon dioxide emissions.				
Method	Operation Condition	CO ₂ Reduction (%)	Insight	Ref
A40 (40% ammonia + 60% biodiesel citronella)	Low-Temperature Combustion Engine - Reactivity Controlled Compression Ignition (LTC-RCCI)	6.6%	Good flame stability, suitable for partial loads	[32]
Ammonia-Diesel Dual Fuel (AES \geq 35.9%)	Marine diesel engines	97%	Reformed hydrogen enhances combustion; CO ₂ reduction is very significant	[29]
IRGR (In-cylinder Reforming Gas Recirculation)	CI engine/ generator	100%	Does not produce CO ₂ ; the main constraints are combustion stability and Nitrogen Oxides (NO _x) emissions.	[43], [44]

3.3.2 Carbon Monoxide (CO) and Unburned Hydrocarbons (HC) Emissions

The use of ammonia as a primary fuel tends to increase CO and HC emissions, mainly due to incomplete combustion due to ammonia's low reactivity. Conversely, the use of biodiesel as a pilot fuel can help reduce these emissions by improving initial flame stability. A study by Elkelawy et al. [33], showed that the D20B80N7.5 blend, containing a

higher portion of biodiesel, produced lower CO and HC emissions than a diesel-dominated blend. In addition, injection strategies such as split injection and ignition timing adjustment have been shown to reduce CO emissions by up to 25% compared to conventional combustion. The results of the study on CO and HC emissions from the use of ammonia as a fuel can be seen in Table 3.

Table 3. Carbon monoxide and unburned hydrocarbons emissions.

CO Emission Results	HC Emission Results	Description	Ref.
Down 21.4%	Reduced 15.68%	Optimal split injection	[38]
Decrease	Increased (33 ppm vs 14 ppm on diesel)	Incomplete combustion due to low temperature	[33]
Decrease	Not reported quantitatively	NH ₃ /CH ₄ produces lower CO	[45]
Decrease	Decrease	A40 (40% NH ₃ + citronella) showed high combustion efficiency.	[32]
Down 3.8%	Down 10.4%	The addition of NH ₃ increases evaporation and mixing.	[46]

3.3.3 Nitrogen Oxide (NO_x) Emissions

Various fuel injection parameters significantly influence the combustion and emission characteristics of ammonia-fueled engines. Increasing Total Start of Injection (TSOI) has been shown to shorten ignition delay, accelerate combustion, and suppress NO_x and N₂O emissions, although this is accompanied by an increase in ammonia slip. Setting the Start of Ammonia Injection (SOAI) at 8° CA ATDC has been reported to reduce NO_x emissions by more than 50%, while higher Ammonia Injection Pressure (AIP) improves combustion quality but tends to increase N₂O [47]. The impact of these parameters depends on the type of emissions observed. At high Ammonia Energy Share (AES), N₂O

emissions can increase up to >1000 times compared to nheptane, but remain low under optimal conditions (high temperature and low equivalence ratio). NO_x emissions are formed through three main pathways fuel-NO, prompt-NO, and thermal-NO with thermal-NO dominant above 2600 K. Meanwhile, the potential for soot formation decreases with lower carbon content. The soot formation equivalence ratio limit was recorded at ϕ = 2.20 for n-heptane, ϕ = 2.65 (AES 20%), ϕ = 5.05 (AES 50%), and was not reached at AES \geq 80%, confirming that the ammonia-based mixture has a very low tendency towards soot formation [48]. The summary of NO_x emission results is shown in Table 4.

Table 4. Nitrogen oxide emissions.

	8	
NO _x Emission Results	Description	Ref.
Increase	Because of the nitrogen in the fuel NH ₃	[22]
Decreased (to 91.2% N ₂ O)	With IRGR (in-cylinder reforming circulating gas)	[29]
Decrease	Because the exhaust temperature is lower	[34]
Decreasing (in rich condition)	The use of H ₂ /CH ₄ on NH ₃ limits NO _x	[45]
Down 17%	The result of A40 mixture in RCCI engine	[32]

3.3.4 Unburned Ammonia Emissions

One critical aspect of the ammonia combustion process is the formation of unburned ammonia due to slow reaction kinetics and combustion characteristics that tend to be difficult to trigger. The presence of NH₃ in the exhaust gas not only reflects the imperfection of the oxidation process, but also has significant toxicological and environmental implications. This compound has an acute irritating effect on the respiratory system, and contributes to the formation of secondary particulates through atmospheric reactions with acidic compounds. Therefore, controlling ammonia slip is a major technical challenge in the development of ammonia-fueled engines and dual-fuel configurations. Zhou et al. [29], showed that, under operating conditions without an integrated emission control strategy, the concentration of unburned NH₃ can reach 250 ppm—350 ppm. This value is

far above the exposure limits recommended by occupational safety standards and international ambient air quality guidelines, so it cannot be ignored in practical implementation. These findings underscore the urgency of implementing appropriate mitigation technologies, such as catalytic oxidation, equivalence ratio optimization, incylinder reforming, or temperature-based control strategies, to ensure that ammonia utilization does not pose secondary environmental risks. A summary of ammonia slip measurement results from various experimental and simulation studies is presented in Table 5, which shows variations in NH3 emission concentrations based on fuel configuration, injection strategy, engine operating conditions, and the presence of additional emission control technologies.

Table 5. Summary of unburned ammonia emission results under various conditions.

NH ₃ Emission Results	Operating Condition / Method	Description	Ref
High	General observation	Indicates the need for after-treatment technology	[22]
Down 89.3%	Implementation of IRGR (Internal EGR)	Significant reduction achieved with IRGR method	[29]
High (14,800 ppm)	Diesel-ammonia dual-fuel combustion	Substantial unburned NH3 observed in dual-fuel mode	[41]

3.3.5 Dinitrogen Oxide (N2O) Emissions

Nitrous oxide (N₂O) is a greenhouse gas with a global warming potential approximately 298 times greater than CO₂. This gas is formed in significant quantities when ammonia combustion occurs at moderate temperatures, especially when incomplete combustion occurs. A study by Jang et al. [49] noted that N₂O emissions can reach 0.3–0.5 g/kWh at high ammonia ratios. Controlling these emissions remains a major challenge, requiring high-precision combustion technology and effective post-combustion systems. Overall, the combination of ammonia and biodiesel

in a dual-fuel system has great potential to reduce carbon emissions, but still carries the risk of reactive nitrogen emissions. The success of its implementation is largely determined by the combustion strategy, adaptive injection system design, and the integration of appropriate postemission technologies.

3.3.6 Soot Emissions

Soot formation in diesel engines generally results from the incomplete combustion of carbon-rich fossil fuel mixtures. Ammonia, as a carbon-free fuel, does not form particle nuclei through the hydrocarbon pyrolysis pathway, thus theoretically eliminating the potential for soot formation. A study by Pedersen et al. [48] showed that increasing the Ammonia Energy Share (AES) significantly reduced the propensity for soot formation. At AES \geq 80%, the equivalence ratio for soot initiation was not reached, resulting in near-zero particulate emissions. Even at AES of 20–50%, the equivalence ratio limit for soot formation increased (ϕ = 2.65–5.05), significantly higher than that of n-heptane (ϕ = 2.20), indicating a significant reduction. Biodiesel as a pilot fuel also contributes to reduced soot emissions. Its internal oxygen content accelerates carbon oxidation during the diffusion phase of combustion [19]. However, a high biodiesel fraction can increase peak temperatures and promote NO_x formation. Therefore, blend

ratio optimization strategies need to consider the balance between soot reduction and reactive nitrogen emission control. A summary of factors affecting performance and emissions in the ammonia-biodiesel system can be seen in Table 6.

Ammonia-Biodiesel System Emission Summary:

- Biodiesel reduces CO, HC, and particulate matter, but tends to increase NO_x.
- Ammonia substitution of up to 80% can reduce CO₂ emissions by >90%, but has the potential to increase CO, HC, and NH₃ slip.
- Soot formation is virtually eliminated in blends with a high ammonia fraction.

Table 6. Summary of factors affecting performance and emissions in ammonia-biodiesel systems.

Parameters	Increasing Factors	Decreasing Factors	Determining Factors
NOx	 High ammonia fraction without control [41], [48] Long ignition delay [47] Small pilot or late injection [31] 	 Retard timing or split injection [47], [50] Dual injection staged [28] Lean burn, EGR, SCR [29], [34] 	Peak temperature,Combustion phasing,N content
СО & НС	 Low load with high AES [33], [41] Low combustion chamber temperature [33] Pilot too small/retarded [31] 	 High cetane biodiesel pilot [32], [33] Split injection [48] High injection pressure [47] 	Flame stability,Oxidation, internal oxygen
N ₂ O	 High AES, medium temperature [48] Long ignition delay [41] High EGR [29]	High temperature lean burn [48]In-situ hydrogen reforming [29]Fast injection [47]	Temperature 900–1100 K,Fuel-N₂O pathway
Soot	 Poor atomization [37] Low injection pressure [31]	 AES ≥80% (nearly zero soot) [44], [48] Oxidative pilot biodiesel [18], [41] Precise injection staging [29], [48] 	Fuel carbon,Internal oxygen,Mixture homogeneity
BTE	 Moderate AES (40–60%) [32], [33] Optimal CA50 [47] In-cylinder hydrogen reforming [29] 	High AES without optimization [41], [48]Low load (quenching) [36]	Combustion phasing,Injection strategy,
BSFC	 Low calorific value high AES [41], [48] Low efficiency, high CO/HC [33] 	 Injection optimization (ANN, RSM, GA) [32], [33], [50] In-cylinder reforming [29] Moderate AES with biodiesel pilot [32], [33] 	Mixture calorific value,Thermal efficiency,Injection optimization

3.4 Optimization Strategies and Predictive Models

Nitrous oxide (N2O) is a greenhouse gas with a global warming potential approximately 298 times greater than CO₂. In diesel engine regulations, the N₂O emission threshold is typically set at 0.3g/kWh. However, a study by Elbaz et al. [51] showed that in an ammonia-biodiesel dualfuel system, N₂O emissions can reach 0.3-0.5g/kWh, well within or even exceeding the recommended limit. This increase generally occurs during combustion at intermediate temperatures, particularly if the ignition delay is long or the flame is unstable. Therefore, combustion strategies need to be optimized so that the decarbonization benefits of ammonia are not offset by spikes in reactive nitrogen emissions. Mitigation measures include: (i) adjusting the ammonia-biodiesel energy ratio to maintain flame stability; (ii) adjusting the biodiesel injection timing to shorten the ignition delay and control the rate of heat release; and (iii) the application of staged or differential injection that effectively reduces local temperature peaks and N2O emissions without sacrificing efficiency [47], [50]. Integrating these strategies into an adaptive combustion model allows for real-time parameter adjustment, maintaining engine performance while minimizing N2O emissions.

3.4.1 Dual Fuel Injection Strategy

Injection timing and pattern play a key role in ammonia—biodiesel dual-fuel systems because they directly affect the ignition process, combustion stability, and emission

characteristics. Three main strategies commonly applied in the literature include.

(1) Pilot Injection

This strategy injects a small portion of biodiesel early to trigger ammonia ignition through the formation of active radicals (OH·, CH₃O·). Elumalai et al. [50] reported that injection at 25° BTDC increased Brake Thermal Efficiency (BTE) by 7.5% and reduced CO and HC emissions. The increase in BTE can be explained by Eq. (2):

$$\eta_{bth} = \frac{P_b}{\dot{m}_f x L H V} \times 100\% \tag{2}$$

(2) Multi-Stage Injection

Injection is divided into two or more stages to regulate heat distribution and reduce the rate of peak pressure rise. Chiong et al. [52] showed that this strategy effectively suppresses NO_x at high ammonia energy fractions. The total energy can be calculated using Eq. (3).

$$Q_{total} = \sum_{k=1}^{n} \dot{m}f, k \times LHV$$
 (3)

(3) Injection Pressure and Equivalence Ratio (φ) Settings

High pressure improves fuel atomization, resulting in a more homogeneous mixture. The equivalence ratio is calculated using Eq. (4).

$$\phi = \frac{(F/A)_{actual}}{(F/A)_{stoich}} \tag{4}$$

Operating under lean conditions (ϕ < 1) has been shown to reduce combustion temperature and NO_x emissions. Overall, the application of pilot injection, staged injection, and pressure and ϕ regulation are strategic foundations for achieving high thermal efficiency while controlling reactive carbon and nitrogen emissions in an ammonia–biodiesel dual-fuel system.

3.4.2 Application of Artificial Neural Network (ANN)

The complexity of ammonia-biodiesel dual-fuel systems is often difficult to address using conventional experimental approaches or deterministic models, primarily due to the non-linear relationships between parameters. In this context, Artificial Neural Networks (ANNs) have proven effective in predicting engine performance and optimizing operational parameters. Elkelawy et al. [52], developed an ANN model based on experimental data to map the effects of fuel ratio (diesel/biodiesel/ammonia) and injection angle on outputs such as thermal efficiency (BTE), specific fuel consumption (BSFC), and NO_x and CO emissions. The model demonstrated high accuracy with an R² > 0.99, confirming the reliability of ANNs in engine performance modeling. The advantages of ANNs include their ability to handle complex parameters, time efficiency compared to direct testing, and the potential to identify optimal configurations without trial and error. ANNs can also be used to design fuel injection maps, accelerate engine calibration, and support artificial intelligence-based control systems. Furthermore, the combination of ANN with optimization methods such as RSM or Genetic Algorithm (GA) improves design process efficiency and overall system performance. This approach opens up opportunities for developing smarter and more adaptive combustion engines, supporting the transition to low-carbon energy technologies.

3.4.3 Response Surface Method (RSM)

Response Surface Method (RSM) is a statistical technique used to design experiments, analyze interactions between variables, and build quadratic equation-based predictive models for multi-objective optimization. In a study by Krishnamoorthy et al. [32], RSM was applied to evaluate the effect of ammonia substitution ratio, injection

pressure, and ignition angle on thermal efficiency (BTE) and NO_x emissions. The results showed that the optimal configuration was achieved at 60% ammonia substitution, 700 bar injection pressure, and 27° BTDC injection angle, resulting in the highest BTE and the lowest NO_x emissions. The advantages of RSM lie in its efficiency in reducing the number of experiments, visually identifying parameter relationships, and providing reliable statistical model-based optimization solutions for engine operation settings.

3.4.4 Integration of ANN-RSM and Evolutionary Algorithms

The integration of Artificial Neural Networks (ANNs) and Response Surface Method (RSM) with evolutionary algorithms such as Genetic Algorithm (GA) and Particle Swarm Optimization (PSO) has proven effective in identifying optimal configurations for ammonia-biodiesel dual-fuel systems. This approach allows for the search for operating parameters that simultaneously maximize thermal efficiency (BTE) and minimize specific fuel consumption (BSFC). Experimental results show that in-cylinder reforming with 70%-80% ammonia energy substitution results in a consistent increase in BTE and decrease in BSFC [29]. Variation in composition from D80B20N7.5 to D20B80N7.5 shows a BTE increase of up to 21.26% and a BSFC decrease of 4.06% [33]. Ammonia energy substitution of 84% can maintain BTE up to 70%, but BSFC increases at higher ratios [41]. Meanwhile, RSM simulations identified an optimal point at 60% ammonia with an injection pressure of 700 bar [32]. The A40 formulation (40% ammonia) also showed a 5.4% increase in BTE compared to diesel [53], and the use of 20%-60% ammonia with a biodiesel pilot resulted in a 6–8% increase in BTE, despite an increase in BSFC [54]. In general, optimization success is determined not only by the ammonia energy ratio, but also by the injection strategy and the application of predictive algorithms capable of adaptively adjusting operating parameters. A comprehensive overview of performance and emission metrics from various experimental studies can be observed in Table 7. Combustion Strategy and Optimization:

- Dual pilot injection and injection timing are effective in reducing ignition delay and controlling NO_x emissions.
- The optimal blend is at a B10–B20 ratio with 40%–60% ammonia substitution, which provides the best balance between efficiency, performance, and emissions.

Table 7. A Comprehensive overview of performance and emission metrics from diverse experimental studies.

Fuel Configuration	Method	Ammonia Energy Substitution	Effect on BTE	Effect on BSFC	Ref.
In-cylinder NH ₃ Reforming	Experiment (multi- cylinder)	NH ₃ as 70% to 80% of the energy	Steady increase	Decrease	[29]
D80B20N7.5 to D20B80N7.5	ANN and Experiment	7.5% NH ₃ in all mixtures	Increase up to 21.26%	Decrease 4.06%	[33]
Ammonia and Biodiesel dual-fuel	Experiment CI engine	84%	Stable up to 70%; decreases above that	Increase when substitution >70%	[41]
RSM – D/B/N Variation	Simulation and Optimization	30% to 70% NH ₃	Optimum at 60%	Minimum at 700 bar pressure	[32]
Ammonia 40% and Biodiesel 60%	Experiment	40%	Increase 5.4% over diesel	Significant decrease	[53]
NH ₃ with Biodiesel pilot	Experiment	20% to 60%	Increase 6% to 8%	Increase	[54]

3.5 Challenges, Research Gaps, and Future Directions

Although ammonia—biodiesel blends hold promise as low-carbon diesel fuels, their industrial-scale implementation is hampered by the difficult-to-control nature of ammonia. High ignition temperatures (~650°C)

and low cetane number (<10) cause ignition delays, misfires, and NH₃ slip at low loads [16], [22], [55]. Furthermore, NO_x emissions increase through thermal and fuel-NO₂ pathways, which still rely on control systems such as EGR, SCR, or lean combustion most of which have not

yet progressed beyond the laboratory stage [8], [48], [56]. Most studies have been conducted on single-cylinder engines [28], [30], so the system response to variable loads and transient conditions in multi-cylinder engines is not yet fully understood. Practical experience shows that real-world implementation requires high-precision injection systems, multi-stage strategies, controlled air cooling, and adaptive thermal management. Additional challenges include metal corrosion (especially copper), elastomer damage, lubricant degradation, and component wear all of which have generally not been tested in long-term durability scenarios [35], [51], [56]. Future research directions include: (i) full testing on multi-cylinder engines with varying loads; (ii) integration of ANN-RSM models with multi-objective optimization (NSGA-II, MOPSO); (iii) development of sensor-based injection and closed-loop control; and (iv) long-term field testing to assess performance, material durability, and emissions. Life-cycle cost evaluation and economic analysis are also essential to assess its commercial viability. If technical challenges can be overcome, this system has the potential to be a low-carbon energy transition solution compatible with internal combustion engines.

4. Conclusions

The use of ammonia and biodiesel as alternative fuels in compression ignition diesel engines offers strategic opportunities in the transition to a low-carbon energy system. Ammonia effectively reduces CO2 and particulate emissions, while biodiesel thanks to its cetane number and oxygen content improves combustion stability. The combination of the two in a dual-fuel system has been shown to improve thermal efficiency, optimize flame characteristics, and reduce fossil fuel consumption. A review of 56 studies shows that ammonia substitution of up to 60% can increase efficiency by up to 20%, accompanied by reductions in BSFC and carbon emissions. However, technical challenges such as increased emissions of NO_x, NH₃ slip, and N₂O remain a concern. Controlling these emissions requires strategies such as injection timing, equivalence ratio optimization, and the implementation of post-combustion systems. Artificial intelligence-based predictive technologies (ANN, RSM) have proven effective in modeling performance and designing optimal operating parameters. The integration of optimization algorithms opens up opportunities for data-driven adaptive combustion systems. Despite its significant potential, issues such as flame stability, the readiness of multi-cylinder injection systems, and the impact of material wear still require further validation, particularly on an industrial scale and in longterm durability testing. By addressing these challenges, ammonia-biodiesel has the potential to become a solution for decarbonizing the transportation sector. Realizing this technology requires cross-sector support from academia, industry, and progressive public policy.

Conflict of Interest

The authors affirm that, to the best of their knowledge and judgment, they have no conflicts of interest whatsoever, whether financial or non-financial. Furthermore, the authors have no affiliations or common interests with any party, including institutions, organizations, or individuals, that could compromise the integrity, objectivity, or independence of the review or preparation of this article.

Credit Author Statement

Dani Hari Tunggal Prasetiyo: Conceptualization, Methodology, Formal analysis, Software, Writing-original draft, Project administration. Andi Sanata: Data curation, Resource, Investigation, Writing- Reviewing and Editing. Gamma Aditya Rahardi: Software, Validation, Visualization. Alief Muhammad: Supervision, Funding acquisition.

Nomenclature

ANN	Artificial Neural Network [-]
AIP	Ammonia Injection Pressure [bar]
AES	Ammonia Energy Share [%]
BTE	Brake Thermal Efficiency [%]

BSFC Brake Specific Fuel Consumption [g/kWh]

CA Crank Angle [°]

CI Compression Ignition [-]
 CO Carbon Monoxide [ppm]
 CO₂ Carbon Dioxide [ppm or %]
 EGR Exhaust Gas Recirculation [-]

HC Hydrocarbon Emissions [ppm]
HRR Heat Release Rate [J/°CA or kW]

NH₃ Ammonia [-]

NO_x Nitrogen Oxides [ppm or g/kWh]

N₂O Dinitrogen Oxide (Nitrous Oxide) [ppm or g/kWh]

RSM Response Surface Method [-]

SOAI Start of Ammonia Injection [°CA ATDC]

TSOI Total Start of Injection [°CA BTDC]

 φ Equivalence Ratio [-]

References:

- [1] P. M. Kadam, D. R. Dolas, S. Pal, and S. S. Gajghate, "Impact of Soybean Biodiesel Blends with Mixed Graphene Nanoparticles on Compression Ignition Engine Performance and Emission: An Experimental and ANN Analysis," *Int. J. Automot. Mech. Eng.*, vol. 21, no. 3, pp. 11512–11525, 2024, doi: 10.15282/ijame.21.3.2024.5.0888.
- [2] A. Valera-Medina et al., "Ammonia-methane combustion in tangential swirl burners for gas turbine power generation," Applied Energy, vol. 185, pp. 1362–1371, 2017, doi: 10.1016/j.apenergy.2016.02.073.
- [3] E. Spatolisano, L. A. Pellegrini, A. R. de Angelis, S. Cattaneo, and E. Roccaro, "Ammonia as a Carbon-Free Energy Carrier: NH3 Cracking to H2," *Ind. Eng. Chem. Res.*, vol. 62, no. 28, pp. 10813–10827, 2023, doi: 10.1021/acs.iecr.3c01419.
- [4] M. Zhou *et al.*, "Ammonia as an environmentally benign energy carrier for the fast growth of China," *Energy Procedia*, vol. 158, pp. 4986–4991, 2019, doi: 10.1016/j.egypro.2019.01.668.
- [5] G. Langella, M. De Joannon, P. Sabia, P. Iodice, and A. Amoresano, "Ammonia as a fuel for internal combustion engines: Latest advances and future challenges," *J. Phys. Conf. Ser.*, vol. 2385, no. 1, 2022, Art. no. 012036, doi: 10.1088/1742-6596/2385/1/012036.
- [6] A. Yapicioglu and I. Dincer, "A review on clean ammonia as a potential fuel for power generators,"

- Renew. Sustain. Energy Rev., vol. 103, pp. 96–108, 2019, doi: 10.1016/j.rser.2018.12.023.
- [7] W. Tutak, M. Pyrc, M. Gruca, and A. Jamrozik, "Ammonia Combustion in a Spark-Ignition Engine Supported with Dimethyl Ether," *Energies*, vol. 16, no. 21, p. 7383, 2023, doi: 10.3390/en16217283.
- [8] A. Valera-Medina, H. Xiao, M. Owen-Jones, W. I. F. David, and P. J. Bowen, "Ammonia for power," *Prog. Energy Combust. Sci.*, vol. 69, pp. 63–102, 2018, doi: 10.1016/j.pecs.2018.07.001.
- [9] M. Vijay Kumar, A. Veeresh Babu, and P. Ravi Kumar, "The impacts on combustion, performance and emissions of biodiesel by using additives in direct injection diesel engine," *Alexandria Eng. J.*, vol. 57, no. 1, pp. 509–516, 2018, doi: 10.1016/j.aej.2016.12.016.
- [10] L. Razzaq *et al.*, "Response Surface Methodology and Artificial Neural Networks-Based Yield Optimization of Biodiesel Sourced from Mixture of Palm and Cotton Seed Oil," *Sustain.*, vol. 14, no. 10, p. 6130, 2022, doi: 10.3390/su14106130.
- [11] İ. Temizer, Ö. Cihan, and B. Eskici, "Numerical and experimental investigation of the effect of biodiesel/diesel fuel on combustion characteristics in CI engine," *Fuel*, vol. 270, no. 3, 2020, Art. no. 117523, doi: 10.1016/j.fuel.2020.117523.
- [12] Y. Wang, X. Zhou, and L. Liu, "Theoretical investigation of the combustion performance of ammonia/hydrogen mixtures on a marine diesel engine," *Int. J. Hydrogen Energy*, vol. 46, no. 27, pp. 14805–14812, 2021, doi: 10.1016/j.ijhydene.2021.01.233.
- [13] S. Semin, A. Iswantoro, and F. Faris, "Performance and NOx Investigation on Diesel Engine using Cold EGR Spiral Tube: A Review," *Int. J. Mar. Eng. Innov. Res.*, vol. 1, no. 3, pp. 213–220, 2017, doi: 10.12962/j25481479.v1i3.2372.
- [14] K. Uddeen, Q. Tang, H. Shi, and J. W. G. Turner, "Ammonia-methanol and ammonia-ethanol dual-fuel combustion in an optical spark-ignition engine: A multiple flame generation approach," *Appl. Therm. Eng.*, vol. 265, 2025, Art. no. 125544, doi: 10.1016/j.applthermaleng.2025.125544.
- [15] A. A. Levikhin and A. A. Boryaev, "Low-carbon ammonia-based fuel for maritime transport," *Results Eng.*, vol. 25, 2025, Art. no. 104175, doi: 10.1016/j.rineng.2025.104175.
- [16] M. Alnajideen *et al.*, "Ammonia combustion and emissions in practical applications: a review," *Carbon Neutrality*, vol. 3, no. 1, p. 13, 2024, doi: 10.1007/s43979-024-00088-6.
- [17] C. Park *et al.*, "Investigation on the reduction in unburned ammonia and nitrogen oxide emissions from ammonia direct injection SI engine by using SCR aftertreatment system," *Heliyon*, vol. 10, no. 18, 2024, doi: 10.1016/j.heliyon.2024.e37684.
- [18] M. A. Asokan, S. S. Prabu, S. Prathiba, V. S. Akhil, L. D. Abishai, and M. E. Surejlal, "Emission and performance behaviour of flax seed oil biodiesel/diesel

- blends in di diesel engine," *Mater. Today Proc.*, vol. 46, no. 17, pp. 8148–8152, 2021, doi: 10.1016/j.matpr.2021.03.108.
- [19] S. S. Wirawan, M. D. Solikhah, H. Setiapraja, and A. Sugiyono, "Biodiesel implementation in Indonesia: Experiences and future perspectives," *Renew. Sustain. Energy Rev.*, vol. 189, no. 6, 2024, Art. no. 113911, doi: 10.1016/j.rser.2023.113911.
- [20] V. K. Shahir, C. P. Jawahar, and P. R. Suresh, "Comparative study of diesel and biodiesel on CI engine with emphasis to emissions A review," *Renew. Sustain. Energy Rev.*, vol. 45, pp. 686–697, 2015, doi: 10.1016/j.rser.2015.02.042.
- [21] E. Nadimi, G. Przybyła, T. Løvås, and W. Adamczyk, "Effects of biodiesel injector configuration and its injection timing on performance, combustion and emissions characteristics of liquid ammonia dual direct injection engine," *J. Energy Inst.*, vol. 114, 2024, Art. no. 101605, doi: 10.1016/j.joei.2024.101605.
- [22] P. Dimitriou and R. Javaid, "A review of ammonia as a compression ignition engine fuel," *Int. J. Hydrogen Energy*, vol. 45, no. 11, pp. 7098–7118, 2020, doi: 10.1016/j.ijhydene.2019.12.209.
- [23] S. Babamohammadi, A. R. Birss, H. Pouran, J. Pandhal, and T. N. Borhani, "Emission control and carbon capture from diesel generators and engines: A decade-long perspective," *Carbon Capture Sci. Technol.*, vol. 14, 2025, Art. no. 100379, doi: 10.1016/j.ccst.2025.100379.
- [24] A. Valera-Medina *et al.*, "Review on ammonia as a potential fuel: From synthesis to economics," *Energy and Fuels*, vol. 35, no. 9, pp. 6964–7029, 2021, doi: 10.1021/acs.energyfuels.0c03685.
- [25] R. Payri, J. M. García-Oliver, G. Bracho, and J. Cao, "Experimental characterization of direct injection liquid ammonia sprays under non-reacting diesel-like conditions," *Fuel*, vol. 362, 2024, Art. no. 130851, doi: 10.1016/j.fuel.2023.130851.
- [26] Z. Huang, H. Wang, Q. Meng, K. Luo, and J. Fan, "Combustion Characteristics of Liquid Ammonia Direct Injection Under High-Pressure Conditions Using DNS," *Energies*, vol. 18, no. 9, p. 2228, 2025, doi: 10.3390/en18092228.
- [27] K. Ryu, G. E. Zacharakis-Jutz, and S. C. Kong, "Effects of gaseous ammonia direct injection on performance characteristics of a spark-ignition engine," *Appl. Energy*, vol. 116, pp. 206–215, 2014, doi: 10.1016/j.apenergy.2013.11.067.
- [28] E. Nadimi, G. Przybyła, T. Løvås, G. Peczkis, and W. Adamczyk, "Experimental and numerical study on direct injection of liquid ammonia and its injection timing in an ammonia-biodiesel dual injection engine," *Energy*, vol. 284, 2023, Art. no. 129301, doi: 10.1016/j.energy.2023.129301.
- [29] X. Zhou *et al.*, "Ammonia marine engine design for enhanced efficiency and reduced greenhouse gas emissions," *Nat. Commun.*, vol. 15, no. 1, p. 2120, 2024, doi: 10.1038/s41467-024-46452-z.

- [30] E. Nadimi, G. Przybyła, D. Emberson, T. Løvås, Ł. Ziółkowski, and W. Adamczyk, "Effects of using ammonia as a primary fuel on engine performance and emissions in an ammonia/biodiesel dual-fuel CI engine," *Int. J. Energy Res.*, vol. 46, no. 11, pp. 15347–15361, 2022, doi: 10.1002/er.8235.
- [31] A. Yousefi, H. Guo, S. Dev, B. Liko, and S. Lafrance, "Effects of ammonia energy fraction and diesel injection timing on combustion and emissions of an ammonia/diesel dual-fuel engine," *Fuel*, vol. 314, Art. no. 122723, 2022, doi: 10.1016/j.fuel.2021.122723.
- [32] K. Ramalingam *et al.*, "An experimental and ANN analysis of ammonia energy integration in biofuel powered low-temperature combustion engine to enhance cleaner combustion," *Case Stud. Therm. Eng.*, vol. 63, 2024, Art. no. 105284 doi: 10.1016/j.csite.2024.105284.
- [33] M. Elkelawy, H. A. Bastawissi, M. O. Elsamadony, and A. Salem, "Investigation into the Impact of Ammonia Hydroxide on Performance and Emissions in Compression Ignition Engines Utilizing Diesel / Biodiesel Blends," *J. Eng. Res. Vol.*, vol. 8, no. 1, pp. 1–16, 2024.
- [34] M. Elkelawy, H. Alm ElDin Mohamad, M. Samadony, and A. Abdalhadi, "Utilization of Ammonia Hydroxide /Diesel Fuel Blends in Partially Premixed Charge Compression Ignition (PPCCI) Engine: A Technical Review," *J. Eng. Res.*, vol. 7, no. 3, pp. 319–331, 2023, doi: 10.21608/erjeng.2023.234219.1229.
- [35] S. Wüthrich, P. Cartier, P. Süess, B. Schneider, P. Obrecht, and K. Herrmann, "Optical investigation and thermodynamic analysis of premixed ammonia dualfuel combustion initiated by dodecane pilot fuel," *Fuel Commun.*, vol. 12, 2022, Art. no. 100074, doi: 10.1016/j.jfueco.2022.100074.
- [36] C. Cheng, R. F. Cordtz, N. L. Førby, and J. Schramm, "Experimental and simulation investigation of nheptane/ammonia dual fuel on a light-duty compression ignition engine," *Int. J. Hydrogen Energy*, vol. 57, pp. 1339–1353, 2024, doi: 10.1016/j.ijhydene.2024.01.130.
- [37] A. Uyumaz *et al.*, "Experimental investigation on the combustion, performance and exhaust emission characteristics of poppy oil biodiesel-diesel dual fuel combustion in a CI engine," *Fuel*, vol. 280, 2020, Art. no. 118588, doi: 10.1016/j.fuel.2020.118588.
- [38] R. Elumalai, K. Ravi, P. V. Elumalai, M. Sreenivasa Reddy, E. Prakash, and P. Sekar, "Development of an ammonia-biodiesel dual fuel combustion engine's injection strategy map using response surface optimization and artificial neural network prediction," *Sci. Rep.*, vol. 14, no. 1, p. 543, 2024, doi: 10.1038/s41598-023-51023-1.
- [39] İ. Temizer and Ö. Cihan, "International Journal of Automotive Engineering and Technologies Investigation of combustion and emission in a DI diesel engine fueled with hydrogen-biodiesel blends," *Int. J. Automot. Eng. Technol.*, vol. 8, no. 4, pp. 150–164, 2019.

- [40] M. Ince, S. Çelebi, U. Demir, and C. Haşimoğlu, "Evaluating Engine Performance, Emissions, Noise, and Vibration: A Comparative Study of Diesel and Biodiesel Fuel Mixture," *Int. J. Automot. Sci. Technol.*, vol. 8, no. 3, pp. 288–302, 2024, doi: 10.30939/ijastech.1495167.
- [41] E. Nadimi, G. Przybyła, M. T. Lewandowski, and W. Adamczyk, "Effects of ammonia on combustion, emissions, and performance of the ammonia/diesel dual-fuel compression ignition engine," *J. Energy Inst.*, vol. 107, 2023, Art. no. 101158, doi: 10.1016/j.joei.2022.101158.
- [42] D. R. MacFarlane *et al.*, "A Roadmap to the Ammonia Economy," *Joule*, vol. 4, no. 6, pp. 1186–1205, 2020, doi: 10.1016/j.joule.2020.04.004.
- [43] J. S. Cardoso, V. Silva, R. C. Rocha, M. J. Hall, M. Costa, and D. Eusébio, "Ammonia as an energy vector: Current and future prospects for low-carbon fuel applications in internal combustion engines," *J. Clean. Prod.*, vol. 296, 2021, Art. no. 126562, doi: 10.1016/j.jclepro.2021.126562.
- [44] A. Yapicioglu and I. Dincer, "Performance assessment of hydrogen and ammonia combustion with various fuels for power generators," *Int. J. Hydrogen Energy*, vol. 43, no. 45, pp. 21037–21048, 2018, doi: 10.1016/j.ijhydene.2018.08.198.
- [45] W. S. Chai, Y. Bao, P. Jin, G. Tang, and L. Zhou, "A review on ammonia, ammonia-hydrogen and ammonia-methane fuels," *Renew. Sustain. Energy Rev.*, vol. 147, 2021, Art. no. 111254, doi: 10.1016/j.rser.2021.111254.
- [46] R. Sivasubramanian, J. B. Sajin, and G. Omanakuttan Pillai, "Effect of ammonia to reduce emission from biodiesel fuelled diesel engine," *Int. J. Ambient Energy*, vol. 43, no. 1, pp. 661–665, 2022, doi: 10.1080/01430750.2019.1663367.
- [47] Z. Chen, Y. Wan, O. I. Awad, and Z. Pan, "Effect of Multiple Injection Strategy Under High Ammonia Ratio on Combustion and Emissions of Liquid Ammonia/Diesel Dual DI Engine," *Atmosphere*, vol. 16, no. 1, p. 94, 2025, doi: 10.3390/atmos16010094.
- [48] K. A. Pedersen, M. T. Lewandowski, C. Schulze-Netzer, M. Pasternak, and T. Løvås, "Ammonia in Dual-Fueled Internal Combustion Engines: Impact on NOx, N2O, and Soot Formation," *Energy and Fuels*, vol. 37, no. 22, pp. 17585–17604, 2023, doi: 10.1021/acs.energyfuels.3c02549.
- [49] A. Hayakawa, T. Goto, R. Mimoto, Y. Arakawa, T. Kudo, and H. Kobayashi, "Laminar burning velocity and Markstein length of ammonia/air premixed flames at various pressures," *Fuel*, vol. 159, pp. 98–106, 2015, doi: 10.1016/j.fuel.2015.06.070.
- [50] E. Pv *et al.*, "Split injection timing optimization in ammonia/biodiesel powered by RCCI engine," *Results Eng.*, vol. 23, 2024, Art. no. 102607, doi: 10.1016/j.rineng.2024.102607.
- [51] A. M. Elbaz, S. Wang, T. F. Guiberti, and W. L. Roberts, "Review on the recent advances on ammonia combustion from the fundamentals to the

- applications," *Fuel Commun.*, vol. 10, 2022, Art no. 100053, doi: 10.1016/j.jfueco.2022.100053.
- [52] A. Motevali, N. Hooshmandzadeh, E. Fayyazi, M. Valipour, and J. Yue, "Environmental Impacts of Biodiesel Production Cycle from Farm to Manufactory: An Application of Sustainable Systems Engineering," *Atmosphere*, vol. 14, no. 2, p. 399, 2023, doi: 10.3390/atmos14020399.
- [53] R. Senthil, R. Silambarasan, and N. Ravichandiran, "Influence of injection timing and compression ratio on performance, emission and combustion characteristics of Annona methyl ester operated diesel engine," *Alexandria Eng. J.*, vol. 54, no. 3, pp. 295–302, 2015, doi: 10.1016/j.aej.2015.05.008.
- [54] E. Ramachandran *et al.*, "Multicriteria Decision-Making Technique for Choosing the Optimal Ammonia Energy Share in an Ammonia-Biodiesel-

- Fueled Reactivity-Controlled Compression Ignition Engine," *ACS Omega*, vol. 9, no. 5, pp. 5203–5214, 2024, doi: 10.1021/acsomega.3c04005.
- [55] M. Yazdi, E. Zarei, S. Adumene, and A. Beheshti, "Navigating the Power of Artificial Intelligence in Risk Management: A Comparative Analysis," *Safety*, vol. 10, no. 2, p. 42, 2024, doi: 10.3390/safety10020042.
- [56] V. Sharma, A. Panesar, G. de Sercey, and S. Begg, "A Review of Ammonia Combustion and Emissions Characteristics in Spark-Ignition Engines and Future Road Map," *Energies*, vol. 18, no. 1, p. 41, 2025, doi: 10.3390/en18010041.